Chair of Applied Geophysics

Doctoral Thesis

Blast Array Optimization for Vibration Reduction in Heterogeneous Models

Dipl.-Ing. Bernd Trabi, BSc

August 2024

MONTANUNIVERSITÄT LEOBEN
www.unileoben.ac.at

AFFIDAVIT

I declare on oath that I wrote this thesis independently, did not use any sources and aids other than those specified, have fully and truthfully reported the use of generative methods and models of artificial intelligence, and did not otherwise use any other unauthorized aids.

I declare that I have read, understood and complied with the "Good Scientific Practice" of the Montanuniversität Leoben.

Furthermore, I declare that the electronic and printed versions of the submitted thesis are identical in form and content.

Date 19.08.2024

Signature Author
Bernd Trabi

Acknowledgements

I would like to thank Prof. Florian Bleibinhaus for his guidance and support throughout my PhD thesis.
I am also deeply grateful to my wife Lara Emmanuelle Garrido Trabi for her love, patience and support. Her understanding and encouragement were crucial to the completion of this work. In particular, the last few weeks and months have tested her patience and required significant sacrifice, for which I am deeply thankful.
Special thanks go to my PhD fellow student Cornelia Tauchner for her contributions in planning the first field campaigns, the preparatory work and for the creation of the 3D velocity model, where the forward simulations are done.
I am also thankful to my PhD fellow student Damian Pasiecznik and all the students who helped deploy the seismic stations. Their hard work was crucial for the data collection and the overall success of this study.
Special thanks go to Peter Schimek from the mine operator VA Erzberg, who provided crucial support for the station deployments and the coordination with the blasters.
I would also like to thank the secretary of the Chair of Applied Geophysics, Christiane Pretzenbacher, for her administrative support and help in ensuring the smooth running of this research.
Last but not least, I am very grateful to my family, friends and colleagues for their constant support. Thank you all for your support and encouragement.

Abstract

Predicting Peak Ground Velocity (PGV) is crucial for blast mining operations to ensure that the charge weights are designed to stay within safe limits and to prevent surrounding structures from potential damage. The problem is often complicated by significant scatter in observed PGV, mainly due to unknown complexities of seismic wave propagation. It is difficult to estimate the contribution of each wave type to the PGV, as it involves a mix of overlapping seismic phases. The data generally suggest that the direct P-wave is the primary contributor. Traditional PGV prediction models often rely on empirical approaches, and the Scaled Distance (SD) method is particularly popular. This method, which has the fewest parameters to calibrate, is also effective for single-sensor setups. A dataset of 55 mining production blasts recorded with an array of 81 seismic sensors is used to compare the performance of different methods. The large array also allows to apply a multi-sensor inversion that provides more insight into the physical parameters. The findings reveal that the classical SD approach underperforms at this particular site, mainly because the empirical relationship between the radial amplitude decay constant b and charge weight exponent c does not hold in this context. The determined charge weight exponent value of 0.5 likely reflects a fundamental physical relationship between charge, energy, and amplitude, suggesting its potential applicability across various sites. A new numerical prediction method is presented based on forward-modelled waveforms on a 3D velocity model. The numerical simulations were done with the Barcelona Subsurface Imaging Tools for 80 predefined blast positions. The final data is then further processed to simulate future blasts at arbitrary positions with a realistic source time function and amplitude spectrum. The numerical method can simulate waveforms that match well with the observed waveforms, at least in the P-wave window. The observed data show no clear S-wave but a considerable amount of surface waves, which cannot be reflected by the numerical waveform modelling method. Even though the method can predict PGV, which is a highly non-linear measure, PGV prediction is outperformed by simple engineering methods. With the interference of seismic waves from spatially separated production blasts, a reduction in impact on specific target zones should be achievable. While modifying the blast pattern in a homogeneous model to minimize the effect on a specific target zone is relatively straightforward, it is challenging to find such optimal configurations in a complex numerical model that includes velocity variations and topography. A Markov Chain Monte Carlo (McMC) method is used to find such a configurations. The cost function of the McMC seeks to minimize the PGV in certain target zones. These derived configurations were later implemented in real production blasts.

Zusammenfassung

Die Vorhersage der maximalen Bodengeschwindigkeit (Peak Ground Velocity, PGV) ist für Sprengungen im Bergbau entscheidend, um sicherzustellen, dass die Sprengladungen so dimensioniert sind, dass sie innerhalb sicherer Grenzen bleiben und potenzielle Schäden an umliegenden Strukturen vermieden werden. Das Problem wird oft durch eine erhebliche Streuung des beobachteten PGV erschwert, hauptsächlich aufgrund der unbekannten Komplexitäten der Ausbreitung seismischer Wellen. Die Schätzung des Beitrags jeder Wellenart zum PGV ist schwierig, da es eine Mischung überlappender seismischer Phasen beinhaltet. Die Daten deuten allgemein darauf hin, dass die direkte P-Welle der Hauptbeitragende ist. Traditionelle PGV-Vorhersagemodelle basieren oft auf empirischen Ansätzen, wobei die Skalierte Entfernungs-Methode (Scaled Distance, SD) besonders beliebt ist. Diese Methode, welche die geringste Anzahl an zu kalibrierenden Parametern aufweist, funktioniert auch für Einzelmessstellen. Ein Datensatz von 55 Sprengungen im Bergbau, der von einem Array von 81 seismischen Sensoren aufgezeichnet wurde, wird verwendet, um die Leistung verschiedener Methoden zu vergleichen. Das große Array ermöglicht auch die Anwendung einer Multi-Sensor-Inversion, die tiefere Einblicke in die physikalische Bedeutung verschiedener Parameter bietet. Die Ergebnisse zeigen, dass der klassische SD-Ansatz an diesem speziellen Standort unterperformt, hauptsächlich weil die empirische Beziehung zwischen dem radialer Amplitudenabfallkoeffizienten b und dem Ladungsgewichtsexponenten c in diesem Kontext nicht gilt. Der ermittelte Wert des Ladungsgewichtsexponenten von 0,5 spiegelt wahrscheinlich eine grundlegende physikalische Beziehung zwischen Ladung, Energie und Amplitude wider, was auf seine potenzielle Anwendbarkeit an verschiedenen Standorten hindeutet. Eine neue numerische Vorhersagemethode wird vorgestellt, die auf vorwärtsmodellierten Wellenformen in einem 3D-Geschwindigkeitsmodell basiert. Die numerischen Simulationen wurden mit den Barcelona Subsurface Imaging Tools für 80 vordefinierte Sprengpositionen durchgeführt. Die endgültigen Daten werden dann weiterverarbeitet und kalibriert, um zukünftige Sprengungen an beliebigen Positionen mit einer realistischen Quellzeitfunktion und einem realistischen Amplitudenspektrum zu simulieren. Die numerische Methode kann Wellenformen simulieren, die zumindest im P-Wellen-Fenster gut mit den beobachteten Wellenformen übereinstimmen. Die beobachteten Daten zeigen keine klaren S-Wellen, aber eine beträchtliche Menge an Oberflächenwellen, die durch die numerische Wellenformmodellierung nicht erfasst werden können. Obwohl die Methode das PGV vorhersagen kann, was ein stark nichtlineares Maß darstellt, wird die PGV-Vorhersage durch einfache ingenieurtechnische Methoden übertroffen. Mit der Interferenz seismischer Wellen aus räumlich getrennten Produktionssprengungen sollte eine Reduzierung der Auswirkungen auf spezifische Zielzonen erreichbar sein. Während die Anpassung des Sprengmusters in einem homogenen Modell zur Minimierung der Wirkung auf eine spezifische Zielzone relativ einfach ist, ist es schwieriger solche optimalen Konfigurationen in einem komplexen numerischen Modell, das Geschwindigkeitsvariationen und Topographie beinhaltet, zu finden. Eine Markov-Ketten-Monte-Carlo-Methode (McMC) wird verwendet, um solche Konfigurationen zu finden. Die Kostenfunktion der McMC zielt darauf ab, das PGV in bestimmten Zielzonen zu minimieren. Diese Konfigurationen wurden später bei echten Produktionssprengungen verwendet.

Contents

List of Figures

List of Tables

List of Recurring Abbreviations and Symbols

$\Delta\tau$	Delay time between blastholes
γ	Acceptance ratio in Metropolis-Hastings Algorithm
κ	Global site-factor
ρ_j	Site-factor of recording position j
β_i	Site-factor of blasting position i
σ	Standard deviation
q	Maximum charge per delay
c	Weighting exponent for q
r	Offset of recording position to hole with q
b	Exponent for radial spatial decay of amplitude
BSIT	Barcelona Subsurface Imaging Tools
CBG	Common Blast Gather
CRG	Common Receiver Gather
DEM	Digital Elevation Model
DIN	Deutsches Institut für Normung, is the German Institute for Standardization, responsible for developing and publishing norms and standards in Germany
DSU-SA	Stand-alone 3-component Digital Sensor Unit
HPC	High Performance Computing
LDI	Laplace Domain Inversion
McMC	Markov chain Monte Carlo
NONEL	Non-electric detonation system
PGV	Peak Ground Velocity
R^2	Coefficient of determination
RAU-D	Digital Remote Acquisition Unit
RMS	Root Means Square
SD	Scaled Distance
SEGD	Specialized format, which is intended for field recordings of seismic data
SEGY	Standard file format used in the geophysical industry for storing and exchanging seismic data
SLIM	Sustainable Low Impact Mining
STF	Source Time Function
SU	Seismic Unix, is a data processing software package and format used for processing and analysing seismic reflection data in geophysics
USBM	United States Bureau of Mines
xcc	Cross-correlation coefficient

1 Introduction

In the mining industry, explosives are primarily used to break up rock to facilitate the extraction of valuable minerals and ores. They enable the efficient removal of large quantities of material, increase productivity, and reduce the cost and time required for mining operations. Most of the energy from production blasts is used for crushing the rock mass, but an estimated 5-10% is released as seismic energy (Ouchterlony et al., 2004). This seismic energy can cause adverse effects, such as ground vibrations in the surrounding area of the mine. For this reason, it is crucial to generate reliable ground vibration predictions and maintain safety in the surrounding areas.
A key measure of the strength of vibrations caused by blasting is the Peak Ground Velocity (PGV). PGV represents the maximum vector sum of the three components of a velocity seismogram. However, predicting PGV is challenging due to its non-linearity, spatial variability, and the connected poor prediction quality. Underestimations may cause harm in the form of unintended structural damage, negative ecological effects, and accidents that can threaten human life. Therefore, the mining industry is constantly searching for approaches that not only predict the seismic impact of its activities but also find methods to reduce it. The production blasts can be optimized to reduce the impact of the seismic energy. The optimization of blasting operations is a very important issue both as a step toward efficient operation and as a means of environmental protection and safe operation of nearby buildings and communities. Before optimizing, it is important to be able to model blast vibrations from production blasts.
Hinzen (1988) developed, a hybrid method for modelling blast vibrations from production blasts. Hybrid denotes as a combination of field measurement and computer simulation. This method uses the recording of the seismic signal from a single hole charge in-situ, which captures the seismic energy radiation and travel path filtering effects. Assuming linear superposition, the vibrations from multiple holes in a production blast are simulated by convolving the single shot signal with an impulse series which is representing the firing sequence. The method assumed that the source time functions (STF) are identical, and although the spatial distribution of the sources was ignored, the synthetic seismogram and the data showed excellent fit. The study highlights the potential for reducing the PGV by optimizing firing times, which can be achieved through electronic initiation systems. While this method shows effectively how to predict and reduce blast vibrations for the specific blast site, it is difficult to apply it on large scale mines with different blast sites. Prior to modelling, single blasts would be required at all blast sites, which is not preferred by mining operators and could lead to interruptions in mining operations.
Mansouri & Farsangi (2015) built their study on Hinzen's work by applying the method to a more complex and varied set of field data. They expanded the scope by conducting multiple blasts (single-hole and double-hole) and taking measurements at seven points. They also studied the effects of medium and distance on simulation results and examined the linearity or non-linearity of blast vibration superposition with distance from the blast. They validated the method and compared synthetic seismograms with measured ones, which showed excellent fit. Also a strong agreements between the measured and observed frequency spectra was observed.
Blair (1993) investigated strategies to minimize blast-induced vibrations, particularly in urban areas near mining operations. The frequency domain approach uses the Fourier transform to convert vibration signals from the time domain to the frequency domain, which facilitates the analysis of the spectral components. The full vibration spectrum is derived from delay times and random fluctuations between blastholes, with spectral control investigated by calculating the amplitude response of the

blast vibrations. It was shown that optimal delay times should lie in the range of 10-35 ms, and for effective vibration control, it was necessary to have a highly accurate electronic ignition system. Random fluctuations significantly affect the predictability of the spectrum.

Bleibinhaus & Trabi (2023) discussed the principles of blast array design for vibration reduction. Their analysis of the frequency-domain interference term provides general guidelines for choosing delay time intervals that minimize ground vibrations. The interference term's spectral density predicts amplitude maxima and notches, which are useful for designing blast arrays. To apply their guidelines, a single blast's dominant frequencies must be known. They developed a parametric Laplace-domain model to predict STFs for mine blasts that accounts for the dependency of the signal bandwidth on the charge weight. Their study included the relatively small spatial component of the delay, which was seen in the observed Doppler shifts. They modelled waveforms of production blasts, which showed a highly variable waveform match. They showed that a significant mismatch is not due to an erroneous STF model but to unaccounted site response functions and path effects. Their parametric STF provides a basis for more realistic waveform predictions, considering the test site's strong topography and variable lithology.

This thesis aims to further enhance the prediction and reduction of blast-induced vibrations and to provide a more generalized and scalable solution across different mining sites by developing a new numerical prediction method based on forward-modelled waveforms.

To simulate production blasts, forward-modelling of seismic waveforms was performed using a 3D velocity model that included topography. The computations were done using the Barcelona Subsurface Imaging Tools (BSIT), with wave fields pre-computed on the 3D model of Mt. Erzberg (Tauchner et al., 2018). This forward-modelled data was used to identify blasting configurations that minimize seismic effects on target areas by optimizing blasting parameters. A Markov Chain Monte Carlo (McMC) technique, specifically the Metropolis-Hastings algorithm, was employed to find the optimized blast configurations. These configurations were later tested in verification experiments. This research was funded by the European Union's Horizon 2020 research and innovation programme under grant agreement 730294 SLIM: Sustainable Low Impact Mining (SLIM). The project aims to develop cost-effective and sustainable low-impact mining solutions. One sub-project focuses on developing a vibration reduction technique based on the spatial interference of vibrations discussed in Bleibinhaus & Trabi (2023). The interference of vibrations is achieved through spatially separated production blasts. Verifying the potential success of these experiments was challenging. Due to the complexity of such double blasts in mining operations, only 8 of the 15 planned for the project were ultimately conducted. These blasts were temporally spread out for logistical reasons, leading to three follow-up experiments in 2019 and 2020. This staggered approach proved advantageous, allowing for iterative learning and improvement, with apparent deficiencies in the modelling being addressed. In total, eight double blasts were simulated and practically executed.

Before predictions can be made by forward-modelling, it is important to characterise the site and seismic phases. In two case studies, Gao et al. (2018) investigated the contribution of various wave types from vertical blastholes. The first case study, involving four vertical blastholes, was conducted during the foundation excavation of a plunge pool for a hydroelectric power plant. Three geophones were deployed for monitoring, with two of them placed in very close proximity (within 8 m), and one positioned at a distance of 70 m. The second case study, consisting of six blasts, was conducted in a geological exploration tunnel, with nine geophones spaced unevenly along the tunnel at distances of up to 150 m. However, the blasting parameters, with hole depths ranging from 4.5 to 8.0 m and charge weights up to 12.0 kg, are not comparable to those used in the mining operations at Mt. Erzberg. The

hodogram analysis they conducted revealed that for a vertical blasthole, the P-wave is a significant component in both near and far fields. It becomes the dominant wave beyond a distance of r = 2.3 h, where r is the radius and h is the height of the blast column.
Using a hodogram analysis of the Erzberg data, it was not possible to determine seismic phases. Due to the long blast sequence, all seismic phases overlap in most of the data. Therefore, Chapter 4 provides a general overview of the data and attempts to identify the different seismic phases. Then theoretical foundations of the state-of-the-art engineering PGV prediction methods, which are typically used by mining operators, are established in Chapter 5. Empirical formulas and traditional techniques, such as the Scaled Distance (SD) approach, are explored and compared for their effectiveness using a comprehensive dataset from multiple production blasts. The chapter also examines multi-sensor inversions to gain deeper insights into the physical parameters influencing PGV, highlighting the limitations and potential improvements of these conventional methods. The content of that entire chapter has already been published in a paper of Trabi & Bleibinhaus (2023). However, the thesis includes some minor modifications and additional deeper insights. Chapter 6 describes the numerical method, in which waveforms are forward-modelled to simulate real-world production blasts and the associated blast vibrations. The aim of the work is to reduce the PGV in certain target areas by the interference of double blasts based on a numerical simulation of waveforms. Therefore, a significant part of the thesis focuses on the quality and improvement of seismic waveform predictions for production blasts with the numerical approach. To achieve the best results, the numerical approach has to be properly calibrated. The calibration and evaluation of this method is presented in Chapter 7. This chapter also discusses the feasibility and reliability of PGV predictions with the numerical forward-modelling method.
The spatio-temporal time delay between blasts influences the interference pattern and can be adjusted by the spatial distance between blasts. Since the spatial distance of production blastholes cannot be altered, the only feasible approach is initiating spatially separated production blasts and identifying suitable delay times that cause negative interference in specific target areas. A production blast has a very wide-band signal; therefore, the distance between the blasts and the number of simultaneously performed blasts play a significant role in reducing PGV in a specific target area. The blasting officer of the mining operator, VA Erzberg, did not allow to perform blasts with more than 150 m distance because of safety concerns. Also, the number of blasts was restricted to a maximum of two. It was necessary to work with predetermined blast configurations determined by the mining operator. This blast configuration will be referred to as double blasts. Double blasts are a combination of two blast arrays from different tiers, designed to control radiation patterns. Without all these constraints, there are likely better blast configurations, with more than two production blasts and different distances, to minimize the PGV at certain target areas. Such configurations could have been investigated in a pre-study. However, this step has been skipped due to constraints of the mining operator, and therefore, not having the possibility to choose the desired configuration. Chapter 8 continues with fundamentals of the McMC method and how delay times are perturbed to find a configuration that minimizes the impact at the target areas. It presents theoretical case studies for PGV reductions at certain target areas. In these target areas, the seismic waves are supposed to interfere destructively, which should result in a lower PGV. Chapter 9 evaluates the production blasts conducted in a real experiment with optimized delay times. Unfortunately, due to the project's tight time constraints, delay time optimization had to be performed before the first verification experiment and before quality assurance was completed. Due to the discomfort by the mining operator during double blasting operations, the resulting dataset is statistically insignificant. With such a small dataset, it is difficult to successfully

demonstrate a PGV reduction within the target areas.
In general, this work aims to improve the understanding of blast prediction and enhance the possibilities for mining operators to conduct safer and lower-impact mining operations. Overall, mining should become more sustainable and careful, causing less harm to the area and reducing the likelihood of endangering nearby communities and the environment.

2 Test Site

2.1 Overview

The mine at Mt. Erzberg is situated in central Austria, in the Eastern Alps (Fig. 1). The blue rectangle on the map outlines the study area. Managed by VA Erzberg GmbH, the mine is considered one of the largest iron ore deposits in Europe and looks back on at least 1,300 years of mining history (Sperl, 1984). It is located in close vicinity to the city of Eisenerz (Fig. 2). The city lies in the valley, located north and west of the mine. To this day, the mine is of supra-regional importance and it has the exclusive status of being Austria's only iron ore production facility. The mined ore concentrate plays an important role in steel production, especially in the industrial centres of Linz and Donawitz.
The mine has significantly altered the topography of the 1465 m high mountain through extensive mining activities, leading to approximately 40 tiers with an height between 20 and 24 meters. Every workday two production blasts are being shot, which creates noticeable vibrations for the residents of the neighbouring town of Eisenerz.

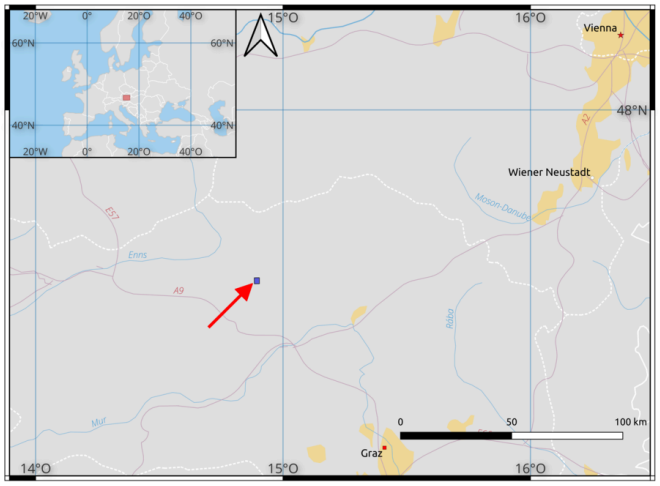

Figure 1: The location of the Mt. Erzberg mine. The red arrow points at the location of the study area (Fig. 2).[1]

The buildings, predominantly residential buildings, are located mainly on top of the sedimentary fill (Fig. 2). Green and black crosses on the map represent blastholes from the observed production blasts, some of them are located near the residential buildings. The green crosses on the map are different from the black ones because they represent production blasts, which were blasted simultaneously, with the specific aim of actively reducing the PGV on certain target zones.

[1] Vector and raster map data - naturalearthdata.com.

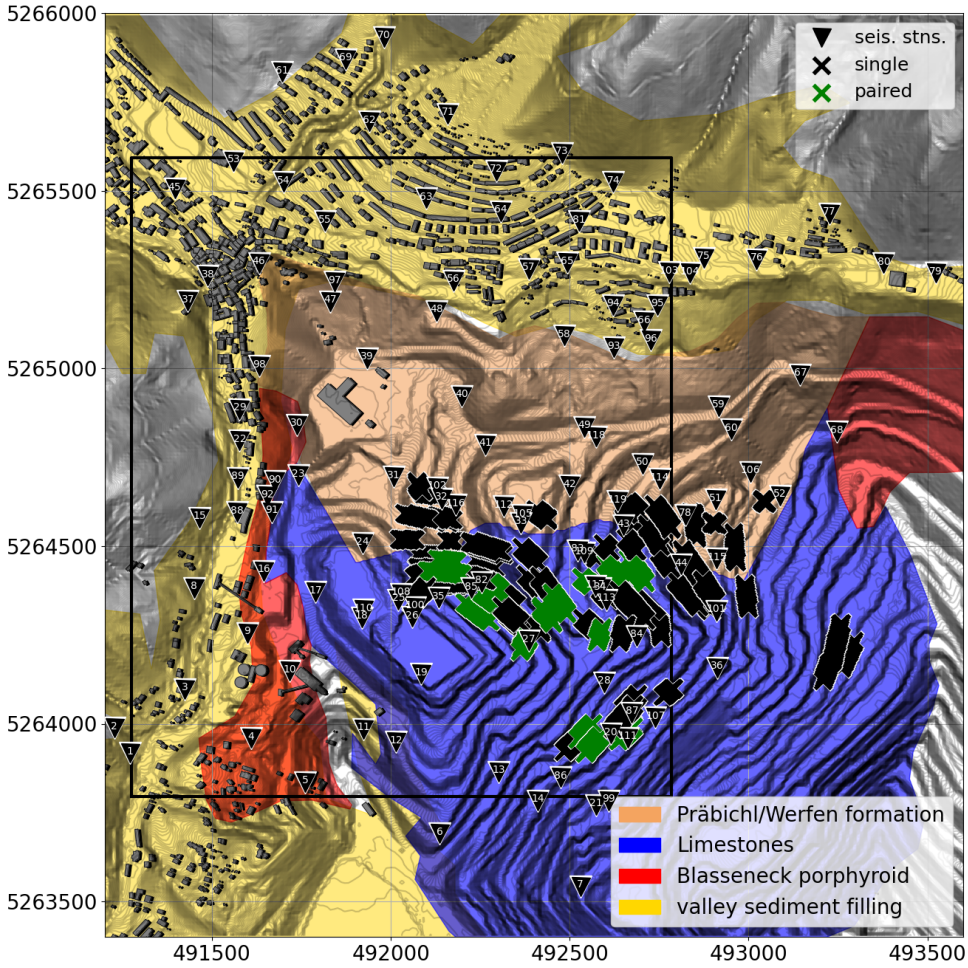

Figure 2: A relief map of Mt. Erzberg and surroundings with geology overlaid. Buildings are marked by grey polygons on the map and they are predominantly residential buildings. Distinct tiers indicate the area of the mine. Inverted triangles are recording positions and crosses are blastholes. The green crosses on the map are different from the black ones because they represent production blasts, which were blasted simultaneously. The numerical forward-modelling was done for the area within the black rectangle.[1,2]

[1]Geological map and DEM data source: CC-BY-4.0: State of Styria - data.steiermark.gv.at
[2]Building polygons source: www.openstreetmap.org. The data is made available under ODbL.

2.2 Geology

The Erzberg mine hosts the world's largest siderite deposit, a mineral predominantly associated with sedimentary and vein-type iron ore formations. Siderite exhibits a complex genesis, discussed in Ebner et al. (2000); Prochaska (2012) and Schulz et al. (1997). The siderite deposits are actively mined and found in some European and Mediterranean countries. One example is the Erzberg mine in Austria, the only existing one doing iron mining in the country. The geology of the Erzberg is characterized by Variscan nappes, which are structured into a syncline (Fig. 3). The hanging wall of the mountain is mainly Permoscythian Präbichl and Triassic Werfen formations, which consist of conglomerates, sandstones and shales. Both layers lie uniformly on the ore-bearing formation. In the southern and deeper sections of the mine much of the hanging wall has been excavated, but to the north remnants of the Werfen Formation remain overlying the ore-rich strata (Fig. 2). The ore bodies at Mt. Erzberg are embedded in thick limestone layers from the Silurian-Devonian period. They are part of the Upper Variscan tectonic unit (Schönlaub, 1982). The seismic velocity for the ore body is expected to reach up to 6950 m/s for the P-wave and 3590 m/s for the S-wave. The P-wave velocity for the limestone is expected to range between 3700 and 6250 m/s, while the S-wave velocity is expected to range between 2000 and 3700 m/s (Schön, 2011). Schmidbauer (2023) confirmed the P-wave velocities for the limestones, which range between 3500 m/s and 6600 m/s, and for the orebody, which reached up to 6900 m/s in laboratory measurements. The densities have also been measured and confirm the values in the literature (Schön, 2011). The densities of the limestones range between 2.3 and 2.75 g/cm^3 and those of the siderite reach up to 3.9 g/cm^3. This significant variation in velocity and density is not expected to significantly influence the seismic wavefield at the expected frequency below 30 Hz, as the ore bodies are dispersed within the limestones. The footwall of the Erzberg consists of Late Ordovician Blasseneck porphyry, an igneous rock formed by volcanic activity and part of the deeper Variscan unit. Schön (2011) estimates the velocities for the porphyry to range between 4200 and 5850 m/s for the P-wave and between 2600 and 3250 m/s for the S-wave. The density is expected to range between 2.6 and 2.8 g/cm^3. The region is also defined by the Christoph Fault, an east-dipping normal fault with a dip angle of 20 to 30 degrees (Schönlaub, 1982; Schulz et al., 1997). The valley is covered with a sedimentary filling. The related amplification of seismic amplitudes increases the seismic hazard. In earthquake and engineering seismology it is well known that such site effects can amplify or deamplify seismic motions just before reaching the ground or the basement of man-made structures (Kawase, 2003). For more detailed information on the geology of Mt. Erzberg, see Ebner et al. (2000), Neubauer (1994), Prochaska (2012), Schulz et al. (1997) and Schönlaub (1982).

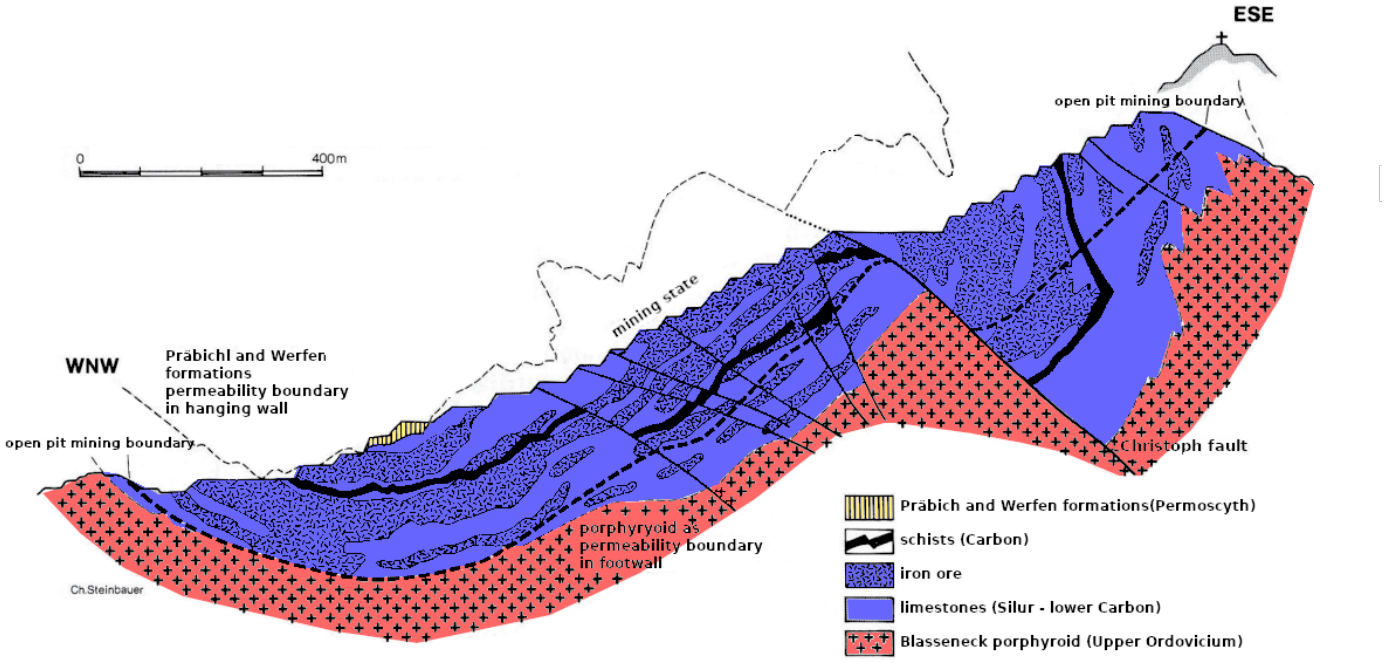

Figure 3: Geological cross-section through the Styrian Erzberg siderite deposit (Schönlaub, 1982)

2.3 The Model of Mt. Erzberg

In November 2016 a seismic characterization experiment was performed at the Erzberg mine. The kinematic evaluation of this experiment was carried out by Tauchner et al. (2018). The main objective of this experiment was to constrain the P-wave velocities at the area of interest. A total of 125 3-component geophones were distributed over a 4 km^2 area in and around the mine. During the deployment period, 21 seismic blasts with an explosive charge of 0.5 to 2 kg and 10 production blasts were conducted. Production blasts have a high signal-to-noise ratio and the uncertainty of the extracted P-wave travel time ranges from 5 ms at near offsets to 15 ms at far offsets. For the seismic shots, the recovery of travel times was below 50%, but they still contributed to covering areas that would otherwise have been missed. In this velocity characterization experiment, they could not extract S-wave travel times. To get a P-wave velocity model from the P-wave travel times they applied an inverse algorithm after Thurber (1983) and Bleibinhaus & Gebrande (2006). The forward calculation was done with an Eikonal solver after Vidale (1990) with modifications for head waves by Hole & Zelt (1995). They chose a simple 1D velocity model for the first starting model with a velocity of 4000 m/s at 1100 m altitude with a vertical gradient of 1 s^{-1}. Due to the lack of seismic sources in the valley, the sediments could not be resolved. Since the valley sediments may significantly affect wave propagation, they manually introduced them into the starting model. The geometrical structure was constrained using a polynomial fitting approach (Pomper et al., 2017). Valley depths can reach up to approximately 150 m. They assumed the velocity to be 2000 m/s with a gradient of 4 s^{-1} resulting in a velocity of 2740 m/s at the base. They introduced the valley structure into the velocity model through a local grid refinement with a 70 m spacing. Outside the valley a horizontal spacing of 420 m was chosen, because that produced more stable results. Vertically a denser spacing of

60 m was used for altitudes with a good ray coverage. Figure 4a shows the final P-wave velocity model Tauchner et al. (2018) obtained from this first arrival travel time tomography. Figure 4b depicts the ray coverage and locations of the sources. The inversion process began with a starting model with a relatively high Root Mean Square (RMS) residual of 31 ms. After ten iterations, this residual was reduced to 11 ms. Considering that they estimated a data uncertainty between 5 and 15 ms, this is an acceptable outcome. The final model has relatively sharp valley boundaries that were introduced as a prior through the local grid refinement. In that fine parametrized valley, the velocity changes in the inversion process were suppressed by the damping factor.

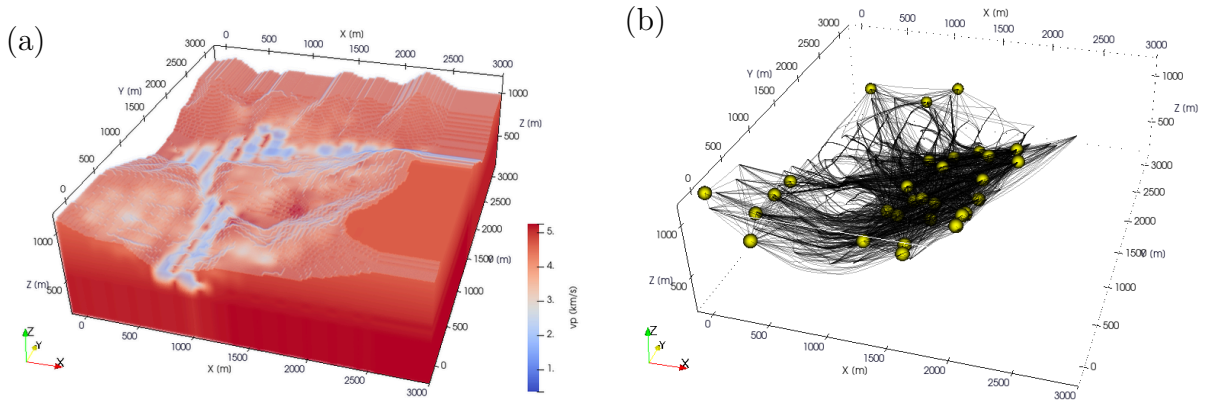

Figure 4: (a) A 3D block view of the 3D velocity model of Mt. Erzberg and (b) the corresponding ray path distribution. The yellow spheres are the blast positions.

3 Mining Process

The mine at Mt. Erzberg is an open pit mine, one of the surface mining methods typically employed to exploit near-surface, non-selective, and low-grade deposits. The advantages of this method include high productivity, low cost, flexibility, and the absence of underground hazards. However, the downsides are significant environmental and visual impacts, as well as the large area required for waste management (Awwad et al., 2021). The iron ore deposit at Mt. Erzberg is mined by drilling and blasting to fracture the rock. In some areas the Werfen Formation overlays the ore-rich strata which requires extensive blasting work to clear the overlying layers and facilitate access to the deposits below. The blastholes are drilled in specific single and multiple-row patterns. After blasting, the fractured rocks are loaded into trucks with front-end loaders and transported for further processing. The blasting operation itself has a significant impact on the local community, and production blasts are typically initiated with non-electric (NONEL) delay detonators . For this study, the type and accuracy of the ignition system are of great importance, while the type of explosive is of lesser significance. Since a very similar explosive composition is used in all blastholes and in most blasts even an identical one, this plays no role in the applied interference approach, especially for a relative PGV reduction. The mining operator, only considers the total amount of explosive for the prediction, although a prediction of the absolute PGV has to be done.

3.1 Production Blasts

In mining operations, production blasts are a crucial part of the process, as they break down the rock and facilitate the excavation of minerals. A production blast typically involves the sequential time delayed detonation of several cylindrical charge columns in blastholes. The number of blastholes for each production blast ranges from 4 to 34 (Fig. 5) with an average of 15 holes. The holes are 15-30 m deep with a spacing of 6 m between the holes. The delay time is a critical parameter that directly affects the efficiency and safety of the blast. They are generally limited to a minimum of 8 ms and maximum of 60 ms. According to Duvall et al. (1962), the maximum charge weight is defined as the maximum amount of explosives that can be detonated within 8 ms. With a shorter delay time, the maximum explosive amount could be exceeded. This limitation is in place to ensure that the blast does not surpass the legal limit and becomes a safety hazard. The maximum delay is specified by the mine operator, as longer delays can lead to unfavourable rock fragmentation. Exemplary configurations of single-row production blasts are shown in Figure 6a, and double-row configurations are shown in Figure 6b. These figures illustrate how blastholes (red and black dots) are typically arranged on the mine site. The numbers next to the blastholes indicate delay times in milliseconds relative to the first ignited blasthole (red dot).

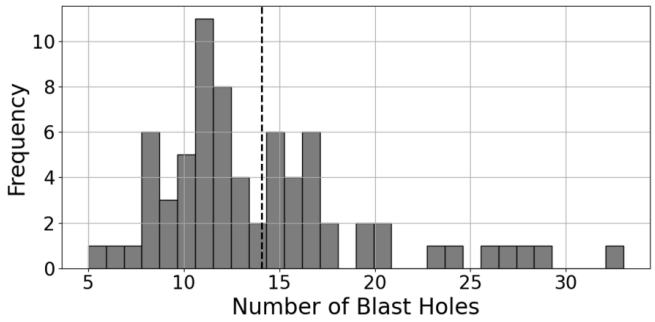

Figure 5: Histogram of the number of blastholes per production blast for the whole dataset.

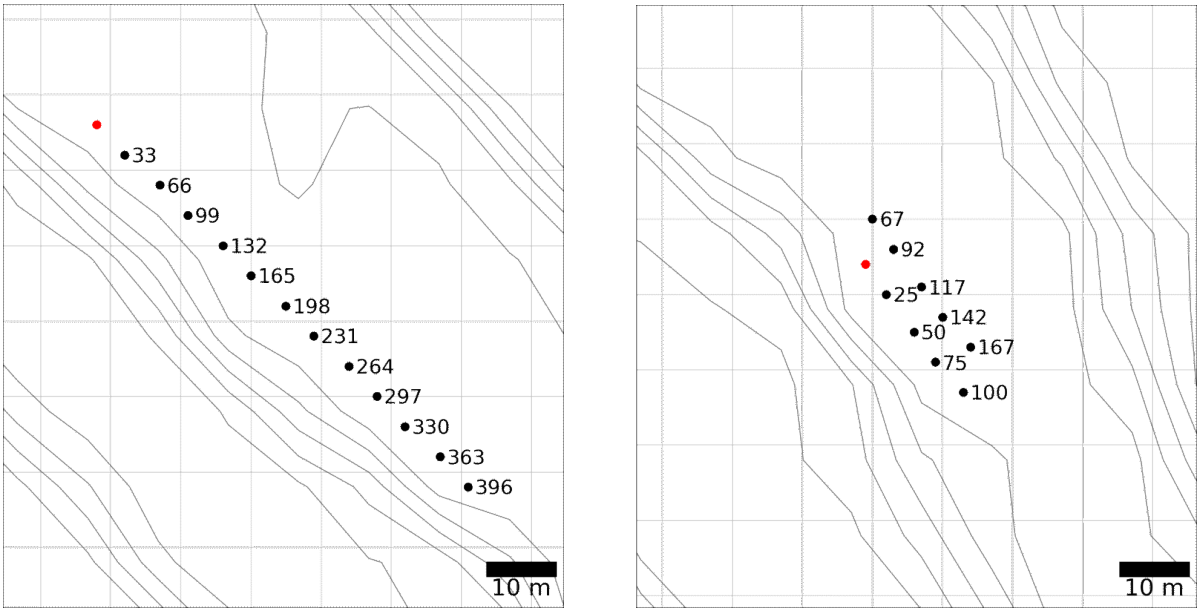

(a) (b)

Figure 6: Maps of two exemplary blasthole configurations for (a) a single-row blast and (b) a double row blast. The red dot indicates the first ignited blasthole and the labels are the delay times relative to the first hole given in milliseconds.

3.2 Ignition

A considerable amount of energy is required to initiate a high explosive, like it is used for production blasts. These high explosives are initiated by a detonator, which is a capsule containing a series of relatively sensitive explosives that can be readily initiated by an outside energy source (Dick et al., 1983). In this study, two different ignition systems were used. The standard NONEL system which is normally used in the mine and precise electronic detonators ensure exact and absolute ignition times for the experiments.

3.2.1 NONEL Detonators

NONEL detonators are non-electrical delay detonators that are activated by a mild detonation that propagates in tubes containing explosive material. Typical delay times of 17 ms, 25 ms, 33 ms, 42 ms and 67 ms are achieved by surface delay connectors. An additional downhole delay of 0.5 seconds is added to prevent cut-off and misfire due to rock movement caused by the detonation of a previous hole (Dick et al., 1983). The additional downhole delay is responsible for an significant additional delay time inaccuracy. For single-row production blasts, the mining operator, VA Erzberg, typically uses a 33 ms time delay between holes (Fig. 6a). In multiple-row production blasts, a 25 ms time delay between holes within a specific row is used, and the second row starts to ignite with an additional delay of 67 ms (Fig. 6b). This pattern can be extended to three or more rows. The theoretical minimum delay time between two holes of different rows is 8 ms in such a configuration.
However, these detonators exhibit a large delay time inaccuracy, often several milliseconds, attributed to the influence of chemical properties. In a small experiment the precise ignition times of eight NONEL detonators with a 33 ms delay were measured. The experiment was carried out by C. Tauchner, and D. Don from Chair of Applied Geophysics, P. Schimeck from VA Erzberg, G. Wölfler and T. Seidl from Chair of Mining Engineering and Mineral Economics. The result of the experiment is summarized in Table 1. Although measurements for holes 6 and 8 are unavailable, the limited data shows a RMS residual of 10.9 ms from their expected ignition time.

Number of hole	1	2	3	4	5	6	7	8
τ_{obs} [ms]	0	39.5	75.5	107.5	144	-	217	-
τ_{exp} [ms]	0	33	66	99	132	165	198	231
$\tau_{\text{obs}} - \tau_{\text{exp}}$ [ms]	0	6.5	9.5	8.5	12	-	19	-

Table 1: Comparison of observed τ_{obs} and expected τ_{exp} delay times, along with their differences $\tau_{\text{obs}} - \tau_{\text{exp}}$, at the blastholes.

The delay time interval in Table. 1 appears to be higher than the nominal 33 ms. Bleibinhaus & Trabi (2023) already estimated a delay time interval closer to 38.5 ms, based on the observed resonance mode of 26 Hz in the frequency spectrum. In Figure 7, the observed delay times follow a trend line with a steeper slope than the trend line of the expected delay times. This discrepancy can be explained by an incorrect accounting of the detonation speed inside the NONEL tube. The slope in the figure suggests that the delay time interval is approximately 35.8 ms instead of the expected 33 ms. Nevertheless, the RMS residual of the line fit is surprisingly low, at approximately 1.6 ms.
Both of these discrepancies, the high RMS residual and the consistent deviation from the expected delay time interval, are very unlikely to affect the outcome of a single-row blast. In multi-row blasts,

with a minimum delay of 8 ms between two holes in different rows (Fig. 6b), both effects, the large scatter of 10.9 ms and the systematic shift to longer delay times can result in significant overlap of ignition times between blastholes from different rows. Only precise absolute delay timing can ensure that there is no overlapping. Such large deviations from the ignition time of the NONEL system are unacceptable for our purposes.

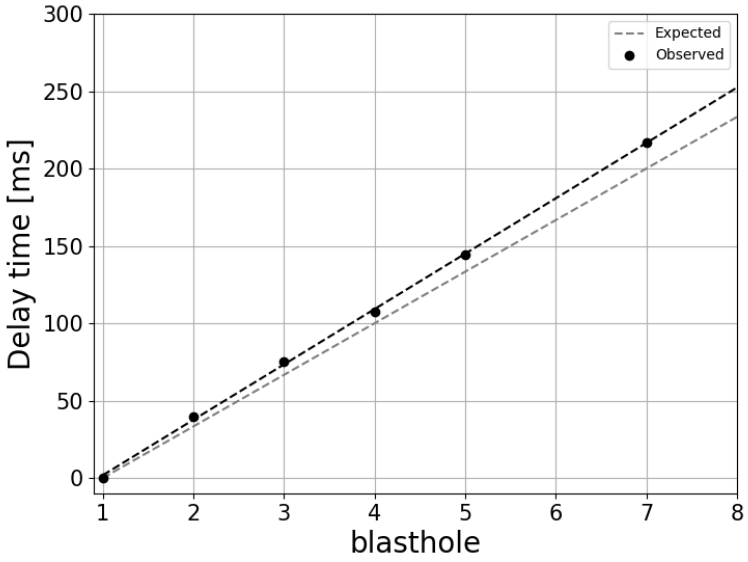

Figure 7: Comparison of Observed and Expected delay times vs. number of holes. The plot displays the observed delay times (black dots) and expected delay times (grey dashed line) as functions of the number of holes.

3.2.2 Electronic Detonators

For electronic detonators, the time delays are provided by the microelectronic circuitry of a microchip which feeds the main ignition current usually from an internal capacitor (Persson et al., 1994). The used electronic detonators in the mine were provided by MAXAM and they have a programmable delay time from 0 ms to 14,000 ms with increments of 0.5 ms. These detonators guarantee an absolute time basis with sub-ms delay time accuracy, because they don't need a fuse like the NONEL detonators.

3.3 Explosives

The explosives used in the mine include ammonium nitrate emulsion, ammonium nitrate fuel oil, and heavy ammonium nitrate fuel oil, with and without the addition of aluminium grit. The differences in blast properties of the explosives are discussed by Kramarczyk et al. (2020). As mentioned at the beginning of this chapter the actual composition of the explosives not significant for the relative reduction. Therefore, only the total amount of explosives is considered, irrespective of the individual properties. The amount of explosive ranges from 20 kg to 740 kg per hole with an average value of 300 kg (Fig. 8a). The relative standard deviation of the amount of explosive within one production

blast is below 20% for approximately half of the blasts (Fig. 8b). This number represents the variability of charge amount within a production blast. For example, a low number means, that all blasts have a similar charge amount.

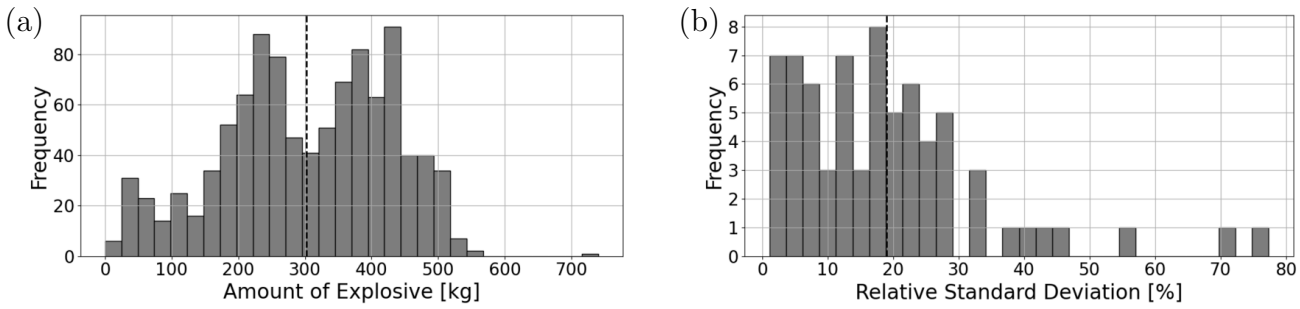

Figure 8: Histograms for (a) the amount of explosive per hole and (b) the relative standard deviation of the amount of explosive per production blast, both for the whole dataset.

3.4 Regulatory Context and Legal Limits

Mining operators in Austria must follow the Mining Explosive Ordinance (Bergbau-Sprengverordnung). For hazard identification and assessment, they must forecast the expected PGV. The PGV is the maximum resulting vibration velocity given in [mm/s]. The PGV is calculated as the maximum of the vector sum of the seismogram of the three translatory directions:

$$PGV = max(v_R) \tag{1}$$
$$v_R = \sqrt{v_x^2(t) + v_y^2(t) + v_z^2(t)}$$

According to the Mining Explosive Ordinance, the measuring devices should be able to resolve at least 1 mm/s. The device should preferably record velocity, but acceleration measurement with subsequent integration is also allowed. Measuring devices are suitable if they have a three-component sensor for a frequency range of at least 2 to 100 Hz. If the prognosis exceeds the maximum allowed legal threshold, the charge quantity per time delay has to be changed or a measure with the same effect must be taken. The same measures have to be taken if a measurement already exceeded the legal threshold. The Mining Explosive Ordinance gives frequency dependent reference values for three different building sensitivity classes (Fig 9). They are classified into commercially used and industrial buildings (solid line), residential buildings (dashed line), and particularly vibration-sensitive buildings like listed monuments (dash-dotted line). These are reference values at the foundation of a building. If no empirical or measured values are available, the accompanying frequency is assumed to be 10 Hz. These values are the same as in the German standard *DIN 4150*. Chapter 5 goes into more detail on how mine operators make their predictions.

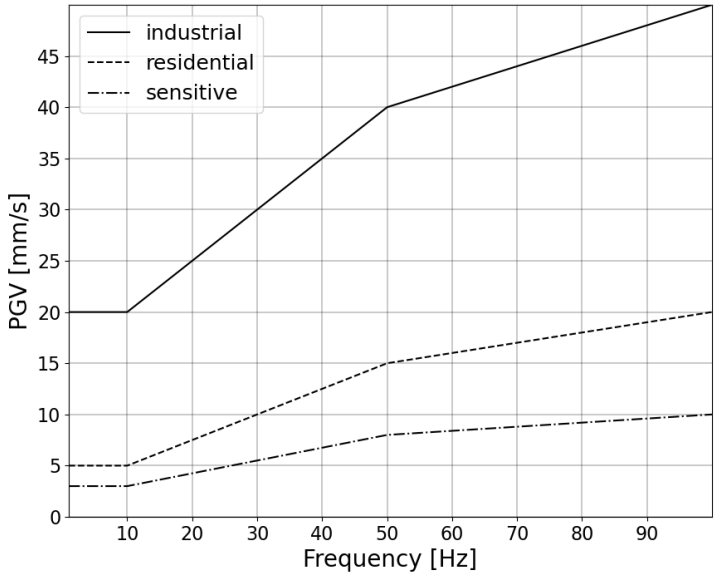

Figure 9: Frequency-dependent reference values for PGV at the foundation according to the Mining and Explosive Ordinance.

4 Survey and Data

4.1 Overview

During four field campaigns in 2016, 2019, and 2020, a total of 75 production blasts and 21 seismic shots were recorded using different receiver arrangements (Fig. 10).
The first deployment was a seismic site characterization experiment, while the subsequent three campaigns were conducted as verification experiments. A total of 66 of these production blasts were shot as normal production blasts, while 8 were conducted as double blasts using electronic detonators. Of the 66 standard production blasts, 16 were shot with standard delay times and electronic detonators, 35 were shot with standard delay times and NONEL detonators, and 15 were shot with optimized blast delay times and electronic detonators.

4.2 Seismic Site Characterization Experiment

The primary purpose of the first field campaign in 2016 was to collect data for travel time tomography. The secondary objective was to gather first information about blast-induced vibrations, with a focus on the far-field. Overall, 125 three-component seismic stations, equipped with 4.5 Hz geophones, were deployed in a relatively regular spacing of ∼200 m (Fig. 10a). The seismic stations were provided by the Geophysical Instrument Pool Potsdam (GIPP), Germany. The sampling interval was set to 2.5 ms. In the four weeks of the deployment data of 10 production blasts and 21 small-scale seismic blasts was collected. All ten production blasts were ignited with NONEL detonators and relative delay times. Attempts to constrain the delay times from the data failed (Reiner, 2018). That prohibited the further analysis of this data regarding the interference of seismic wavefields. The kinematic analysis of those data is discussed in Tauchner et al. (2019), and some of the dynamic aspects in Bleibinhaus & Trabi (2023). This study focuses on data acquired in the three verification experiments conducted in 2019 to 2020.

4.3 Verification Experiments

Several verification experiments were carried out. The follow-up tests were necessary for two main reasons. First, obvious deficiencies in the numerical forward-modelling approach were eliminated over time, and the seismograms became more realistic as a result. Second, the VA Erzberg did not adhere to the agreement set out in SLIM to carry out the 15 planned double blasts.

4.3.1 Receivers

In the verification experiment, Sercel's digital Remote Acquisition Units (RAU-D), which record data autonomously, were used. The RAU-D powers and acquires data from a stand-alone 3-component Digital Sensor Unit (DSU3-SA). The DSU3-SA units were based on Micro-machined Electro-mechanical Sensors (MEMS) and they measure acceleration with a flat amplitude response. Because the internal batteries with 8.4 V and 14 Ah just have a battery life of up to 110 hours of recording, additional external batteries with 12 V and 18 Ah were added to all RAUs to extend the battery life for another 180 h. The units recorded between 12 and 14 hours per day. About half of the sensors are located in soft sediments of varying thickness and the other half is located on top of solid rock (Fig. 2). The

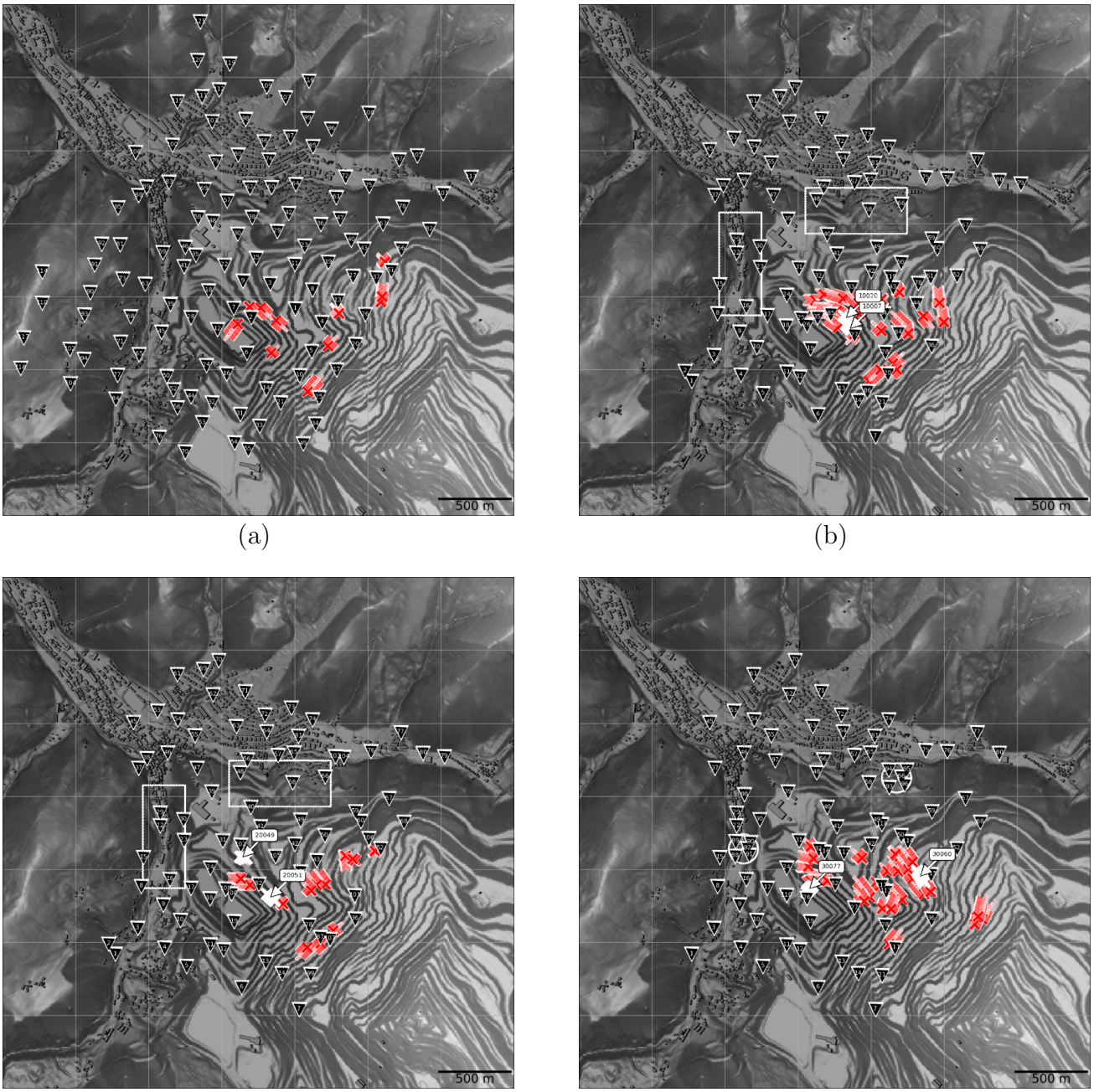

(a) (b) (c) (d)

Figure 10: Map of (a) the site characterization experiment in November 2016, (b) the first verification experiment in June/July 2019, (c) the second verification experiment in October 2019 and (d) the third verification experiment in August/September 2020. The red and white crosses indicate the positions of the production blast holes. The inverted triangles are the receiver positions. The white rectangles and circles outline the sensitive target zones.[1,2]

[1]DEM data source: CC-BY-4.0: State of Styria - data.steiermark.gv.at

[2]Building polygons source: www.openstreetmap.org. The data is made available under ODbL.

sensor units were put in the soil orientated to the north and covered with sand to protect them from unwanted noise (Fig 11). Inside the mine, drill holes had to be made for the placement of the DSU3-SA in the hard rock. The sampling rate was set to 2 ms for all three deployments and according to the Nyquist theorem, the maximum frequency that can be accurately recorded is 250 Hz. The coordinates of the stations are listed in the Appendix in Table 11, where the last 3 columns indicate in which of the three verification deployments the particular position was occupied. To avoid damage from production blasts, some stations within the mine were temporarily removed and when redeployed the previous position was sometimes not available, because of the mining operations.

4.3.2 Instrument Simulation

The data were harvested from the units, exported as SEGD files and converted into Seismic Unix (SU) files. The SU file format is a modification of the SEGY file format and it is used because the data processing is done with the SU software package. In the first step, all seismograms were adjusted by subtracting their mean value. Next a 0.5 Hz high-pass filter was applied to delete spurious or unrelated signals. To convert from sample to $[mV]$ the seismograms get multiplied by a conversion factor of $2.697 \times 10^{-4}\ mV$. To convert from $[mV]$ to $[m/s^2]$ the seismograms get divided by $452\,mV/m/s^2$, which is the sensor sensitivity of a DSU3-SA. Finally, the seismograms were integrated to obtain velocity, and the unit is converted from $[m/s]$ to $[mm/s]$ by multiplying by a factor of 1000. Now it is possible to derive the PGV in $[mm/s]$ directly from the amplitude of the seismogram.

Figure 11: DSU3-SA covered with sand and RAU-D deployed in a field outside the mine.

4.3.3 First Verification Experiment

In June 2019 79 seismic stations were deployed at the Erzberg mine for the first verification experiment. Where possible, the same positions were chosen as those used in the November 2016 experiment. The final receiver distribution is depicted in Figure 10b. The stations recorded continuously from June 3, 2019, to July 8, 2019, from 6 am to 8 pm. Data from 25 production blasts were collected during this deployment. One blast had to be rejected due to incomplete documentation, and three were performed as double blasts. 11 production blasts were shot with NONEL ignition system, 14 used electronic ignition, of which 3 were carried out as electronically shot double blasts.

4.3.4 Second Verification Experiment

A second verification experiment was conducted over two weeks, collecting data from production blasting between October 1 and 9, 2019. The receiver distribution is depicted in Figure 10c) and it is almost identical to the previous field campaign (Fig. 10b). Some stations within the mining area had slightly different locations, because of the mining operations. During this campaign, 11 regular production blasts with NONEL system and two electronic ignited double blasts were conducted.

4.3.5 Third Verification Experiment

During the third verification experiment in August/September 2020, a denser sensor spacing within the target zones was used. Stations were relocated from regions with closely neighbouring stations to achieve an increased density in the target zones (represented by white circles in Figure 10d). The goal was to better evaluate the PGV reduction in those zones compared to a regular production blast. Data from 26 production blasts were collected during this deployment. Four blasts were carried out using NONEL ignition systems, one of which had to be discarded due to incomplete documentation. 22 production blasts were electronically detonated, of which three were carried out as double blasts.

4.4 Data

In this subchapter, a closer examination of two representative production blasts from each verification experiment will be done. In general, the data from the production blasts show an excellent signal-to-noise ratio. The objective is to determine whether different seismic phases can be identified in the data and to observe which phase can be predominantly associated with the PGV.

4.4.1 First Verification Experiment

The first verification experiment production blasts, 10007 and 10020, were selected as representative examples for the examination. The locations of those production blasts are marked with white arrows in Figure 10b. Production blast 10007 used an average amount of explosives of 239 kg $\pm$ 12.8 kg, 17 holes and a constant blast delay of 33 ms between the blastholes, ignited by an electronic detonator. The ignition sequence lasted 0.528 s. Production blast 10020 used an average amount of 330 kg $\pm$ 3.9 kg of explosive per hole, with 11 holes and a variable ignition sequence totalling 0.356 s.
All seismogram sections show a distinct first arriving phase, identified as the P-wave, with an apparent velocity of approximately 4250 m/s. The seismogram sections are trace-normalized and time-reduced with the P-wave velocity (Fig. 12). For the vertical component a clear onset of the P-wave (Fig. 12e, f)

can be observed. After the onset of the P wave, the amplitude of the vertical component remains in the same range throughout the entire wave train, which corresponds to the duration of the blast sequence plus the length of the wavelet. With a wavelet length of estimated 0.1 s the wave train has a total length of 0.628 s. While this is also true for the inline and cross-line component for production blast 10007 (Fig. 12a, c), blast 10020 shows some later-occurring low-frequency phases with an apparent velocity of 1700 m/s in the respective components. This is significantly lower than the S-wave velocity one would expect for a Poisson body, of approximately 2400 m/s. This suggests that it is a surface wave, potentially generated by the conversion of the P-wave at the free surface. Alternatively, it could have been created by falling rock mass.

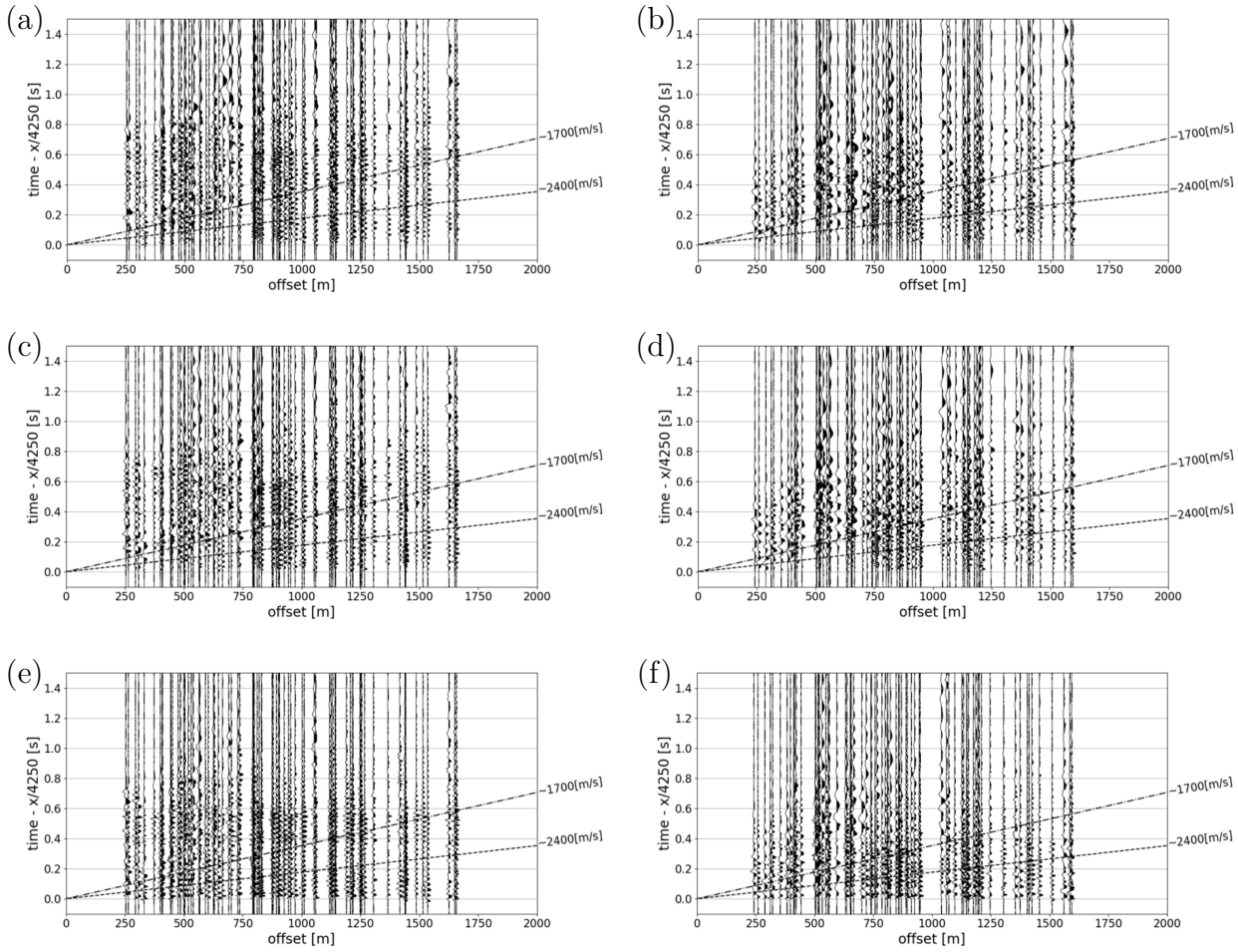

Figure 12: Trace-normalized time-reduced seismogram section of the (a, b) E-W, (c, d) N-S and (e, f) vertical component of production blast 10007 and 10020, respectively. Reducing velocity corresponds to the mean apparent P-wave velocity. Dashed lines mark the first arrival of the direct S-waves for a Poisson body. Dash-dotted lines mark the first arrival of the surface waves.

A production blast is a sequence of shots, each of which is expected to emit both P-waves and S-waves. A blast sequence can last up to 1 second. This means that direct S-waves from earlier blastholes can arrive before later P-waves. Consequently, S-waves from earlier ignited blastholes can arrive before P-waves from later ignited blastholes. Complete separation of P-waves and S-waves is only achievable

at very large offsets. The time windows of direct P- and S-wave arrivals separate only at about 2 km offset where we generally have no or very few, observations. The dark grey area indicates the time range within which the first and last P-waves are expected to arrive at a station. Similarly, the light grey area represents the corresponding time window for the S-waves. In this plot, the S-wave velocity was estimated to be 1.75 times slower than the P-wave velocity, as expected for a Poisson body. The medium grey area is the spatio-temporal area in which both phases are to be expected. The dash-dotted line indicates the earliest possible onset of the surface wave, with an estimated velocity of 1700 m/s. This estimated velocity stems from first observations of the 2016 survey. Also a seismic phase with an apparent velocity of around 1700 m/s can also be seen in the data of this experiment. The black dots indicate the times at which the PGV was measured in the observed data at each station, depending on the offset. For both blasts, the offset range was not large enough to have a complete temporal separation of P- and S-waves (Fig. 13). PGVs almost exclusively occur within the P-wave and mixed-phase windows. Notably, the PGVs are concentrated along the apparent velocity of the P-wave window, specifically at the beginning and end of the P-wave window for production blast 10007 (Fig. 13a). This production blast has the highest amount of explosive inside the last three holes (243-263 kg), and the first blasthole is likely to have better coupling compared to later blastholes due to the continuing destruction of the bench as subsequent blastholes ignite. This makes it likely that a PGV-causing phase is emitted either from the first hole with the best coupling or from the holes with the largest amount of explosive.

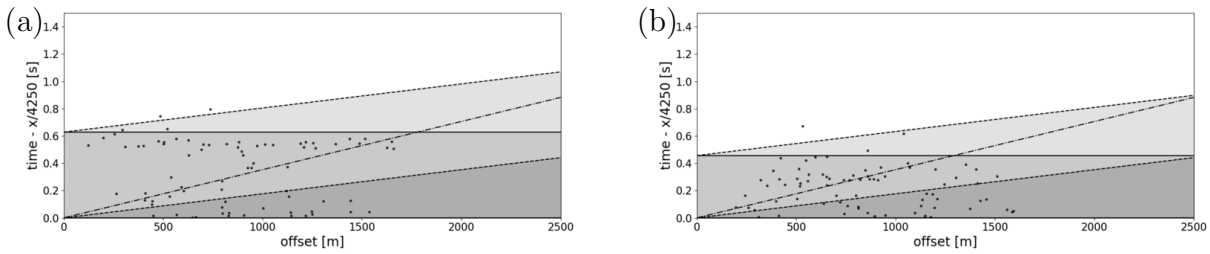

Figure 13: Time-reduced time windows of expected direct P- (dark grey) and S-wave arrivals (light grey) for blasts (a) 10007 and (b) 10020. Reducing velocity corresponds to the mean apparent P-wave velocity. The dash-dotted line is the expected surface wave arrival time. The dots mark the observed time of the occurrence of the PGV.

Production blast 10007 has a constant blast delay timing of 33 ms between the blastholes, ignited by electronic detonators and have therefore an accurate ignition timing. This can be observed through the strong resonance modes at multiples of 30 Hz in the amplitude spectrum (Fig. 14a). Production blast 10020 has variable blast delay times and the resonance modes are therefore not visible in the spectrum (Fig. 14b). The amplitude spectrum of both production blasts represents the mean spectrum of the trace-normalized z-component from all stations. For a discussion of the relation between delay times and resonance modes see, for example, Bleibinhaus & Trabi (2023).

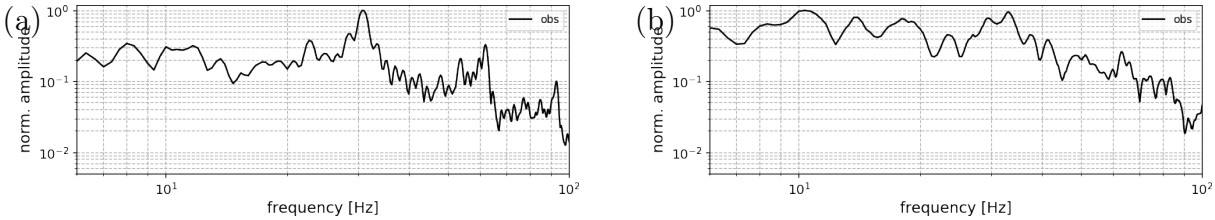

Figure 14: Normalized mean amplitude spectrum of production blasts (a) 10007 and (b) 10020.

4.4.2 Second Verification Experiment

For the second verification experiment, production blasts 20049 and 20051 were chosen as examples. The locations of those production blasts are marked with white arrows in Figure 10c. Production blast 20049 used an average amount of 464 kg $\pm$ 87.6 kg explosives of explosives across 12 holes, with a constant blast delay of 33 ms between the blastholes, ignited with NONEL detonators and an ignition sequence lasting 0.363 s. Production blast 20051 used an average amount of 253 kg $\pm$ 14.9 kg of explosives per hole, with a total of 13 holes, a constant blast delay of 33 ms between the blastholes, ignited by NONEL detonators and an ignition sequence lasting 0.396 s.
Again the trace-normalized and time-reduced seismogram sections (Fig. 15) show a clear onset of the P-wave, especially for the vertical component (Fig. 15e, f). In none of the production blasts, on any of the components, is a clear second phase visible, particularly for the vertical component. For the horizontal components in blast 10049 (Fig. 15a, c), one could argue that there is an onset of a low-frequency phase with the apparent velocity of the surface wave and an intercept of approximately 0.4 s.
A separation of P-wave and S-wave windows does not occur in these production blasts. For production blast 20049, the PGV time follows the apparent velocity of the P-wave, with the majority of the PGVs falling into the exclusive P-wave window (Fig. 16a). The blasthole with the largest amount of explosive is the 4th hole, with a total delay of approximately 99 ms, considering the inaccuracy of the NONEL ignition system and a charge weight of 290 kg in that particular hole. A trend line fit for that particular PGV cluster would result in an intercept time close to the ignition time of the 4th hole. In contrast, production blast 20051 does not show such a clear trend. The PGV times are completely randomly distributed, with the smallest number corresponding to the P-wave window.
Both production blasts where ignited by NONEL detonators resulting in no accurate ignition timing. Therefore, no resonance modes can be observed in the amplitude spectrum of production blast 20049 (Fig. 17a) and 20051 (Fig. 17b).

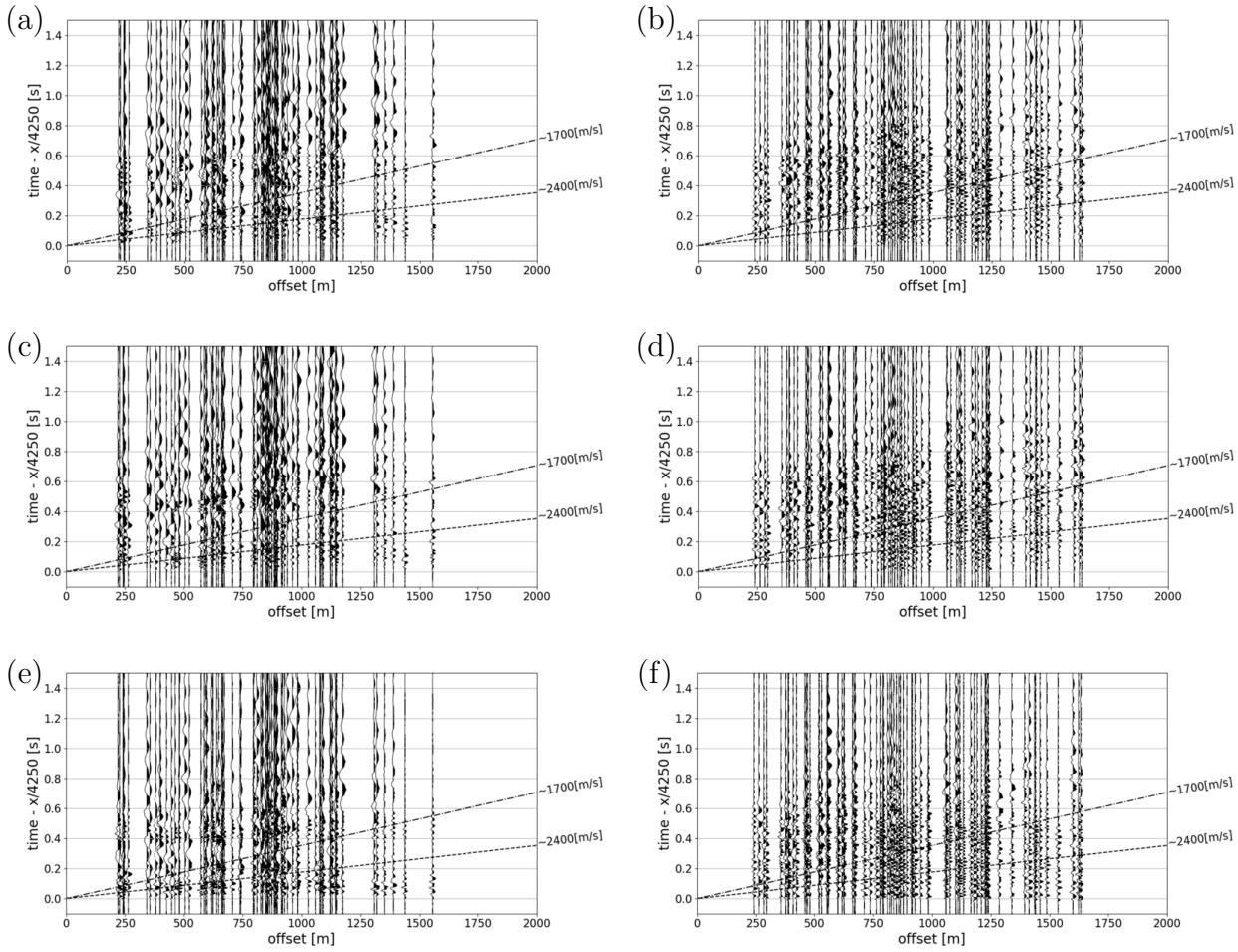

Figure 15: Trace-normalized time-reduced seismogram section of the (a, b) E-W, (c, d) N-S and (e, f) vertical component of production blast 20049 and 20051, respectively. Reducing velocity corresponds to the mean apparent P-wave velocity. Dashed lines mark the first arrival of the direct S-waves for a Poisson body. Dash-dotted lines mark the first arrival of the surface waves.

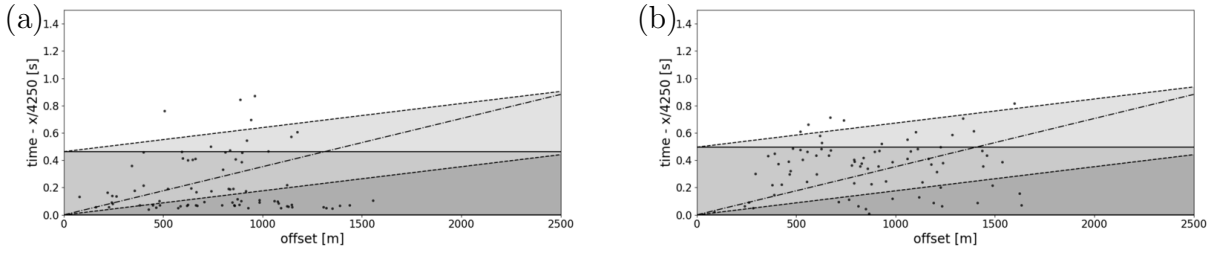

Figure 16: Time windows of expected direct P- (dark grey) and S-wave arrivals (light grey) for blasts (a) 20049 and (b) 20051. The dash-dotted line is the expected surface wave arrival time. The dots mark the observed time of the occurrence of the PGV.

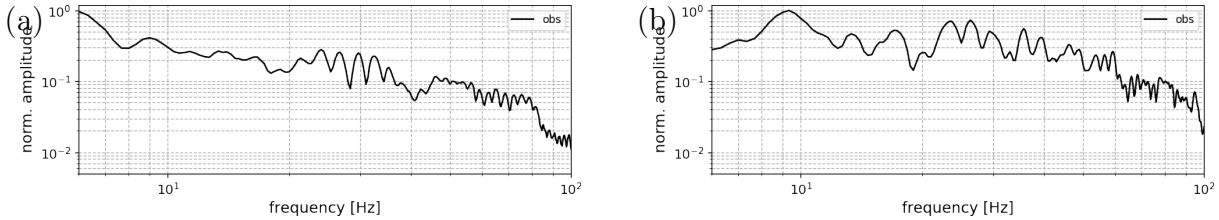

Figure 17: Normalized mean amplitude spectrum of production blasts (a) 20049 and (b) 20051.

4.4.3 Third Verification Experiment

For the third verification experiment, production blasts 30061 and 30077 were chosen as examples. The locations of those production blasts are marked with white arrows in Figure 10d. Production blast 30061 used an average amount of explosives of 332.5 kg ± 28.8 kg, with 5 holes and a variable blast delay timing. The blast sequence is particularly short, lasting only 0.091 s, and therefore it is more likely that temporal a separation of the seismic phases can be recognized. Production blast 30077 used an average amount of 215.4 kg ± 49.2 kg of explosive per hole, with a total of 12 holes and a variable blast delay timing between the blastholes. The high standard deviation for this blast is somewhat misleading because the first blasthole contained only 60 kg of explosive, while the following holes each contained a nearly similar amount of explosives of approximately 230 kg.
For production blast 30061, the P-wave arrival time is visible in the vertical component, along with a strong, very low-frequency phase occurring after the surface wave arrival time (Fig. 18e). This strong phase is even more dominant in the horizontal components (Fig. 18a,c), clearly showing an apparent velocity of approximately 1700 m/s. An S-wave is not observable. One reason for the clearly visible surface wave is the complete separation of both wavefields at a 500 m offset. Nevertheless, this production blast has more low frequencies than the majority of the production blasts. For production blast 30077, the P-wave onset is visible in the vertical component (Fig. 18f), while the amplitude slightly increases in the horizontal components after the expected surface wave onset (Fig. 18b,d). Noteworthy is the relatively high amplitude, just below 0.35 s, which follows the P-wave velocity, with the intercept indicating that it originates from the last blasthole. Since all blastholes, except the first one, contain a similar amount of explosive, this is likely due to the coupling of that particular hole.
The P-wave and S-wave windows are fully separated at a distance of approximately 1000 meters for production blast 30061 (Fig. 19a). A large portion of the PGVs occur after the last S-wave arrival in the surface wave window, suggesting they likely originate from the surface wave, with only a small part falling within the P-wave window. The minority of the PGVs fall within the mixed phase and the S-wave window. Nevertheless, a cluster, following the P-wave window can be observed. In the second example from that field campaign, blast 30077, no spatio-temporal separation of the seismic phases can be expected, but it has a cluster of PGV times following the apparent P-wave velocity near the end of the time window (Fig. 19b). A phase with particularly high amplitude, following the apparent P-wave velocity with the same intercept time, was already visible in the seismogram of the vertical component (Fig. 18f). This confirms that, in this particular case, the PGV is mainly caused by a P-wave, while the previous example indicates that the PGV is primarily caused by surface waves. This highlights the presence of unpredictable factors that are difficult to capture by any prediction method.
Because of the variable delay times of both production blasts resonance modes are not visible in both spectrums (Fig. 20a and 20b). The spectrum of production blast 30061 is notably lower in frequency.

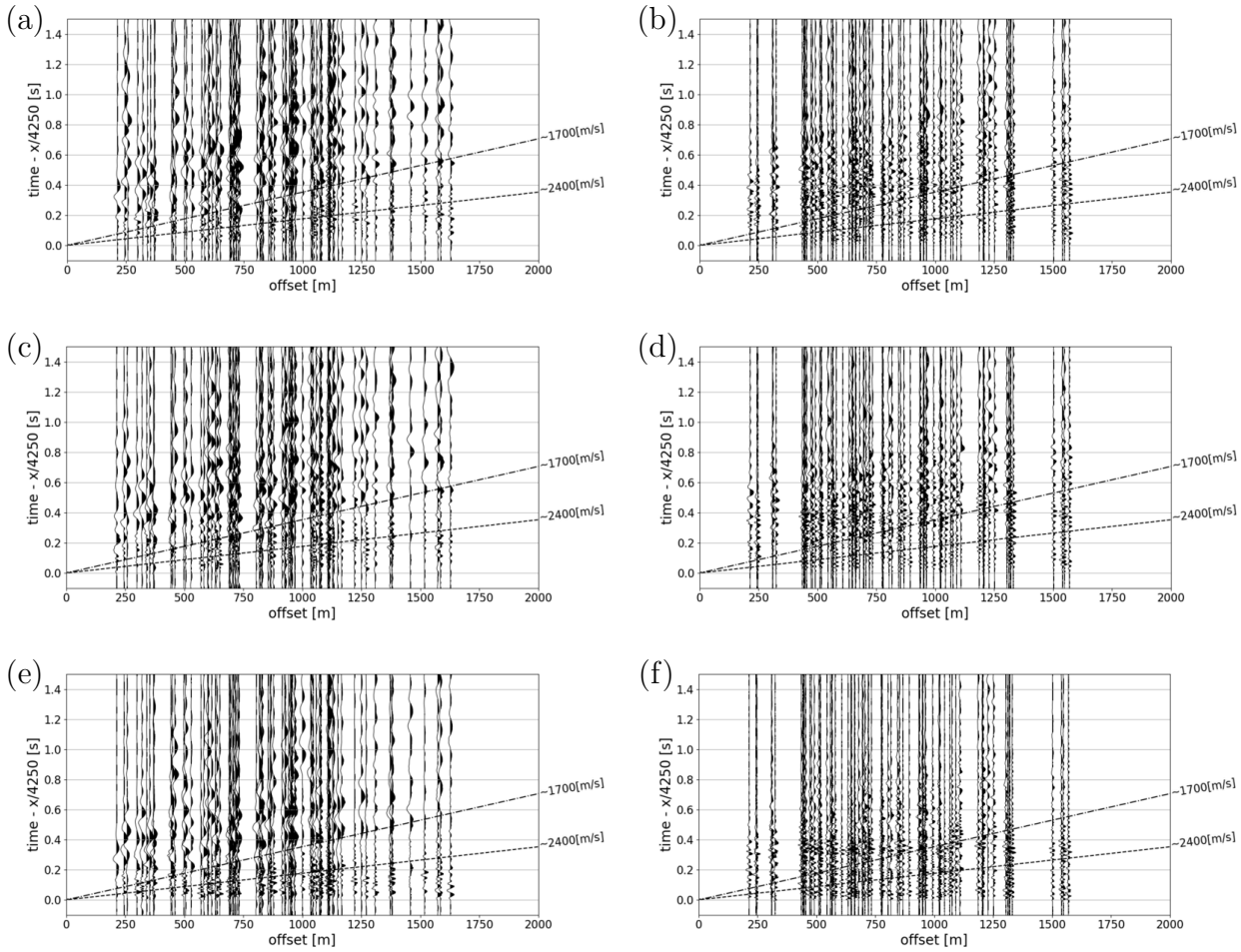

Figure 18: Trace-normalized time-reduced seismogram section of the (a, b) E-W, (c, d) N-S and (e, f) vertical component of production blast 30061 and 30077, respectively. Reducing velocity corresponds to the mean apparent P-wave velocity. Dashed lines mark the first arrival of the direct S-waves for a Poisson body. Dash-dotted lines mark the first arrival of the surface waves.

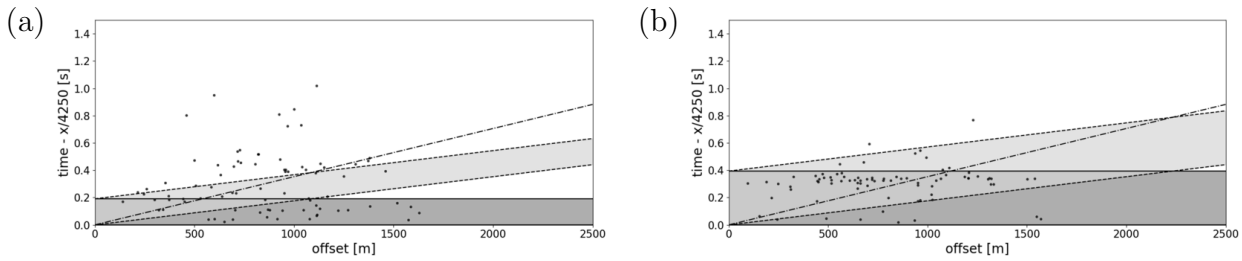

Figure 19: Time-reduced time windows of expected direct P- (dark grey) and S-wave arrivals (light grey) for blasts (a) 30061 and (b) 30077. Reducing velocity corresponds to the mean apparent P-wave velocity. The dash-dotted line is the expected surface wave arrival time. The dots mark the observed time of the occurrence of the PGV. Dashed lines mark the arrival of the direct S-waves for a Poisson body. Dash-dotted lines mark the arrival of the surface waves.

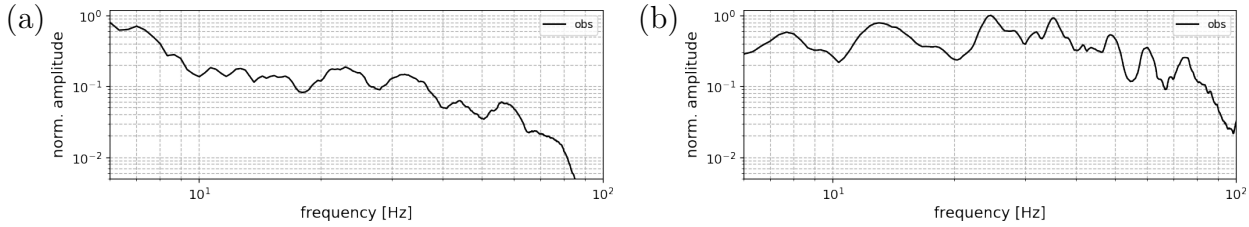

Figure 20: Normalized mean amplitude spectrum of production blasts (a) 30061 and (b) 30077.

4.4.4 PGV Arrival Times

The observed data shows a clear P-Wave, arriving at the speed characteristic of the P-Wave. In the majority of blasts, the highest amplitude appears to originate from the P-wave. An S-wave could not be observed from any of the production blasts discussed in the previous subchapters. In the horizontal components, the P-wave is less pronounced, and a later phase becomes visible, which is most likely the surface wave. The time at which the PGV occurs is qualitatively evaluated for the previously discussed example blasts. Consequently, the next step is to investigate the time at which the PGV occurs for the whole dataset. If a significant portion of the PGV is concentrated in a time window associated with a certain phase, the other phases might be less significant for the potential PGV prediction.
The sequence of waves that reach the receiver from a production blast can be divided into four distinctive time windows. The initial window exclusively contains P-waves. The subsequent window includes both P-waves and S-waves, where the first S-waves have already reached the station along with the P-waves from later ignited blastholes. In the third window, which is a pure S-wave window, the last P-wave has already arrived, and only S-waves are expected. After the third window, only surface waves and maybe also reflected P- and S-waves arrive. Across all production blasts, 28.7% of PGVs occur in the first P-wave-only window, 50.6% in the mixed window, 10.3% in the pure S-wave window, and an additional 10.5% of the PGVs occur following the last arrival of the S-wave, likely attributed to surface waves. 50.6% of all PGVs occur before the first possible onset of surface waves (dash-dotted line in Figures 13, 16 and 19). The surface wave velocity is estimated to be 1700 m/s, as this velocity lines up best with the late low-frequency phase in the horizontal components. This indicates that at least half of the PGVs can just stem from body waves and up to 89.5% of the PGVs are located within the body wave window. The majority of these PGVs originate from the pure P-wave window compared to the pure S-wave window, making the P-wave more likely to be the body wave responsible for the PGV.

4.4.5 Contribution of the Surface Waves

To confirm the velocity of the low-frequency phase and assign it to the surface wave a 4-15 Hz bandpass filter was applied. In most of the blasts, there is a clear onset of a slow phase visible in the horizontal components, as shown for blast 10020 in Figure 21a. For the vertical component, this onset is less pronounced (Fig. 21b). The intercept at zero time suggests a primary origin from the blast itself. This pattern can be recognized in most of the production blasts.
In the Figures 22 the P-wave and the surface wave windows with the origin of the production blasts are shown. In the two examples of the production blasts 30065 and 30069, the windows have completely spatio-temporal separated after an offset of about 500 m and 1200 m, respectively. The PGVs of production blast 30065 appear to cluster around the two windows, showing a clear concentration within and after the surface wave window. For production blast 30069, the PGVs predominantly occur within the pure P-wave window, with only a few outliers observed afterwards. In this particular blast, the PGV time pattern aligns with the P-wave velocity, suggesting that the PGVs may be primarily caused by one specific blasthole in the production blast. To quantify the contribution of the surface wave to the observed phases, one can calculate the energy in the respective window and compare it to the P-wave window. The energy is expressed as the RMS of the vector amplitude. From these two RMS values, the ratio is calculated for each station and each production blast. Figure 23 displays the calculated geometric mean of the ratio for all production blasts at each station. A higher value (indicated in red) signifies a relatively higher RMS amplitude during the P-wave window as opposed to

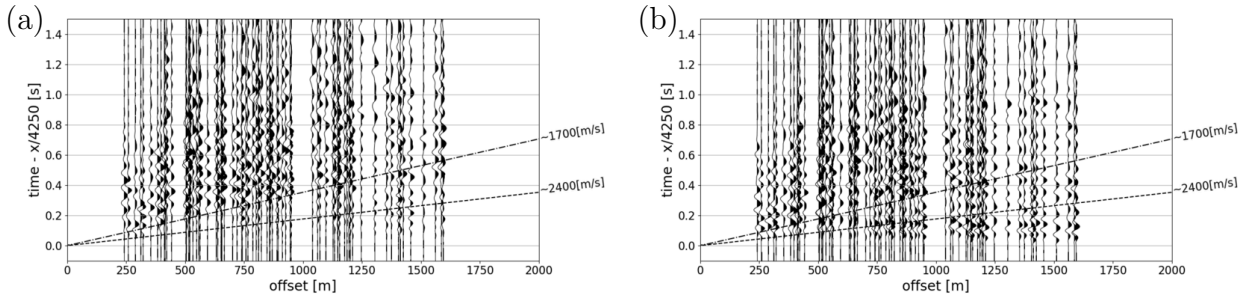

Figure 21: Trace-normalized time-reduced seismogram section of the (c) horizontal (N-S) and (b) vertical component of production blast 10020 after a 4-15 Hz bandpass filter was applied. Reducing velocity corresponds to the mean apparent P-wave velocity. Dash-dotted lines mark the onset of the low-frequency phase. Dashed lines mark the first arrival of the direct S-waves for a Poisson body.

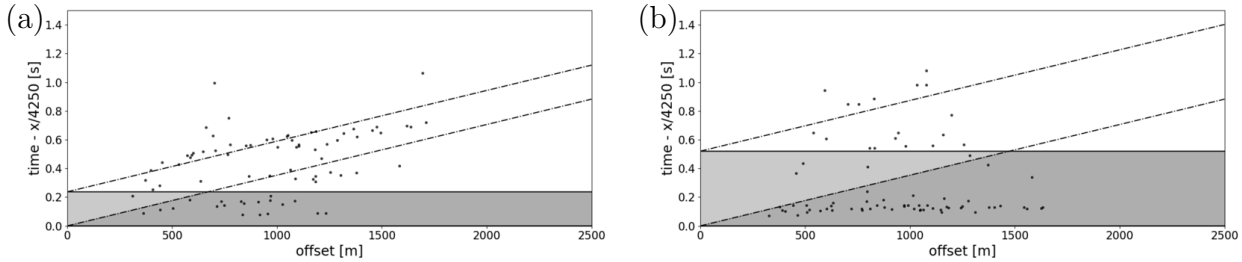

Figure 22: Time-reduced PGV times of production blast (a) 30065 and (b) 30069. Reducing velocity corresponds to the mean apparent P-wave velocity. The dark grey is the P-wave window, the window enclosed by the dash-dotted lines is a surface wave window and the grey window is the mixed phase window.

the surface wave window, suggesting a reduced impact of surface waves at those stations. The data in Figure 23 reveals a notably higher presence of surface waves inside the mine compared to the city area. This suggests that the topography acts as a barrier, effectively shielding the city from the surface wave impacts observed within the mine. Figure 24 illustrates the geometric mean ratio for all stations at each production blast. This should show whether there are specific production blasts at specific locations that produce significantly different P-wave ratios. Notably, blasts conducted at the lowest levels of the mine (highlighted in red) appear to emit a smaller amount of surface waves.

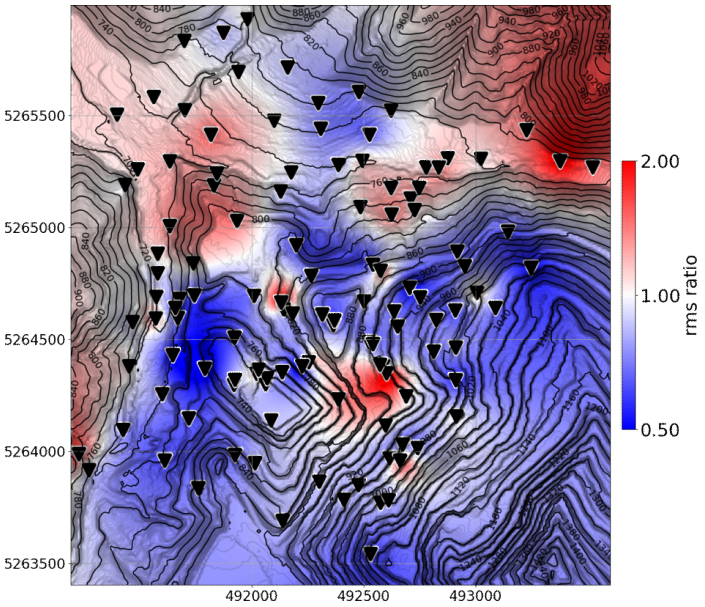

Figure 23: Map displaying the average ratio of RMS amplitude within the P-wave window divided by the RMS amplitude in the surface wave window across all seismic stations. The colour gradient represents the extent to which P-waves predominate over surface waves, with warmer colours indicating areas where P-waves are relatively stronger compared to surface waves.[1]

[1]DEM data source: CC-BY-4.0: State of Styria - data.steiermark.gv.at

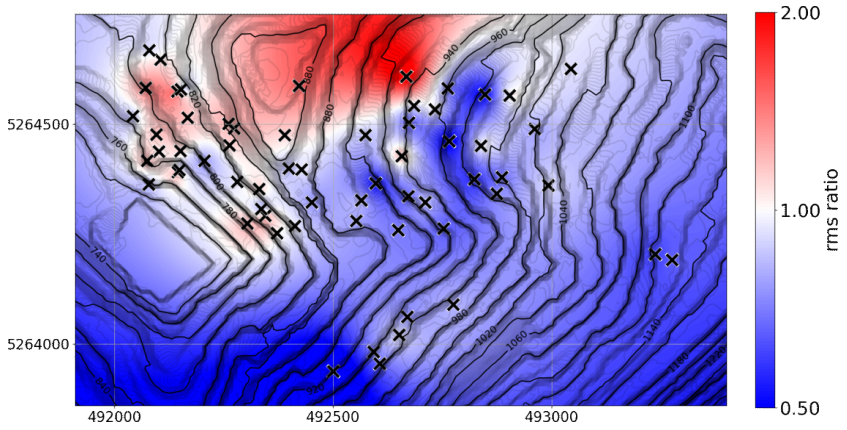

Figure 24: Map displaying the average ratio of RMS amplitude within the P-wave window divided by the RMS amplitude in the surface wave window across all production blasts. The colour gradient represents the extent to which P-waves predominate over surface waves, with warmer colours indicating areas where P-waves are relatively stronger compared to surface waves.[1]

4.4.6 Unfolding Seismograms with Deconvolution

The technique helps to separate the different seismic phases from the complex recorded data. This makes it easier to identify the arrival times and properties of these waves, which are often obscured in the raw seismogram due to overlapping signals and noise. Generally, a seismogram of a blast sequence can be written as an STF convolved over the Green's function:

$$h(t) = f(t) * g(t), \tag{2}$$

where $h(t)$ represents the recorded seismogram, $f(t)$ is the STF of the blast sequence, and $g(t)$ is the Green's function. Because there are no reflectors, the Green's function simplifies to an impulse response. Therefore, the recorded seismogram $h(t)$ is simply a time-shifted version of the STF $f(t)$. The STF of the blast sequence can be written as the sum of the individual STFs $f_i(t)$ of each blasthole at a certain time delay Δt_i relative to the first hole:

$$f(t) = f_0(t) + f_1(t + \Delta t_1) + f_2(t + \Delta t_2) + \ldots + f_n(t + \Delta t_n). \tag{3}$$

Under the assumption that all STFs are identical, the STF of the blast sequence equals to the STF of a single blasthole $f_w(t)$ convolved over the spike sequence $f_s(t)$:

$$f(t) = f_w(t) * f_s(t). \tag{4}$$

Each spike of the spike sequence corresponds to a detonation of a blasthole. In a production blast, the spike sequence is known, and the STF of a single blasthole can be extracted with a deconvolution. After Fourier transformation, the recorded seismogram of a production blast is divided by its spike sequence in the frequency domain (Eq. 5).

[1]DEM data source: CC-BY-4.0: State of Styria - data.steiermark.gv.at

$$F_w(\omega) = \frac{F(\omega)F_s(\omega)}{|F_s(\omega)|^2 + stab} \tag{5}$$

Here $F(\omega)$ represents the recorded seismogram, $F_w(\omega)$ is the STF of one blasthole and $F_s(\omega)$ is the spike sequence. A water level regularization is applied as a stabilizer, which is shown as the denominator term of stab. The stabilizer is set to some fraction of the mean of the spike sequence power spectrum. With a small stabilizer, the deconvolution becomes unstable, with a too large stabilizer the denominator becomes a constant and it simply scales the seismogram. A fraction of 0.1 for the stabilizer was determined by visual inspection of the deconvolution result. The result is then transformed back into the time domain. Here the example seismogram of blast 10020, recorded at station 38 (Fig. 25a) gets divided by its spike sequence (Fig. 25b). The position of each spike in the sequence signifies the spatio-temporal time delay for each blasthole position and the corresponding ignition time relative to the receiver. For spatial correction, a P-wave velocity of 4250,m/s was used, approximately representing the mean P-wave arrival time of the production blasts. The size of each spike is scaled by q^c, where q is the amount of explosive in [kg], and $c = 0.5$, as determined in Chapter 5 which is also the expected physical reasonable value. Reiner (2018) attempted to recover the STF from a master trace, where all traces are stacked after alignment at the P-wave arrival time. This method did not account for the spatio-temporal position of the spikes and it was hindered by the inaccuracy of the time delays associated with the NONEL ignition system. A Monte Carlo approach, involving randomized spike positions searching for a cost function that aims to minimize the energy of the source wavelet in the anti-causal part, proved unsuccessful. The small case study (Subchapter 3.2.1) revealed a high standard deviation for NONEL detonators. The model space is too large when searching for the accurate ignition times of a blast with multiple blastholes. The model space increases further when considering the varying coupling of each blasthole and, consequently, the size of each spike. The coupling of each blasthole may be attributed to the blast site factors, which will be determined in Chapter 5. Those blast site factors show a significant variation. This introduces an additional random effect which cannot be mitigated. However, with the accurate delay time of the last verification deployments, the deconvolution workflow to recover the STF proved successful. Instead of applying it to the master trace, the deconvolution is applied to every seismogram at every recorder position. The STF can then be recovered for every seismogram like it is shown for the seismogram at station 38 (Fig. 25c).

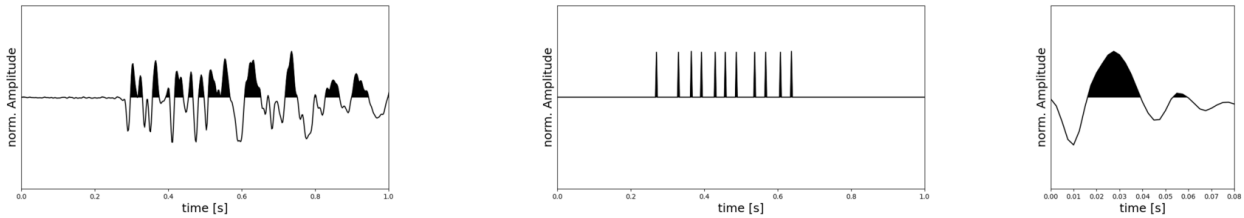

(a) (b) (c)

Figure 25: (a) Vertical component of an observed seismogram at station 38 from shot 10020, (b) the corresponding spike sequence and (c) the deconvolved STF.

An exemplary deconvolution outcome for production blasts 10020 and 30061 is shown in Figure 26 for the radial, transversal and vertical components. The dash-dotted line indicates the observed onset of

the low-frequency phase, likely the surface wave, while the dashed line represents the expected onset of the S-wave. Both blasts show a clear P-wave onset for the vertical component (Fig. 26e,f), which is not visible in the radial and transversal component (Fig. 26a,b,c,d). A late low-frequency phase, roughly following the dash-dotted line of the surface wave is visible, especially in production blast 10020 (Fig. 26a,c,e). A low-pass filter of 20 Hz makes the late phases slightly more visible (Fig. 27). However, the onset of the surface wave is less clear compared to the non-deconvolved data (Fig. 21a). While the deconvolution works well for the direct P-wave in the vertical component, it is less effective for the strongly scattered surface waves caused by the complex topography and related caustics in a heterogeneous medium. Nevertheless, an S-wave is not visible in any of the components in both example production blasts, 10020 and 30061, in either the unfiltered or low-pass filtered data.

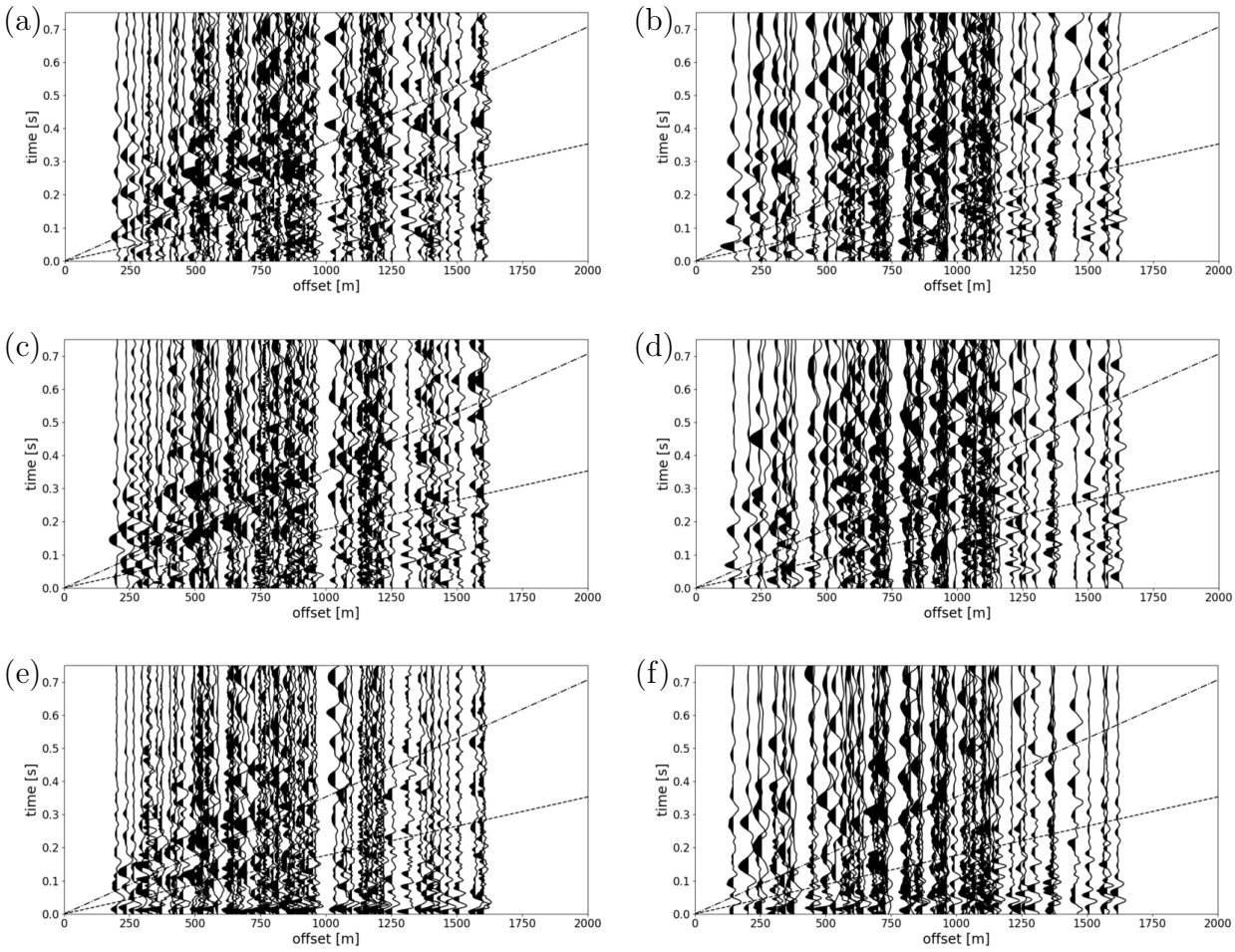

Figure 26: Trace-normalized time-reduced seismogram section of the deconvolution for the (a, b) radial, (c, d) transversal and (e, f) vertical component of production blast 10020 and 30061, respectively. Reducing velocity corresponds to the mean apparent P-wave velocity. Dashed lines mark the first arrival of the direct S-waves for a Poisson body. Dash-dotted lines mark the first arrival of the surface waves.

The S-wave is expected to follow a similar ray path to the P-wave but at a slower velocity. Stacking the whole data set in the common-offset gather of ±10 m offset stacks may highlight phases with similar

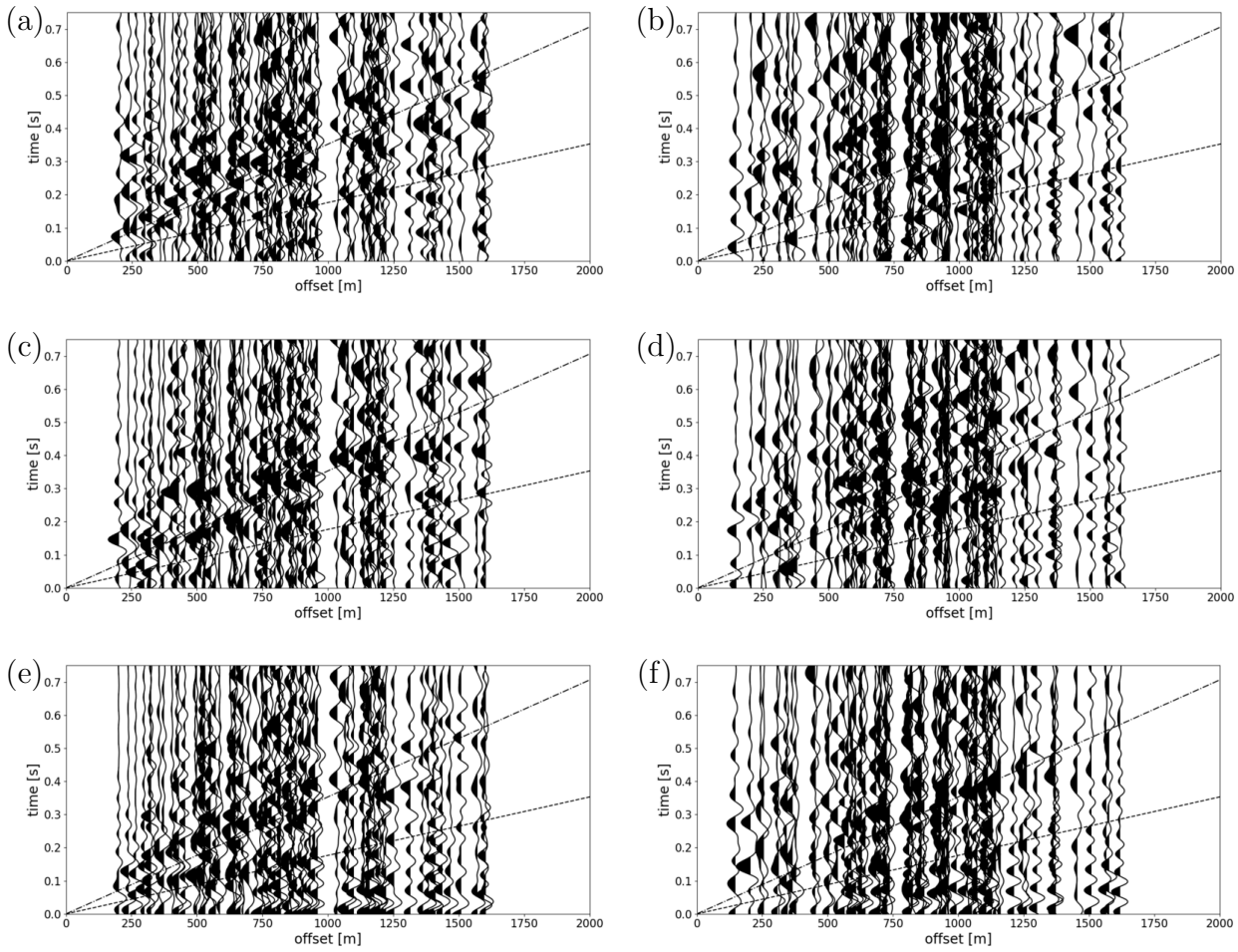

Figure 27: The time-reduced seismogram section of the deconvolution for the (a, b) radial, (c, d) transversal and (e, f) vertical component of production blast 10020 and 30061 after a 20 Hz low-pass filter, respectively. Reducing velocity corresponds to the mean apparent P-wave velocity. Dashed lines mark the first arrival of the direct S-waves for a Poisson body. Dash-dotted lines mark the first arrival of the surface waves.

apparent velocities. This approach enhances the P-wave for the vertical component (Fig. 28c). The real ray path most likely does not match the radial and transversal components, especially on top of the sediments an almost vertical incidence is to be expected. The P-wave onset is not observed in the radial and transversal components (Fig. 28a,b). The vertical component also shows a very clear surface wave with an apparent velocity of approximately 1700 m/s. This slow phase is mainly visible below 1000 m. This can be explained by two phenomena. First, the complex topography and the resulting scattering attenuation, and second, a shielding effect from parts of the mine situated at a lower elevation than the city area. Surprisingly after deconvolution, the surface wave is least visible on the horizontal components (Fig. 28a, b). If the surface wave is predominantly visible in the vertical component, it generally indicates the presence of Rayleigh waves, as they involve both vertical and horizontal retrograde elliptical particle motion. This result becomes less surprising upon considering the underlying reasons. The radial component very likely does not correspond to the actual direction of the surface waves, due to the complex topography and travel paths at the surface. Love and Rayleigh waves have slightly different phase velocities (Shearer, 2009) and because of the complex travel path, the radial and transversal components are a mix of both phases with a small phase shift. Stacking multiple offset gathers makes the mutual interference of the horizontal components even stronger, as they also include blasts from multiple directions. The same offset means similar travel times for body waves, but the complex topography may have a significantly higher impact on the travel path of the slow surface waves and hence on the travel time. This leads to a generally worse result for the deconvolution process for that particular phase, especially for far offsets. Overall the deconvolution generally works well for the vertical component, as it highlights the P-wave onset and the surface wave onset for offsets below 1000 m. The vertical component (Fig. 28c) also shows some strong amplitude around the expected S-wave time, between 250 m and 750 m offset. The intercept time does not pass through zero and between 500 m and 750 m the apparent velocity is almost identical to the P-wave velocity.

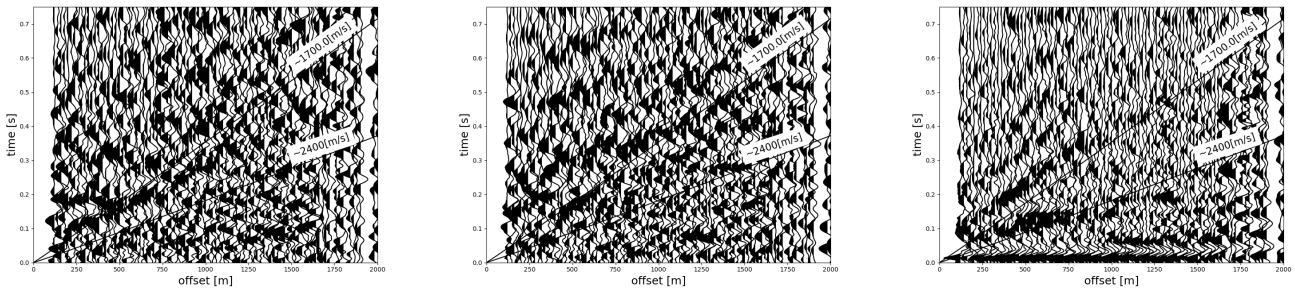

(a) (b) (c)

Figure 28: Deconvolution of all production blasts and station, sorted and stacked in common offset gathers, for the (a) radial, (b) transversal and (c) vertical component.

4.4.7 Conclusion

Overall, the P-wave phase was most reliably observed in all production blasts, while S-waves may be obscured by overlapping seismic windows and complex geological conditions. The PGV was mostly measured within the body wave window (89.5% of all PGVs). Because there was no single clear observation of an S-wave, the PGV is likely mainly attributed to the P-wave. In some blasts the PGV primarily occurs within the pure P-wave window, while in others, the PGV is almost exclusively caused by surface waves. The two example blasts shown in Figure 22 represent the two end members of a spectrum of possible PGV patterns. In one production blast, the PGV is likely caused by post-blast movement, while in the other, it is likely caused by a single blasthole with significantly higher coupling. This enhanced coupling could be due to geological conditions or the presence of water in the blastholes. For most production blasts the PGV time lies somewhere in between. These conditions underscore the challenges in simulating a production blast through numerical modelling, as it is nearly impossible to predict such variations in advance. Surface waves were identified in the low-pass filtered horizontal seismograms and the vertical component of the deconvolved data. Surface waves were more pronounced within the mine area as the energy ratio to the P-wave window was stronger. At a larger offset, the energy within the P-wave window increases and surpasses the energy of the surface wave window, which is surprising as the energy of body waves decreases by $1/r^2$ and the energy of surface waves decreases by $1/r$. This anomaly can be explained by a shielding effect due to the complex topography or by scattering attenuation of the surface waves. While the surface wave is best visible in the low-pass filtered horizontal components, it is almost not visible after the deconvolution. The apparent surface wave time window is in many blasts significantly longer than the blast sequence. This may be due to effects caused by the lifting and lowering of the rock mass due to the blasting or other post-blast movements of the rock mass. Nevertheless, the result of the dominant P-wave aligns very well with the outcome of a study of Gao et al. (2018).

5 Analytical PGV Prediction

Before moving on to the complicated numerical prediction method based on forward-modelling of seismic waveforms, a closer look at conventional prediction methods will be taken. This is usually done with an empirical formula of the form:

$$PGV = kr^{-b}q^{c}, \tag{6}$$

where k is the site factor measured at 1 m distance for a charge weight of 1 kg, r is the distance from the receiver to the blasthole with the maximum charge in [m], b is the decay exponent, q is the charge weight in [kg], and c is the charge exponent. The radial decay exponent and the charge exponent are important parameters that describe the behaviour of seismic waves as they propagate through the subsurface. The radial decay exponent is related to the geometrical spreading of seismic waves and is a fundamental parameter in many seismic wave propagation models. As seismic waves propagate away from their source, they spread out over an expanding sphere, and their amplitude decreases with distance. The geometrical spreading model predicts that the amplitude of the seismic wave decreases with distance from the source as $1/r^b$. The value of b depends on the type of seismic wave, the frequency of the wave, and the properties of the medium through which the wave travels. In homogeneous media, the energy density for body waves diminishes with $1/r^2$, where r represents the radius of the wavefront. The wave amplitude is directly proportional to the square root of the energy density and diminishes with $1/r$. In practical scenarios, the rock velocity tends to increase with depth, leading to a further divergence of the wavefront and a more rapid decay in amplitude over distance (Yilmaz, 2001). Another type of wave expected to cause ground vibrations is the surface wave, which travels along the surface. They are slower than P- and S-waves and the energy density for surface waves diminishes by $1/r$, where r represents the radius of the wavefront. The wave amplitude is directly proportional to the square root of the energy density and diminishes with $1/\sqrt{r}$. Therefore, a minimum radial decay exponent of 0.5 can be expected for surface waves, while a decay exponent greater than 1 is likely if a body wave is the primary contributor.
The charge exponent balances the energy of the blast with the amplitude. The amplitude of a seismic wave is proportional to the square root of the energy, and the energy is proportional to the amount of charge weight. Thus, a charge exponent $c = 0.5$ can be expected. The charge delay between all boreholes is at least 8 ms. Duvall et al. (1962) defines the maximum charge weight as the maximum amount of explosive detonated within 8 ms. To calibrate this equation, a wide variation of offsets and charge weights is desirable but often limited due to production constraints and the extent of the mine, leading to unstable inversion. To address this issue, mining operators use the scaled distance (SD) approach:

$$PGV = k'(r/q^{m})^{-b'} = k'(SD)^{-b'} \tag{7}$$

The SD is the offset divided by some power of q. For an overview of these methods, see Ainalis et al. (2017), Murmu et al. (2018) or (Yilmaz, 2016). The charge exponent c is typically related to the decay exponent b by a fixed ratio m that typically ranges between 1/3 and 2/3. This projects the charge exponent c into the variables k and b, so they become k' and b'. The ratio m is somewhat arbitrary and lacks physical justification, but this does not matter if it does not affect the accuracy

of the prediction for practical purposes in mining. However, the prior limits the possible models, as seen in a grid search which has been performed with the data from the mine (Fig 29). There is a clear global minimum for the entire dataset, and the predictor equations only allow for models where the b and c values lie on the yellow lines. None of the models make it possible to reach the global minimum. One optimized c/b ratio of approximately 1/5 (red line) crosses the global minimum.

PGV Predictor Approach	Formula	m=c/b
USBM (Duvall & Petkof, 1959)	$PGV = k' \left(\frac{r}{q^{1/2}}\right)^{-b'}$	m=1/2
Ambraseys & Hendron (1968)	$PGV = k' \left(\frac{r}{q^{1/3}}\right)^{-b'}$	m=1/3
Indian Standard (Khandelwal & Singh, 2009)	$PGV = k' \left(\frac{r}{q^{2/3}}\right)^{-b'}$	m=2/3

Table 2: Some widely used PGV predictor approaches.

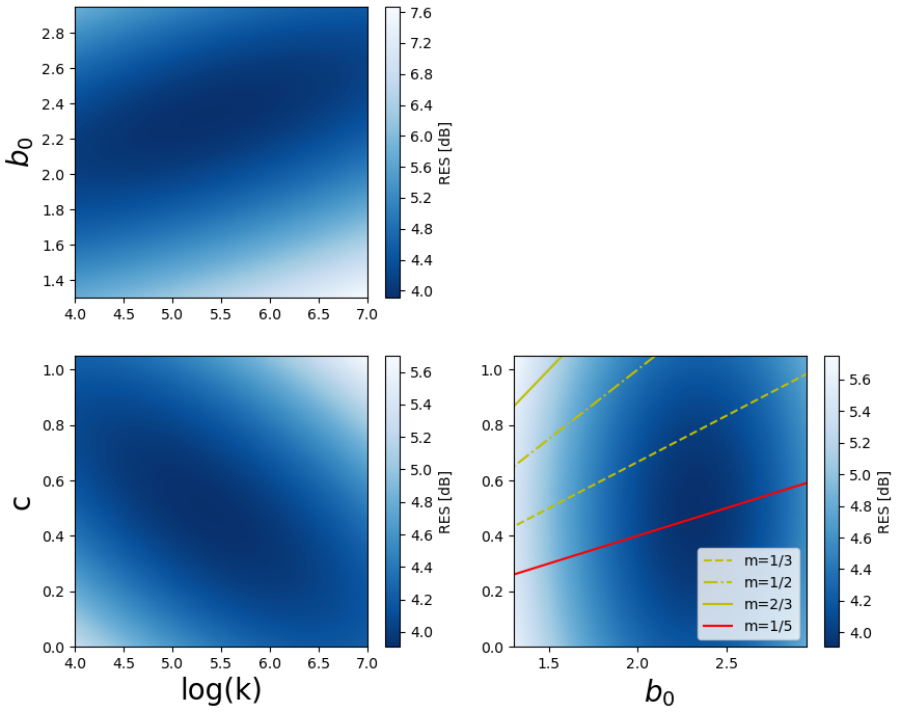

Figure 29: Grid search for the minimal cost function for the 3 parameters κ_0, b_0 and c applied on the whole dataset The yellow lines represent the prior of different PGV predictor approaches listed in Table 2 and the red line shows an optimized ratio (Trabi & Bleibinhaus, 2023).

Some widely used PGV predictor approaches are shown in Table 2. In this particular mine, the USBM SD approach (Duvall & Petkof, 1959) with a ratio of $m = 0.5$ is used. To evaluate the performance of this approach, the Equation 6 is aimed to be calibrated and to improve the data fit. For the calibration of the engineering formula, 55 regular production blasts were taken from the whole dataset.

5.1 Accuracy Measurement of Predictions and Line Fits

To measure the accuracy of the predictions and line fits, the RMS residual is used. Here, the RMS residual is calculated by taking the square root of the mean squared difference between the calculated and observed logarithmic values:

$$RMS = \sqrt{\frac{1}{n}\sum_{i=1}^{n}(log(PGV_{obs})_i - log(PGV_{calc})_i)^2} \tag{8}$$

The RMS residual is given in Decibel [dB]:

$$dB = 20log(\frac{PGV_{obs}}{PGV_{calc}}) \tag{9}$$

5.2 Subset Inversion

The standard approach for calibrating equation 6 involves the use of Common Receiver Gathers (CRG). A CRG typically involves one or a few stations within a mining operation that record production blasts over an extended period. However, due to the large receiver array, it is also possible to calibrate this equation using Common Blast Gathers (CBG). The use of CRG for calibrating equations to predict PGV from blasting activities has been widely used in the mining industry for many years. CBG are not typically used for predictions, but they can be used to evaluate model parameters. In both CRG and CBG approaches, offsets below 300 m are generally excluded to avoid distortions when a borehole within the same blast sequence is significantly closer to the receiver than the borehole with the maximum charge per delay. The empirical equation 6 is then calibrated using a line fit to the collected data. With the line fit, the values for the site factor k, the decay exponent b, and the charge exponent c are determined. Overall, the calibration of equation 6 is essential for predicting and mitigating PGV within legal limits. The use of both CRG and CBG approaches, as well as the SD approach, can help to improve the accuracy and stability of the calibration process.

5.2.1 Common Blast Gathers

A CBG is a set of seismic traces that are recorded at different receivers in response to the same source. In the CBG the source function is assumed to be constant. This allows to drop the corresponding scaling factor q_i^c from the inverse model, reducing the number of unknown parameters to two (k, b). As a result, no additional constraints are required for the calibration of the CBG. However, to account for the effect of site amplification at the receiver locations, receiver site amplification factors ρ_j need to be included for the calibration. When the receiver site amplification factors were included in the calibration, equation 6 for the PGV becomes equation 10. This revised equation takes the source amplitude decay and the receiver site amplification into account.

$$PGV = k_i' \rho_j r^{-b_i} \tag{10}$$

The variable k_i' is an auxiliary parameter that accounts for all the factors that are constant for CBG i, including local site conditions, charge weight, and blast coupling, whether known or unknown. The

amplification factors ρ_j are initially unknown and are set to a value of 1. A logarithmic least squares fit is performed using the example shown in Figure 30. The total RMS residual for this approach is 5.95 dB. Figure 31 displays the corresponding distribution of b_i. The mean value of 1.3 is roughly in agreement with the empirical estimate of the balanced scaling.
In a subsequent step, the amplification factors ρ_j were computed as the geometric mean of the misfit at receiver site j in all CBGs. Equation 11 expresses this computation, where $PGV_{i,j}^{obs}$ and $PGV_{i,j}^{pre}$ denote the observed and predicted PGV values, respectively, at CBG i and receiver site j.

$$\rho_j = \prod_i \frac{PGV_{i,j}^{obs}}{PGV_{i,j}^{pre}} \tag{11}$$

To ensure that equation (10) is not under-determined, it is necessary to impose the condition that $\prod_j \rho_j = 1$. This is achieved by appropriately normalizing the site factors. When the site factors are included in equation (10), the inversion for k_i' and b_i results in different values, which in turn leads to different site factors. Therefore, an iterative procedure is needed to alternate between subspace inversions for k_i' and b_i, and for ρ_j. After 15 iterations, all parameters converge to a constant value.
Figure 32 displays the final distribution of the ρ_j values after an iterative process to compute them. Sensors located within the mine on hard rock exhibit consistently lower amplitudes compared to sensors on soft sediments in the valley or on hill-slopes due to the difference in seismic impedance. By including these site factors in the prediction, the overall RMS residual is reduced from 5.95 dB to 3.0 dB. To demonstrate the significance of this reduction, the observed PGV values are divided by the receiver site factors rather than scaling the predicted PGV values, as shown in Figure 30b.

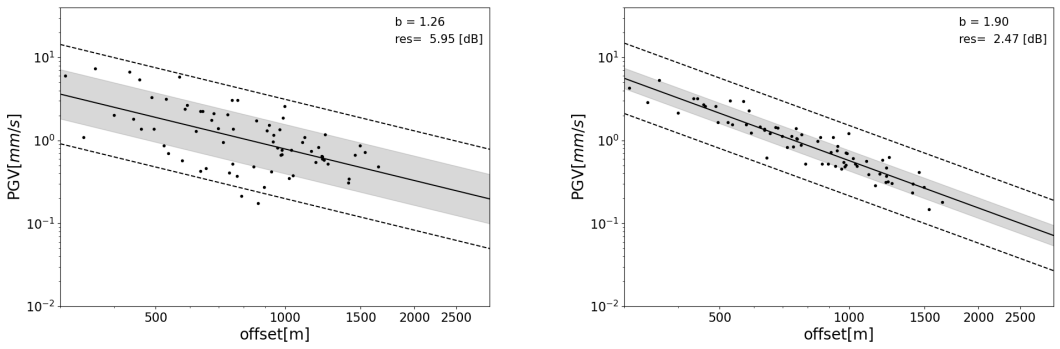

(a) (b)

Figure 30: Inversions for CBG 10005 (a) without and (b) with receiver site factors applied. Black dots are observed PGV values. The solid line is prediction, and the grey bar and dotted lines represent the 68% and 95% confidence intervals, respectively. For blast location see Fig. 2 (Trabi & Bleibinhaus, 2023)

When considering the effects of the site amplification factors ρ_j, it becomes clear that the spatial decay factors b_i are systematically larger. This can be seen in Figure 31b, where it is evident that the inclusion of ρ_j leads to an increase in the magnitude of b_i. This effect can be attributed to the

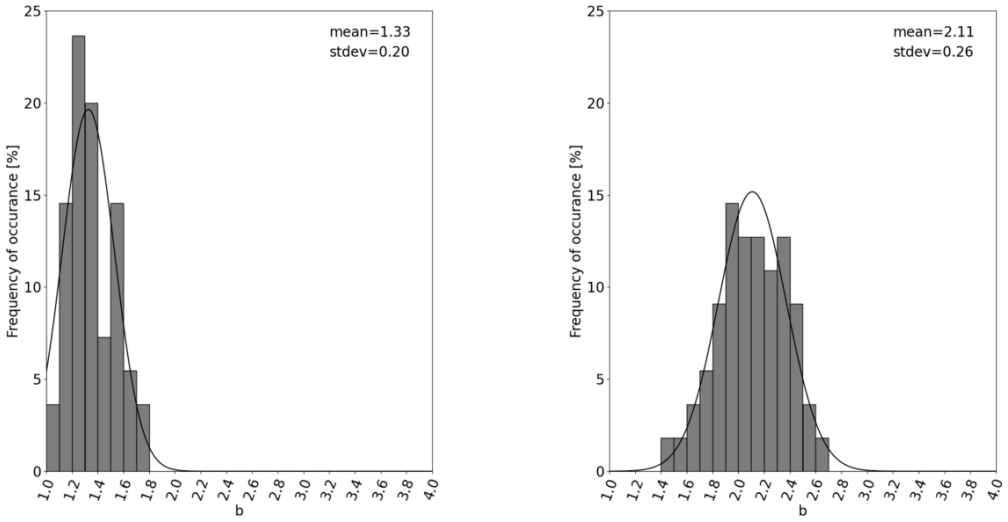

(a) (b)

Figure 31: Distribution of b_i from CBG inversions (a) without and (b) with receiver site factors with Gaussian fit (Trabi & Bleibinhaus, 2023).

biased geometry of the blast survey. Specifically, large ρ_j values in the valley correlate with long offsets, while small ρ_j values within the mine correlate with short offsets. When ρ_j is not accounted for, this systematic variation is projected into artificially low b_i values.
Moreover, in addition to the spatial correlation of ρ_j, there is also a spatial correlation of b_i, as seen in Figure 33. b-values to the south are systematically higher than those to the north. This is unexpected, as the amplitude decay should depend on the subsurface between the blast and the receiver. The fact that b_i correlates with the blast position is an artefact of the biased geometry. Specifically, the southern blasts with large b_i values correlate with long offsets, while the northern blasts with small b_i values correlate with short offsets.
To illustrate how a velocity model with a gradient that decreases with depth might create such a trend, Figure 34 shows the RMS values in a window around the P-wave first arrivals of seismograms computed with the two-dimensional viscoelastic code of Robertsson et al. (1994), converted to 3D by multiplying them with $t^{-0.5}$. The amplitudes correspond to a model derived by inverting the first arrival travel times of ten blasts recorded from the earlier site characterization survey. Although the model is exemplary, the velocities correspond well to a model that could result from the water table or deep erosion. The strong near-surface gradient causes much less energy to be refracted back to the surface at corresponding long offsets, which could explain the observed trend in b-values.
It should be noted that the b-values in the model are smaller than the observed b_i values, which can have many reasons, including the complex topographic structure that partially shields remote stations from direct waves. Overall, it is clear that accounting for the site amplification factors ρ_j is crucial for properly estimating the b_i values, and for reducing the overall RMS residual to a much lower level of 3.0 dB.

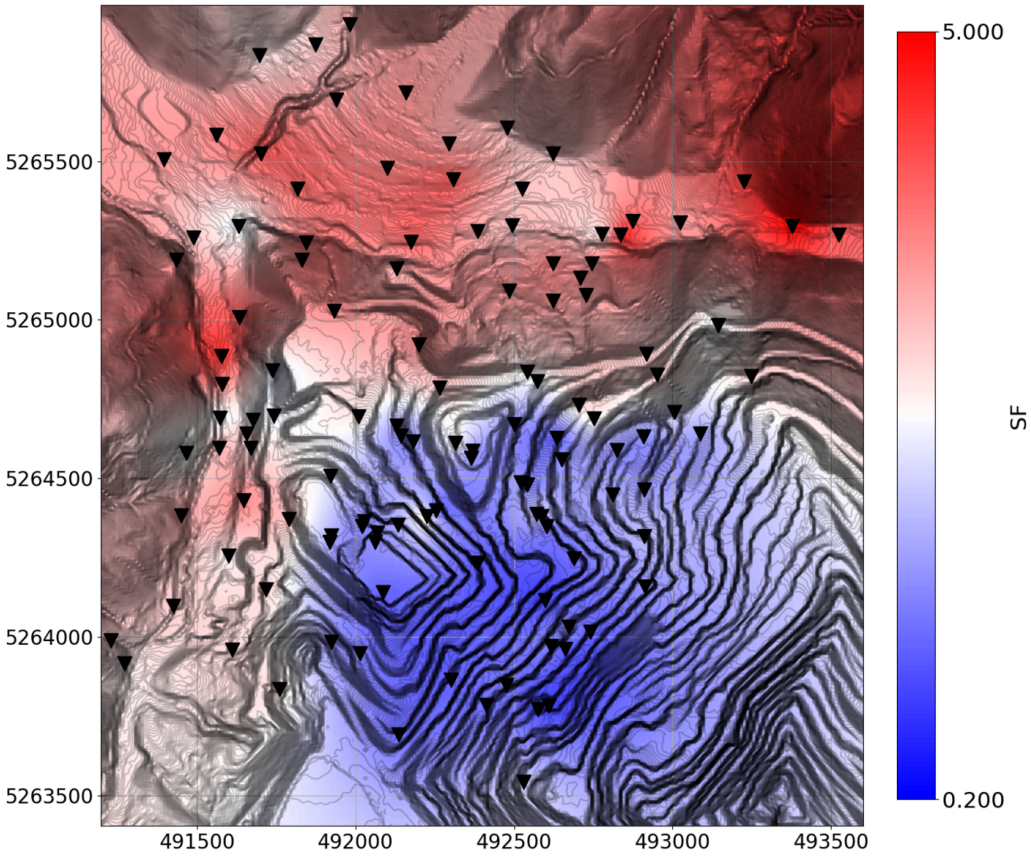

Figure 32: Spatial distribution of receiver site factors ρ_j (Trabi & Bleibinhaus, 2023).[1]

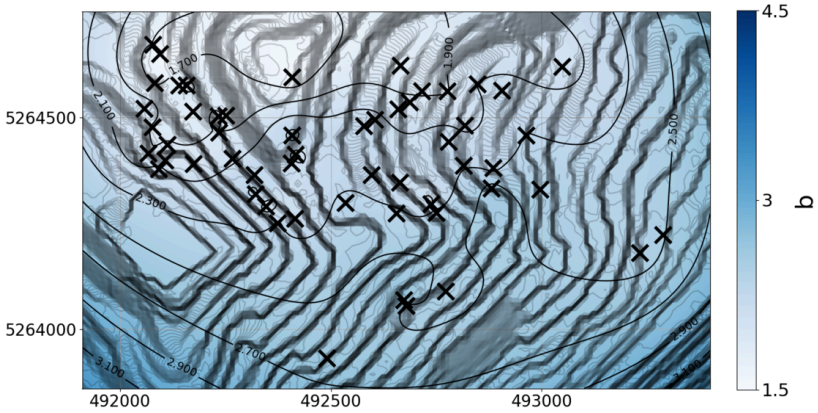

Figure 33: Spatial distribution of radial decay constants b_i obtained from CBG inversions plotted at the corresponding blast position (crosses) (Trabi & Bleibinhaus, 2023).[1]

[1]DEM data source: CC-BY-4.0: State of Styria - data.steiermark.gv.at

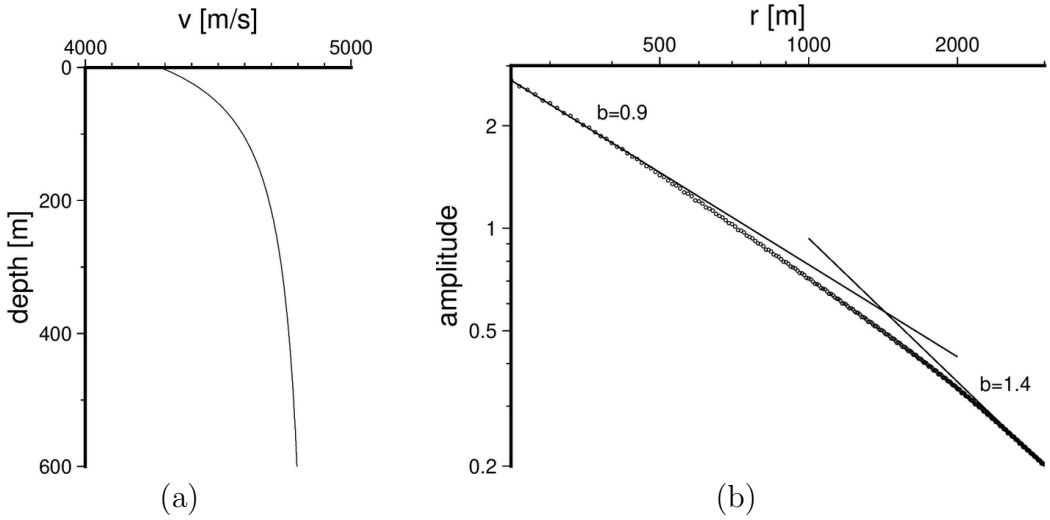

Figure 34: (a) Velocity model and (b) corresponding amplitudes of the direct P-wave with line fit of near and far offset trends (Trabi & Bleibinhaus, 2023).

5.2.2 Common Receiver Gathers

The calibration of equation (6) is typically made in the context of CRG, where PGV is measured at only a few points, making prediction from the calibrated curves straightforward. An additional advantage of this approach is that the receiver site factors do not need to be explicitly considered, as they are projected into the site factor k'_j. However, to enhance the accuracy of the data fit, blast site factors β_i are also computed using the same iterative approach that was employed to derive receiver site factors for the CBG inversion.
It is important to note that the blast site factors, while not directly useful for prediction, can still provide valuable insights into the data. By examining the blast site factors, patterns or correlations in the data that may be obscured by overall trends can be identified. For example, consistent higher or lower PGV values for specific blasts, regardless of the receiver distance, can be discovered. This information helps in isolating and identifying unique factors that influence seismic data, leading to more accurate predictions.

5.2.3 Scaled Distance

The SD method with a ratio of $m = 0.5$ is commonly used in CRG, including by VA Erzberg, the operator of the Mt Erzberg mine. To demonstrate this, Figure 35 provides an example of SD regressions for $m = 0.5$. The RMS residual for that CRG is 4.57 dB, and the mean RMS residual for all CRG is 4.2 dB. However, when accounting for blast site factors, it is reduced to 3.0 dB. Figure 36 shows the corresponding distributions of the decay constants b'_j, which are similar to the b_i distributions from the CBG inversions with receiver site factors. Introducing blast site factors leads to higher b'_j, though not as significantly as introducing receiver site factors did for the CBG inversions. The ratio $m = 0.5$ implies mean c-values of 1.0 and 1.1 for inversions without and with blast site factors, respectively. The equation (7) is calibrated for a specific recording position, employing a fixed ratio of m. The selection of m is somewhat arbitrary, and varying ratios may result in different fitting outcomes depending on

the site properties. To optimize the ratio m, a grid search over a wide range of values is performed. Six representative stations were selected for calibration purposes, each situated in distinct geological settings. Station 8 is located in the sediments west of the mine, while stations 56 and 70, positioned to the north in the sedimentary region, differ in offset distances. Additionally, three stations situated in the hard rock areas were chosen: one in the eastern part (12), one in the central region (28), and one in the northern part (67) of the mine. These stations were employed in the calibration process, covering a range of m ratios from 0 to 0.66, corresponding to the maximum value within the known predictor formulas. The results of these calibrations are illustrated in Figure 37 (a) to (f). The x-axis represents the chosen m ratio, while the left y-axis displays the cost function of the fit. The right y-axis displays the calibrated parameters, showing parameters b and $\log(k)$ and parameter c, where c is derived from the m ratio. In none of these stations, $m = 0.5$ is a good choice. It appears that, based on the conducted fits, there is a consistent trend where the optimal m ratio corresponds to a c-value of approximately 0.5. To eliminate any suspicion of deliberate station selection, the grid search was carried out for all CRG. The results for all CRG without blast site factors (Fig. 37g) highlight again that $m = 0.5$ is not the best choice. The corresponding residual of 4.2 dB is more than 0.6 dB higher than the global minimum of 3.6 dB at $m = 0.18$. The mean $\overline{b'_i}$ of 2.5 for the global minimum also implies a significantly smaller c-value of close to 0.5. When accounting for blast site factors, the best results are obtained by ignoring the charge weight scaling entirely ($c = 0$), as all charge weight scaling can be accounted for by blast site factors (Fig. 37h). However, there is still sensitivity to c because the SD method demands a constant charge weight scaling c_j per receiver, which cannot be fully compensated by β_i and is therefore rejected.

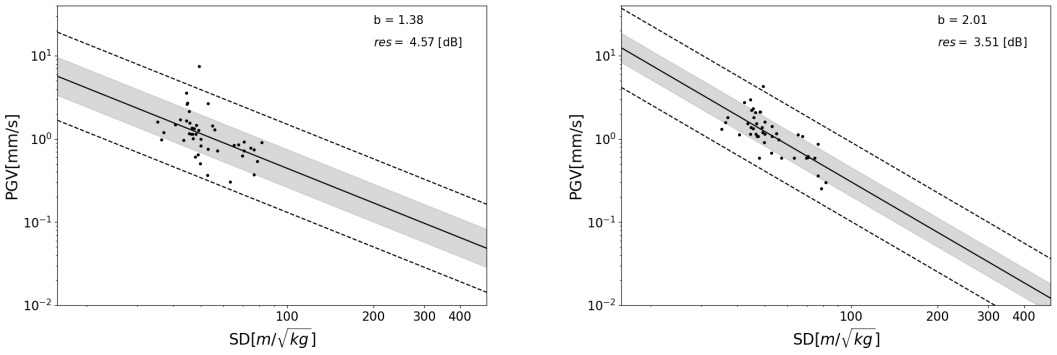

Figure 35: SD regression for $m = 0.5$ for receiver 75 (a) without and (b) with blast site factors applied (solid line). The grey area and dotted line represent the confidence intervals of one and two standard deviations, respectively. For receiver location see Fig. 2 (Trabi & Bleibinhaus, 2023)

5.2.4 Sequential Inversion of c and b

The alternate approach involves calibrating equation (6) sequentially to determine the charge exponent c independently of the spatial decay b. A subset of CRG is selected that has at least 15 PGV observations within ±20% offset variation around their corresponding mean $\overline{r_j}$ to consider only those PGV values

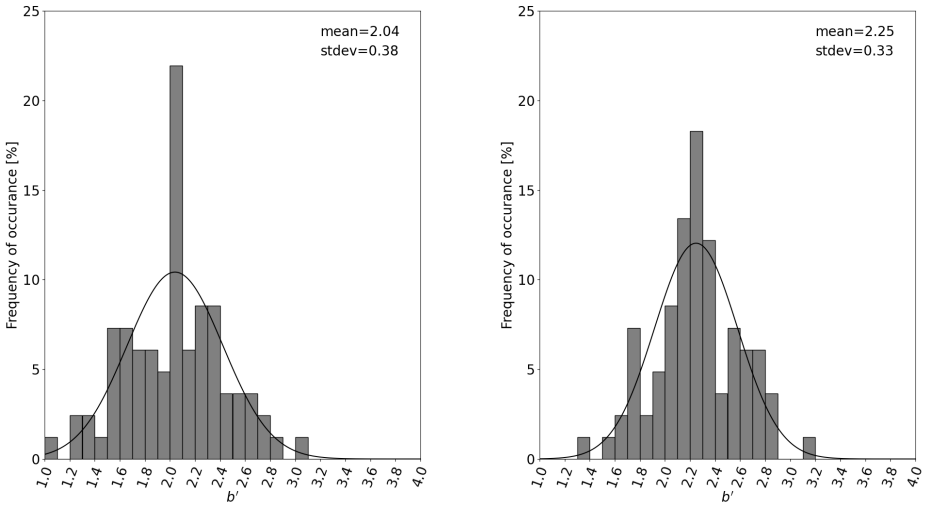

(a) (b)

Figure 36: Distribution of SD b'_j-values for $m = 0.5$ obtained (a) without and (b) with blast site factors (Trabi & Bleibinhaus, 2023).

that have little offset variation. The treatment of r^{-b} as a constant drops it from equation (6), enabling the determination of c independently of b. Figure 38a shows an exemplary line fit, and Figure 39a shows the corresponding distribution of all c_j. The distribution is roughly Gaussian with a clear maximum around $c = 0.5$. The next step involves fixing c to this mean value and inverting the equation (6) for b_j. Fig. 38b shows an example CRG, and Fig.39b the corresponding distribution.
It is worth noting that the spatial correlation of the b_j (Fig. 40) is even stronger than for blasts, simply because the correlation with offset is stronger for CRG. The most distant receiver stations to the North only see the portion of the amplitude curve (Fig. 34b) with the strongest decay. Overall, the strong variability seems to be an advantage regarding the data fit. At 3.6 dB without and 2.9 dB with blast site factors, the RMS residuals are smaller than the other inversion strategies. The main advantage of this approach is the determination of the charge exponent c independently of the spatial decay b, leading to a more accurate estimation of the charge weight scaling factor, which is an essential parameter for predicting future seismic events. Additionally, a larger dataset can be used, as only those PGV values with little offset variation need to be considered. This results in a more comprehensive analysis of the data, leading to a deeper understanding of the underlying factors that influence seismic measurements.
However, this approach also has limitations. One of the main limitations is the need to select a subset of CRG that has at least 15 PGV observations within ±20% offset variation around their corresponding mean $\overline{r_j}$, which may result in a smaller dataset compared to other inversion strategies. Additionally, fixing c to the mean value assumes that all CRG have the same charge weight scaling factor, which may not always be the case and could affect the accuracy of the charge weight scaling factor. Despite these limitations, this approach provides a valuable alternative to other inversion strategies and can be useful in predicting future seismic events. Figure 41 shows the spatial distribution of the blast site

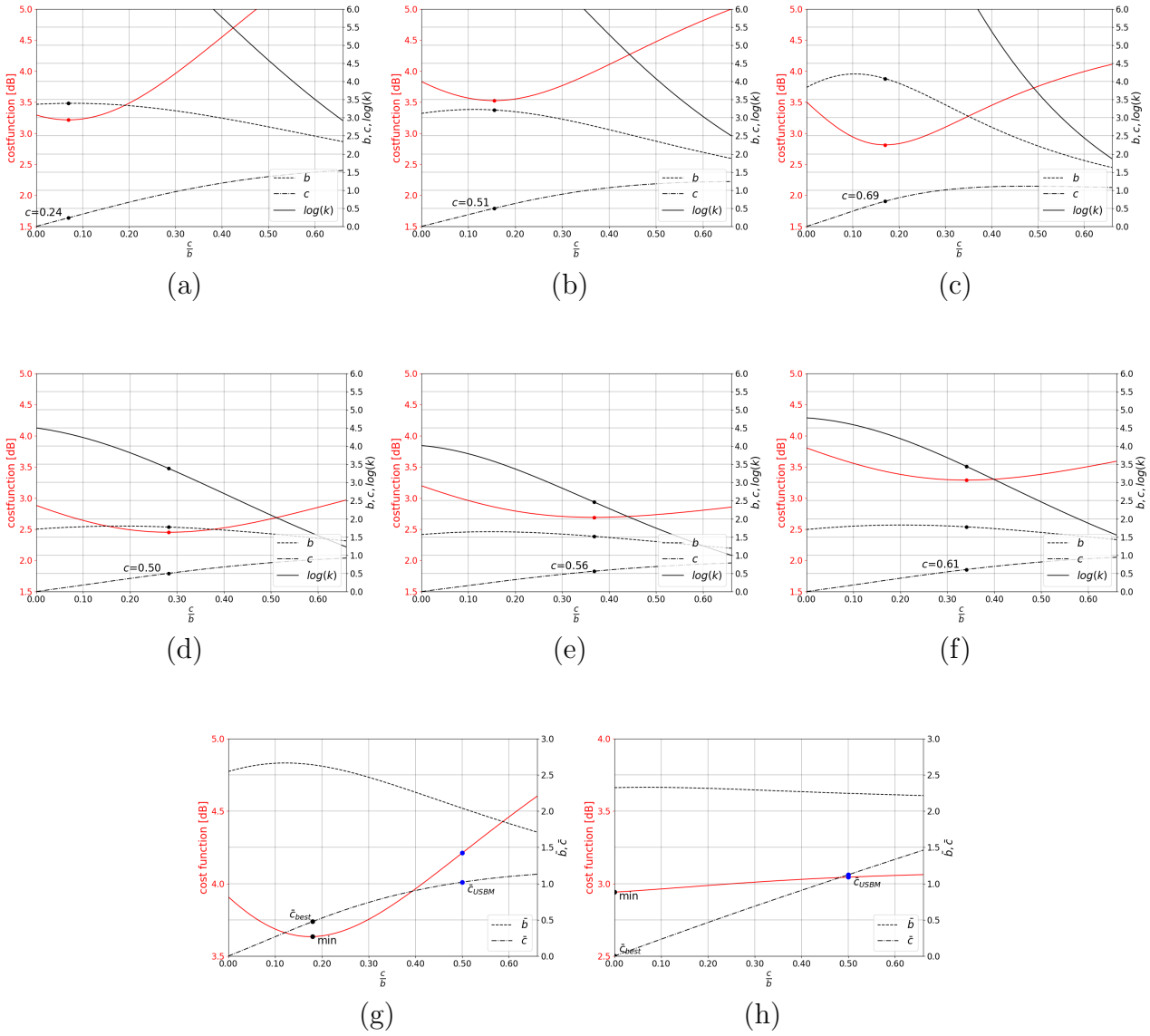

Figure 37: RMS residuals and model parameters for SD inversions for exemplary (a-c) stations (8, 56, and 70) in sediment and (d-f) stations (12, 28, and 67) in hard rock. RMS residuals and mean model parameters for all SD inversions with different c/b-ratios shown (g) without and (h) with blast site factors (Trabi & Bleibinhaus, 2023).

factors β_i. They are less pronounced than the receiver site factors and appear more scattered. However, they also exhibit a spatial trend of higher amplifications for the Northern blasts, mostly shot in the Werfen formation.

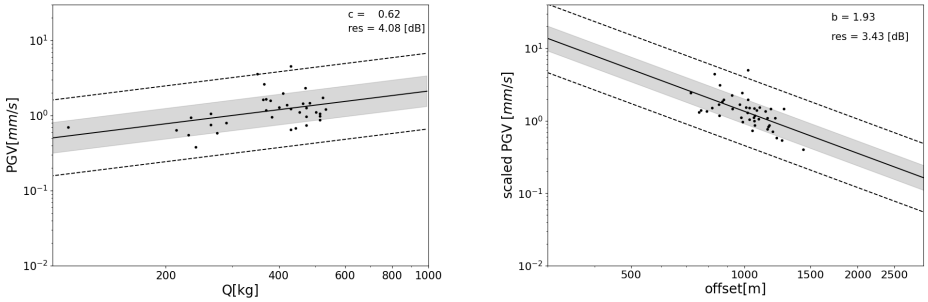

(a) (b)

Figure 38: Sequential CRG (a) charge weight exponent and (b) radial decay inversion for receiver 75 with blast site factors applied. For (b), all observations were scaled to a unit charge weight of 500 kg. For receiver location see Fig. 2 (Trabi & Bleibinhaus, 2023)

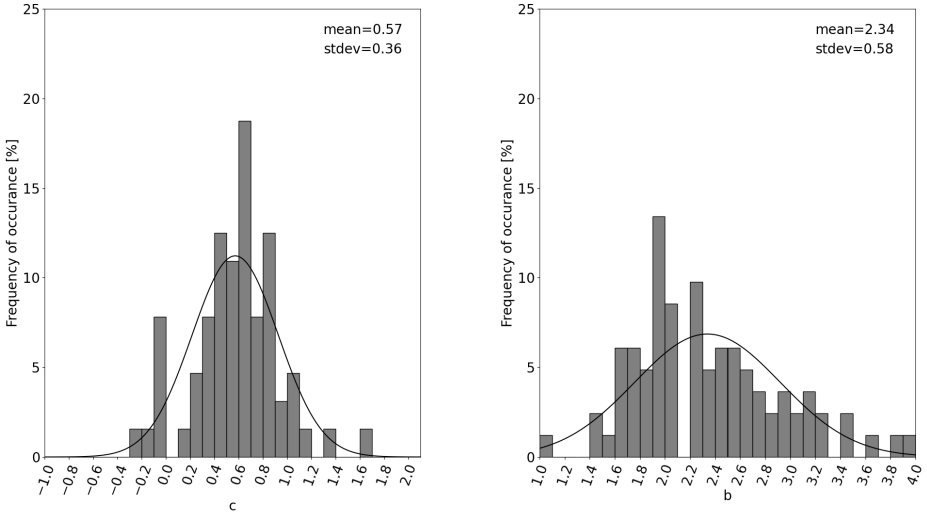

(a) (b)

Figure 39: Distribution of sequential CRG (a) charge weight exponents c_j and (b) radial decay constants b_j with blast site factors applied (Trabi & Bleibinhaus, 2023).

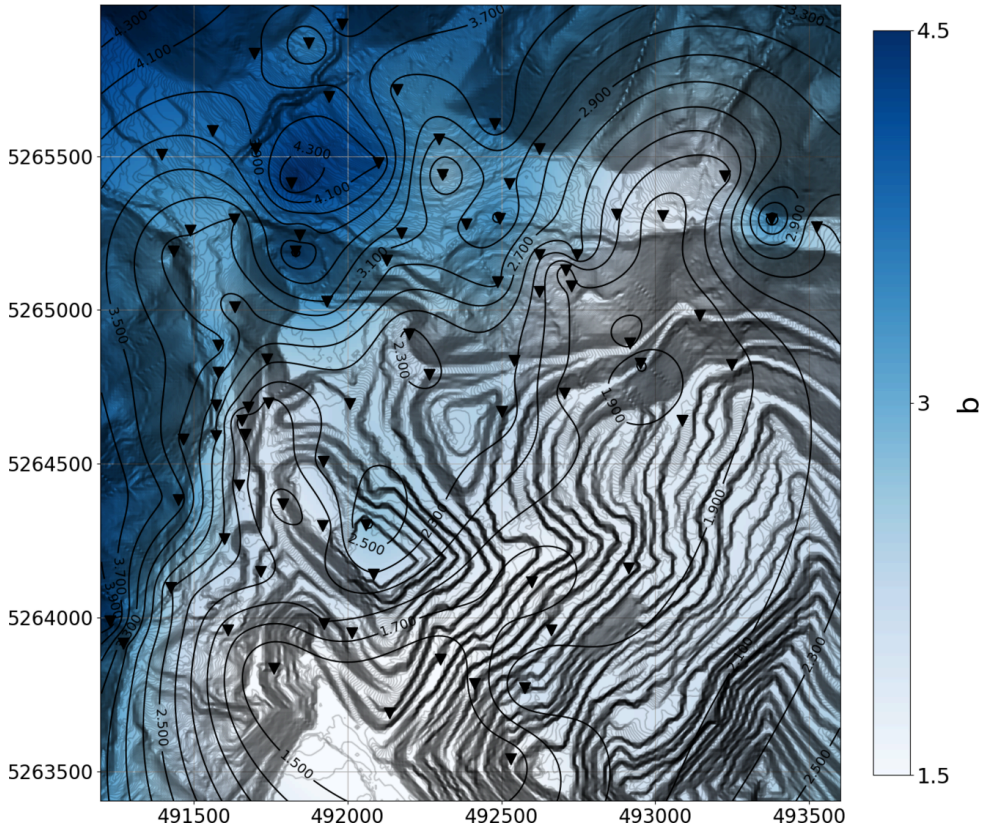

Figure 40: Spatial distribution of the radial decay constants b_j from sequential CRG inversions (Trabi & Bleibinhaus, 2023).[1]

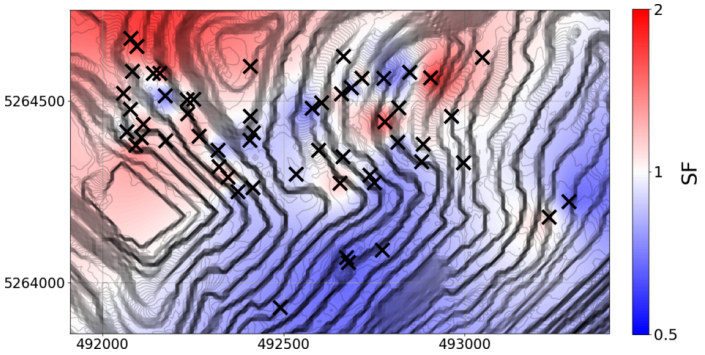

Figure 41: Spatial distribution of the blast site factors β_i from sequential CRG inversions (Trabi & Bleibinhaus, 2023).[1]

[1]DEM data source: CC-BY-4.0: State of Styria - data.steiermark.gv.at

5.3 Joint Inversion

Calibrating equation (6) is crucial for determining the relationship between ground motion and distance, which is essential for predicting future production blasts. One alternative approach to calibrate this equation is to jointly invert all data to constrain global b_0 and c_0 values. Utilizing the entire dataset offers the benefit of providing enough variability in offset and charge weight to independently resolve these parameters. However, a global amplitude decay constant b_0 is not supported by the data, as indicated in Figures 33 and 40. To account for data variations, a linear increase of $b(r)$ is incorporated. Consequently, with blast and receiver site factors, equation (6) is modified to:

$$PGV_{i,j} = \kappa_0 \beta_i \rho_j r^{-(b_0 + r\partial b/\partial r)} q^{c_0} \tag{12}$$

The site factors ρ_j and β_i are subject to a condition that ensures that their geometric mean equals 1, maintaining the constancy of their product across the dataset to prevent overfitting. The allowance for a linear increase of $b(r)$ addresses spatial data variability unaccounted for by a global amplitude decay constant. The varying slope of amplitude decay with distance is captured through this adjustment. Despite its benefits, this method relies on a linear increase of $b(r)$, which might not suit all datasets, and alternative models may be necessary.

5.3.1 Deterministic Inversion

In the deterministic inversion method, the four global variables κ_0, b_0, $\partial b/\partial r$, and c_0 are first iteratively inverted using equation (12). This first iteration is referred to as iteration 0 in Figure 42. Subsequent steps involve subspace inversions for the blast site factors β_i, receiver site factors ρ_j, and the global variables. After each iteration, the receiver site factors become more extreme, as indicated by their increasing standard deviation σ_ρ, and the global decay b_0 adjusts accordingly. This correlation between receiver site factors and b-values was previously observed in the CBG calibrations. The values of $b_0 = 1.32$ and $c = 0.50$ stabilize after 15 iterations, and the RMS residual reaches its final value of 3.0 dB. An exemplary data fit for a CBG is shown in Figure 43, where the curvature of the line is well constrained, but the overall improvement of the residual is small. The inversion with a constant amplitude decay yields an average $b = 2.0$ and explains the data with an error of 3.1 dB. In the current implementation, the inversion of the blast site factors, the receiver site factors and the global variables are done in multiple steps, with each step consisting of a subspace inversion for the blast site factors, receiver site factors, and the four global variables. However, it would be possible to invert for all variables simultaneously in one step. This approach would have the advantage of reducing computational time and providing a more comprehensive solution, as all variables would be optimized together. However, this approach would also require a larger and more complex matrix inversion, which may result in numerical instability or convergence issues. Therefore, the current stepwise approach is used to balance the computational efficiency and numerical stability of the inversion process. Notably, performing an inversion for all receiver site factors and the global site variables simultaneously produced the same result. In this approach, the global site factor κ_0 can be excluded from the inversion process and later extracted from the receiver site factors under the condition that the geometric mean of the receiver site factors equals 1. To obtain reliable blast site factors, it was necessary to fix the global variables and receiver site factors and perform separate inversions for each blast site. The blast site factors are specific to each blast and are related to the charge weight and the distance between the

blast and the receiver. The charge exponent, on the other hand, is related to the attenuation of the wave with distance and is a property of the material through which the wave travels. In fact, the charge exponent is often used to infer information about the geological structure of the subsurface. Therefore, while the blast site factors are important for calibrating the PGV equation, they cannot fully explain the variation in charge exponents observed in the data. However, the blast site factors can explain the variability in the observed PGV amplitudes that is not explained by the charge exponent and are, therefore, essential for accurately modelling and predicting ground motion from future blasts.

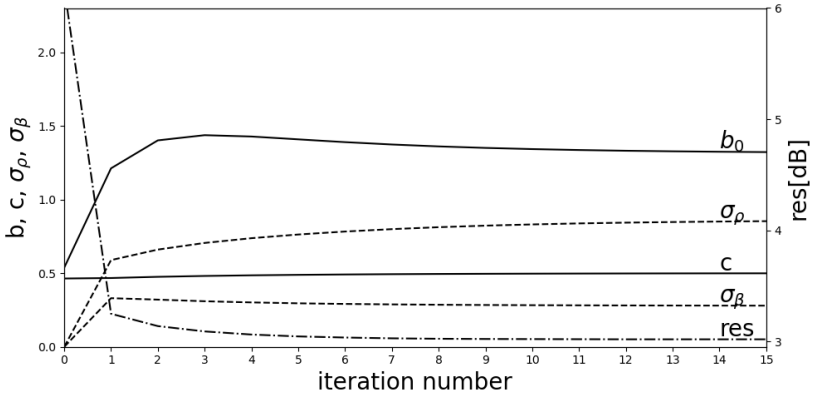

Figure 42: Evolution of the model parameters b_0, c_0, and of the standard deviations of the receiver and blast site factors, σ_ρ and σ_β (Trabi & Bleibinhaus, 2023).

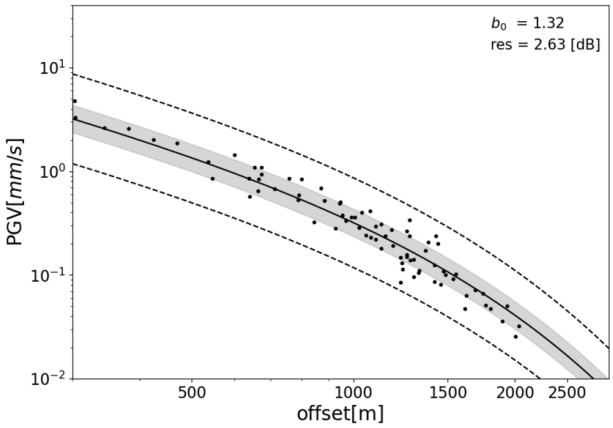

Figure 43: Data fit from the joint inversion of equation (12) for blast 30055 (Trabi & Bleibinhaus, 2023).

Figure 44 shows the distribution of the residuals per receiver station and blast. The receiver stations exhibit a strong variability: Residuals tend to be small for stations within the mine but also in the broad valley to the North, and large residuals cluster at the northwestern perimeter of the mine and in the narrow valley to the West. Blast residuals are more regular, but they also show some spatial variation with higher residuals to the West.

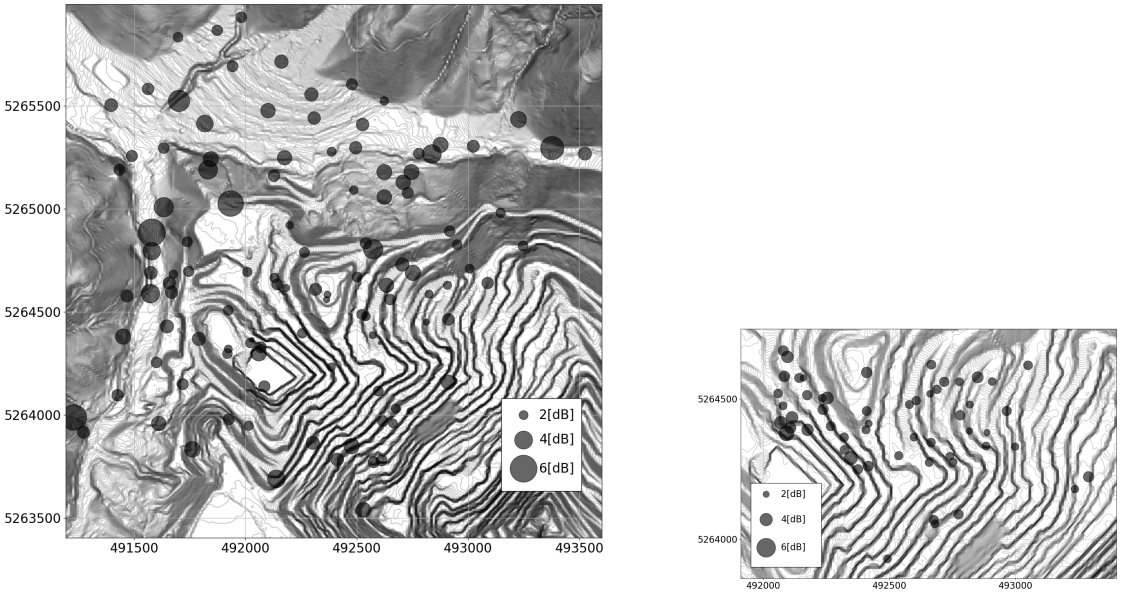

(a) (b)

Figure 44: Distribution of RMS residuals from the joint deterministic inversion (a) per receiver and (b) per blast (Trabi & Bleibinhaus, 2023).[1]

[1]DEM data source: CC-BY-4.0: State of Styria - data.steiermark.gv.at

5.3.2 Probabilistic Global Inversion

To better assess uncertainties and parameter correlations, a McMC inversion is applied to equation (12). The theory behind the McMC is briefly described in Chapter 8. To evade the indefiniteness of c and the blast site factors β_i two separate subspace inversions were performed. In one inversion, the site factors from the joint deterministic inversion as prior information were used and only inverted for the global parameters. Figure 45 shows crossplots of the corresponding posterior parameter distributions from a thinned chain of 10^6 models. The strongest correlation is between b_0 and κ_0. The reason is that larger κ_0 increases PGV, while larger decay b_0 decreases PGV so that increasing both at the same time does not alter the PGV too much within a limited offset range. The anti-correlation of the gradient $\partial b/\partial r$ with b_0 is because a larger gradient and a larger b_0, both increase the effective b, so that one parameter trades off with the other. Despite this trade-off, b_0-values of 95% of the models lie within the narrow range of 1.32 ± 0.14. Of course, b_0 is a nominal decay constant at a 1 m distance. Effective b-values at the remote stations are as high as 4.2 at offsets of 2500 m.
That the gradient shows an anti-correlation with κ_0 is a direct consequence of the correlation of b_0 with κ_0 and the anti-correlation of b_0 with the gradient. In contrast, c is mainly independent from the other parameters. There is only a minor trade-off with κ_0 because larger c and larger κ_0 both increase the PGV. Consequently, the deviation of c_0 is only 0.50 ± 0.04 for 95% of the models.
In a second McMC inversion, the global parameters from the joint inversion as prior information were used and inverted for the site factors, only. Figure 46 shows the corresponding distributions along with the values from the deterministic inversion, which generally align well with the central mode. Some receiver site factors are poorly determined. Those are sites that recorded only very few blasts. Blast site factors are generally better constrained because there are more observations per blast than per receiver.

5.4 Performance and Prediction Tests of the Engineering Formulas

One common way to evaluate the prediction with the observed values is to use statistical metrics such as the RMS residual and coefficient of determination (R^2). The R^2 measures the proportion of the variation in the observed values that is explained by the predicted values. It ranges from 0 to 1, where 1 indicates perfect agreement between the predicted and observed values. The coefficient of determination, R^2, between $\log(PGV_{obs})$ and $\log(PGV_{pred})$ can be calculated as:

$$R^2 = 1 - \frac{\sum_{i=1}^{n}(\log(PGV_{obs,i}) - \log(PGV_{pred,i}))^2}{\sum_{i=1}^{n}(\log(PGV_{obs,i}) - \frac{1}{n}\sum_{j=1}^{n}\log(PGV_{obs,j}))^2} \tag{13}$$

where n is the number of observations, $log(PGV_{obs,i})$ and $log(PGV_{pred,i})$ are the observed and predicted log(PGV) values of the ith observation, and the term $\frac{1}{n}\sum_{j=1}^{n}\log(PGV_{obs,j})$ is the mean of the observed log(PGV) values. These statistical metrics can provide a quantitative evaluation of the performance of a prediction model and can be used to compare the performance of different models or parameter settings. However, it is essential to also consider the context and purpose of the prediction, as well as any limitations or uncertainties in the observed data or the prediction model.
The performance of the methods in fitting measured PGV data is only one aspect of their practical usefulness. In addition, they need to be able to predict PGV for a projected blast to determine the maximum allowable charge. To test this capability, a bootstrap test was done in which 27 randomly

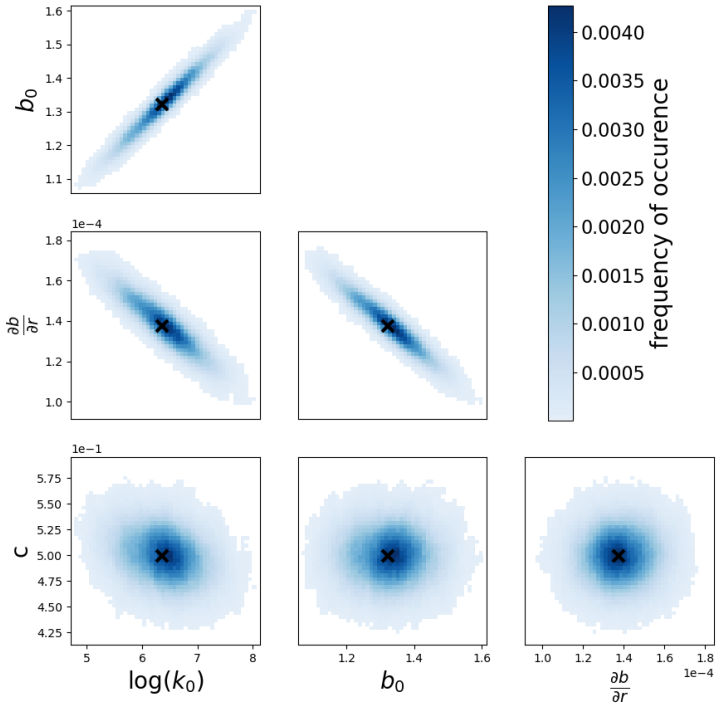

Figure 45: Posterior distribution crossplots of the four global parameters. A cross marks the result from the deterministic joint inversion (Trabi & Bleibinhaus, 2023).

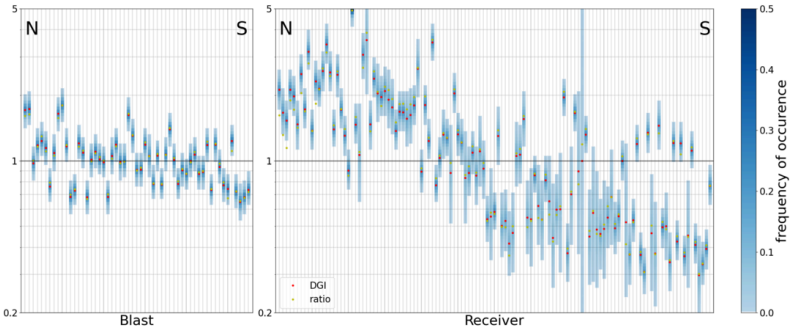

Figure 46: Posterior distributions of the blast and receiver site factors. Green dots are the mean ratios from the subset (CBG and sequential CRG) inversions, red dots are from the joint inversion (Trabi & Bleibinhaus, 2023).

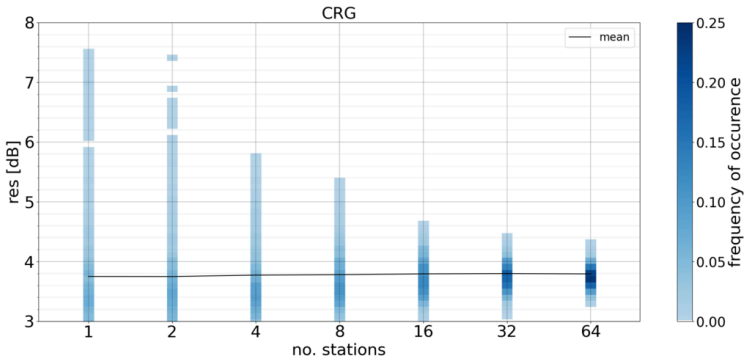

Figure 47: Distribution of the RMS residuals from the bootstrap prediction tests with the fixed-c CRG method for different receiver array sizes. The solid line is the mean rms residual of predicted blasts (Trabi & Bleibinhaus, 2023).

selected blasts were removed from the data set to create a reduced set of 28 blasts that were used to constrain the model parameters. To ensure that the c-value was adequately calibrated, a fixed c-value of 0.58 was used for the sequential CRG method. Receiver stations that recorded at least 20 blasts were used for the test, and the test was repeated 1000 times to obtain statistically relevant results. The fixed-c CRG method produced a mean residual of 3.8 dB, while the SD method with $m = 0.18$, the joint inversion method, and the SD method with $m = 0.5$ produced mean residuals of 3.9 dB, 4.0 dB, and 4.5 dB, respectively. The mean RMS residual was independent of the size of the receiver array, indicating that a single station is sufficient for making good predictions. However, the scatter in PGV predictions was large for some stations compared to others, as shown in Figure 44a.

5.5 Discussion

Table 3 summarizes the data fit of the different inverse methods and prediction tests. The normalized correlation coefficients of observed and predicted PGV are listed to compare the results to those of other studies. When site factors are not explicitly accounted for, the differences between the inverse methods are large. The CRG methods generally perform best. When optimized for the c/b ratio, the SD method and the sequential CRG method perform equally well, essentially because they both constrain c, either implicitly through optimizing c/b, or explicitly. In contrast, the SD performance with an arbitrary choice of $c/b = 0.5$ is significantly worse because b-values at Mt Erzberg are around 2 (Fig. 36, 39b), so that this ratio implies unrealistic c-values around 1. Despite that, it is still superior to the CBG method. That is because the subset methods implicitly account for the corresponding site factors, and these are less important for blasts (Fig. 46). While that can be explained by the much smaller geologic variations of blast sites compared to the receiver sites, their lesser importance is still remarkable since blast site factors also account for differences in coupling, decking, and burden.
Not using any local site factors, the joint inversion understandably shows the largest RMS residual. Judging from those differences, blast site factors improve the residual only by 0.7 dB, and receiver site factors by up to 2.6 dB. When all site factors are accounted for, the differences between the inverse methods largely disappear. That is so even for the SD method with $c/b = 0.5$ because it can project most of the erroneous charge-scaling into blast site factors. From Occam's viewpoint, the joint inversion

is to be preferred because it employs the least parameters to obtain the same residual. In the prediction test, where blast site factors cannot be employed, the differences between the CRG methods resurface. In particular, the performance of the SD method with $c/b = 0.5$ is, again, dominated by its erroneous c-value.

	w/o site factors			with site factors			prediction	
	N	R^2	res	N	R^2	res	R^2	res
CRG/seq	239	0.61	3.6	293	0.65	2.9	0.56	3.8
CRG/SD$_{0.2}$	238	0.61	3.6	292	0.66	3.0	0.57	3.9
CRG/SD$_{0.5}$	238	0.60	4.2	292	0.67	3.0	0.54	4.5
CBG	110	0.39	5.5	228	0.69	3.0	-	-
JI	4	0.27	6.2	177	0.69	3.0	0.62	3.9

Table 3: Performance of the various PGV predictors. N is the number of model parameters. R^2 is normalized. The RMS residual is in dB. The first two supercolumns refer to the inversion of the full data set. The prediction refers to the mean value of 1000 bootstrap tests with randomly selected 64 stations and 28 constraining blasts.

Judging from the b and c distributions of the subset methods (Fig. 31, 39, 36) it appears that both parameters are poorly determined. But the most extreme c-values occur for CRG with few observations with little charge weight variation. In the joint inversion of all data, $c = 0.5$ is well established (Fig. 45). This is a physically meaningful value when it is assumed that the fraction of charge c that is translated into seismic energy (E) is constant so that $c \propto E$, and $E \propto A^2$, the seismic amplitude. Because of the simplicity of this relation, it is hypothesized that it might be globally valid so long as the blasts are within similar rocks and the blaster appropriately adapts burden and decking to the charge weight. Regarding the amplitude decay constant b, the wide distribution of the subset inversions reflect a physical variation with offset due to a combination of a velocity gradient that decreases with depth (cf. Fig. 34) and presumably subsurface heterogeneity and topographic effects. When accounted for that variation in the joint inversion (eq. 12), a relatively well-defined value for b_0 is obtained. Despite that, the additional achieved residual reduction with the $b(r)$-variation is only ∼0.1 dB.

5.6 Conclusion

Due to the unaccounted non-linearity of PGV observations, their scatter is large for simple radial decay models, and the corresponding model parameters are poorly determined from small data sets, especially when the variation of the independent variables is small. Using data from a large station array, this limitation can be overcome with a joint inversion that provides a well-defined global amplitude decay constant b_0 and charge exponent $c = 0.5$. Based on the consistency with the physical expectation from the energy-amplitude relation of oscillations, it can be suspected that $c = 0.5$ may be a global value that needs no further calibration. The JI equation can be used to predict the PGV for all receiver locations on the map. However, the blast site factor should be excluded from the prediction, as it is an a posteriori fit to the actual amplification of the blast. To predict the PGV the slightly modified equation simplifies to:

$$PGV_j = \kappa_0 \rho_j r^{-(b_0 + r\partial b/\partial r)} q^{c_0}, \tag{14}$$

where the global site factor $\kappa_0 = 580.22$, r is the distance of hole with the maximum amount of explosives to the receiver j, with the radial decay exponent $b_0 = 1.32$ and it's gradient $\partial b/\partial r = 1.4 \times 10^{-4}$ and q is the maximal amount of explosive in kilograms, with the charge decay exponent $c = 0.5$. The site factors, ρ, are listed in the in Table 13.

In a bootstrap test, the most accurate predictions were obtained from a CRG method in which a fixed value for $c = 0.5$ was used as prior information. In contrast, the worst predictions were obtained for the SD method with a fixed ratio of $b/c = 0.5$ because that implies very unrealistic c-values, at least in the particular case. In addition, the data indicates that b varies for receiver stations at differing offsets, which implies that also c would vary for different stations: That is another reason why fixing the b/c-ratio is not advisable. Setting $c = 0.5$ instead will probably provide more accurate predictions, independent of the site.

The bootstrap tests have also shown that a single receiver station suffices to calibrate equation (6) and to make useful predictions (Fig. 47). However, the choice of the receiver site is quite important for the prediction accuracy (Fig. 44a), and probing different sites is strongly advised. Of course, selecting receiver sites with the highest prediction accuracy does not cancel the more erratic points that regularly show large outliers. These outliers and the correspondingly large final residual of ∼3.0 dB are primarily attributed to the complexities of seismic wave propagation and related caustics in a heterogeneous medium. Predicting those would require a detailed knowledge of the subsurface structure and numerical modelling that are beyond this study.

6 Modelling Seismic Waveforms

The main task of this research is the reduction of mining blast vibrations in a selected target zone through the interference of double blasts using realistic waveforms. Therefore production blasts had to be simulated based on configurations that were announced 24-48 hours before the actual blasts took place. The provided parameters included the actual positions of the blastholes and an estimated amount of explosives. Performing a 3D waveform simulation for the site within that short time frame was not possible for the local high-performance computing (HPC) cluster. Therefore, the numerical simulations were performed on Europe's fastest supercomputer, Marconi-Broadwell, using the Barcelona Subsurface Imaging Tools (BSIT), a code developed at the Barcelona Supercomputing Center and Centro Nacional de Supercomputación by a research group led by Dr. de la Puente. The BSIT code that was used to predict the wave propagation accounts for all seismic phases (P-, S- and surface waves). The seismic wave equation is solved with a finite difference scheme for 3D elastic wave propagation with the presence of topography (de la Puente et al., 2014). The waveform forward-modelling was conducted on a 3D model of Mt. Erzberg (Tauchner et al., 2018). The access to the super-computer, Marconi-Broadwell, was granted for one month, and in that time, waveforms were pre-calculated. At the time of calculation, the actual positions of the future production blasts were unknown. Consequently, blast shots were simulated from 80 uniformly spaced positions (crosses in Figure 51) across the designated area for planned production blasts. From that predetermined positions the interpolation is done within minutes, allowing for immediate searching for an optimal blast configuration. The method aims to simulate waveforms emitted from production blasts by the superposition of the seismograms generated by numerical simulated blastholes. From the final waveforms of the simulated production blasts, the PGV can be directly derived from the amplitude. Several processing steps are necessary before using the numerical data to predict PGV at any arbitrary location. This chapter, along with its subsequent subchapters, outlines the processing steps that were undertaken. These processing steps can be applied to any position on the map. For simplicity, the whole process is explained by using the position of stations 24 and 47 (Fig. 51) for the vertical component only.

6.1 Finite Difference Modelling of Seismic Waveforms

The wave equation has to be solved to describe wave propagation in a medium. Several methods can be used to solve the seismic wave equation, including, for example, the finite difference method, the finite element method, and the spectral element method. Each of these techniques offers different strengths and is selected based on the specific requirements of the simulation, such as accuracy, computational power, and complexity of the geological model. The finite difference method is a widely used technique for full waveform modelling. It is easy to implement and efficient for large scale simulations. It solves the wave equation on a grid by approximating derivatives with finite differences. However, these methods have difficulties with non-flat topography (de la Puente et al., 2014). One approach used for numerical modelling is the staggered-grid time-domain finite difference method introduced by Virieux (1984, 1986). A staggered grid is a numerical method where different physical quantities, like velocity and stress, are not located at the same grid point but are staggered by half the distance between two grid points. This method has limitations when modelling strong anisotropy or topography. The approach of de la Puente et al. (2014) solves the seismic wave equation on a finite difference grid, using the Fully Staggered Grid approach from Lebedev (1964) and a first-order stress-velocity formulation after Virieux (1984). To respect the topography, Cartesian coordinates are deformed

onto a curved grid (Fig. 48). The deformation is Cartesian and regular in the xy-plane but deformed in the z-direction. However, deforming is unsuitable for accurately representing distinct tiers' sharp edges. A 50-meter-wavelength high-cut filter was applied to Styria's 10-meter Digital Elevation Model (DEM). The smoothing affects waveforms at around 100 Hz, but the dominant frequency is generally around or below 30 Hz. While smoothing has little influence on the far-field at that frequency, it can result in a loss of detail and less accurate predictions in the near-field. The explosive source is introduced at a specific location in the domain, typically modelled with a Ricker wavelet as the source time function. The source's location, depth, and wavelet parameters, such as peak frequency, are critical initial conditions for the simulation (de la Puente et al., 2014). In the first forward modelling, the shots were implemented as isotropic point sources that did not radiate S-waves. The smoothing of the topography resulted in some blast shots being located above the surface, while others were positioned far below it. The secondary phases, which are conversions, had amplitudes strongly dependent on the depth of the sources. To ensure uniform conditions, in a second attempt, the depth was arbitrarily set to 10 m for all blast shots below the surface. The free-surface condition is a Dirichlet boundary condition applied to the stress tensor. This condition is crucial for accurately modelling the interaction of seismic waves with the surface. The condition ensures that the stress components normal to the surface vanish, which is critical for simulating how waves reflect or refract at the surface. However, finite difference methods have difficulty obtaining accurate results close to the boundary. The free surface condition has been handled with mimetic operators. Mimetic operators are a class of discrete operators designed to preserve critical properties of the continuous differential operators they approximate. In the context of seismic wave modelling, these operators are used to ensure that the numerical solution adheres to the physical laws governing wave propagation, such as conservation laws and the correct behaviour of wavefields across interfaces and boundaries (de la Puente et al., 2014). To handle the computational domain's boundaries and prevent reflections from the model's edges, which could interfere with the simulation, sponge-like absorbing boundary conditions are applied (Cerjan et al., 1985).

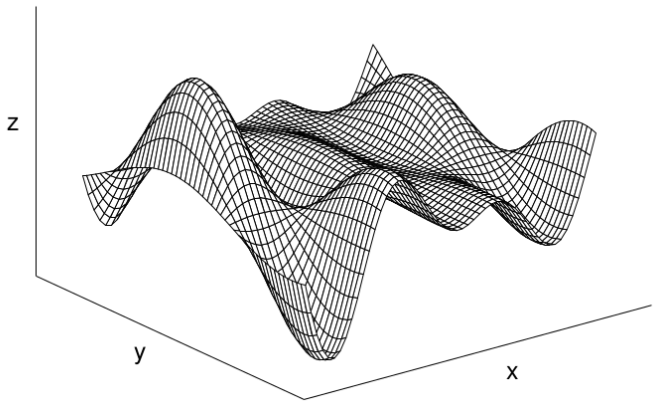

Figure 48: Exemplary curved finite difference grid (Hestholm, 1999).

BSIT requires all waves to be sampled at least 8 points per wavelength. With a minimum velocity of 600 m/s in the sedimentary basin and a frequency of up to 120 Hz, a grid spacing of 0.4 m was required. This corresponds to a discretization of 3000 x 3600 x 2000 ($=2.16 \times 10^{10}$) grid cells. The

spatial discretization require a time discretization of 15 μs to ensure stability following the Courant-Friedrichs-Lewy conditions. With 240 bytes per cell, including the wavefields that have to be stored to integrate in time, the amount of memory required, including boundary conditions for computing one shot is ∼8.0 TByte (Bleibinhaus et al., 2019). The final data is stored at the free surface with a 4x4 m grid spacing and a sampling rate of 2.5 ms. The high computational demand is primarily due to the extremely low sedimentary velocities in the model, combined with frequencies up to 120 Hz, which demands a small grid spacing. The computational demand is proportional to the number of grid cells, and the number of grid cells is inversely proportional to the cube of the grid spacing, which is dictated by the lowest velocity. Figure 49 plots the number of grid cells versus the minimal velocities at a frequency of up to 120 Hz. A lowest velocity of 3000 m/s would already result in approximately 100 times less computational demand. The wavefields had to be pre-computed because the supercomputer, was not available on demand, and the calculations were too demanding for the local HPC. If the valley fill, and therefore its low velocities, had been ignored in the model, the computational expense would have been much lower, allowing for on-demand waveform modelling. At that time, the decision was made to continue with the approach of interpolating the waveform from the pre-computed position to a new position.

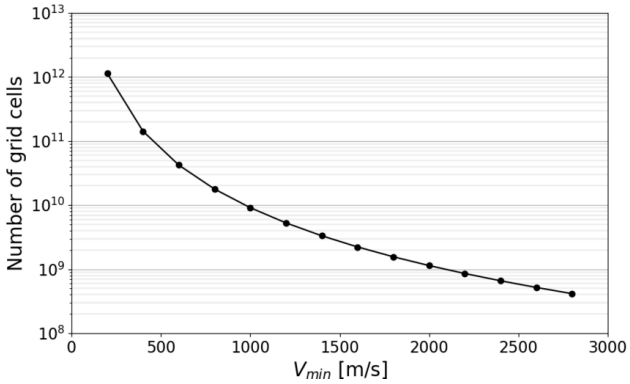

Figure 49: The minimum velocity in the model plotted on the x-axis versus the number of grid cells required on the y-axis.

6.2 Derivation of the physical parameters of the subsurface model.

The seismic site characterization provided a high-resolution P-wave velocity model but did not provide any information on S-waves. For the elastic modelling, P-wave velocity, S-wave velocity and density models were also required. The empirical relation of Gardner et al. (1974) is used to obtain the densities (Eq.15).

$$\rho = 310 \sqrt[4]{V_p} \tag{15}$$

with density ρ and P-wave velocity V_p given in SI-units. Using the derived P-wave velocities from the travel time inversion, the density is estimated to be approximately 2.5 g/cm^3. This value falls within the range of laboratory measurements for limestones reported by Schmidbauer (2023) and aligns

with values for limestone and porphyry found in the literature of SCHÖN (2011). The S-waves were computed from the P-waves with the relationship of equation 16.

$$V_S = \begin{cases} \frac{V_p}{1.75} & \text{if } V_p > 2200\,\text{m/s} \\ \frac{V_p}{1.75+5.25f} & \text{if } V_p < 2200\,\text{m/s} \end{cases} \qquad \text{with scaling factor} \qquad f = \frac{2200 - V_p}{2200 - 1500} \tag{16}$$

6.3 Source Wavelet

A Ricker Wavelet with a peak frequency of $f_p = 40$ Hz is used as source wavelet. A Ricker wavelet is a zero-phase wavelet that is typically employed for forward-modelling because it has a steep roll-off at high frequencies, while it is still relatively short in time. Figure 50 shows the frequency spectrum of the stacked, trace-normalized numerical data. The amplitude spectrum in Figure 50 falls within the range of the used Ricker wavelet with a peak frequency of f_P= 40 Hz.

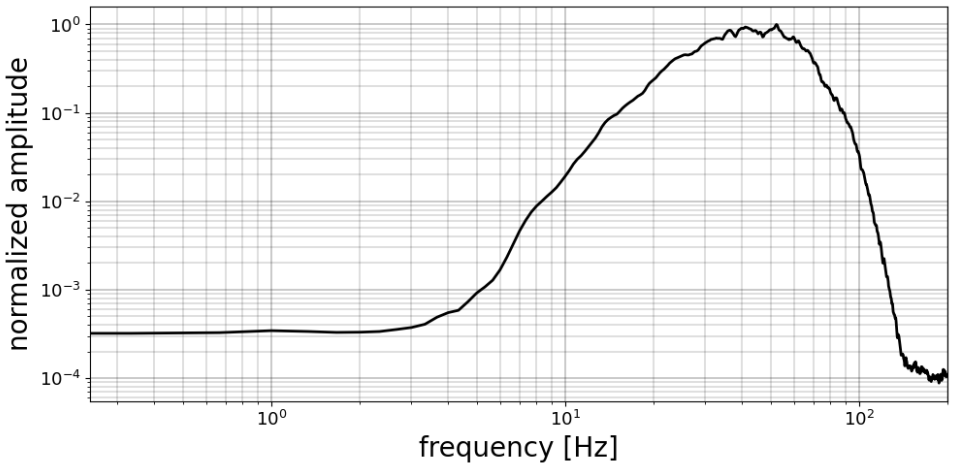

Figure 50: The mean amplitude spectrum of the raw numerical data after trace-normalizing all seismograms.

6.4 Interpolation for an Arbitrary Position

The black dot marker in Figure 51 represents the blast position in which the seismogram is aimed to be interpolated using data from the four nearest neighbouring simulated blasts (black plus marker). The interpolation can be performed for any grid point across the entire area, but for simplicity, it is demonstrated using seismograms at positions 24 and 47. Position 24 has a small offset to the blast, while position 47 is located further away.

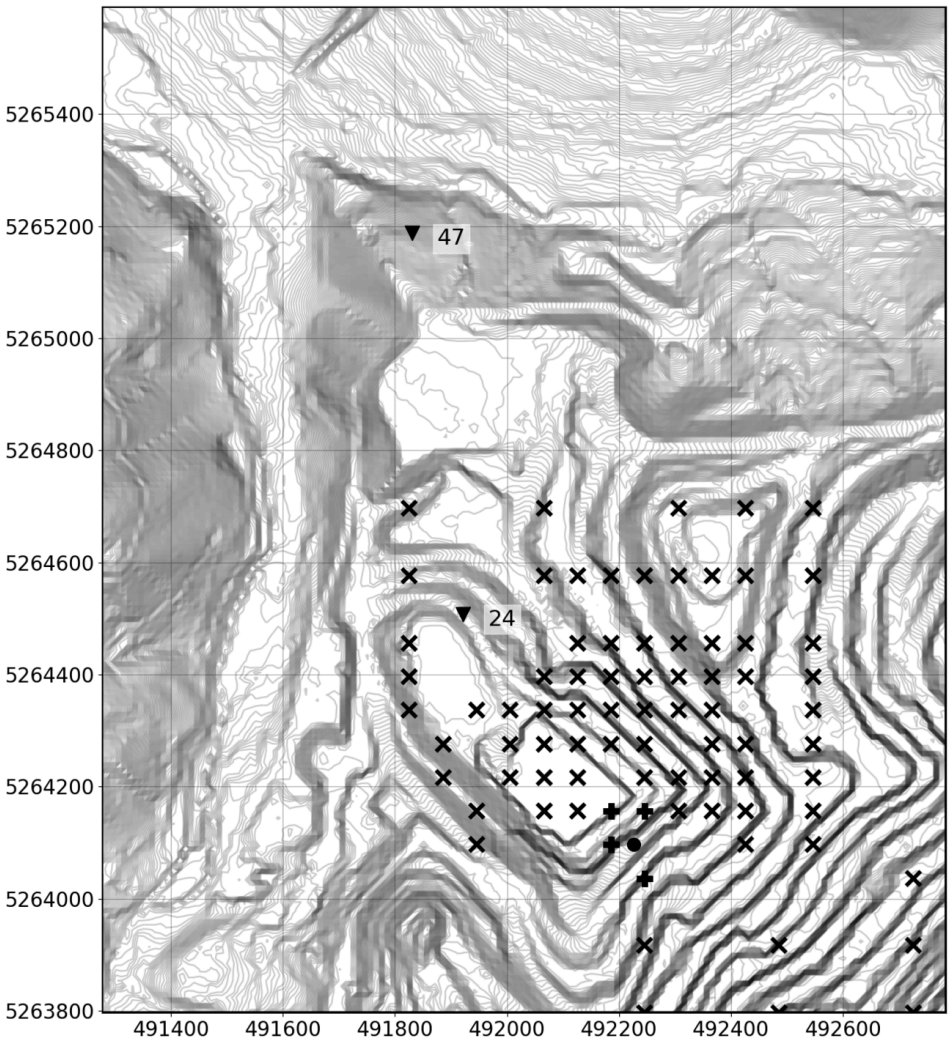

Figure 51: The black crosses and plus markers are the positions from where the forward-modelling was performed. The plus markers are the 4 next neighbours, which are used to interpolate a blast at the position with the black dot.[1]

For the interpolation it is important to get the P-wave travel time from the new interpolated blast to the receiver positions. The smoothed velocity model suggests a very small variation in velocity domain. Therefore it was decided to do an interpolation to derive the average P-wave velocities from the new

[1]DEM data source: CC-BY-4.0: State of Styria - data.steiermark.gv.at

interpolated blast position ($v_{p,i}$) to all receivers. The P-wave onset in the seismograms of the numerical data is easy to pick as they are free of noise before the onset of the P-wave (Fig. 52a). By picking the P-wave onset, the travel time for each receiver-shot pair can be determined from the data. The next step is to calculate the offset for all these pairs, which is straightforward. With this information, the average P-wave velocities from all blasts to all receivers can be calculated. The average P-wave velocities for the blast-receiver pairs at the interpolated blast position ($v_{p,i}$) are then determined as the inverse distance-weighted mean of the average P-wave velocities of the four nearest neighbours ($v_{p,n}$), calculated using the formula (17):

$$v_{p,i} = \frac{\sum_{n=1}^{N} \frac{v_{p,n}}{d_n}}{\sum_{n=1}^{N} \frac{1}{d_n}} \tag{17}$$

Here d_n is the distance between interpolated blast position i and the nearest neighbour n. As the four nearest neighbouring blast positions are in very close vicinity, the differences in ray paths are assumed to be negligibly small, and the average P-wave velocity is, therefore, expected to be relatively similar in all nearest neighbours. The accuracy of this next-nearest neighbour interpolation algorithm is sufficient for the smoothed velocity model without drastically increasing computational complexity. This interpolation algorithm can still capture the slight variation in P-wave velocity. The next step is to calculate the offset of the interpolated blast position to all receiver positions. With the known offset and derived average P-wave velocities, the P-wave travel time from the interpolated blast to all receivers can then be determined. Another approach would be to calculate the travel times with an interpolation in slowness domain, as this maintains the direct relationship. Also directly interpolating in travel time would be possible. However, the additional calculation step has an insignificant impact on both the computation time and the result, given the almost negligible velocity variations. In contrast travel time variations to different blasts are large and that would have made the interpolation result sensitive to the interpolation approach. The S-wave onset arrives with a $\sqrt{3}$-fold delay after the P-wave onset. The seismograms of the four neighbouring shots are shifted at the onset of the P-waves and S-waves to the onset of the interpolated shot (Fig. 52b). Between the P-wave and S-wave onset, the seismograms are stretched or compressed linearly. For the shifting of the seismograms, the sample rate is up-sampled to a rate of 0.625 ms. The interpolated seismogram (Fig. 52c) is then calculated by summing the inverse distance-weighted seismograms of the neighbouring production blasts using the formula (18):

$$A_i = \frac{\sum_{n=1}^{N} \frac{A_n}{d_n} \frac{o_n}{o_i}}{\sum_{n=1}^{N} \frac{1}{d_n}} \tag{18}$$

In formula (18), the amplitudes of the neighbouring seismograms (A_n) are scaled by their offsets (o_n) relative to the offset of the interpolated blast (o_i), to account for the amplitude decay. An amplitude decay exponent of 1 is assumed for the energy decay of body waves. The same procedure is demonstrated for near offsets at position 24 (Fig. 53).

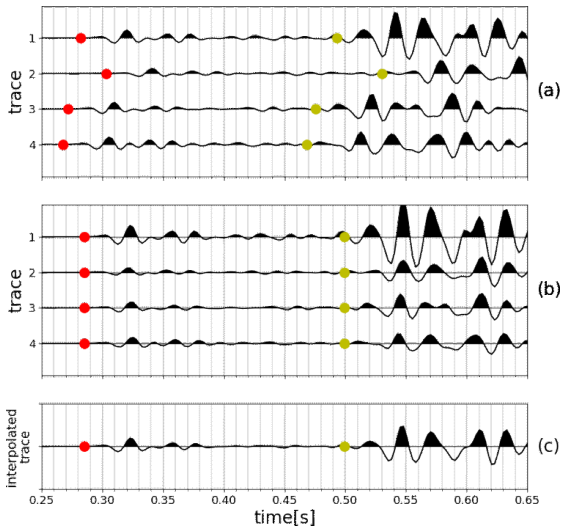

Figure 52: (a) The seismograms of the 4 nearest neighbouring simulated blasts at receiver position 47 with the P-wave pick (red dot) and the time of the S-wave (yellow dot). (b) The seismograms of the 4 nearest neighbours were shifted to the expected travel time of (c) the interpolated seismogram.

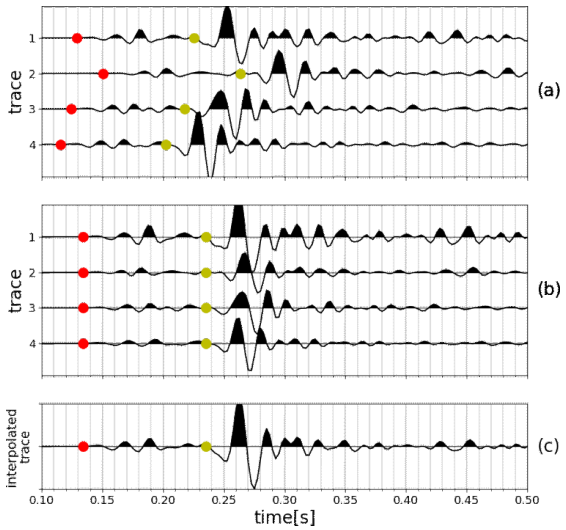

Figure 53: (a) The seismograms of the 4 nearest neighbouring simulated blasts at receiver position 24 with the P-wave pick (red dot) and the time of the S-wave (yellow dot). (b) The seismograms of the 4 nearest neighbours were shifted to the expected travel time of (c) the interpolated seismogram.

6.5 Conversion of Zero-Phase Wavelet to Minimum-Phase Wavelet

The seismogram can now be calculated for any arbitrary blast position on the map. To predict a production blast, it is essential to know a more realistic STF. The next step involves to convert the zero-phase wavelet to a minimum-phase wavelet. Previous attempts of deconvolution failed to produce a meaningful STF (Reiner, 2018). At that point in the research, I didn't have a good minimum-phase STF. So, the decision was made to take a Kuepper wavelet for the predictions. Later, from the data of the 2016 survey, Bleibinhaus & Trabi (2023) derived the STF from a Laplace-domain inversion (LDI). At that time the SLIM project already ended and this STF was not available at the time when the predictions were made. With the data from the electronic production blasts made in the SLIM project, the STF was finally able to be reconstructed through a deconvolution of a spike sequence on the recordings of the production blasts. However, this method had limitations as the STF could only be extracted under certain conditions.

6.5.1 Kuepper Source Time Function

The zero-phase Ricker wavelet is converted to a minimum-phase Kuepper wavelet (Kuepper, 1958) with an equivalent amplitude spectrum. The Ricker wavelet is given by:

$$f(t) = (1 - 2\pi^2 f_P^2 t^2) e^{-\pi^2 f_P^2 t^2} \tag{19}$$

The formula for the Kuepper wavelet is:

$$f(t) = \begin{cases} \sin(2\pi t f_P) - \frac{1}{2}\sin(4\pi t f_P) & \text{if } 0 \leq t \leq T_0 \\ 0 & \text{otherwise} \end{cases} \tag{20}$$

Two filters were created to perform this conversion. The first filter was designed to transform the 40 Hz peak Ricker wavelet (Eq. 19) to a Kuepper wavelet (Eq. 20) with a peak frequency of 40 Hz. A second zero phase filter transforms the amplitude response of the Kuepper wavelet to the amplitude response of the Ricker wavelet. These two filters can be summarized as one filter with an amplitude ratio equal to one and the phase difference of the Ricker and Kuepper wavelet. After applying the filter on the Ricker wavelet, the result is a Pseudo-Kuepper wavelet with the amplitude spectrum of the Ricker wavelet. This resulting wavelet is not a Kuepper wavelet, but for simplicity the term Kuepper will still be used in this thesis. Figure 54 displays the Ricker wavelet, and its amplitude and phase spectra in the first column. The Ricker wavelet is zero-phase, the linear trend in the phase spectrum is the time shift by feeding the wavelet into the FD modelling at $-T_0$ (Fig. 54g). The resulting filter, with its amplitude and phase spectrum is shown in the second column. The third column, shows the Ricker wavelet after convolution with the filter, which results in the (Pseudo-)Kuepper wavelet. The resulting Kuepper wavelet is point-symmetric with respect to the first zero crossing and therefore has a constant phase of $\pi/2$. Superimposed on this is a linear trend that corresponds to the time difference between $t = 0$ and the first zero crossing. This wavelet was used for the forward-modelling and the predictions of the first verification experiment.
The amplitude magnitude of the numerically forward-modelled data is artificially small, with amplitude values in the order of 10^{-15}. For the numerical forward-modelling a zero-phase Ricker wavelet with a peak frequency of $f_P = 40$ Hz was used and therefore the frequency spectrum of the numerical forward-modelled data is in the range of the used source wavelet. To match the observed amplitude spectrum

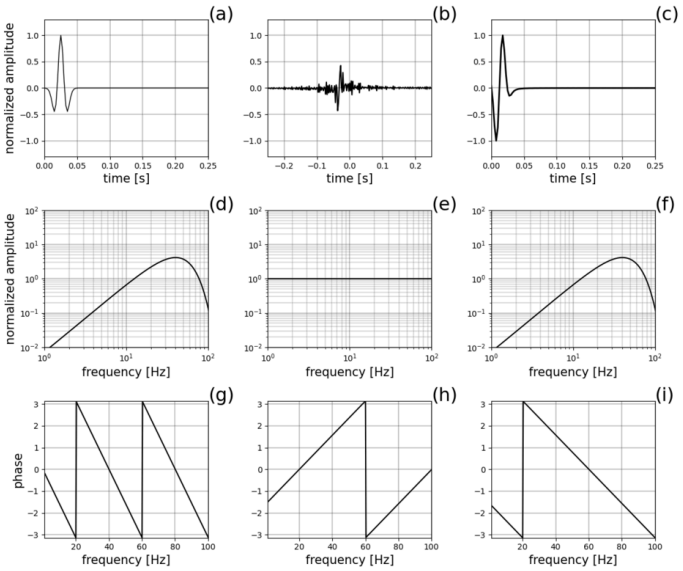

Figure 54: (a) The Ricker wavelet gets convolved with (b) the filter to create (c) a minimum phase wavelet. (d) The amplitude spectra of the Ricker wavelet, (e) the filter and (f) the Kuepper wavelet and (g, h, i) their phase spectra.

with the numerical method, a third filter was constructed based on the data from the first verification experiment. A ratio of the amplitude spectra of the observed data to the amplitude spectra of the numerically forward-modelled data was determined at every recording position. The amplitude spectra were obtained by performing a Fourier transform of both the observed and numerical seismograms. The ratio of the amplitude spectra was then calculated at each station and each production blast. The geometric mean ratio was computed from all these ratios. Figure 55a displays the mean amplitude ratio (depicted by the black line) after applying smoothing. A moving average filter was employed with an increasing window size with frequency. Specifically, the window size ranges from +/-0.5Hz at 1Hz, linearly increasing to +/-50Hz at 100Hz. Otherwise, the amplitude ratio becomes unstable at high frequencies. The phase spectrum was ignored by this filter because the mean phase shift (Fig. 55b) converged to zero across all production blasts and stations. For this reason, a zero-phase filter was applied to match the numerical amplitude response to the observed amplitude response. This was the first attempt to fit the observed amplitude spectrum with the numerical forward-model by using the Kuepper wavelet. All three filter can again be summarized in one filter (Fig. 56b). Convolving the Ricker wavelet (Fig. 56a) with this filter results in a Kuepper wavelet (Fig. 56c) with an amplitude response, which is more similar to the observed amplitude response.

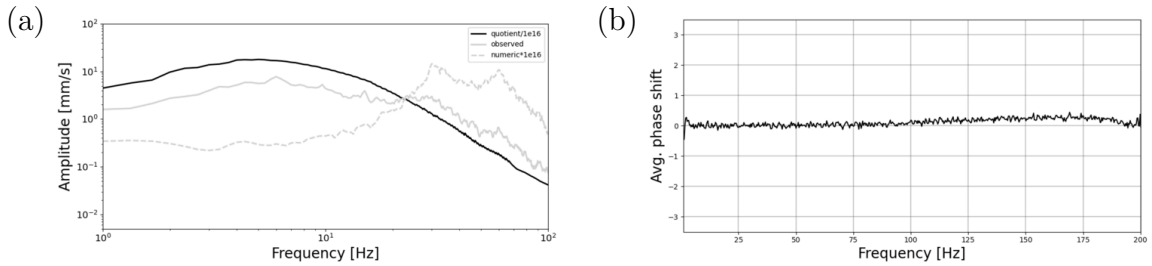

Figure 55: (a) The black line is the smoothed ratio of observed to numerical amplitude at every receiver position, where the grey line represents the mean amplitude spectrum of all observed blasts at all receivers, and the grey dashed line represents the same for the numerical blasts, scaled by 1e16 to fit on the figure. (b) The mean phase shift was calculated from the numerical and observed production blasts.

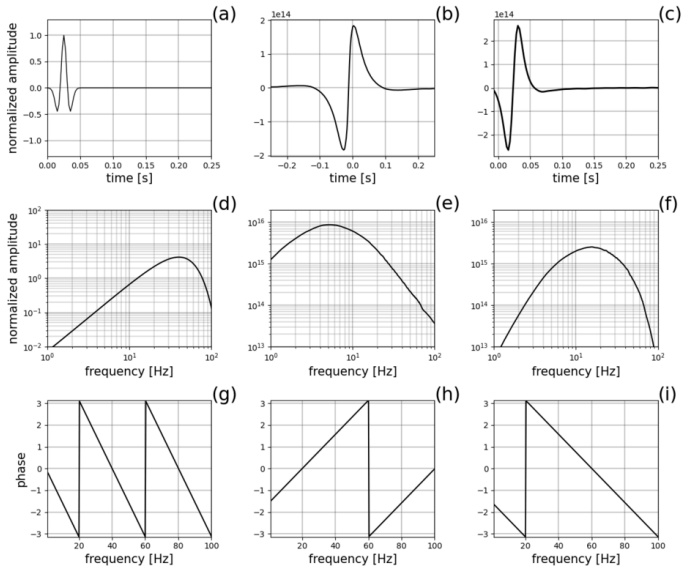

Figure 56: (a) The Ricker wavelet gets convolved with (b) a filter to create (c) a minimum phase wavelet. (d) The amplitude spectra of the Ricker wavelet, (e) the filter and (f) the Kuepper wavelet and (g, h, i) their phase spectra.

6.5.2 Source Time Function from Laplace-domain Inversion

The Kuepper wavelet served as a temporary aid to mimic the STF of a single blast shot. Later Bleibinhaus & Trabi (2023) derived the STF from an LDI of the mean spectral amplitude distributions of ten NONEL production blasts recorded in 2016. Their LDI STF model can be used to create a wavelet representing a seismic waves generated by mine blasts, taking into account the frequency and amplitude characteristics observed in real blast data.
Based on their work I created STFs for all possible charge weights in 5 kg increments. For every generated STF, a filter was created that converts the Ricker wavelet into that particular STF with that particular charge weight. This filter will then be convolved on the original seismograms which were created with the Ricker wavelet, taking into account the respective amount of explosives per hole. The example filter in Figure 57 was created for a shot with a charge weight of 300 kg. The first column in Figure 57 shows from top to bottom: The time series of the Ricker wavelet, its amplitude spectrum and its phase spectrum. The second column shows the generated filter, with the respective amplitude and phase spectra in rows two and three. The last column finally shows the final STF after the convolution of the Ricker wavelet with the filter. A water level of 1% of the maximum amplitude was introduced because the Ricker wavelet contains little signal below 3 Hz (Fig. 50). This ensures stability and prevents the amplification of noise in the low-frequency range where the Ricker wavelet's signal is weak. While the Kuepper wavelet was used as a temporary aid for the prediction, it turned out that the LDI-STF has a slightly better fit in terms of waveform match. In Chapter 7, among other methods these two methods are compared and it shows that the LDI-STF (Fig. 73e) has generally a higher cross-correlation coefficient (xcc) with the observed data than the Kuepper wavelet (Fig. 73d). One big advantage of the LDI-STF over the Kuepper STF is that the dominant frequency is is scaled by the charge weight, which is one reason that can explain the better xcc.

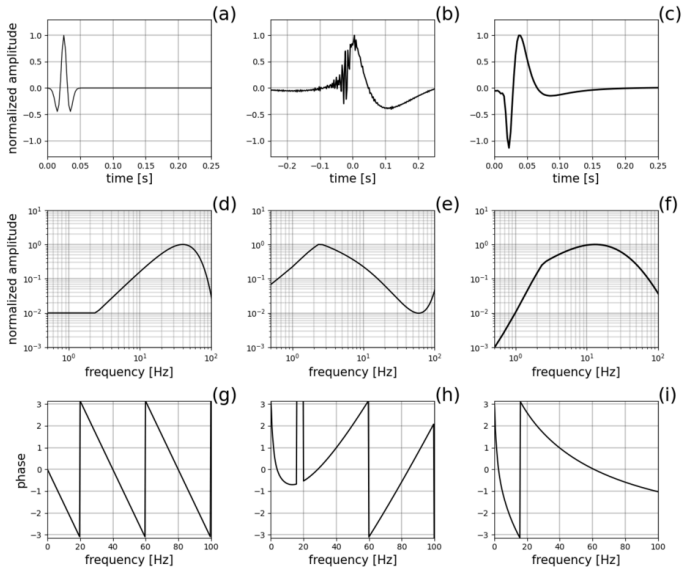

Figure 57: (a) The Ricker wavelet gets convolved with (b) a filter to create (c) a minimum phase wavelet. (d) The amplitude spectra of the Ricker wavelet, (e) the filter and (f) the LDI wavelet and (g, h, i) their phase spectra.

6.5.3 Source Time Function from Deconvolution with the Delay Time Spike Sequence

A third way to obtain the STF is by extracting it from the data by deconvolving a recorded seismogram by a spike sequence. This method has some disadvantages; for example, the STF can only be extracted from electronically ignited production blasts where the delay timing is exact and in blasts where the amount of explosives does not vary significantly. Although this STF is not used for forward-modelling in this study, it can still provide deeper insights and verify the LDI-STF. The LDI-STF is derived from another dataset, and the properties of both STFs can be compared in terms of waveform fit or dominant frequency. Because there is no seismic record of a single-hole shot, this derived STF could be used for a hybrid approach similar to the method of Hinzen (1988). The number of production blasts in this study is very small, which is making it challenging to have enough comparable blasts to verify the extracted STF. This study has yet to use the extracted STF of one production blast to predict another similar production blast. In an example for production blast 10020 (Fig. 58), the same procedure is applied as in Subchapter 4.4.6. The resulting STF at each station (Fig. 58a) is then trace-normalized and stacked to the final STF (Fig. 58b). The strong onset of the P-wave is clearly visible at time 0 s. The stacking process also suppresses the later arriving phases.

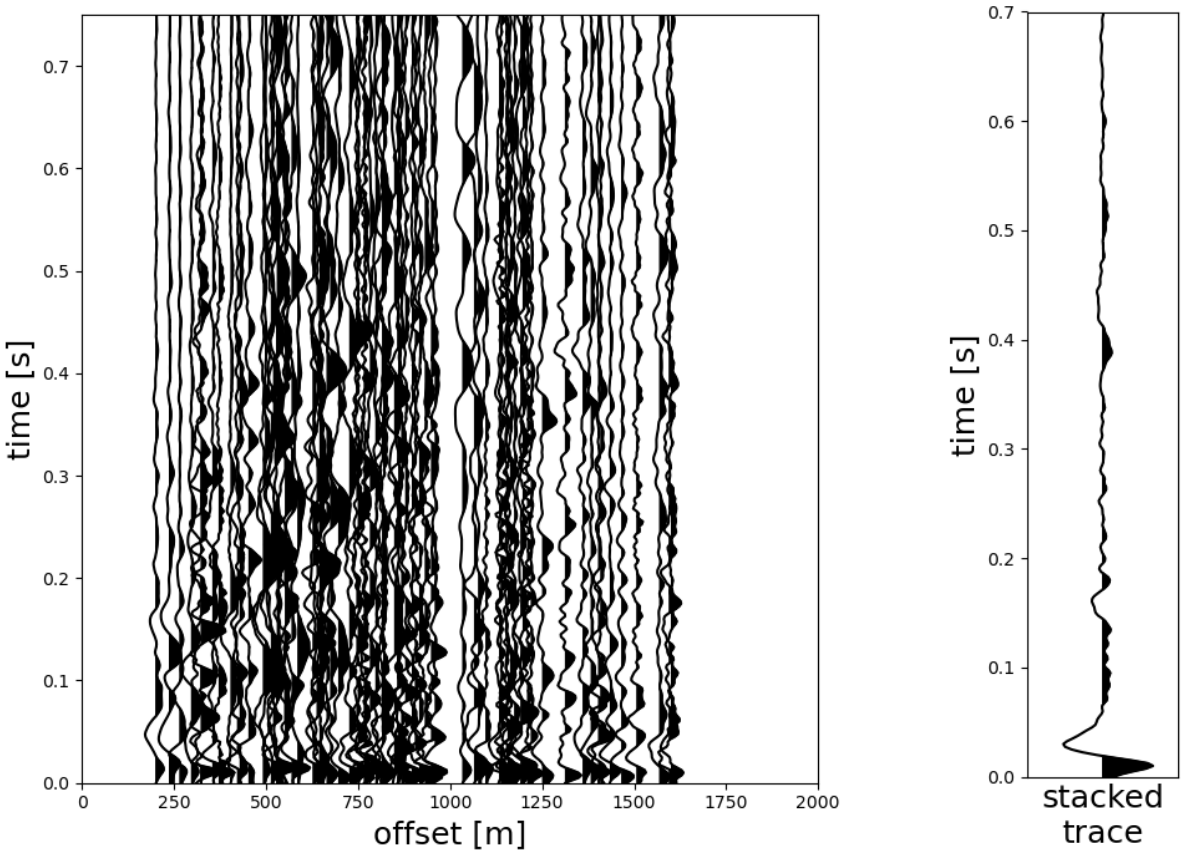

Figure 58: (a) The deconvolved seismograms for production blast 10020 sorted by offset and (b) the STF derived by stacking of all deconvolved seismograms.

6.6 Accounting for the Amplitude Effect of Charge Weight

The numerical amplitude value needs to be scaled by the amount of explosive used in the blast simulation. This scaling is crucial as each blasthole in the sequence contains a different amount of explosives, resulting in varying magnitudes of amplitudes. The seismic energy E released by the blasts is proportional to the charge weight. Most of the energy is used in comminution of the rock, and only a fraction is converted to seismic waves, However, it can be assumed that this fraction is constant, and that the assumption $E \propto A^2$ hold. It can then be concluded that $A^2 \propto c$, or $A \propto c^{0.5}$. Chapter 5 demonstrated empirically that $c = 0.5$ provides a good match.

6.7 Tapering S-waves

In the numerical model, a strong conversion of P-wave to S-wave and surface waves was observed. Figure 59a shows the numerical data from the single simulated blast shot at the previously mentioned interpolated position, sorted by offset. The amplitude in the figure is scaled by 4 times the maximum value to emphasize the onset of the P-wave. The numerical data clearly shows the onset of a relatively small peak from the P-wave, with an apparent velocity of about 4250 m/s. At an apparent velocity of 2400 m/s, which is 1.75 times slower than the P-wave velocity, the first onset of the S-wave can be observed. There are also onsets of later arriving phases, likely waves travelling along the surface. Waves which travel along the surface can pass through the low-velocity area in the model, where the sedimentary basin is located. Compared to the late phases, the P-wave amplitude is very small in the numerical forward-modelled data. This dominance of S-wave in the numerical data is not observed in the recorded data from the real production blasts. To address this discrepancy, it was decided to reduce the amplitude of the seismogram from the onset of the S-waves. To minimize truncation effects, a cosine-taper was applied (Fig. 60). The example illustrates the original seismogram (grey) with the dominant S-wave onset at 0.25 sec. The cosine-taper window length is set to 30 samples. The window length is chosen so that P- and S-waves have already separated at an offset of 300 m. At the calculated onset of the S-wave, the taper reaches its minimal value. The resulting seismogram (black) shows a reduced S-wave amplitude, with a ratio of 0.1 to the initial S-wave amplitude. After tapering, the amplitude for the late arriving seismic phases in this single blast example (Fig. 59b) looks more similar to the observed data discussed in Chapter 4.4.

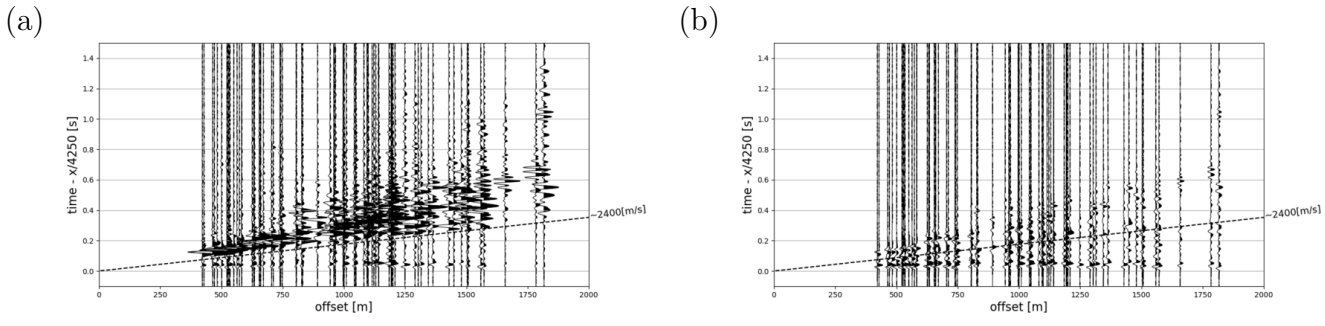

Figure 59: A time-reduced seismogram section of the z-component of a numerical forward-modelled single shot (a) before taper and (b) after taper.

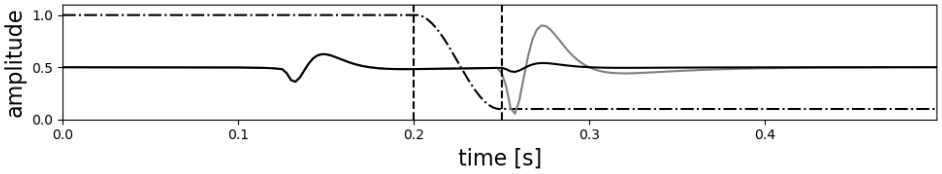

Figure 60: A sketch of an exemplary seismogram (black line) after tapering with a cosine-taper (dashed-dotted line) applied to the raw seismogram (grey) is shown.

6.8 Frequency-dependent gain function for each Receiver

Local site effects play an important role in the hazard assessment of a specific site. These site effects, which are caused by the local geology, can amplify or attenuate seismic energy. Soft sediments in a sedimentary basin, for example, tend to amplify the ground motion and tend to increase lower frequencies. The study area has a quite heterogeneous geology as highlighted in Subchapter (2.2). Approximately half of the stations are located on hard rock, while the other half is situated on a sedimentary layer, which is expected to vary in thickness by up to approximately 150 m. To account for these site effects a filter at every recording position was created which was later applied to the numerical data. For the filter, a spectral ratio of the observed data to the numerical data is calculated. For every production blast, a Fourier transformation is performed, and the absolute value of the complex numbers is calculated to obtain the amplitude spectra of both the numerical and observed data at each station. From these amplitude spectra, ratios were calculated for all production blasts. Then, the geometric mean of all ratios at each station is calculated. To get rid of the spikes at the higher frequencies, the average ratio is slightly smoothed with a moving average filter with an increasing window size with frequency. The window size of the smoothing operator in the frequency domain is set to 1 at the beginning, and it linearly increases to approximately +/-8 Hz at 200 Hz. Frequencies below 3 Hz are manually reduced to prevent the amplification of the erroneous signal below 3 Hz. Figure 61 shows the observed mean amplitude spectrum (grey), the numerical mean amplitude spectrum (grey dashed) of all blasts and the smoothed ratio (black) at station 11, (a), 24 (b) and 47 (c). The distinctive frequency-dependent gain function adapt the respective amplitude spectrum from the numerical modelling to that of the observed data . A normal site factor would have a white spectrum. The phase spectrum is very noisy and fluctuates around zero (Fig . 61d, e, f). As the number of production blasts increases to create a filter, the phase spectrum converges to zero. The resulting restitution filter at each station is a zero-phase filter, which adjusts the amplitude spectrum to the specific site in which the receiver is located.

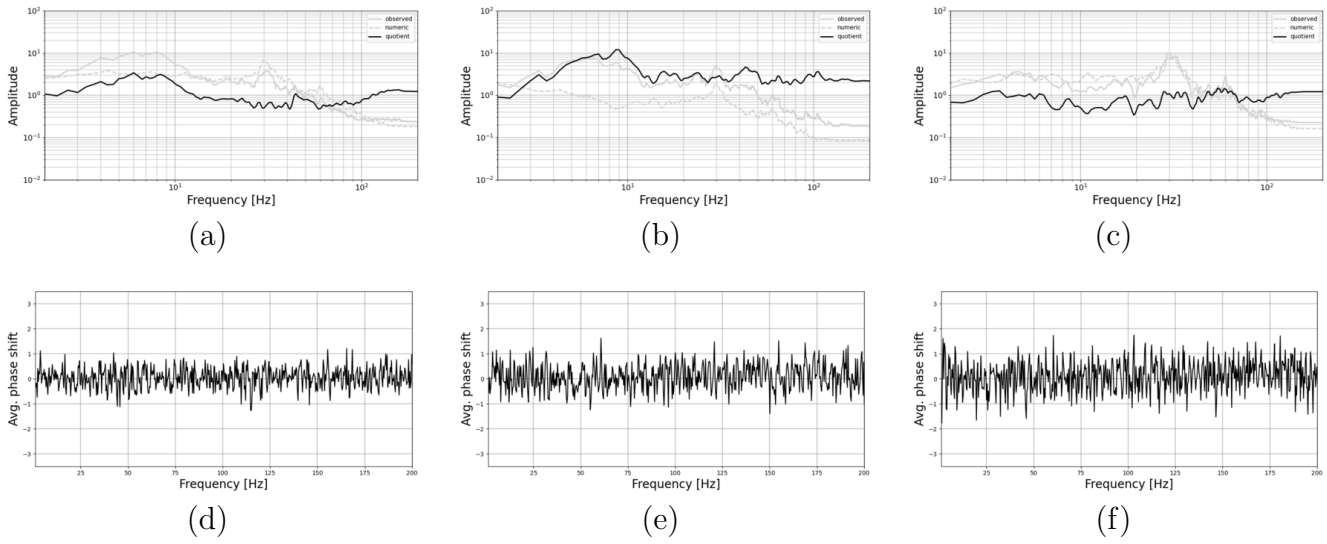

Figure 61: The frequency-dependent gain function at receiver (a) 11, (b) 24 and (c) 47 for the z-component. It shows the observed mean amplitude spectrum (grey), the numerical mean amplitude spectrum (grey dashed), and the geometric mean of the spectral ratios (black) of all blasts. The corresponding phase spectrum of receiver (d) 11, (e) 24 and (f) 47.

6.9 Recap of the Workflow to Simulate one Blast Shot

Here, the entire workflow is summarized, starting with the pre-determined 80 blast shots and ending with a more realistic production blast shot from an arbitrary position measured at a specific location. This chapter highlights the transformation from the original waveform of the numerically forward-modelled data to the final waveform used in the last superposition step.

1. **Interpolation:** For an arbitrary position is performed using inverse distance weighting from the nearest four neighbours (Fig 51 and 52) to get the interpolated seismogram (Fig. 62a) This is done for every receiver position and all three components.

2. **Restitutions filter:** The filter converts the zero-phase Ricker wavelet to a minimum-phase Kuepper wavelet or LDI-STF (Fig. 62b). In this step, the amplitude gets scaled by the amount of explosive.

3. **Late phase removal:** The late phases like the S-waves and subsequent phases get reduced (Fig. 62c). In the observed data, these late phases were by far less prominent than those of the numerical forward-modelled waveforms.

4. **Frequency-dependent gain function:** The final steps involve the frequency-dependent gain function to better mimic the observed amplitude spectrum (Fig. 62d).

6.10 Superposition of the Single Shots

The individual seismograms from the single blasts of each blasthole are superpositioned with a specified time delay. An illustrative example is presented in the seismogram (Fig. 63a), depicting the simulated

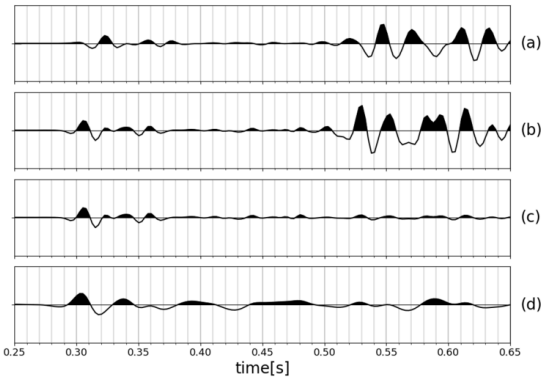

Figure 62: (a)The interpolated numerical seismogram at position 47 with a 40 Hz Ricker wavelet. (b) The same seismogram after restitution to a Kuepper wavelet. (c) The seismogram after tapering the S-wave and surface wave to 10% of their previous magnitude. (d) Final restitution with a zero phase filter to the observed amplitude spectrum.

shots from the nine blastholes of production blast 10014 at receiver position 47. All of the single shots in the simulated production blast sequence look similar, but they are not identical, with slightly different waveforms and ray paths. In Figure 63b, these individual seismograms are summed up to represent the entire blast sequence. This superposition principle allows the prediction of complete waveforms at any arbitrary position within the model. By combining the effects of individual blastholes in a sequence, a more comprehensive understanding of the ground motion at various locations should be achieved. This approach considers the spatio-temporal position of each shot at each blasthole and the travel time along the individual ray paths.

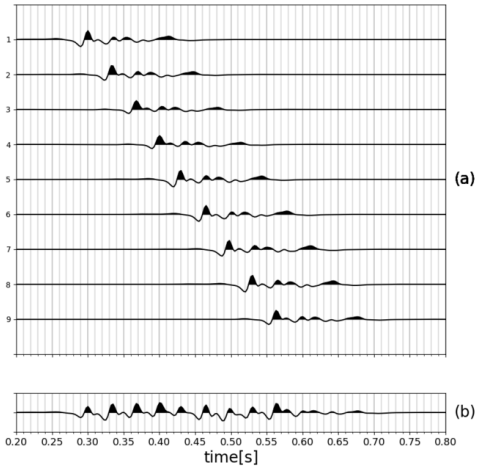

Figure 63: (a) 9 seismograms of the z-component at recording position 47 from individual blastholes were superposed to create (b) the final production blast.

6.11 Amplitude scaling for PGV Prediction

PGV represents the maximum ground speed and predicting it involves dealing with complex, non-linear aspects of ground motion. Using the numerical method for absolute peak amplitude prediction has multiple problems. One major problem is that the amplitude decay of the numerical method differs from the observed amplitude decay because the suspected divergence of the wavefront in the observed data is not fully captured by the numerical approach. In addition, the model is a pure velocity model and it neglects the Q-factor. Another difference is that the P-to-S-wave amplitude ratio in the numerical data is significantly larger than in the observed data and the taper just removes large parts of the P-to-S converted energy. This is likely to influence the PGV decay as well. Therefore, to use the numerical model for PGV prediction, the amplitude decay of the numerical approach had to be artificially altered by an additional amplitude decay modification. This modification aims to better fit the predicted PGV of the numerically modelled data to the PGV of the observed data by applying an additional adjustment to the amplitude decay exponent b_0 and gradient $\partial b/\partial r$ in the numerical data. To find the optimal amplitude decay modification, a grid search with different b_0 and $\partial b/\partial r$ values was done. For each b_0 and $\partial b/\partial r$ pair, the global site factor κ_0, and the receiver site factors ρ_j are determined and a miss fit of the numerical and observed PGVs were calculated. Figure 64 shows the result of the grid search. After identifying the minimum misfit, a second, more refined grid search was conducted around this position to obtain more accurate values.

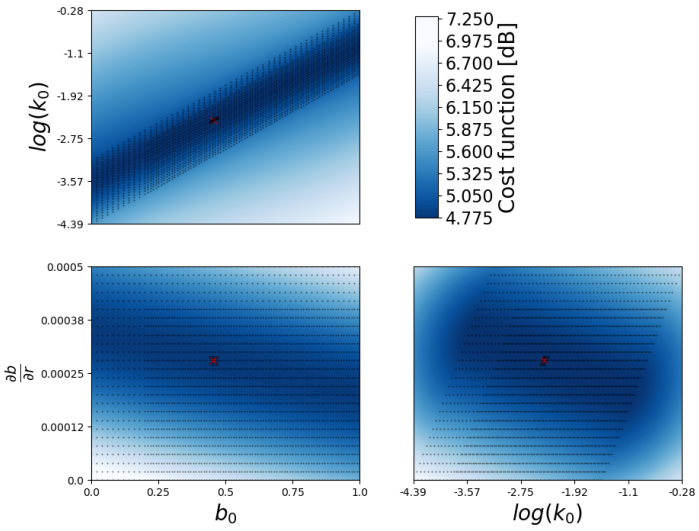

Figure 64: Results of the grid search for optimizing parameters b_0 and $\partial b/\partial r$. Each black dot on the grid represents a combination of parameters that were evaluated. The colour scale from light to dark indicates decreasing values of the cost function. The red cross indicates the position of the minimum cost function.

7 Calibration and Evaluation of the Numerical Waveform Modelling Method

Ensuring the accuracy of predicted waveforms from the numerical waveform modelling method and evaluating calibration assumptions is of paramount importance. In this chapter, the differences between the numerical method and the observed data are investigated and the numerically modelled data are calibrated to be as close as possible to the observed data. In the observed data there is no clear S-wave visible, but a strong P-wave and a later arriving phase at a velocity of 1700 m/s, which is likely to be a surface wave with a zero intercept. The surface wave is best observable up to offsets of approximately 1000 m. Unlike the observed data, the numerical waveform modelling method shows noticeable S-waves. One phase that both the numerical and observed data have in common is the strong P-wave, which is dominant in both. In the observed data, the P-wave is relatively strong, and the PGV mostly occurs within the time window of that seismic phase. Later, the waveform fit of the numerical and observed seismograms will be compared by the xcc of both seismograms. Keeping the entire wave sequence could lead to anti-correlations for the late phases due to the different velocities. The taper vs. xcc plot in Subchapter 6.7 showed that the highest xcc occurs when the late phases are completely removed. For the evaluation, only the vertical component will be considered. The P-wave is the dominant phase and is visible in the vertical component. This is simplifying the analysis of this complex environment. Larger horizontal heterogeneities are expected due to scattering at the complex topography, which is not covered by the numerical model. Differences in ray paths are also expected to be larger in the horizontal component. In the vertical direction, I can be more confident of a well-aligned comparison between the modelled and observed data.

7.1 Evaluation of the Extracted Source Time Functions

While the Kuepper wavelet was used as an auxiliary tool for the predictions, the subsequently extracted STFs were more realistic. However, the STF derived by deconvolution has the limitation that it can only be derived from existing data of production blasts shot with an electronic ignition system. Another requirement of this method is that it assumes the same STF for every blasthole, which is not feasible in real-world production blasts. In practice, only similar STFs can be expected, and having higher similarity is more likely when the same amount of explosive is used for all blastholes. In the deconvolution approach, the height of each spike in the spike sequence can be adjusted, but not the frequency response of each STF. The LDI-STF has the advantage that it was extracted from a different data set, and it accounts for different frequency responses, depending on the amount of explosive. Both methods don't represent the ground truth, but they are both extracted from the data itself. In this subchapter, both STFs will be compared and evaluated.
In Figure 65 the STFs, which are derived by deconvolution (solid line) are plotted together with the STFs derived by the LDI (dashed line), with their respective frequency responses shown in the plots below the STF. The STFs are sorted by their average charge weight per hole, ranging from 180 kg (Fig. 65a) to 455 kg (Fig. 65l). The average charge amount per hole and their standard deviation of the charge weights for each production blast are listed in Table 4. The average charge weight is rounded to the nearest whole 5 kg because the LDI-STF were also calculated in 5 kg increments and these minor differences in charge weight are negligible. The standard deviation of the charge weight illustrates the variability of the charge weight per production blast. The deconvolution of the STF

from production blasts with widely varying amounts of explosives was less effective, because different amounts of explosive lead to different STFs. This procedure works best if every hole has a similar STF, and this is more likely with a similar charge weight per hole. This is visible for blasts 30074 and 30063 (Fig. 65a and 65g). These two blasts have the highest standard deviation of the charge weight (Table 4) and the lowest xcc of 0.52 and 0.73, for blasts 30074 and 30063, respectively. The xcc of the two STFs generated by the different methods is higher when the individual explosive charges of the holes vary less. This can be seen for the production blasts, 10016, 10020, 10022 and 10036 which have all low standard deviation and high xcc of 0.95, 0.95, 0.94 and 0.95. A better way to express this variation is the relative standard deviation (σ_{rel}), which is the standard deviation of the charges of a production blast divided by the average charge weight. For a larger average charge weight, a larger variability is needed to have the same effect on the deconvolution of the STF. A clear trend of decreasing xcc with increasing relative standard deviation can be seen (Fig. 66a). The frequency spectra of each STF, as depicted in Figure 65, show an overall good fit. With an increase in charge weight, the peak frequency shifts towards lower values. Due to the noisy observed spectrum, locating the peak frequency for comparison is difficult. Consequently, the comparison was done on the average frequency of each spectrum. Figure 66b plots the mean frequency of all STFs on the x-axis against their average charge weight on the y-axis. The solid black line is the trend line from the data of the deconvolved STF, and the dashed line shows the trend of the LDI-STF. Despite the observed data being shifted towards lower frequencies, both lines show a similar trend. The deconvolution method assumes an identical STF, making a similar charge weight necessary as a precondition. If this condition is true, the STF recovery works well and confirms that the used LDI-STF is a good choice, as it behaves similarly.

no. blast	avg. charge weight [kg]	σ [kg]	xcc
30074	180	126.4	0.52
30058	195	25.6	0.74
10016	200	22.1	0.95
10036	220	14.4	0.95
10020	255	3.9	0.95
10022	260	7.9	0.94
30063	290	98.9	0.73
30061	330	26.3	0.85
30068	345	71.9	0.88
10018	375	96.2	0.92
10009	425	58.1	0.83
10014	455	39.4	0.93

Table 4: The blasts which are used for the STF deconvolution, their average charge weight per hole, the standard deviation of the charge weight and the xcc of both STFs.

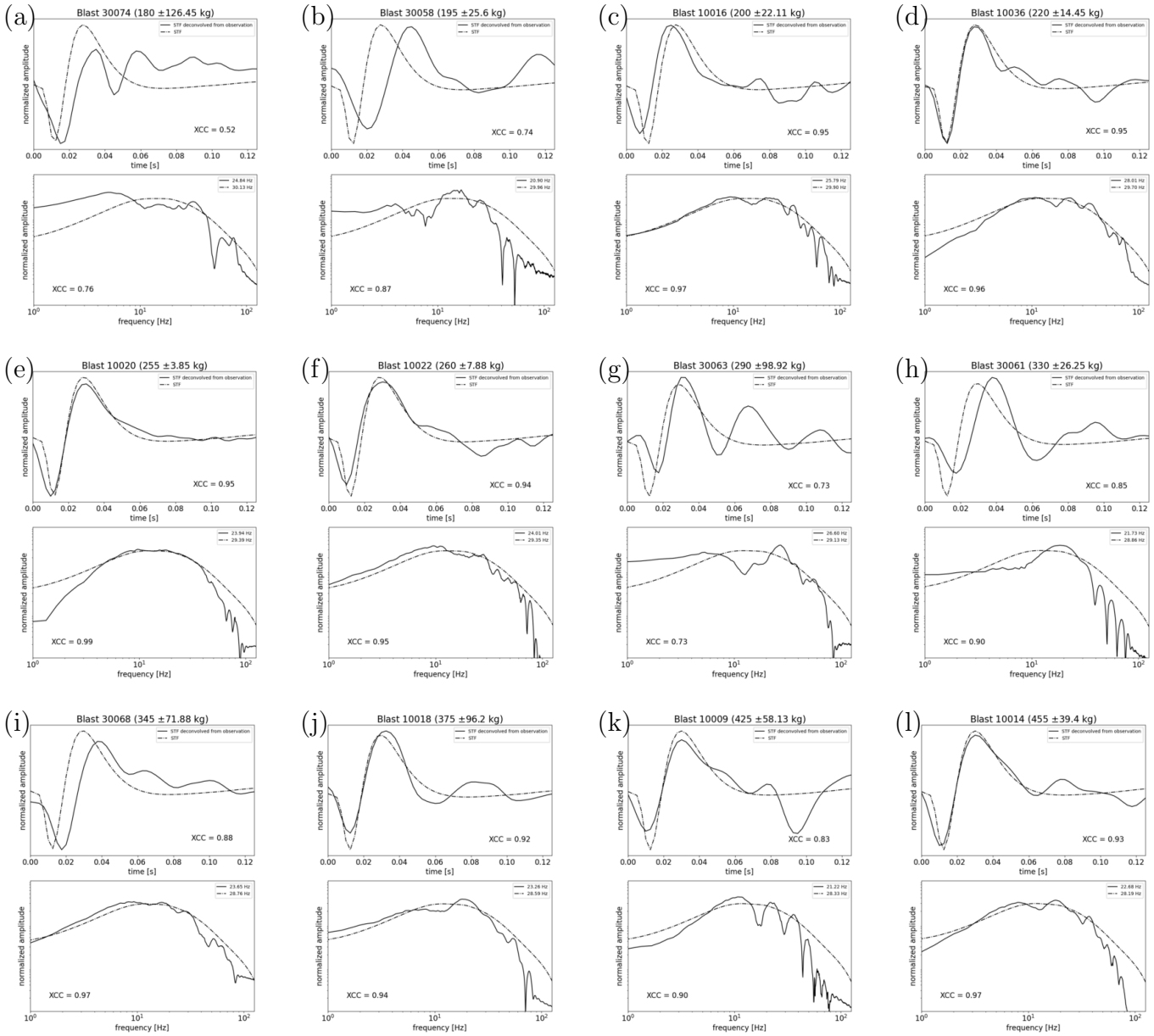

Figure 65: The deconvolved STF of several production blasts and their respective amplitude spectra are sorted by their average amount of explosive per hole, from (a) 180 kg to (l) 455 kg. The black solid line is the derived STF from the deconvolution, and the dashed-dotted line is the STF derived from the LDI.

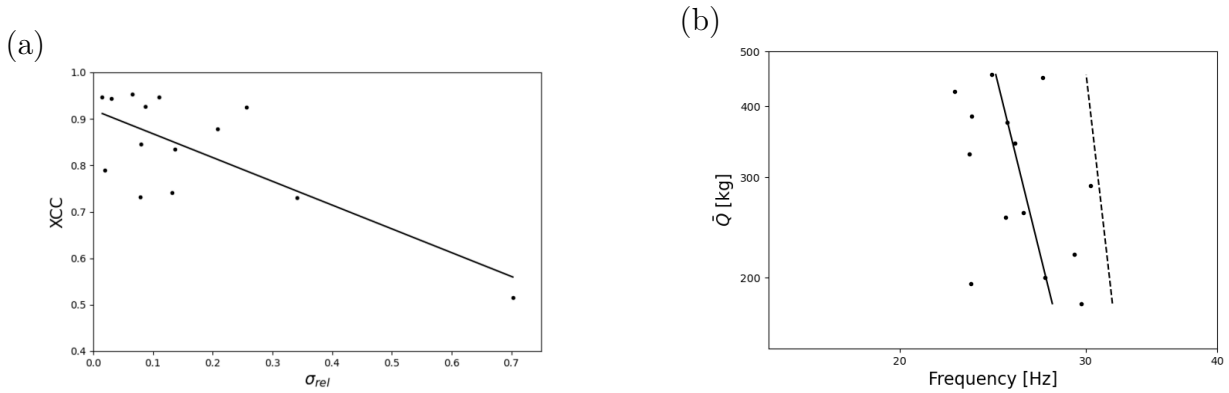

Figure 66: (a) The xcc of the STF derived by LDI with the STF derived by deconvolution plotted against the relative standard deviation of the charge weight and the corresponding trend line. (b) The average frequency is plotted versus the average charge weight. The black dots are from the STF derived by deconvolution with its solid black trend line. The dashed line is the trend of the STF derived by LDI.

7.2 Tapering S-waves and Surface Waves

For the blast vibration predictions of the second verification experiment, the taper factor was determined empirically. It was assumed that when the model contains the same amount of S-waves as the observed data, the time at which the PGV occurs in the numerically modelled waveform would correlate with the PGV time in the observed data. Forward calculations of all production blasts with a taper that retains 1%, 10%, 25%, 50%, 75% and 100% of the S-wave were made. Figure 67 shows an exemplary line fit in a PGV time versus offset plot for production blasts 10014 and 10018. All these tapers (grey dashed lines) were compared to the line fit (black line) of the observed data (black dots). The slope of the line fit with the 10%-taper qualitatively fitted the observed data best, so this percentage was chosen as the best taper. The slope instead of the absolute PGV time was taken because the intercept time for the fitted line is of less importance than the slope. With similar amounts of charge per borehole in a production blast, any borehole may be responsible for the PGV. The variation due to coupling is more substantial than that from the slightly different charge amounts. In the numerical data, the borehole with the highest charge weight is more likely responsible for the PGV, even if the difference in charge amount is negligible. The coupling of the respective borehole is more crucial than marginal differences in loading quantity, leading to potential shifts between observed and numerical data. Nonetheless, the onset of the phases causing the PGV is believed to be consistent in both the numerical and observed data. Due to the highly non-linear nature of PGV, I later switched to other metrics to assess the quality of the modelled data. Despite this transition, this method is described as it was initially used to determine the amount of S-waves for PGV prediction.

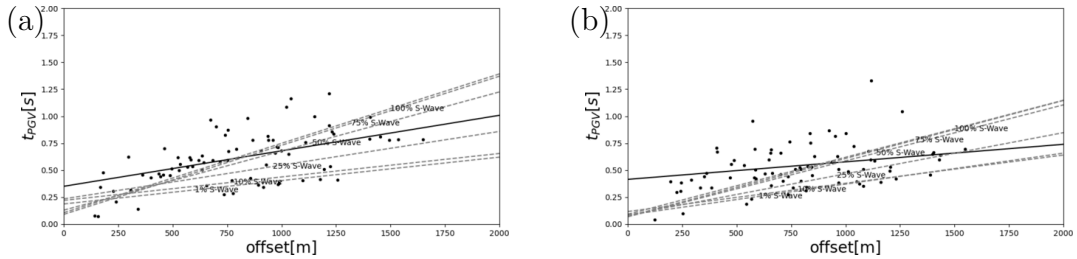

Figure 67: The observed PGV times (black dots) and their linear fits (black solid line) for production blasts (a) 10014 and (b) 10018 are compared to the linear fits of the PGV times from the numerically forward-modelled waveforms with different percentages of S-wave taper (grey dashed line).

To evaluate the quality of the forward-modelled waveforms, the xcc between observed and modelled waveforms is calculated (Fig. 68a). In this xcc, the entire waveform is considered, from the onset of the P-wave to the ending of the S-wave. Given minimal variations in arrival times between observed and numerical data, the time series were allowed to have a small shift to realign within a certain range to the maximum xcc. Figure 68b shows that the highest xcc occurred with a lag of 1 sample, corresponding to a small time shift of 2.5 ms. If the wave train arrives half a wavelength delayed, the xcc could result in an anti-correlation. This effect is shown with a shift of 8 samples or 20 ms in Figure 68b. This would result in an xcc of -0.80, indicating a strong anti-correlation in the xcc analysis, even though the waveforms are qualitatively good matching. This automatic shift was implemented to mitigate the influence of slightly different ray paths in the numerical data compared to the actual data. This is an example of receiver 47 of production blast 10014.

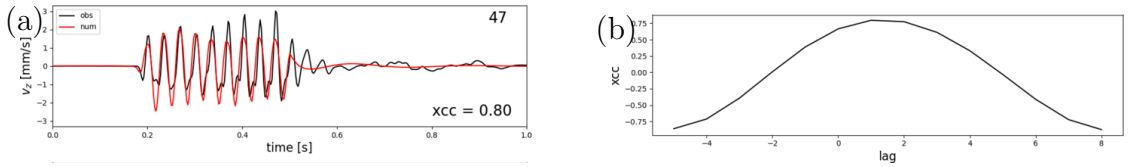

Figure 68: (a) The vertical component of seismogram from the observed (black line) and modelled data (red line) for production blast 10014 and (b) the xcc versus lag plot in samples, illustrating the degree of similarity and the time shift between the two time series.

To get a general overview of how the taper influences the overall prediction, this xcc will be calculated for the whole data set of the electronic ignited production blasts. In Figure 69, the xcc is plotted against different taper factors for production blasts 10014, 10018, 10020 and 10061. A taper factor of 0 means no taper, preserving the S-wave completely, while 1 means all S-waves and later arrivals are entirely removed. The highest xcc for the example production blasts occurs by entirely removing all late phases, which arrive after the P-wave, especially for the z-component (solid black line). For the x-component (dashed line) and y-component (dashed-dotted line), it is less evident. However, the examples in Figure 69 are for production blasts 10014, 10018, 10020 and 10061, where all but the last show the highest xcc by removing the entire late phases after the P-wave. To get an overview of how the removal of the late phases affects the data in general, the xcc is calculated for the whole dataset. The grey lines in Figure 69 represent an average xcc over all recorded production blasts, and here, the xcc is highest when the S-wave is completely removed. This is evident, especially for the vertical component. The horizontal components show an almost negligible improvement, but none of the components show a deterioration. Despite the somewhat minor improvement of the xcc for x- and y-components, for the final production blast modelling with the numerical method, the S-wave and the later phases will be completely removed from the numerical waveform modelling.

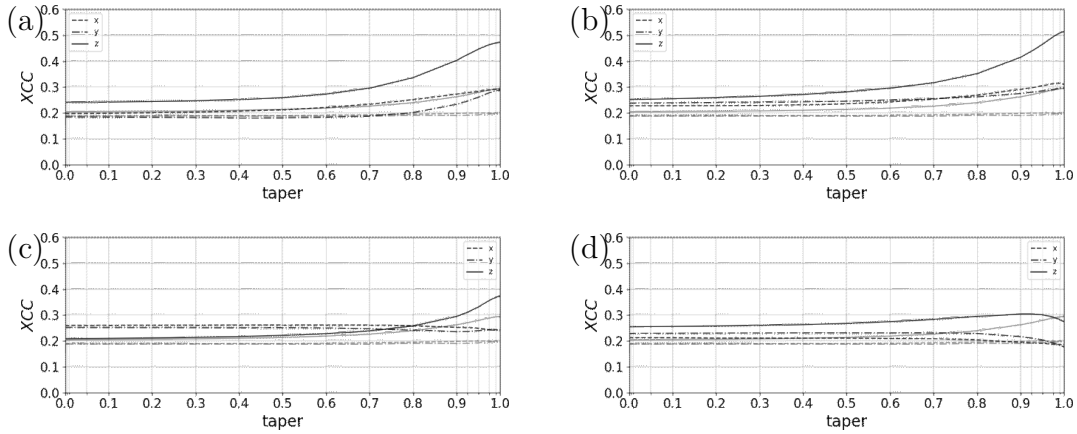

Figure 69: The black lines show the average xcc for the three components from all stations for production blast (a) 10014, (b) 10018, (c) 10020 and (d) 30061. The grey line is the average xcc of all production blasts. Dashed line for the x-component, dashed-doted line for the y-component and solid line for the z-component.

7.3 Waveform Fit of Seismogram from Blast Arrays

One approach to assess the similarity between the numerical and observed data is to calculate the xcc of the modelled and observed waveforms using electronically triggered production blasts. Only for electronically triggered blasts, with the exact delay times, it is possible to simulate waveforms. The waveforms are modelled as detailed in Chapter 6. For the xcc of two seismograms, only the segment, where strong amplitudes occur, the xcc is calculated. The window begins at the start of the P-wave and extends to the beginning of the P-wave plus the duration of the detonation sequence, along with an additional 100 ms to account for the explosive pulse duration. Using the xcc for the window of only the P-wave sequence makes sense, especially considering that only 10.3% of the observed PGVs occur after the last S-waves. Waveforms where the PGV occurs that late are likely beyond the simulation capability of the numerical method, as strong amplitudes are no longer present in this time window. Additionally, 79.3% of all observed PGVs occur within the P-wave sequence. This means that the majority of seismograms, where the PGV occurs within the P-wave window, can potentially be reproduced if the assumption based on the observation holds true. This approach is consistent with focusing on the predominant time window for the occurrence of PGVs. Containing the later phases for the xcc calculation leads to anti-correlation within that late window because the dominant late phases of the numerical and observed data have different apparent velocities of 2400 m/s and 1700 m/s, respectively.
In this subchapter, a comparative analysis of waveforms was conducted between two numerical models employing Kuepper wavelet (Fig. 72a,b) and LDI-STF (Fig. 72c,d) and a simple convolution model (Fig. 72e,f). In the convolution model, the STF, which accounts for the charge amount, is convolved over a spike sequence. This spike sequence is derived from the travel time model and blast sequence ignition times, considering spatial-time delays at each recording position. The comparison with the simple convolution model should show whether the complex numerical waveform modelling approach leads to improvements over the simple model. To provide a qualitative assessment, a closer examination of one production blast 10014 at two stations with distinct frequency-dependent gain function for the LDI-STF was conducted. These stations are station 11, situated on a site, which tends to enhance lower frequencies (Fig.70b,c) and station 47, on a site with a flat amplitude response (Fig. 70e,f). For the Kuepper wavelet, a frequency-dependent gain function for the entire site was already applied. Figure 70a and 70d show frequency-dependent gain functions that correct the receiver site response. All methods will be compared to each other with and without the frequency-dependent gain function. The frequency-dependent gain function at each station was derived from the geometric mean of the receiver site response of all production blasts recorded at that particular station. The frequency-dependent gain function was calculated separately for each method. The amplitude spectrum of the Kuepper wavelet has already been modified to fit the average site response of the entire blast site (Fig.55a), but the site response modifications per receiver (Fig.70a,d) are larger than for the LDI-STF (Fig.70b,e). This is likely due to the strong smoothing applied to the first restitution filter. The LDI-STF already seem to fit the site response quite well. For the specific depicted receivers, the Kuepper wavelet overestimates the low frequencies and they were reduced by the frequency-dependent gain function at both stations. The LDI underestimates the low frequencies for that specific site at receiver 11 and the frequency-dependent gain function therefore increases the low-frequency content. For receiver 47 the frequency-dependent gain function is quite flat (Fig.70e). The simplified convolution model with an LDI-STF convolved over the spike sequence of a production blast 70c,f) shows a similar ratio to the forward-modelled data with the LDI-STF.

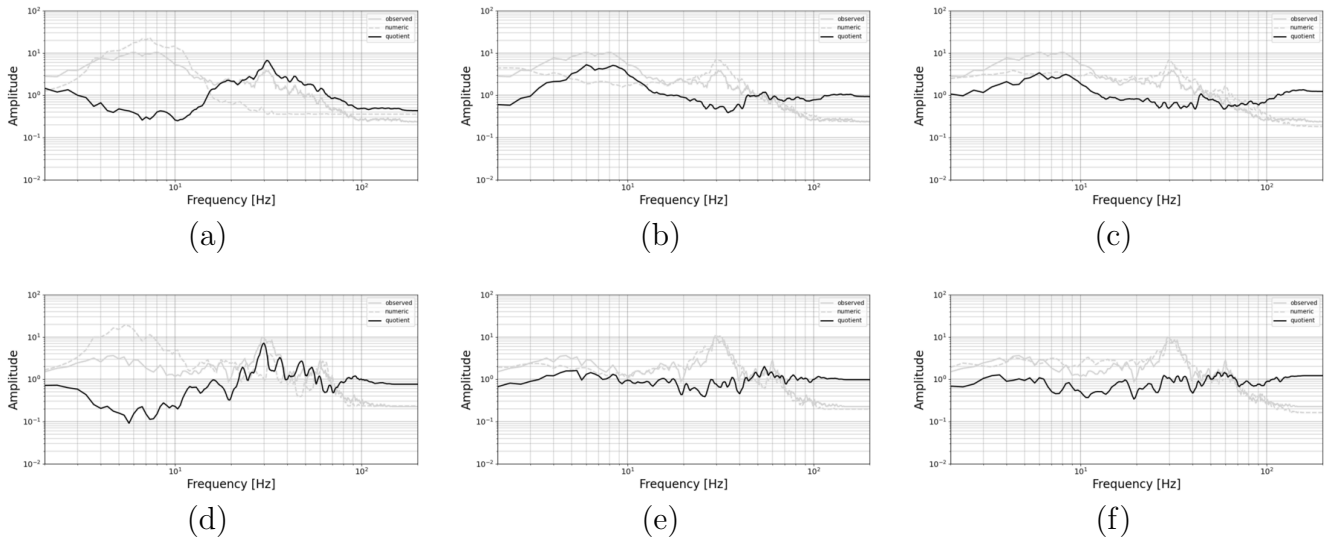

Figure 70: The frequency-dependent gain function for (a, d) the Kuepper wavelet restitution, (b, e) the LDI-STF restitution and (c, f) the LDI-STF convolved over a spike sequence for (a,b,c) station 11 and (d,e,f) station 47. The plots show the observed mean amplitude spectrum (solid grey), the average numerical amplitude spectrum (grey dashed), and the geometric mean of the spectral ratios (black) of all blasts.

Station 11 is located on top of loose sediment. The frequency content is rather low at that particular station. The xcc of blast 10014 at that particular station for the Kuepper, LDI, and convolutional models are 0.53, 0.31, and 0.31, respectively, without applying the frequency-dependent gain function (Fig. 71a,c,e). The low-frequency restitution function for the Kuepper wavelet outperforms the other two methods in that particular case. After applying the frequency-dependent gain function to the waveforms (Fig. 71b,d,f), the xcc changes to 0.21, 0.72, and 0.63, respectively.
For the numerical waveform of station 47 and blast 10014 (Fig. 72a,c,e), the xcc values for the Kuepper, LDI, and convolutional models are 0.50, 0.80, and 0.70, respectively, without applying the frequency-dependent gain function. Upon applying the frequency-dependent gain function (Fig. 72b,d,f), the xcc values for the three methods change to 0.71, 0.51, and 0.55. The xcc for the Kuepper wavelet improves, while the other methods show a decrease in xcc. For the Kuepper wavelet, an amplitude restitution is performed using the average frequency spectrum of the entire blast site, which generally has lower frequency content compared to that specific site. This explains why the frequency-dependent gain function increases the xcc for that particular site, as it adjusts the low-frequency content to match the average frequency content of the specific site. As shown in Figure 70e, the frequency-dependent gain function for the LDI-STF is relatively flat. In such cases, an improvement in xcc is not expected for the other two methods. However, a reduction in xcc was not to be expected.
A conclusion on performance based on these two stations and only one production blast 10014 is not feasible. To get a comprehensive overview, xcc is therefore calculated for all stations and all production blasts which are shot with electronic ignition.
Figure 73 shows the mean xcc across all stations and electronic ignited production blasts. For the Kuepper wavelet, LDI-STF, and convolutional models the xcc is 0.31, 0.35, and 0.38, respectively. The xcc values for all stations and production blasts follow a normal distribution. Surprisingly, the

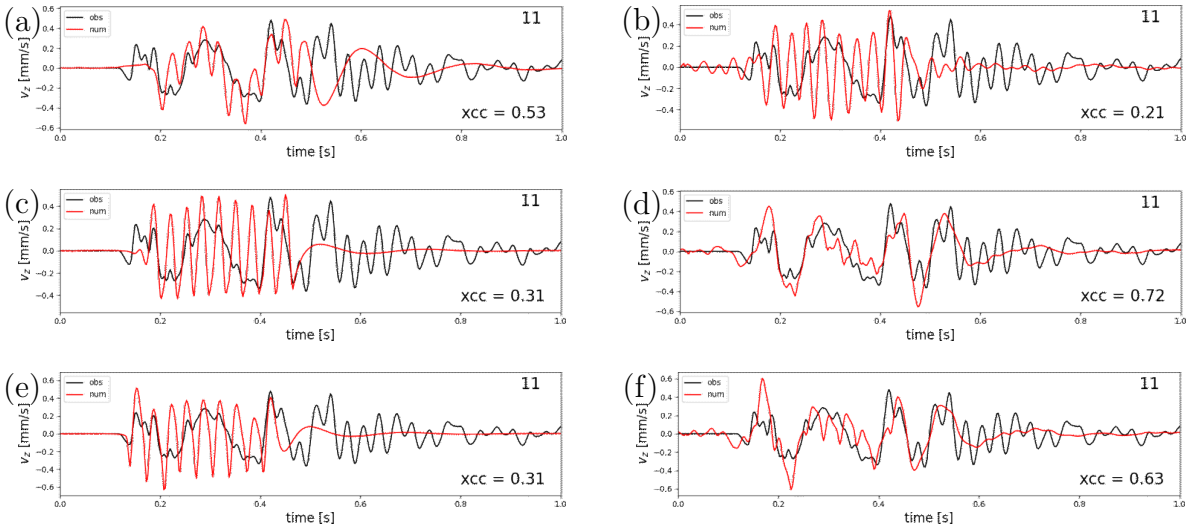

Figure 71: Exemplary observed amplitudes at station 11, calculated with the numerical method (red line) using (a,b) the Kuepper restitution, (c,d) the LDI-STF restitution and (e,f) a simple convolutional model, compared to the observed amplitudes (black line). Figures (a,c,e) are without and (b,d,f) with applying the frequency-dependent gain function.

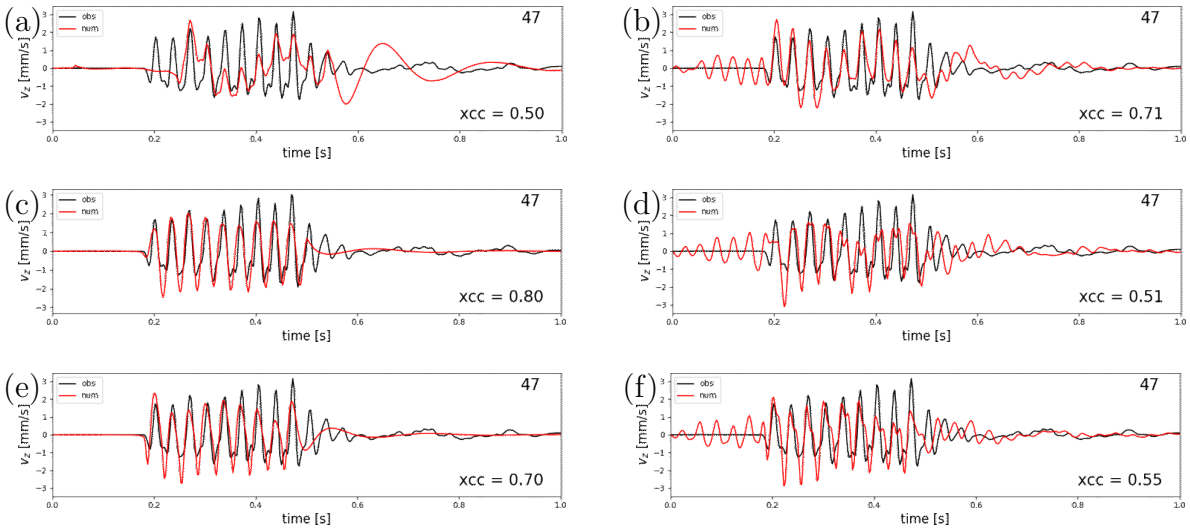

Figure 72: Exemplary observed amplitudes at station 47, calculated with the numerical method (red line) using (a,b) the Kuepper restitution, (c,d) the LDI-STF restitution and (e,f) a simple convolutional model, compared to the observed amplitudes (black line).

simple convolutional model exhibits the best performance. After applying the frequency-dependent gain function, the xcc values for all models increase to 0.34, 0.38, and 0.40, respectively.
Considering only the best-fitting station for each production blast provides insights into how well each model performs at its peak. This approach helps identify which model yields the highest xcc for each blast, providing a clearer understanding of the model's effectiveness in capturing the observed waveforms under optimal conditions (Fig. 74). For the Kuepper restitution method, 8.1% of the blasts

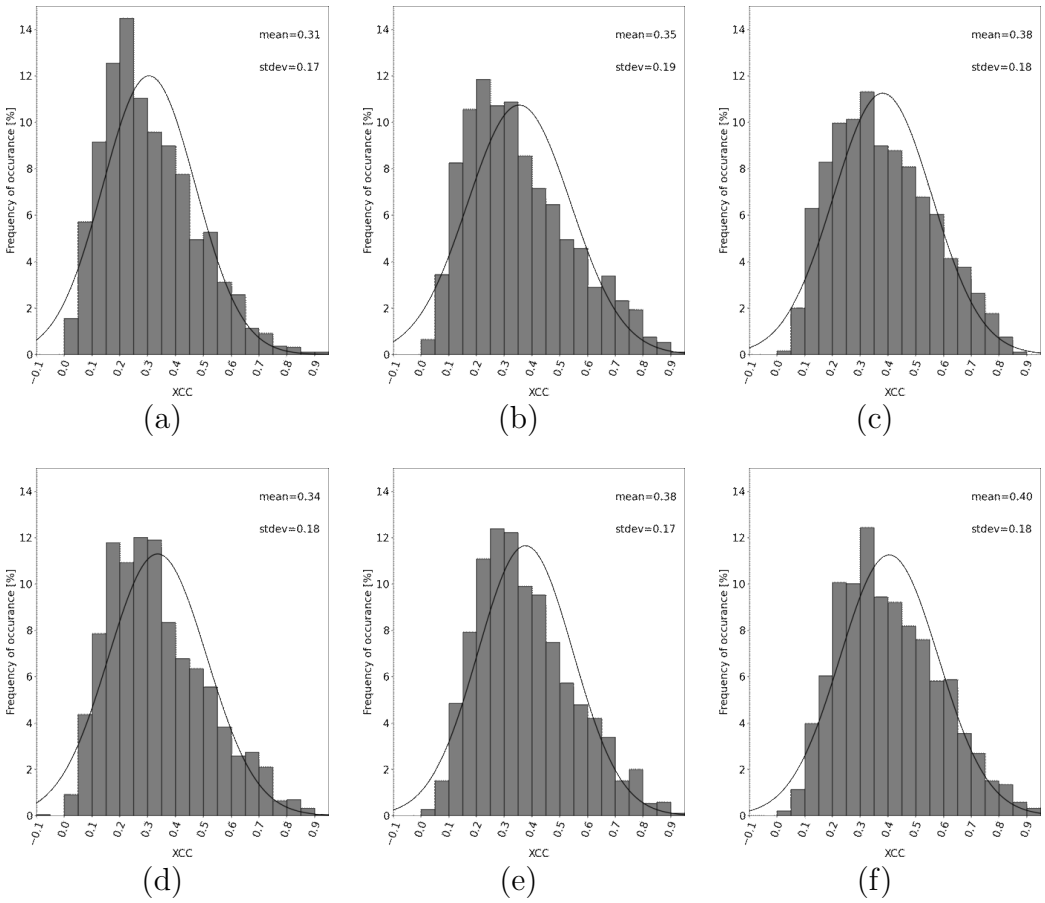

Figure 73: The histogram of all xcc between the numerical method and observed seismogram for all recorded production blasts and receivers for (a) Kuepper wavelet, (b) LDI-STF and (c) LDI-STF convolved over spike sequence, (a,b,c) without considering frequency-dependent gain function and (d,e,f) with consideration of the frequency-dependent gain function.

have at least one station with an xcc greater than 0.8 (Fig. 74a), and with the frequency-dependent gain function, this increases to 29.7% (Fig. 74d). The LDI-STF restitution method shows that 27% of the blasts have at least one station with an xcc greater than 0.8 (Fig. 74b), and this value increases to 35% after applying the frequency-dependent gain function (Fig. 74e). As for the convolutional model, 16% of the blasts have at least one station with an xcc greater than 0.8 (Fig. 74c), and this number also increases to 37% (Fig. 74f) after applying the frequency-dependent gain function. Overall, the simple convolutional method slightly outperforms the others in terms of xcc. The xcc matrix illustrates all computed xcc between observed electronic production blasts and the numerically forward-modelled data with the LDI-STF. The other methods have a similar xcc matrix. It is evident from the matrix that certain blasts exhibit a higher overall xcc between the numerical model and observations across all stations. Notably, blasts 10014, 10016, 10018, 30061, 30065, and 30068 stand out with an average xcc of 0.52, 0.49, 0.51, 0.52, 0.51, and 0.49, respectively, which is significantly above the average of 0.38. Stations 8, 13, 28, 46, 47, 56, 83, 93, 94, and 111 show significantly higher xcc values ranging between 0.45 and 0.52. Among these stations, 6 are located outside the mine, and 4 are inside the mine. There is no clear trend indicating that stations on top of hard rock perform better than those on

top of sediment, or that stations within a specific offset range perform better.

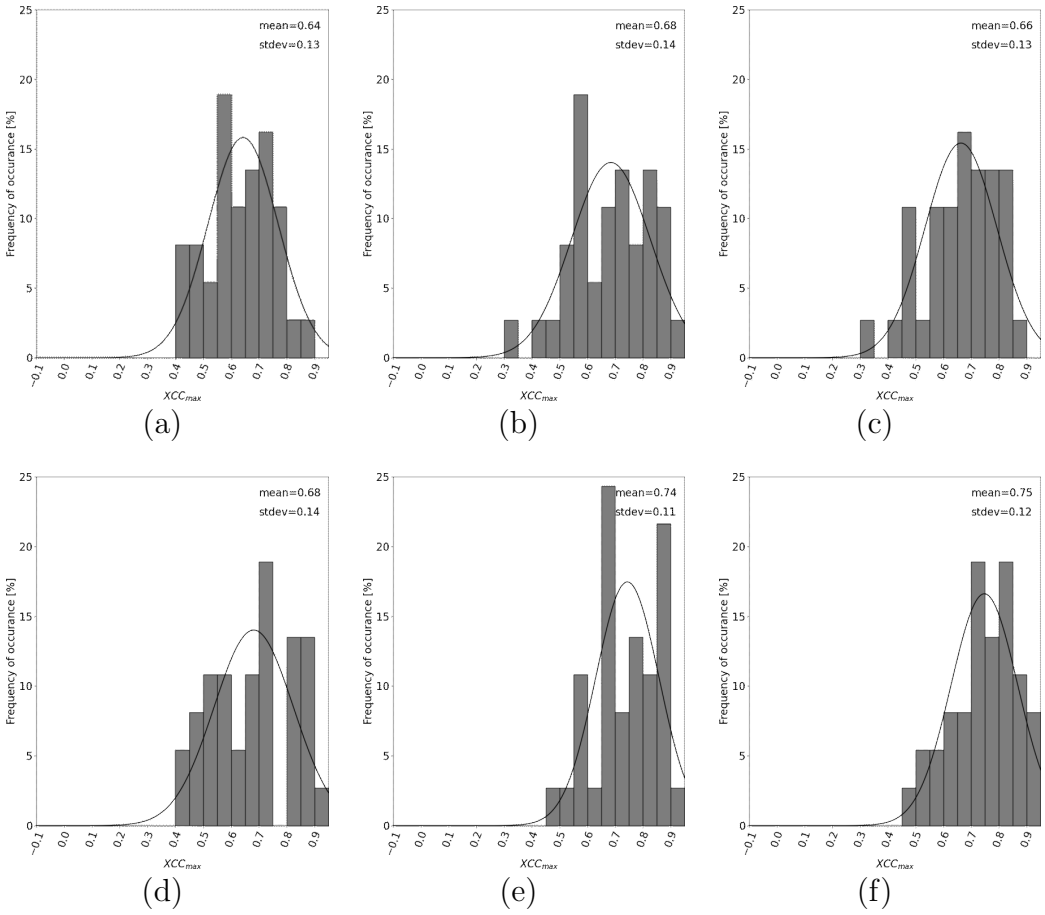

Figure 74: The histogram of the best xcc between the numerical method and observed seismogram for each recorded production blast for (a) the Kuepper wavelet, (b) the LDI-STF, (c) LDI-STF convolved over spike sequence, (a,b,c) without considering frequency-dependent gain function and (d,e,f) with consideration of the frequency-dependent gain function.

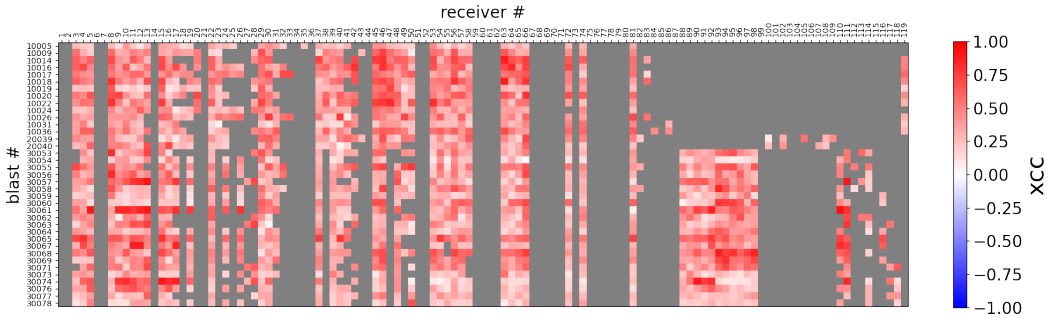

Figure 75: A matrix displaying all xcc for each blast along the y-axis and stations along the x-axis.

7.4 Spectral Fit of Blast Arrays

Another way to evaluate the numerical forward-modelled waveforms is to compare their amplitude spectra to the observed amplitude spectra. This comparison reveals how closely the frequency content of the numerical modelled waveform aligns with the observed data. A high spectral fit suggests that the two waveforms share similar frequency components. Using the metric of xcc, the waveform fit for the LDI-STF is significantly better than for the Kuepper-STF. Nevertheless, the numerical waveform modelling method with LDI-STF is slightly outperformed by a very simple convolutional model. This model cannot be used for PGV prediction as it only utilizes the vertical component, whereas all three components are needed for a PGV prediction. Given that the waveform fit is significantly better for the LDI-STF, the convolutional model is not suitable for PGV prediction. Since all methods have a very similar amplitude spectrum, only the spectrum from the numerical forward-modelling with the LDI-STF will be closely examined. Therefore the numerically modelled mean amplitude spectrum of is compared to the observed mean amplitude spectra from the production blasts. The mean spectrum is derived by stacking all amplitude spectra of the trace-normalized seismograms. A good fit of notches and peaks in these spectra suggests that the prediction method captures the frequency components present in the observed data. The high degree of alignment between the predicted and observed waveforms shows that the model can replicate the observed seismic signals. Particularly in the first verification experiment, the frequency spectra of regular production blasts with standard, evenly spaced time delays show a perfect match. With a 33 ms delay between blasts (Fig. 76a, b, c, d, e), the observed peaks in the frequency spectrum are centred around 30 Hz, corresponding to the reciprocal of the time period (1/0.033 Hz). Harmonics, which are whole number multiples of the fundamental frequency are generated and evident in both the numerical and observed datasets. The peaks for the two blasts shot with a 30 ms delay (Fig. 76f, h) align at the expected 33.3 Hz. Additionally, the four blasts with variable ignition times (Fig. 76i-l) still show a satisfactory spectral fit.
During the second verification experiment, two electronic double blasts were initiated, each with variable ignition times. Blast 20040 exhibits no distinctive peak (Fig. 77b) due to the highly variable ignition times. The spectral match is relatively low, likely due to the higher presence of surface waves in this production blast. In contrast, Blast 20039 displays a more regular spacing of ignition times, resulting in an expected peak around 33 Hz and it has a slightly better spectral fit (Fig. 77a).
In the third verification experiment, the majority of blasts were initiated electronically. Overall, there is a satisfactory spectral fit (Fig. 78). Most of the blasts shot with a standard delay time (Fig. 78b, c, f, h, n, o, p, q) show the expected peak around 33 Hz. The other blasts, which were shot with an irregular ignition time still show a satisfactory spectral fit.

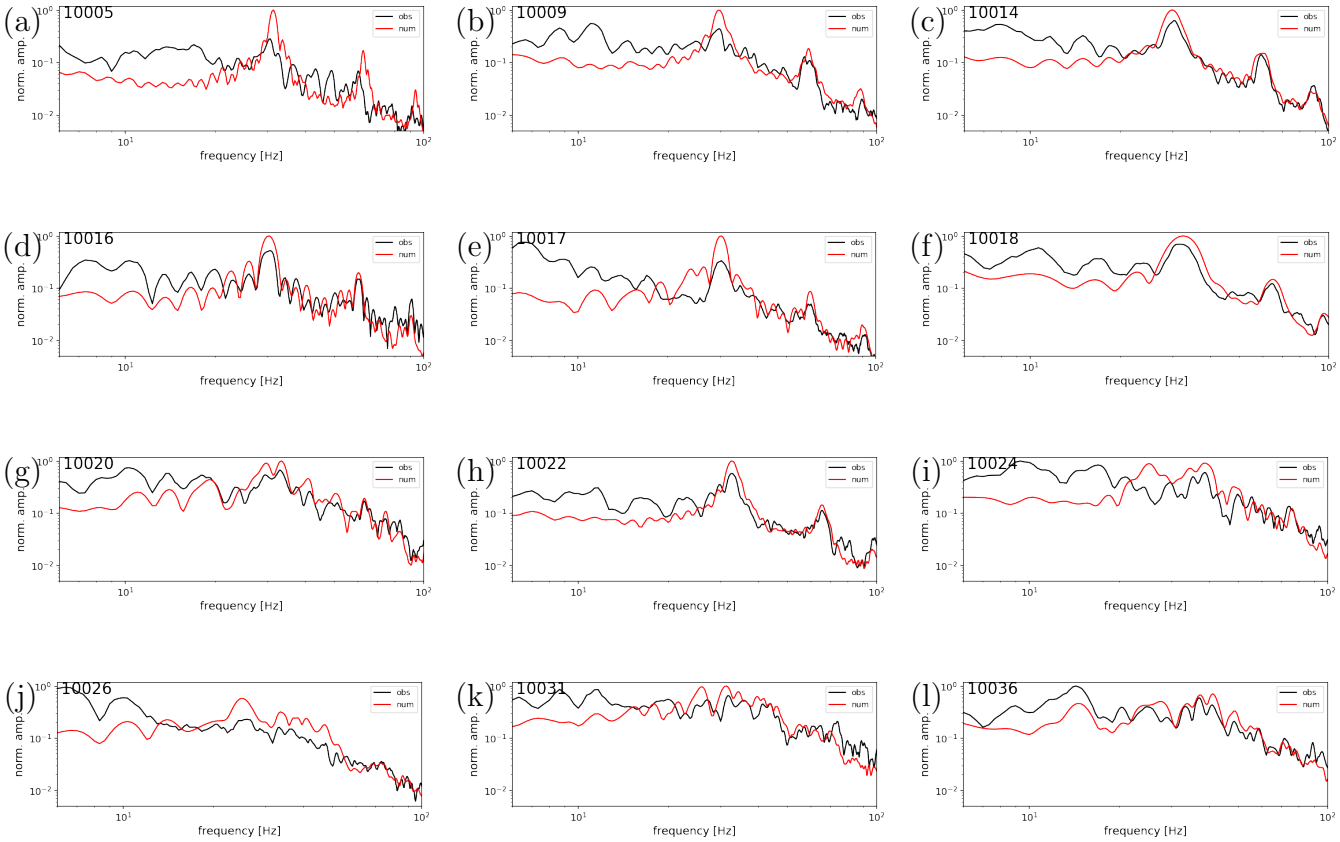

Figure 76: Comparison of mean amplitude spectra between observed (black) and numerical (red) data from the first verification experiment for production blasts (10005, 10009, 10014, 10016, 10017, 10018, 10020, 10022, 10024, 10026, 10031, and 10031), depicted from a to j.

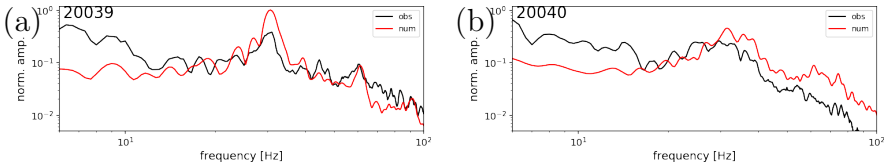

Figure 77: Comparison of mean amplitude spectra between observed (black) and numerical (red) data from the second verification experiment for production blasts (a) 20039 and (b) 20040.

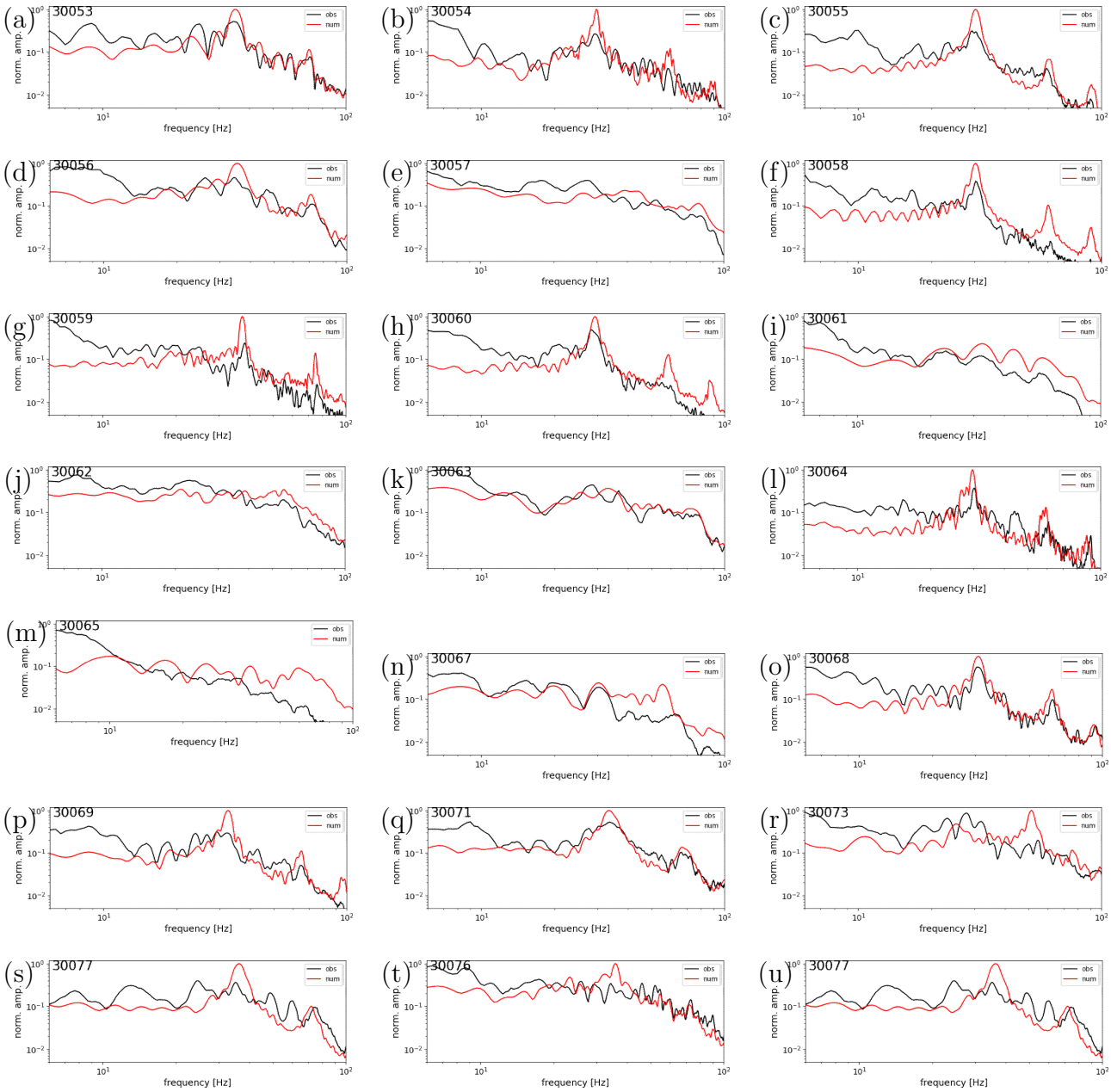

Figure 78: Comparison of mean amplitude spectra between observed (black) and numerical (red) data from the third verification experiment for production blasts (30053, 30054, 30055, 30056, 30057, 30058, 30059, 30060, 30061, 30064, 30065, 30067, 30068, 30069, 30070, 30073, 30074, 30076, 30077), depicted from a to u.

7.5 Comparison of Analytically and Numerically computed PGV

7.5.1 Settings for PGV Prediction

For the PGV prediction using the numerical forward-modelling method, the settings that achieved the best waveform fit were selected. In these settings, the LDI-STF was chosen (Chap. 6.5.2), the S-wave was completely removed (6.7 and 7.2), the frequency-dependent gain function at the receiver position was applied (Chap. 6.8), and the amplitude decay was scaled to better fit the observed data (Chap. 6.11). With these settings, the most realistic numerical seismograms can be achieved.

7.5.2 Verification of PGV Prediction

The calibrated numerical method proves effective in predicting PGV. The final PGV prediction just relies on input parameters such as the position, time delay, and charge amount for each blasthole. A qualitative assessment of PGV predictions for all production blasts shows satisfactory results. As an illustrative example, Figure 79 compares different prediction methods for an in-sample prediction of production blast 10014. Both the numerical method (Fig. 79a) and the JI method (Fig. 79b) exhibit PGV values that closely align with the observed values (Fig. 79c). It is important to note that, for this comparison, only the stations located within the model boundaries were considered for all of the methods. Outside the model boundaries, the PGV is extrapolated, and therefore not reliable.

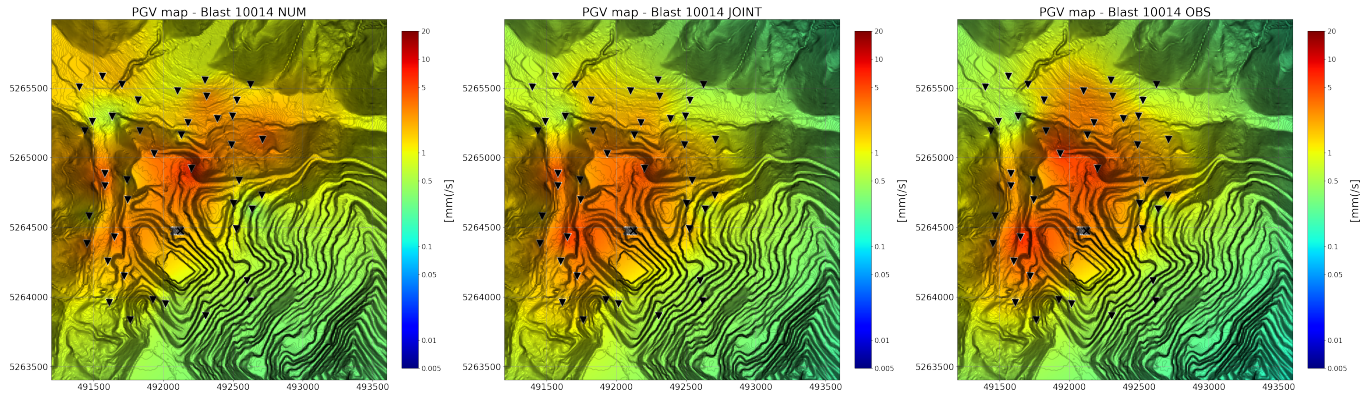

(a) (b) (c)

Figure 79: An in-sample PGV prediction for production blast 10014 with (a) the numerical waveform modelling method and (b) JI compared to (c) the measured PGV at selected receiver positions (inverted triangles).[1]

When considering all production blasts, the R^2 and RMS residuals for the JI method (Fig. 80b) surpass those of the numerical method (Fig. 80a). The numerical method displays R^2_{num}=0.50, while for the JI method R^2_J=0.60, with respective RMS residuals of RMS_{num}=4.66 dB and RMS_J=3.76 dB. For this comparison, double blasts have been excluded. The PGV time crossplot of all production blast shows that the data points are relatively wide clustered around the line of equality (Fig. 80c). The R^2 value of 0.15 is relatively low and the RMS residual of 339 ms indicates considerable scatter. The

[1]DEM data source: CC-BY-4.0: State of Styria - data.steiermark.gv.at

trend line highlights a trend of later PGV times towards the observed data. This is caused by late surface waves that are beyond the capabilities of the numerical modelling approach with the applied configuration. Decreasing the S-wave taper would shift the occurrence of the PGV in the modelled data to later times, increasing similarity in this context, but it would result in a lower xcc between the modelled and observed seismograms.

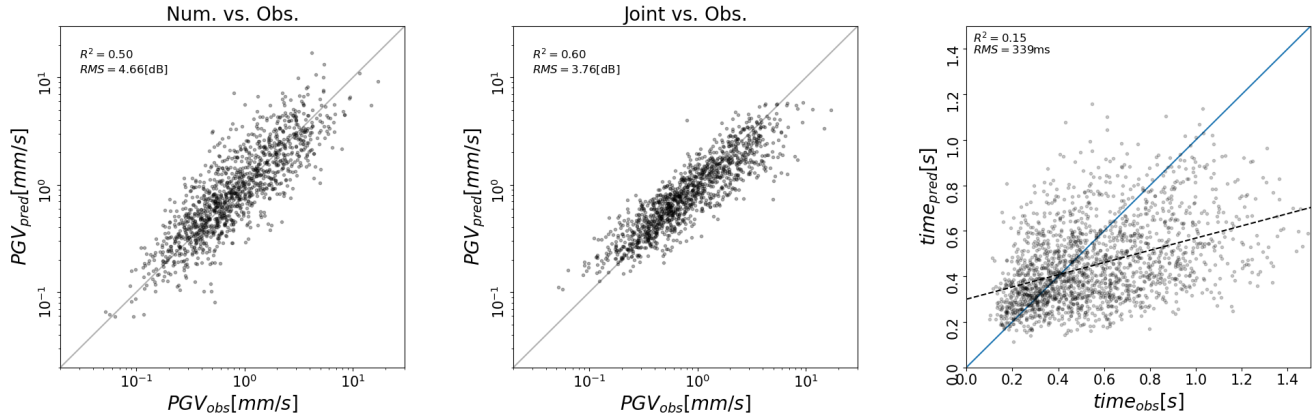

Figure 80: Crossplot of all calculated PGV values of (a) the JI, (b) the numerical versus the observed PGV values and (c) the PGV times of the numerical approach versus the observed PGV times.

7.6 Conclusion

The results of waveform similarity assessment by their xcc suggest that among the compared methods, the simple convolutional model consistently performs better in capturing observed waveforms. This conclusion applies to various conditions, including different frequency-dependent gains and blast operations. Surprisingly, the performance of the convolutional model exceeds that of the more complex numerical modelling approach. After applying the frequency-dependent gain function, which adapts to site-specific frequency content, the convolutional model continues to slightly outperform the other methods, which is reflected in higher xcc values. The detailed analysis of all stations and production blasts confirms this. An Examination of the best-fitting station for each production blast shows that the convolution model achieves high xcc values in a significant percentage of production blasts, especially after applying the frequency-dependent gain function. In summary, the results suggest that for the given scenarios and data, the simple convolution model is the most effective in predicting observed waveforms for the vertical component.
The calibrated numerical method, using, LDI-STF restitution, including the frequency-dependent gain function and a fully tapered S-wave has shown to be effective in estimating PGV for production blasts. The qualitative evaluation of PGV estimations across production blasts indicates satisfactory outcomes. However, when compared to prediction methods like the JI it appears that the JI performs better than the numerical approach in terms of R^2 and RMS residual. A detailed comparison for each production blast can be found in the Appendix in Table 12. Just for production blast 10017, the numerical

method outperformed the JI method with a higher R^2 value (0.71 compared to 0.68) and a lower RMS residual (3.25 dB compared to 5.17 dB) making it the sole instance where the numerical approach demonstrated superior performance based on the specified criteria. It is crucial to be able to predict detailed ground motion patterns or waveforms for reliable PGV estimations and a better understanding of how production blasts impact specific sites and nearby structures. The primary challenge lies in the discrepancy between numerical simulations and real data concerning the second dominant seismic phase. Including the late phase in the xcc calculation also decreased its value. In numerical simulations, this dominant phase appears to exhibit an S-wave velocity, whereas in observed data, it likely corresponds to a slower surface wave. The P-to-S conversion in the numerical data is magnitudes stronger than in the observed data. The conversion occurs at the free-surface of the model. In the observed production blast most of the energy is aimed to be used for the mining process and the fragmentation of the rock. The surface where the conversion to S-waves occurs is removed by the blasting process itself, likely with the speed of the P-wave. The fracturing itself creates a different environment which can lead to attenuation of later following phases, such as the S-wave. These effects can have an influence of the S-wave generation in the observed data. Addressing this discrepancy could potentially improve the accuracy of waveform predictions and consequently PGV predictions. Additionally, the surface waves observed may be caused by post-blast movements.

8 Markov Chain Monte Carlo for Delay Time Optimization for Double Blasts

This chapter examines whether the PGV can be reduced for specific target zones by choosing appropriate delay times. All other blasting parameters are considered strict boundary conditions determined by a framework of conditions for blasting operations.

8.1 Markov Chain Monte Carlo

A Markov chain is a stochastic process that generates a sequence of models, where each model depends only on the previous one. In other words, the future state of the chain depends solely on its current state and not on any prior states. A small random perturbation of the previous sample is made to produce a new sample in the chain. In this specific case, the aim is to perturb delay times to obtain a minimum cost function. Finding the optimal delay times can be challenging, as the space of possible delay times can be large and high-dimensional. The Markov chain was operated for an extended period to ensure thorough exploration, as determining the saturation point of the Markov Chain can be challenging. Several methods can be employed to determine whether the Markov chain has converged to its stationary distribution, like the the Gelman-Rubin convergence $\hat{R}$ discussed in Gelman & Carlin (2014). Another method is proposed by Radford Neal in Kass et al. (1998), which is a heuristic method to calculate the effective sample size with the autocorrelation function. The effective sample size measures the approximate number of independent samples. It is a standard sample quality measure based on asymptotic variance (Brooks et al., 2011). A cumulative mean plot for individual parameters is another good visual indication of the convergence of a Markov chain. For each parameter, the cumulative mean is computed as the mean of all sample values up to and including a given iteration (Smith, 2001). Visual inspection is a simple and effective method to assess whether a Markov chain has reached a stationary distribution. A trace plot shows the sampled values as a function of iteration number, in this case, the delay times (Fig. 81). The commonly used heuristic method is to observe the behaviour of the parameter trace plots to evaluate the convergence of a Markov chain to its stationary distribution. If a parameter fluctuates around its mean and the trace appears as a "fuzzy caterpillar", this visual pattern suggests that the chain has likely converged. However, the main concern is that the Markov chain has found a meaningful minimum that leads to a significant reduction in the objective function. To ensure this, the parameters of the Markov chain are visually inspected, and the distribution of the 100 best models after the burn-in phase is examined. The burn-in phase represents the initial phase of the chain run, during which the chain may not yet have reached its stationary distribution. If the best models are normally distributed throughout the chain after burn-in, this indicates that the McMC process has been well mixed and is not trapped in a local region of the parameter space. A normal distribution suggests that the burn-in period was long enough for the chain to explore the parameter space effectively. While optimizing the performance and evaluating the saturation of McMC is a significant topic on its own, the focus of this study is primarily on optimizing the numerical prediction. All applied McMC typically run as long as computational and time resources allow, often evaluating between 500,000 and 1,000,000 models per chain. However, in some cases, the McMC process may terminate earlier due to time constraints or software bugs.

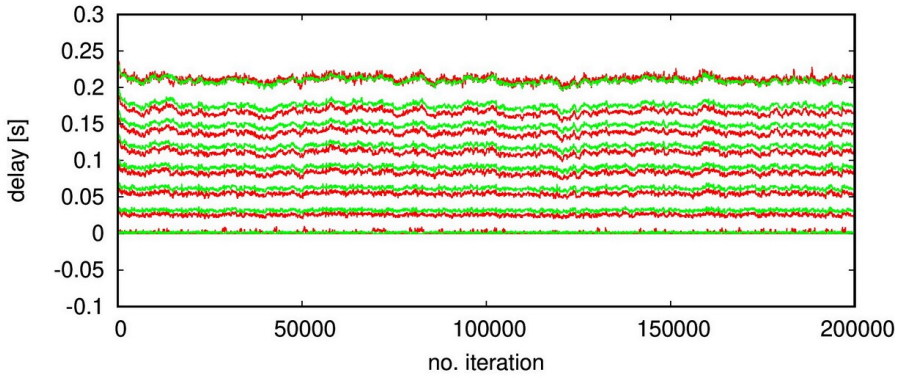

Figure 81: Delay times of the McMC plotted against the number of iterations. Blastholes from different blasts of double blast 30056 are indicated in red and green.

8.2 Likelihood Function

The likelihood function is a fundamental concept in Bayesian inference and is defined as the probability of observing the data given a certain set of model parameters (Gelman et al., 2003). In this study, the likelihood function is given as:

$$L(\mathbf{m}) = \frac{1}{\prod_{i=1}^{N}(\sigma_d\sqrt{2\pi})} \exp[-E(\mathbf{m})], \tag{21}$$

where σ_d is the data uncertainty, assumed to be constant for all measurements. The term $1/\prod_{i=1}^{N}(\sigma_d\sqrt{2\pi})$ is a normalizing factor. If $E(m)$ is quadratic, $L(m)$ represents a normalized multivariate Gaussian distribution. The exponent $E(\mathbf{m})$ in Equation 21 is the cost function, which measures the misfit between the observed data and the predicted data based on a set of model parameters. In this study, the cost function is defined as:

$$E(\mathbf{m}) = \sum_{i=1}^{N}(PGV_i w_i)^2 \tag{22}$$

where PGV_i is the predicted PGV at position i, and w_i is the weight factor for position i calculated by Equation 23. The weight factor w_i is a function of the distance r_i between the spatial position i and the midpoint of the nearest target region, with r_{max} of the target region.

$$w_i = 1 - \frac{0.75 r_i}{r_{max}} \tag{23}$$

PGV values at the centre of the target region receive a weight of 1, while values near the outer edge receive a weight of 0.25. The radius r_{max} of each target region is set to 100 m in this study. The target region is chosen so that the point of interest is weighted with the highest value. The nearby region

within the radius r_{max} still contributes to the cost function of the target region. The mining operator manages two sensitive target zones where high PGV values occasionally occur. The centre coordinates of these target zones, given in UTM Zone 33N, are E 491628.12, N 5264638.50 and E 492675.38, N 5265124.50. Both target regions are included in the final cost function. The PGV itself contributes to the cost function. Therefore, the weighting is additionally based directly on their respective PGV values, with the region with the higher PGV receiving a higher weight. This automatically favours the target region with higher PGV values for the inversion. In the first two verification experiments, two large rectangular target regions were used (Fig. 10b and c) instead of the circular target regions from the later experiments (Fig. 10d). Both rectangular target zones measure approximately 700 m in length and 300 m in width, encompassing an area of roughly 0.21 km^2. Within these target zones, PGVs were also weighted inversely proportional to the distance to the sensitive locations, ranging from 1 (near the centre) to 0.3 (for the furthest point within the zones).

8.3 Metropolis-Hastings Algorithm

The Metropolis-Hastings algorithm is the crucial component of the Markov chain, as it allows for efficient exploration of the parameter space by accepting or rejecting proposed perturbations based on their cost function (Metropolis & Ulam, 1949; Metropolis et al., 1953; Hastings, 1970). The algorithm is a widely used method for generating a sequence of random samples from a probability distribution that is difficult to sample from directly. This algorithm is particularly useful when the number of parameters and possible values is huge, and the relationship to the cost function is highly non-linear. In such cases, purely random sampling can be inefficient, and grid search methods may miss the optimal solution if it lies between the grid points. The Metropolis-Hastings algorithm compares the likelihood of a proposed trial model $\mathbf{m}_{trial}$ to the current model $\mathbf{m}_{curr}$ via their likelihood ratio, which is computed as:

$$\gamma = \frac{L_{(\mathbf{m}_{trial})}}{L_{(\mathbf{m}_{curr})}}, \tag{24}$$

where L is the likelihood function of the model. The Metropolis-Hastings algorithm compares the current and trial samples via their ratios. Therefore, the term with the normalization factor can be dropped from the likelihood function, leaving the ratio of the exponentials of the cost function:

$$\gamma = \exp\left[E(\mathbf{m}_{\text{curr}}) - E(\mathbf{m}_{\text{trial}})\right]. \tag{25}$$

The acceptance or rejection of the proposed model depends on the value of γ and a randomly generated number u from the uniform distribution $U[0,1]$. If $\gamma \geq 1$, the proposed model is always accepted; otherwise, the random number $u \in U[0,1]$ gets generated.
If $\gamma > u$, the proposed model is accepted. Otherwise, it is rejected. The algorithm's efficiency depends on the perturbation size used to generate the proposed trial models. If the perturbation is too small, the distance between consecutive samples is also small, and the acceptance rate of the proposed models is very high. However, this can lead to poor parameter space exploration, resulting in getting stuck at a local maximum instead of the global maximum of the likelihood function. On the other hand, if the perturbation is too large, the acceptance rate of the proposed models is low, and many samples get

rejected, resulting in a slow convergence. Therefore, the choice of the perturbation size is critical for the algorithm's performance. To optimize the performance of the Metropolis-Hastings algorithm, various techniques have been proposed, such as adaptive methods to automatically adjust the perturbation size during the sampling process (Haario et al., 1999) or using multiple chains with different starting points to explore the parameter space more thoroughly (Gelman & Gilks, 1996). Implementing the adjustment of perturbation size can further enhance the efficiency of the McMC algorithm. This study used the approach of starting multiple chains to improve the exploration of the parameter space. In terms of the cost function, all outcomes showed insignificant differences. However, the McMC result with the lowest cost function was selected and will be further discussed in this thesis.

8.4 Delay Time Perturbation

One delay time i between two blastholes of a blast sequence gets randomly selected for the perturbation of the delay times. A new delay time, $\Delta\tau'$, is suggested from a Gaussian density distribution, which is centred on the old value:

$$\Delta\tau_i' = \Delta\tau_i + n\sigma_t \tag{26}$$

where $\Delta\tau$ is the original delay time $n \in N(0,1)$ is a normally distributed random number and σ_t is it's standard deviation. The size of the standard deviation is set empirically to achieve an optimal acceptance rate between 20% and 30% (Gelman & Gilks, 1996). This approach leads to a minimal delay time perturbation and, therefore, a slow progression in the Markov chain. A faster progression can be achieved if $\Delta\tau_i$ is perturbed and the shift to all subsequent delay times is propagated. The formula can be written as:

$$\Delta\tau_j' = \begin{cases} \Delta\tau_j & \text{for } j < i, \\ \Delta\tau_i + n\sigma_t & \text{for } j = i, \\ \Delta\tau_j + (\Delta\tau_i' - \Delta\tau_i) & \text{for } j > i. \end{cases} \tag{27}$$

where $\Delta\tau_j$ are the original delay times, $\Delta\tau_j'$ the new perturbed delay times, $n \in N(0,1)$ is a normally distributed random number and σ_t is it's standard deviation. The value of σ_t typically ranges between 4 ms and 5 ms. With this perturbation method, the delay times for $j < i$ stay unchanged; for $j = 1$, the delay time is perturbed by adding the term $n\sigma_t$ and for $j > i$, the delay times are adjusted by the difference between the new and the old delay time at i, which is $(\Delta\tau_i' - \Delta\tau_i)$. Delay time limitations are in place, as mentioned in Chapter 3. The minimum allowed delay time between two holes in one blast row is set to 8 ms according to Duvall et al. (1962), and the maximum is set to 60 ms, dictated by the mining operator. The specified ignition sequence must also be adhered to. This limitation was ignored between holes of different blast rows. The goal of the interference approach is to control the cumulative effect of vibrations in the target zone by using both constructive and destructive interference patterns. Imposing strict delay time constraints between rows would limit the ability to fine-tune these blast delay times and reduce the effectiveness of vibration control. Since there are no restrictions between holes of different blasts, it is more likely to achieve a better delay time optimization to limit the PGV at target zones. After all, it is intended that shots from different production blasts interfere with each other.

8.5 McMC Optimization Experiments

For all three conducted verification experiments, optimized blast configurations were determined. The mining operator provided the coordinates of the blast holes and their expected charge amounts. Since shots from different blasts are expected to interfere with each other, it is preferable to have the same number of blast holes and the same charge amount for each blast of the double blast. Table 5 provides important key data of the planned production blasts. Large rectangular target regions were optimized for the first two verification experiments, while for the third verification experiment smaller circular target regions were used. The achieved reduction is given as a ratio in [dB] comparing the optimized configuration to two reference configurations. One reference configuration is the start configuration of the McMC, and the other consists of two double blasts shot sequentially with a 1 s delay in between, both with standard delay times. The comparison to the first configuration shows whether a reduction relative to the start configuration was achieved and if the Markov chain was properly functioning. The second configuration aims to assess whether a double blast, simultaneously detonated, can achieve lower PGV in specific areas compared to two single blasts shot sequentially without affecting each other. The cost function tries to minimize the overall PGV and, as a result, naturally favours the target zone that produces the higher PGV, which is likely the one closer to the double blast. Therefore, the reduction in each target zone (W and N), both target zones together, and the mean PGV of the entire area are separately examined. The global mean value is expected to be larger than in the case of a single blast because the energy is only redirected and not destroyed. The global mean serves as a base value for the strength of the double blasts.

Double blast	Blast 1		Blast 2	
	Holes per Blast	Avg. Charge Weight (kg)	Holes per Blast	Avg. Charge Weight (kg)
10026	8	458±7	11	365±15
10031	15	212±3	17	239±5
10036	11	232±6	8	206±8
20039	11	348±96	12	273±50
20040	15	424±108	14	421±13
30056	8	381±42	8	296±63
30062	11	152±18	20	202±36
30076	13	450±63	16	304±130

Table 5: Summary of key data for double blasts used in delay time optimization, including the number of holes and average charge weights with their standard deviations (kg).

8.5.1 First Verification Experiment

This subchapter examined predictions made without suppressing the S-wave in the numerical model. For the prediction, the first Kuppper wavelet was used as STF, without the amplitude response modification, as described in Subchapter 6.5.1. No other modification to the numerical data was done. The target zones were the two rectangles, and the initial grid spacing with an approximate distance of 100 m between the grid points was much higher for these predictions. Three double blasts were executed with this setting. The initial configuration for each simulated double blast is established as a standard configuration with 33 ms delay times. The simulation results for the relative reduction of the optimized configuration compared to the two reference configurations are summarized in Table 6.

Blast	optimized/start				optimized/serial			
name	Target W	Target N	2 Targets	Overall	Target W	Target N	2 Targets	Overall
10026	-0.81 dB	0.53 dB	-0.11 dB	0.19 dB	1.06 dB	1.79 dB	1.43 dB	1.86 dB
10031	-0.97 dB	-0.31 dB	-0.63 dB	-0.24 dB	1.86 dB	1.31 dB	1.59 dB	1.80 dB
10036	-0.78 dB	2.94 dB	1.27 dB	1.16 dB	2.08 dB	4.23 dB	3.22 dB	2.63 dB

Table 6: The reduction of PGV for a double blast compared to the start configuration and two standard configured production blasts, shot sequentially with a delay of 1 s between the two double blasts.

The cost function for double blast 10026 (Fig.82a), 10031 (Fig.82c) and 10036 (Fig.82e) shows a sharp decrease after the first 1,000 models. After the sharp decrease, the burn-in phase is completed. Just the cost function of double blast 10036 was followed by another slight decrease after 750,000 iterations. The red dots, representing the top 100 models, are scattered throughout the entire length of the Markov chain for double blasts 10026 and 10031, indicating saturation. Double blast 10036, with almost all of the top 100 models located towards the end of the Markov chain, suggests that the Markov chain may not be saturated. The acceptance rate of all double blasts stabilizes to 15% , 36% and 20% after around 10,000 iterations for double blasts 10026 (Fig.82b), 10031 (Fig.82d) and 10036 (Fig.82f), respectively. The acceptance rates of the first two chains are slightly outside the optimal range, which suggests an inefficient sampling process, possibly due to a step size that is too small or too large. A too-large step size leads to the rejection of numerous configurations, while a too-small step size also leads to slow progress by accepting too many models. At this point in the project, the issue of inefficient exploration was ignored because there were still other major problems to be solved. Due to time constraints, the Markov chain for double blast 10026 was terminated after 580,000 iterations. Nevertheless, the first among the 100 minimum models was attained before reaching 50,000 iterations. The other two were terminated after 1,000,000 iterations.

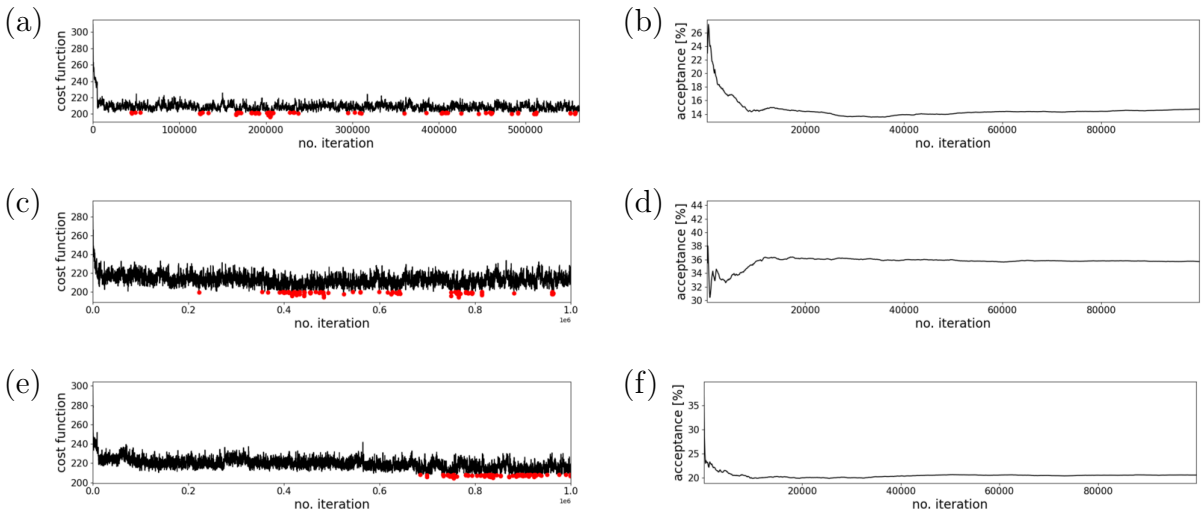

Figure 82: (a), (c) and (e) The cost function for the whole McMC and (b), (d) and (f) the acceptance rate for the first 100,000 iterations of double blast 10026, 10031 and 10036, respectively. The red dots represent the top 100 models.

The final models were chosen based on the minimum cost function for all double blasts. The optimized

delay times are depicted in Figure 83a, 83b and 83c. For double blast 10031, a delay of 83 ms exists between the first holes of the two blast arrays, accompanied by a corresponding difference in the travel path of 204 m between these specific holes relative to the Western Target zone. Notably, this spatio-temporal arrangement aligns precisely with the conditions required for S-wave interference in the numerical model. In the final configuration for double blast 10036 (Fig. 83c), the shorter blast is shifted to the centre of the longer blast. The first and last ignition of the longer blast may not interfere with the other blast array.

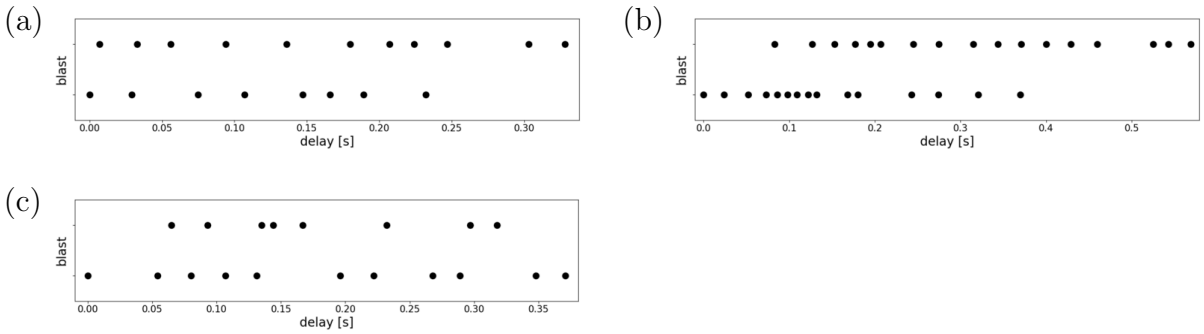

Figure 83: The final optimized time delay configuration for double blast (a) 10026, (b) 10031 and (c) 10036, respectively.

The final model for double blast 10026 reveals a decrease in the western target zone compared to the initial model (Fig. 84a). Despite both target zones being roughly equidistant from the double blast, the cost function slightly favours the western area. This results in a relative reduction of -0.81 dB for the western target zone and an increase of 0.53 dB for the northern target zone. Although the PGV outside the target zone remains consistent, within the target zone, it is minimized. In the serial configuration, no reduction is observed within the target zones (Fig. 84d). Despite producing an overall PGV, which is almost a factor of 1.86 dB higher, the PGV within the target zone is less significantly increased. The final model for double blast 10031 achieved a reduction of -0.63 dB in both target zones compared to the initial model (Fig. 84b), with a slight preference for the closer Western target zone (-0.91 dB). Overall, the PGV of the entire area did not significantly change compared to the initial model. When comparing the optimized model to both blasts shot sequentially with a 1 s delay (Fig. 84e), a higher PGV ratio is observed in every target zone, as well as across the entire area (Tab. 6). For double blast 10036, a slight reduction in the slightly closer target zone W was achieved compared to the initial configuration (Fig. 84b). While there is a decrease of -0.78 dB in target W, the target N increases PGV by 2.94 dB. Compared to the serial configuration, the double blast, in that case, resulted in a higher PGV in all target zones (3.22 dB) and across the entire area (2.63 dB).
Overall, in all Markov chains, a reduction in PGV, at least for the nearest target zone, was achieved compared to the start configuration. The calculation was performed on a coarse grid within the target zone of relatively large rectangles. This prediction has two issues. The first issue is that it is likely to be more challenging to achieve a reduction in a large area. This is evident in the ratio maps (Fig. 84), where relatively small areas exhibit favourable PGV ratios. The second issue is the coarse grid, where spatial details are lost, and variations in PGV can be overlooked. It also smooths the results, leading to potential overestimation or underestimation of the resulting PGV. However, it offers the advantage of lower computational costs. The resulting ratio maps were recalculated using the finer grid for better

visualisation and comparison with later results.

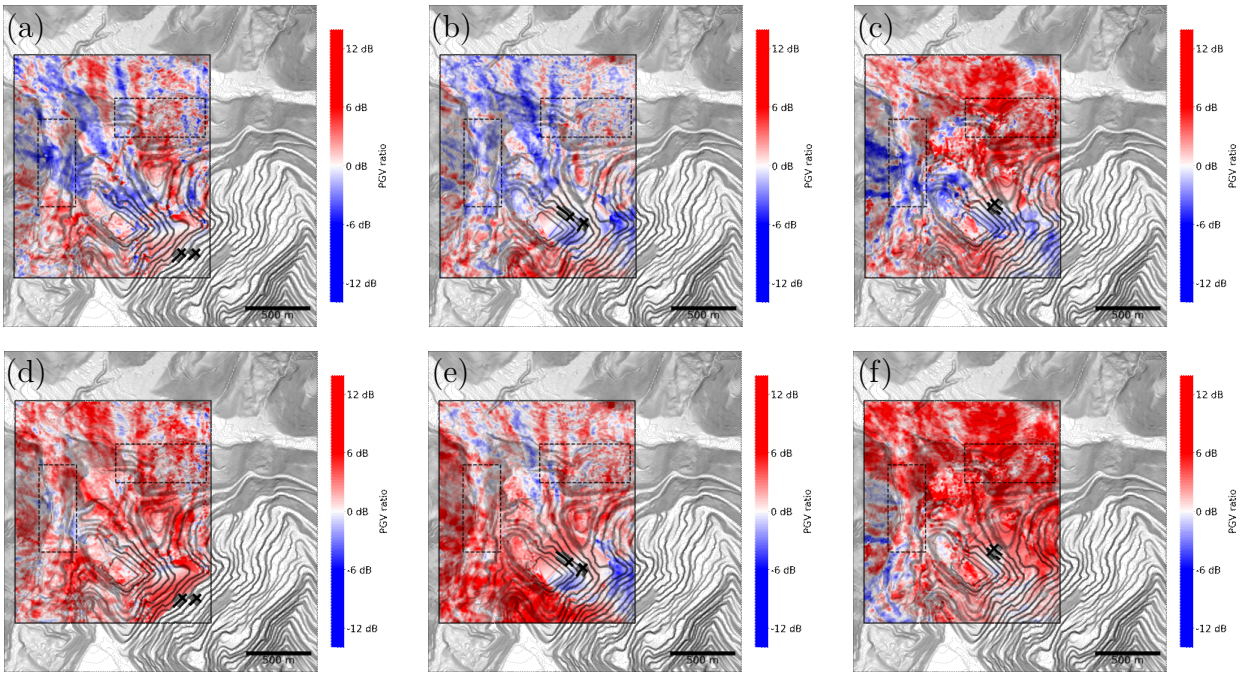

Figure 84: The ratio of the PGV computed for the optimized double blast to the computed PGV of the McMC start configuration for blasts (a) 10026, (b) 10031 and (c) 10036 and to the PGV computed for the sequential shooting with a 1 s delay and a constant 33 ms delay time interval for a blasts (d) 10026, (e) 10031 and (f) 10036.[1]

8.5.2 Second Verification Experiment

This subchapter examines predictions made by suppressing the S-wave in the numerical model to 10% of their initial amplitude. The taper is applied as described in Chapter 6.7. The taper factor of 10% was empirically determined with the first approach described in Chapter 7.2. As STF, the Kuepper wavelet with the amplitude response modification was used (Chap. 6.5.1). The target zones remained the two rectangles, and the initial grid spacing for the prediction was still approximately 100 m. Two double blasts were simulated with this setting. The initial configuration for each simulated double blast is established as a standard configuration with 33 milliseconds delay times. The simulation results for the relative reduction of the optimized configuration compared to the two reference configurations are summarized in Table 7.

[1]DEM data source: CC-BY-4.0: State of Styria - data.steiermark.gv.at

Blast	optimized/start				optimized/serial			
name	Target W	Target N	2 Targets	Overall	Target W	Target N	2 Targets	Overall
20039	-0.95 dB	0.54 dB	-0.17 dB	-0.16 dB	-0.79 dB	3.74 dB	0.65 dB	1.76 dB
20040	-1.29 dB	-2.66 dB	-1.95 dB	-1.28 dB	-1.75 dB	0.55 dB	-0.52 dB	-0.50 dB

Table 7: The reduction of PGV for a double blast compared to the start configuration and two standard configured production blasts, shot sequentially with a delay of 1 s between the two double blasts.

The cost function for double blasts 20039 (Fig. 85a) and 20040 (Fig. 85c) experience a sharp decrease after the first 1,000 models, which indicates the end of the burn-in phase. The Markov chain for double blast 20039 was interrupted due to a bug in the code after 85,540 iterations. Nevertheless, previous Markov chains show no more significant reduction after the first few thousand iterations. The acceptance rate of this blast (Fig. 85b) starts at approximately 18%, progressively dropping to 14% at approximately 10,000 iterations. The best 100 models are clustered along the entire cost function at local minima. The acceptance rate for double blast 20040 started at 20% and rapidly decreased to less than 8%, well below the optimal acceptance rate for a Markov chain (Fig. 85d).

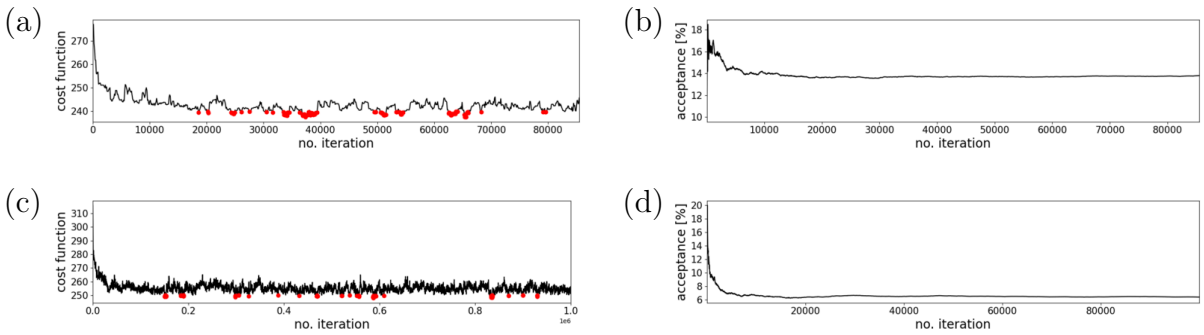

Figure 85: (a) and (c) The cost function and (b) and (d) the acceptance rate for the first 100.000 iterations double blast 20039 and 20040, respectively. The red dots represent the top 100 models.

Based on the minimum cost functions, the final models for double blasts 20039 (Fig. 86a) and 20040 (Fig. 86b) were chosen. The final delay times are distributed with relatively even delays.

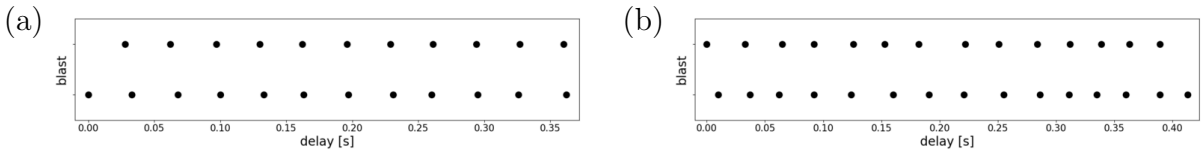

Figure 86: The final optimized time delay configuration for double blast (a) 20039 and (b) 20040.

The final model for double blast 20039 demonstrates a decrease in the western target zone of -0.95 dB, in contrast with no reduction in the northern target zone compared to the initial model (Fig. 87a). Despite both target zones being approximately equidistant from the double blast, the cost function slightly favours the western area. The average PGV for the entire area remains constant compared to the start configuration, with neither a reduction nor an increase. Compared to the second scenario, an

overall increase in PGV is observed for the entire area. However, a slight reduction of -0.79 dB within the western target zone can still be observed.
The final model for double blast 20040 shows that the double blasts are situated in closer proximity to the northern target, resulting in a significant decrease in PGV of -2.66 dB within that zone and a smaller but still significant decrease of -1.29 dB in the western target (Fig. 87b). Overall, the PGV of the entire area decreased by -1.28 dB compared to the starting configuration. The ratio to the sequential configuration shows that the average PGV over the entire area still experiences a slight decrease (Fig. 87d). In contrast to first scenario, in the second scenario the ratio of PGV shows a larger decreases towards the city area. Surprisingly, the PGV decrease in the western target zone by -1.75 dB is even more pronounced than in comparison to the start configuration. In the northern target zone, however, the decrease has turned into an increase of 0.55 dB.
Overall, all blast delay time optimizations led to a theoretical decrease of PGV in at least one target zone compared to the start configuration and the sequential configuration. Blast 20040 experienced a significant reduction in the northern target zone compared to the start configuration and a still significant reduction in the western target zone compared to the sequential blast configuration. This time, the amplitude of the S-wave was reduced, which resulted in an interference based on P-waves. The reduction of PGV appeared more significant in this case.

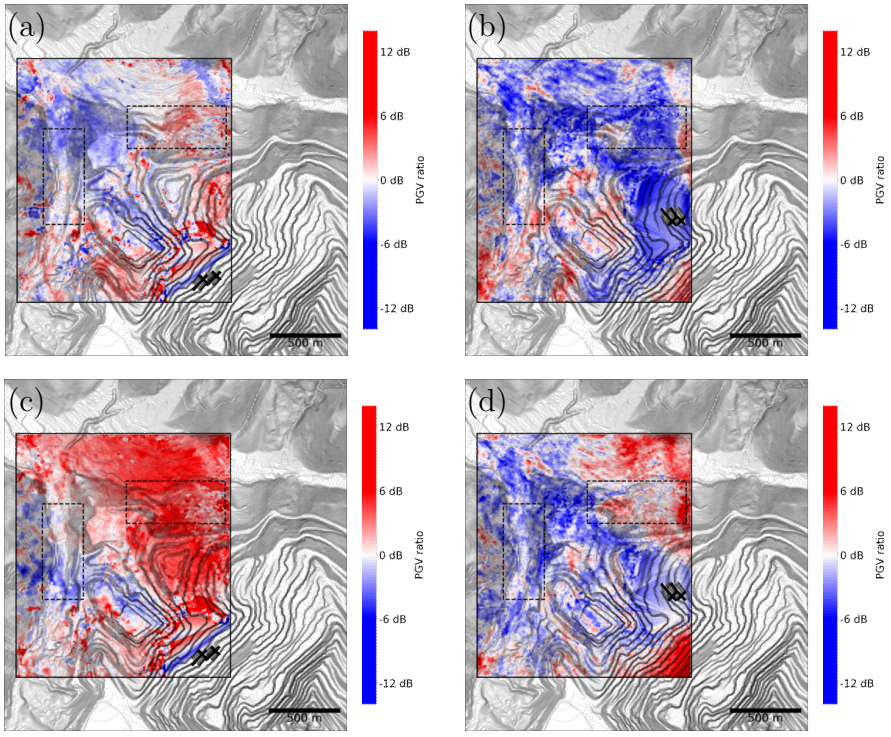

Figure 87: The ratio of the PGV computed for the optimized double blast to the computed PGV of the McMC start configuration for blasts (a) 20039 and (b) 20040 and to the PGV computed for the sequential shooting with a 1 s delay and a constant 33 ms delay time interval for a blasts (c) 20039 and (d) 20040.[1]

[1]DEM data source: CC-BY-4.0: State of Styria - data.steiermark.gv.at

8.5.3 Third Verification Experiment

This subchapter examines predictions made by suppressing the S-wave in the numerical model to 10% of their initial amplitude. A finer grid for numerical modelling was also used. The taper is applied as described in Chapter 6.7. The taper factor of 10% was empirically determined with the first approach described in Chapter 7.2. As STF, the Kuepper wavelet with the amplitude response modification was used (Chap. 6.5.1). The target zones were the two small circles, and a grid spacing with a distance of 12 m was used for that prediction. Three double blasts were executed with this setting. The initial configuration for each simulated double blast is done with a standard configuration with 33 milliseconds delay times. The simulation results for the relative reduction of the optimized configuration compared to the two reference configurations are summarized in Table 8.

Blast	optimized/start				optimized/serial			
name	Target W	Target N	2 Targets	Overall	Target W	Target N	2 Targets	Overall
30056	-2.16 dB	-3.22 dB	-2.73 dB	-0.92 dB	-1.31 dB	0.17 dB	-0.55 dB	1.28 dB
30062	-3.74 dB	-0.45 dB	-2.16 dB	-0.55 dB	-0.26 dB	0.83 dB	0.26 dB	1.28 dB
30076	-5.51 dB	0.09 dB	-2.73 dB	-0.92 dB	-3.22 dB	2.47 dB	-0.35 dB	1.28 dB

Table 8: The reduction of PGV for a double blast compared to the start configuration and two standard configured production blasts, shot sequentially with a delay of 1 s between the two double blasts.

The cost function for double blast 30056 (Fig. 88a), 30062 (Fig. 88c) and 30076 (Fig. 88e) show a sharp decline within the initial 1,000 iterations. The top 100 models of double blast 30056 and 30076 are distributed across the entire length of the Markov chain, which is a sign that the Markov chain is saturated. The cost function of the Markov chain for double blast 30062 experienced another slight drop around iteration 250,000, and following this drop, all top 100 models were distributed throughout the rest of the Markov chain. The acceptance rate of the Markov chains stabilised at 25% and just below 20% for double blast 30056 (Fig. 88b) and 30062 (Fig. 88d), respectively and is therefore in an optimal range. The acceptance rate for the Markov chain of double blast 30076 stabilised at around 15% (Fig. 88f), which is just below the optimal range.
The blast configurations with the minimum cost function were chosen for all production blasts. Both blast arrays of the double blast 30056 have an equal number of shot holes with similar charges, providing favourable conditions for interference to decrease the PGV in the target zones. Delay times of both blasts from the final optimized delay time configuration (Fig. 89a) are likely aligned in a spatio-temporally favourable arrangement. For the final delay time configuration of double blast 30062 (Fig. 89b), the last blastholes of the second blast array can not interfere with the first blast array. Nevertheless, the four blastholes with the largest charge amount are the first four of the second row, and a reduction can still be expected. The final model of double blast 30076 is depicted in Figure 89c).
The optimized configuration for double blast 30056 shows a reduction in both equidistant target zones (Fig. 90a), with PGV ratios of -2.16 dB and -3.22 dB at targets W and N, respectively. Overall, PGV has decreased by -0.92 dB compared to the starting configuration. With the serial blast configuration, only the western target shows a reduced PGV (Fig. 90d) with a ratio of -1.31 dB, while the northern target remains with an insignificant change. The PGV for the whole area increases by 1.28 dB. For double blast 30062 both target zones experience a significant reduction of -2.16 dB, particularly in the western target zone (-3.74 dB), and a slight reduction of -0.55 dB across the entire area, compared to

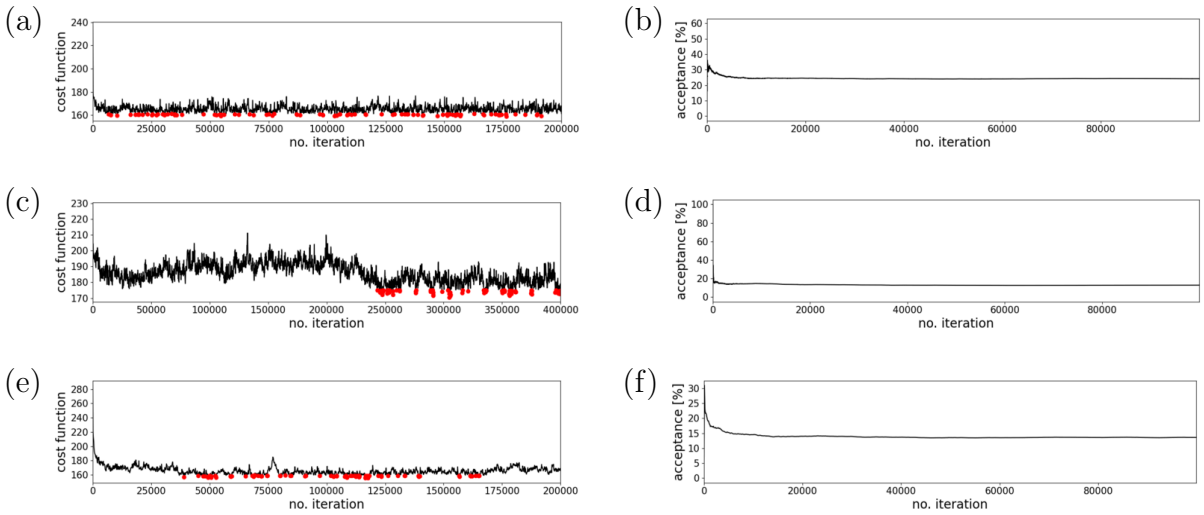

Figure 88: (a), (c) and (e) The cost function for the whole McMC and (b), (d) and (f) the acceptance rate for the first 100,000 iterations of double blast 30056, 30062 and 10036, respectively. The red dots represent the top 100 models.

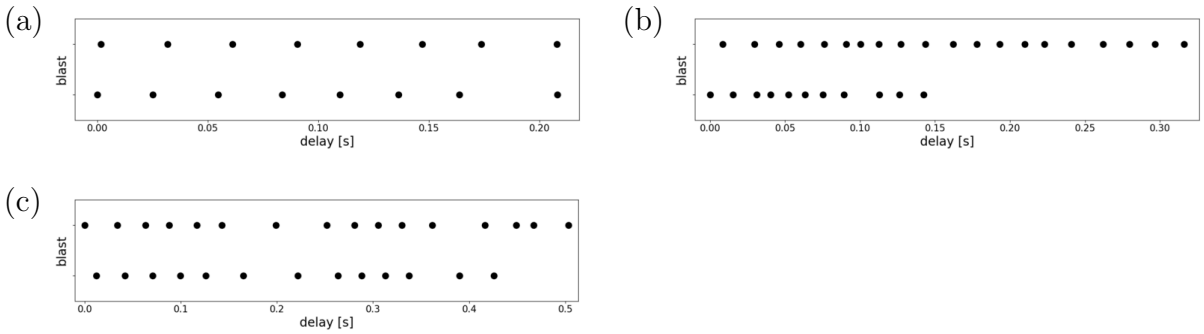

Figure 89: The final optimized time delay configuration for double blast (a) 30056, (b) 30062 and (c) 30076, respectively.

the starting configuration (Fig. 90b). The significant reduction in the western zone is astounding, given that one blast array has far fewer blastholes than the other. The time delays between the blastholes appear to decrease within the same row (Fig. 89b). While the PGV ratio for the entire area is 1.28 dB higher than the serial configuration, the western target zone still achieves a minor reduction in PGV of -0.26 dB (Fig. 90e). Double blast 30076 demonstrates the most significant reduction among all simulations. The overall PGV decreases by -0.92 dB, with the most substantial reduction by almost a factor of -5.51 dB occurring in the western target zone, while the PGV in the northern target remains at the same level (Fig. 90c). Even compared to the serial configuration, the optimized configuration achieves a reduction with a factor of -3.22 dB to the PGV of the serial configuration in the western target zone (Fig. 90f). The theoretical reduction potential was explored that could be achieved by suppressing S-waves in the numerical model and using a fine grid. Three double blasts (30056, 30062, and 30076) were simulated under these conditions. Despite an overall increase in PGV for the entire area compared to the serial configuration, the western target zone still achieved a reduction in PGV in all predicted double blasts. A smaller target zone is likely better suited to achieve minimization.

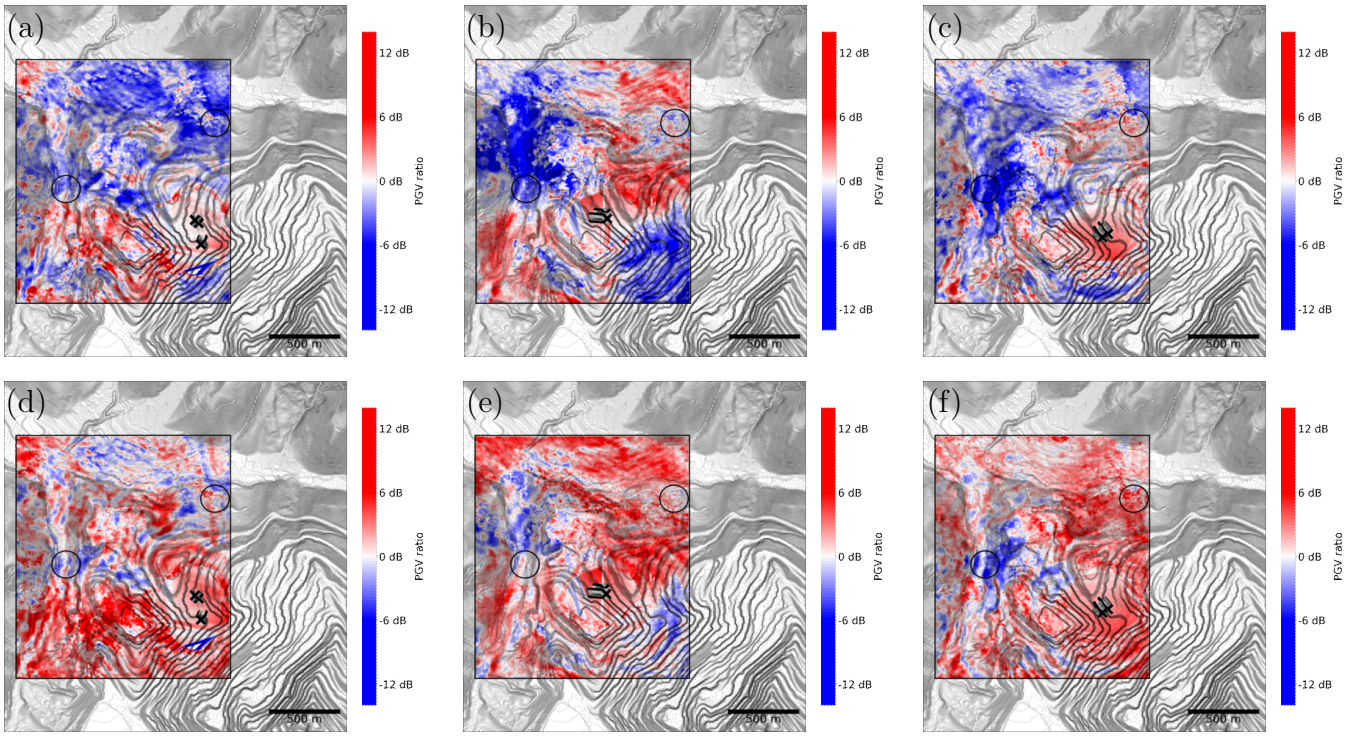

Figure 90: The ratio of the PGV computed for the optimized double blast to the computed PGV of the McMC start configuration for blasts (a) 30056, (b) 30062 and (c) 30076 and to the PGV computed for the sequential shooting with a 1 s delay and a constant 33 ms delay time interval for a blasts (d) 30056, (e) 30062 and (f) 30076.[1]

[1]DEM data source: CC-BY-4.0: State of Styria - data.steiermark.gv.at

9 Verification of Delay Time optimization for Double Blasts

To demonstrate that PGV reductions are successful, many production blasts are required to obtain a statistically significant sample size. The RMS residual obtained in Chapter 5 corresponds approximately to the standard deviation of the observations, which is around 3 dB and the relative reduction is expected to be in a similar range. The sample size can be estimated with the formula:

$$n = \frac{2\sigma_o^2 \left(Z_{1-\beta} + Z_{1-\alpha/2}\right)^2}{\Delta^2}, \tag{28}$$

where n is the required sample size, $Z_{1-\alpha/2}$ is the critical value of the standard normal distribution at the desired significance level, $Z_{1-\beta}$ is the critical value of the standard normal distribution at the desired power level, Δ is the effect size (the PGV reduction), and σ_o is the standard deviation of the observations (Rosner, 2010). To prove a small PGV reduction of 2 dB, i.e. by a factor of 1.26, with a confidence interval of 95% at a desired power of 80%, a sample size of 36 production blasts is needed. To detect a significant reduction of approximately 5 dB, i.e. factor of 1.78, 6 double production blasts were still needed with the same number of comparable single production blasts. It is difficult, if not nearly impossible, to obtain comparable blasts. No production blast is comparable to any of the double blasts performed in the entire data set. An accurate reproduction of the production blast is not possible, but blasts with similar holes, charge weights, and locations would, in theory, suffice if a statistically significant number is available. Achieving a sufficient number of comparable production blasts requires a field campaign that measures seismic data over several years. Even though there is no single blast for comparison, the limited data from double blasts can still be compared to a radial decay model. However, this comparison has weak statistical significance due to the small sample size. The radial decay model is calculated for each blasthole, and the hole responsible for the PGV at every position is identified. This procedure accounts for the spatial separation of the two blasts in the double blast scenario. Finally, receiver site factors were applied to mitigate the site effect and the blast site factors were adjusted to better match the actual measured PGV values. The parameters derived from the JI in Chapter 5 were used for calculating the radial decay model. Table 9 summarizes the ratio of the expected PGV of the radial decay model by the measured PGV of the optimized production blast. The second and third columns show the PGV ratios inside the western and northern target zones, while the fourth column shows the ratio for both target zones. The last column highlights the amplification of the observed data across the entire area relative to the radial decay model. An amplification of 0 dB indicates a good match and emphasizing only the relative amplifications or reductions compared to the expected values.

Blast name	Target W	Target N	2 Targets	Overall
10026	-0.78 dB	-0.61 dB	-0.69 dB	0.0 dB
10031	0.42 dB	2.92 dB	1.67 dB	0.0 dB
10036	2.23 dB	1.32 dB	1.78 dB	0.0 dB
20039	0.67 dB	-1.96 dB	-0.64 dB	0.0 dB
20040	-0.85 dB	1.1 dB	0.12 dB	0.0 dB
30056	0.53 dB	-0.91 dB	-0.19 dB	0.0 dB
30062	-0.26 dB	1.37 dB	0.55 dB	0.0 dB
30076	-0.76 dB	3.0 dB	1.12 dB	0.0 dB

Table 9: The ratio of the expected PGV of the radial decay model and the measured PGV values of the performed optimized double blasts.

9.1 First Verification Experiment

Production blasts with optimized delay times, derived in Chapter 8.5.1, were conducted with the settings discussed in that chapter.

9.1.1 Double Blast 10026

The vertical component of the seismogram from the numerically forward-modelled data shows a very strong S-wave but a very weak P-wave (Fig. 91a) because the S-wave had not been removed at this stage of the project. In contrast, the seismogram of the observed data (Fig. 91b) shows a strong P-wave onset followed by a slow phase with relatively low-frequency content corresponding to the surface wave. In both seismograms, the PGV times, indicated by the red dots, occur very late. In the numerically modelled data, the PGV times occur exclusively within the S-wave window. In contrast, in the observed data, they are almost exclusively caused by the late-arriving surface wave. This dominance of surface waves is an outlier in the dataset, as most of the PGVs are caused by body waves, as discussed in Chapter 4. In the crossplot of the observed versus predicted PGV times (Fig. 92a), the data is scattered around the line of equality. The PGV times show a relatively high R^2 of 0.41 and a very small RMS residual of 251 ms, which outperform most data. At this point in the project, the frequency content of the numerical forward-modelled data did not match the frequency content of the observed data, which is visible in the seismograms. The map of the measured PGV (Fig. 93a) shows that the measured PGV from the double blast was not stronger than that from a standard production blast (Fig. 100-102). Additionally, the map includes a contour line of 3 mm/s, representing the lower limit for listed buildings with the most unfavourable frequency. Outside this contour line, there is no danger to buildings under any circumstances. This contour line is still within the mining area, indicating that an undesirable PGV is far from reaching critical sites near residential areas. The amplification or reduction relative to the radial decay model (Fig. 93d) is minimal, but it primarily indicates a relative increase in PGV in the city area near the mine. Only a few stations measured the PGV within the rectangular target zones in the observed data. These stations show an average decrease in PGV by a factor of -0.78 dB in the western target zone and -0.61 dB in the northern target zone relative to the radial decay model. This reduction in the measured data is unexpected for that particular production blast, as for the numerical forward-modelling that reduction is caused by interference of S-waves. However, in this case, the PGV in the observed data is primarily caused by surface waves from the double blast.

9.1.2 Double Blast 10031

The vertical component of the seismogram from the numerically forward-modelled data shows a very strong S-wave but only a very weak P-wave (Fig. 91c). In contrast, the seismogram of the observed data (Fig. 91d) exhibits a strong P-wave onset, followed by a less pronounced, slower phase with relatively low-frequency content corresponding to the surface wave. This slower phase is visible at near offsets but diminishes at farther offsets. The PGV times in the numerical data (Fig. 91c) follow the S-wave window, while for the observed data (Fig. 91d), they seem to follow the P-wave window. There are relatively more PGV times attributed to surface waves at near offsets. In the crossplot of the observed versus predicted PGV times (Fig. 92b), the data is scattered widely around the line of equality. The data shows a relatively low R^2 of 0.03, and the RMS residual of 313 ms falls within the range of most of the data. The map of the measured PGV (Fig. 93b) indicates that the PGV from the double blast was generally within the normal range expected from a standard production blast. The 3 mm/s contour line slightly touches the western and the northern target regions. The variation relative to the radial decay model (Fig. 93e) is also minimal, showing a relative amplification specifically within the target regions. In the observed data, the stations inside the target zones show an average increase of PGV by a factor of 1.67 dB, relative to the radial decay model. The western target zone shows a slight increase of 0.42 dB, while the northern target zone shows a significant increase of 2.92 dB.

9.1.3 Double Blast 10036

The vertical component of the seismogram from the numerically forward-modelled data (Fig. 91e) and the observed data (Fig. 91f) show a similar pattern to that of the previous double blast. The PGV times in the numerical data (Fig. 91e) also follow the S-wave window, while for the observed data (Fig. 91f), they seem to follow the P-wave window, especially for far offsets. In the crossplot of the observed versus predicted PGV times (Fig. 92c), the data is scattered widely around the line of equality. The data shows a relatively low R^2 of 0.08, and the RMS residual of 241 ms is slightly lower than most of the data. The map of the measured PGV (Fig. 93c) indicates that the PGV from the double blast was generally within the normal range expected from a single blast. The 3 mm/s contour line slightly touches the northern target region. The variation relative to the radial decay model (Fig. 93f) is minimal, showing a relative amplification specifically within the target regions. In the observed data, the stations inside the target zones show an average increase of PGV by a factor of 1.78 dB relative to the radial decay model. The western target zone shows an increase of 2.23 dB, and the northern target zone shows an increase of 1.32 dB.

9.1.4 Conclusion of the First Verification Experiment

The significant problem in the initial verification experiment is still a large amount of S-wave in the numerical model, and it is also incapable of simulating the slow observed surface waves. The observed production blast 10026 exhibits a significant amount of low frequent seismic phase, likely the surface wave (Fig. 91b) and a distinct onset of the P-wave. The observed production blasts 10031 (Fig. 91d) and 10036 (Fig. 91f) show significantly fewer surface waves, a phenomenon that can be attributed to their location in the deep part of the mine and the shielding effect of the topography. In contrast, the numerical waveforms of all production blasts show barely observable P-waves and a clear onset of the S-wave with a velocity of around 2400 m/s. Overall, the difference between the numerically modelled and the observed waveforms is too large for a PGV prediction with these settings. Because

the reduction was based on S-wave interference, there is unlikely a reduction in the observed data. Two of the three observed production blasts show a significant increase in both target zones relative to the radial decay model. Just production blast 10026 shows an insignificant decrease in PGV.

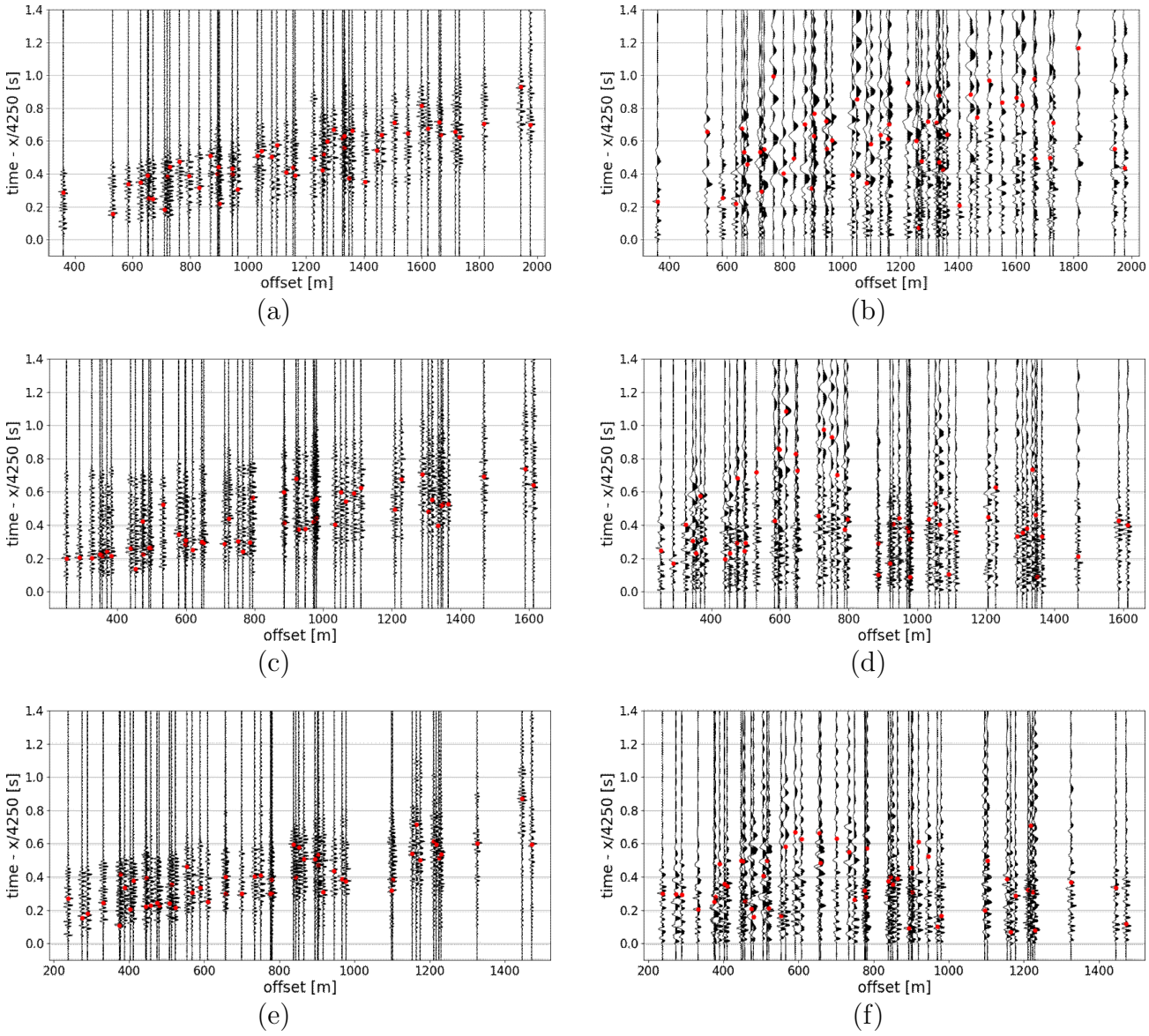

Figure 91: Trace-normalized time-reduced seismogram sections of the vertical component for the numerically modelled double blasts (a) 10026, (c) 10031, and (e) 10036, and the observed double blasts (b) 10026, (d) 10031, and (f) 10036. The red dots indicate the predicted and observed PGV times.

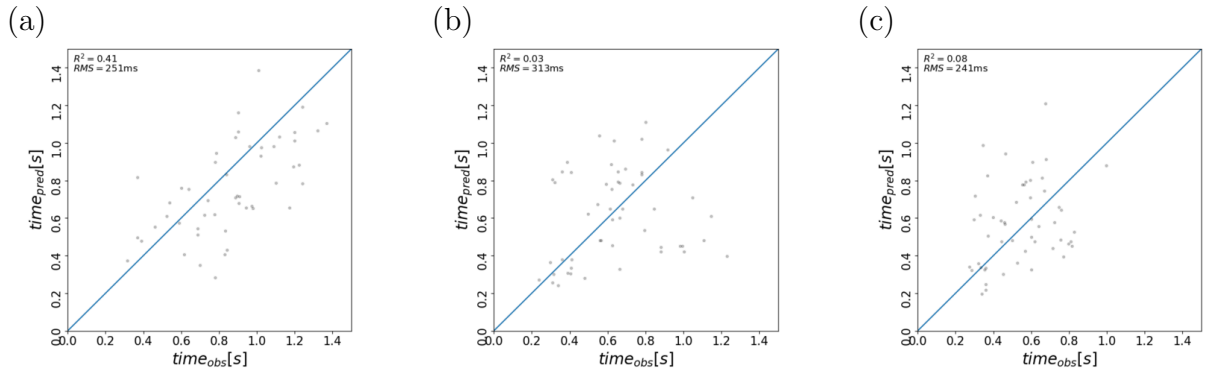

Figure 92: Crossplot of the predicted versus the observed PGV times for double blast (a) 10026, (b) 10031 and (c) 10036.

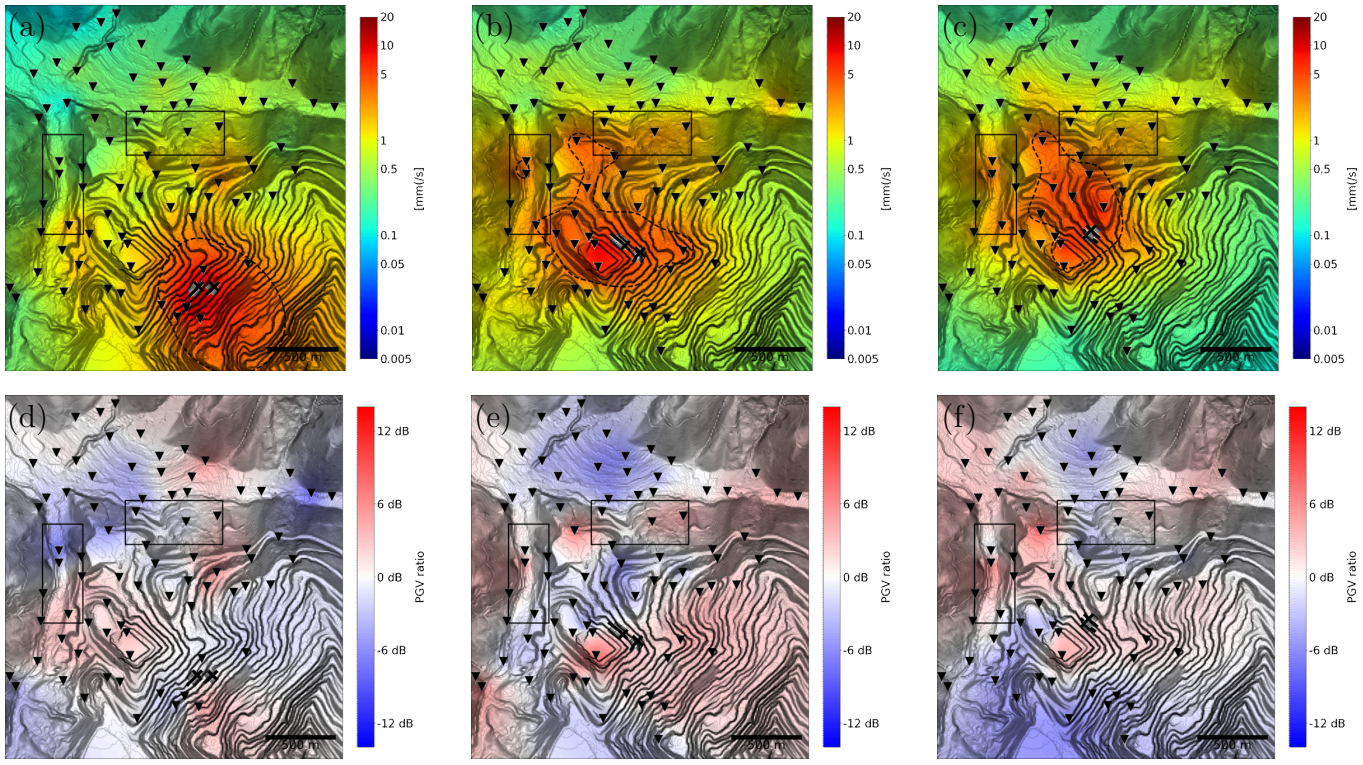

Figure 93: The measured PGV maps for blasts (a) 10026, (b) 10031, and (c) 10036 are shown alongside the ratios of the measured PGV divided by a radial decay model for the same blasts: (d) 10026, (e) 10031, and (f) 10036. The dashed contour line highlights the boundary beyond which the most sensitive buildings under the most unfavourable frequency content would be affected.[1]

[1]DEM data source: CC-BY-4.0: State of Styria - data.steiermark.gv.at

9.2 Second Verification Experiment

Production blasts with optimized delay times, derived in Chapter 8.5.2, were conducted with the settings discussed in that chapter.

9.2.1 Double Blast 20039

The vertical component of the seismogram from the numerically forward-modelled data (Fig. 94a) shows a clear and strong P-wave. The observed data (Fig. 94b) also show a clear P-wave, but a late, low-frequency phase follows it. The PGV times in the numerical data (Fig. 94a) follow the P-wave window, whereas in the observed data (Fig. 94b), they follow the surface wave window. Once again, this production blast is rather an exception. In the crossplot of the observed versus predicted PGV times (Fig. 95a), the data is shifted toward later PGV times on the observed axis. The data shows a relatively low R^2 of 0.11 and a very large RMS residual of 497 ms, significantly above that of most of the data. The map of the measured PGV (Fig. 96a) indicates that the PGV from the double blast was generally within the normal range expected from a single blast. The 3 mm/s contour line is far from the target regions and the city area. The variation relative to the radial decay model (Fig. 96c) is minimal, and it primarily shows a reduction in the area of the city. In the observed data, the stations inside the target zones show an average PGV decrease of -0.64 dB relative to the radial decay model. The western target zone shows an increase of 0.67 dB, and the northern target zone shows a decrease of -1.96 dB.

9.2.2 Double Blast 20040

The vertical component of the seismogram from the numerically forward-modelled data (Fig. 94c) and the observed data (Fig. 94d) show a similar pattern to that of the previous double blast. This time, the strong surface wave almost diminishes for far offsets above 1200 m. In the crossplot of the observed versus predicted PGV times (Fig. 95b), the data is scattered widely around the line of equality, with a slight trend toward later observed PGV times. The data shows a relatively low R^2 of 0.02, and the RMS residual of 314 ms is in the range of the majority of the data. The map of the measured PGV (Fig. 96b) indicates that the PGV from the double blast was generally within the normal range expected from a single blast. The 3 mm/s contour line slightly touches the northern target region. The variation relative to the radial decay model (Fig. 96d) is minimal, and it primarily shows a reduction in the city's western area. In the observed data for double blast 20040, the stations inside the target zones show an insignificant average increase of PGV by a factor of 0.12 dB relative to the radial decay model. The western target zone shows a small decrease of -0.85 dB, while the northern target zone shows a minor increase of 1.1 dB.

9.2.3 Conclusion of the Second Verification Experiment

In the previous verification experiment, interference was caused by S-waves, while in this instance, P-waves interfered due to the reduction of the amplitude in the S-wave window. The arrival time and the entire P-wave train of the numerical model better resemble the observed data. The observed data exhibits some very late phases, likely caused by surface waves that this numerical model cannot simulate. This late, low-frequency phase is evident in the observations of both production blasts. Both of the observed double blasts show a small decrease of PGV in at least one target zone relative to the

radial decay model. Based on the PGV prediction of double blast 20039, a decrease in PGV for the western target zone was expected, but a relative decrease in the northern target zone was observed. For double blast 20040, the small relative decrease of -0.85 dB for the western target zone aligns well with the expected decrease of -0.26 dB. The northern target zone shows a relative increase of 1.1 dB in the observed data, which is approximately the expected magnitude of the prediction (1.52 dB).

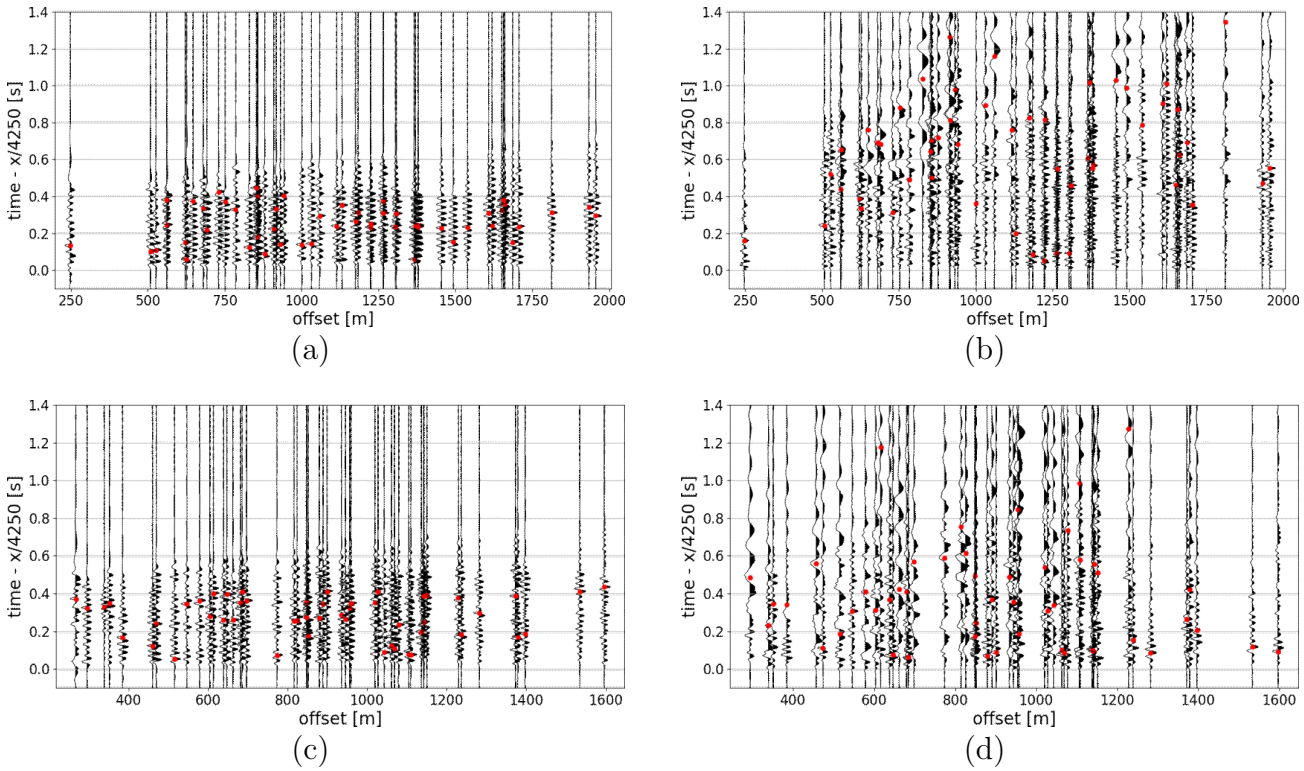

Figure 94: Trace-normalized time-reduced seismogram sections of the vertical component for the numerically modelled double blasts (a) 20039 and (c) 20040, and the observed double blasts (b) 20039 and (d) 20040. The red dots are the predicted and observed PGV times.

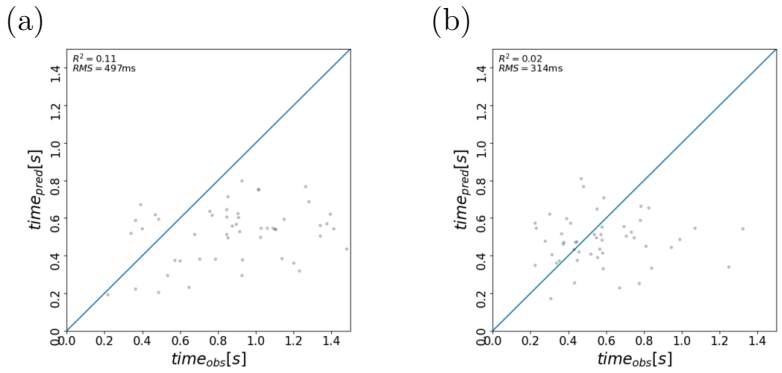

Figure 95: Crossplot of the predicted versus the observed PGV times for double blast (a) 20039 and (b) 20040.

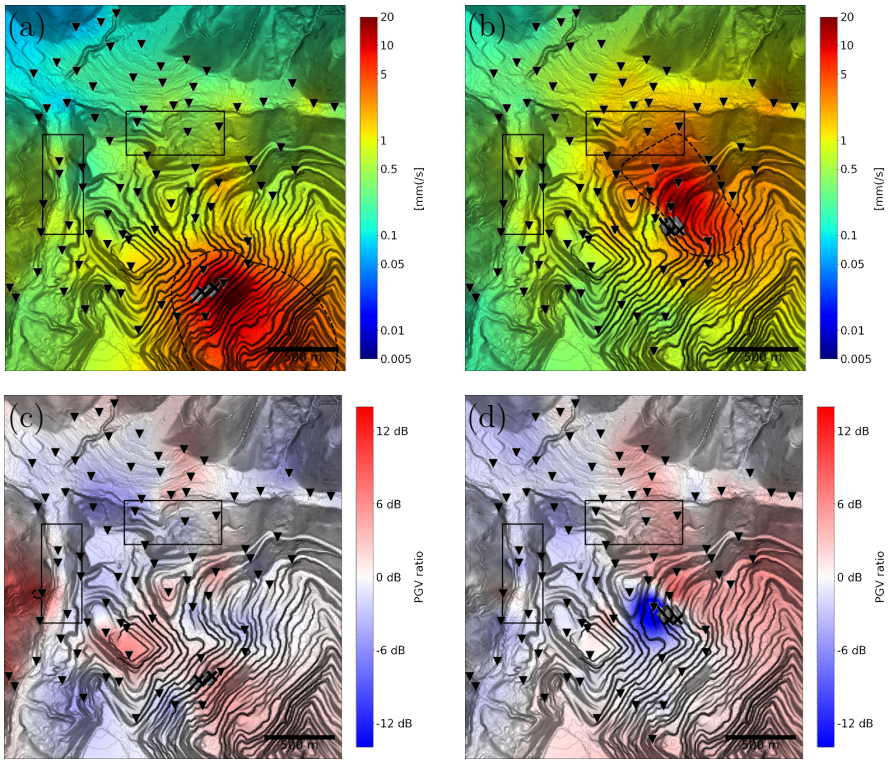

Figure 96: The measured PGV maps for blasts (a) 20039 and (b) 20040 are shown alongside the ratios of the measured PGV divided by a radial decay model for the same blasts: (c) 20039 and (d) 20040. The dashed contour line highlights the boundary beyond which the most sensitive buildings under the most unfavourable frequency content would be affected.[1]

[1]DEM data source: CC-BY-4.0: State of Styria - data.steiermark.gv.at

9.3 Third Verification Experiment

Production blasts with optimized delay times, derived in Chapter 8.5.3, were conducted with the settings discussed in that chapter.

9.3.1 Double Blast 30056

The vertical component of the seismogram from the numerically forward-modelled data (Fig. 97a) distinctly displays a clear and strong P-wave, accompanied by relatively pronounced S-waves. The numerical model indicates a more substantial conversion to S-waves in this blast position. The observed data (Fig. 97b) also show a clear P-wave, but a late, low-frequency phase follows it. The PGV times, marked by the red dots in the numerical data, predominantly align with the P-wave window. In contrast, in the observed data, the PGV times correspond equally to both the P-wave and surface wave windows. In the crossplot of the observed versus predicted PGV times (Fig. 98a), the data is scattered widely around the line of equality. The data shows a relatively low R^2 of 0.07 and an RMS residual of 289 ms, which is in the range of the majority of the data. The map of the measured PGV (Fig. 99a) indicates that the PGV from the double blast was generally within the normal range expected from a single blast. The 3 mm/s contour line is far from the target regions and the city area. Only a small area north of the western target region exhibits a PGV higher than 3 mm/s. The variation relative to the radial decay model (Fig. 99d) is minimal, showing a slight relative reduction in the vicinity of the target zones. In the observed data, the stations inside the target zones show an insignificant average PGV decrease by -0.19 dB relative to the radial decay model. The northern decrease of -0.91 dB while the western target zone shows an increase of 0.53 dB.

9.3.2 Double Blast 30062

The vertical component of the seismogram from the numerically forward-modelled data (Fig. 97c) and the observed data (Fig. 97b) show both a dominant P-wave. The observed data shows a weak surface wave, which diminishes after an offset of 600 m. In both seismogram sections, the PGV times predominantly align with the P-wave window. In the crossplot of the observed versus predicted PGV times (Fig. 98b) the data points are relatively closely clustered around the line of equality, indicating no trend toward later observed PGV times. The data shows a relatively low R^2 of 0.04 and a very small RMS residual of 189 ms, significantly lower than most of the data. The map of the measured PGV (Fig. 99b) indicates that the PGV from the double blast was generally within the normal range expected from a single blast. The 3 mm/s contour line touches the western target region and extends into the city area. The small area north of the western target region exhibits a PGV higher than 3 mm/s. In this instance, the double blast was positioned close to the city area. The variation relative to the radial decay model (Fig. 99e) is minimal. It generally shows a reduction in the western area near the blast and an increase towards the northern area, located further away. In the observed data, the stations inside the target zone show an insignificant average increase of PGV by a factor of 0.55 dB relative to the radial decay model. The western target zones show a small decrease of -0.26 dB, while the northern target zone shows an increase of 1.37 dB.

9.3.3 Double Blast 30076

The vertical component of the seismograms from the numerically forward-modelled data (Fig. 97c) and the observed data (Fig. 97b) show both a dominant P-wave. The observed data also shows a relatively strong surface wave, with an intercept that does not pass through zero, likely due to post-blast movements of the rock mass. In the numerical seismograms, the PGV times predominantly align with the P-wave window, whereas the observed PGV times are equally aligned with both the P-wave window and the surface wave window. In the crossplot of the observed versus predicted PGV times (Fig. 98c) the data points are relatively widely clustered around the line of equality, indicating no clear trend toward later observed PGV times. The data shows a relatively low R^2 of 0.06 and an RMS residual of 361 ms, slightly above most of the data. The map of the measured PGV (Fig. 99b) indicates that the PGV from the double blast was generally within the normal range expected from a single blast. The 3 mm/s contour line extends over the northern target region, and a small area north of the western target region also exhibits a PGV greater than 3 mm/s. The variation relative to the radial decay model (Fig. 99f) is minimal. In the observed data, the stations inside the target zone show an average increase of PGV by a factor of 1.12 dB relative to the radial decay model. The western target zones show a small decrease of -0.76 dB, while the northern target zone shows a relatively significant increase of 3.0 dB.

9.3.4 Conclusion of the Third Verification Experiment

The numerically modelled and observed seismograms exhibit greater similarity in the final verification experiment despite the numerical data not being fully optimized. For double blasts 30062 and 30076, a relative reduction of -0.26 dB and -0.76 dB within the western target zone and an increase of 1.37 dB and 3.0 dB within the northern target zone was observed in relation to the radial decay model. This is consistent with the numerical model that predicted a decrease (-0.26 dB and -3.22 dB) and increase (0.83 dB and 2.47 dB) within the same zones relative to the sequentially shot blast configuration. For production blast 30056, a decrease in the western target zone and an insignificant increase in the northern target zones were predicted. In contrast, the decrease/increase was reversed in the observed data compared to the radial decay model.

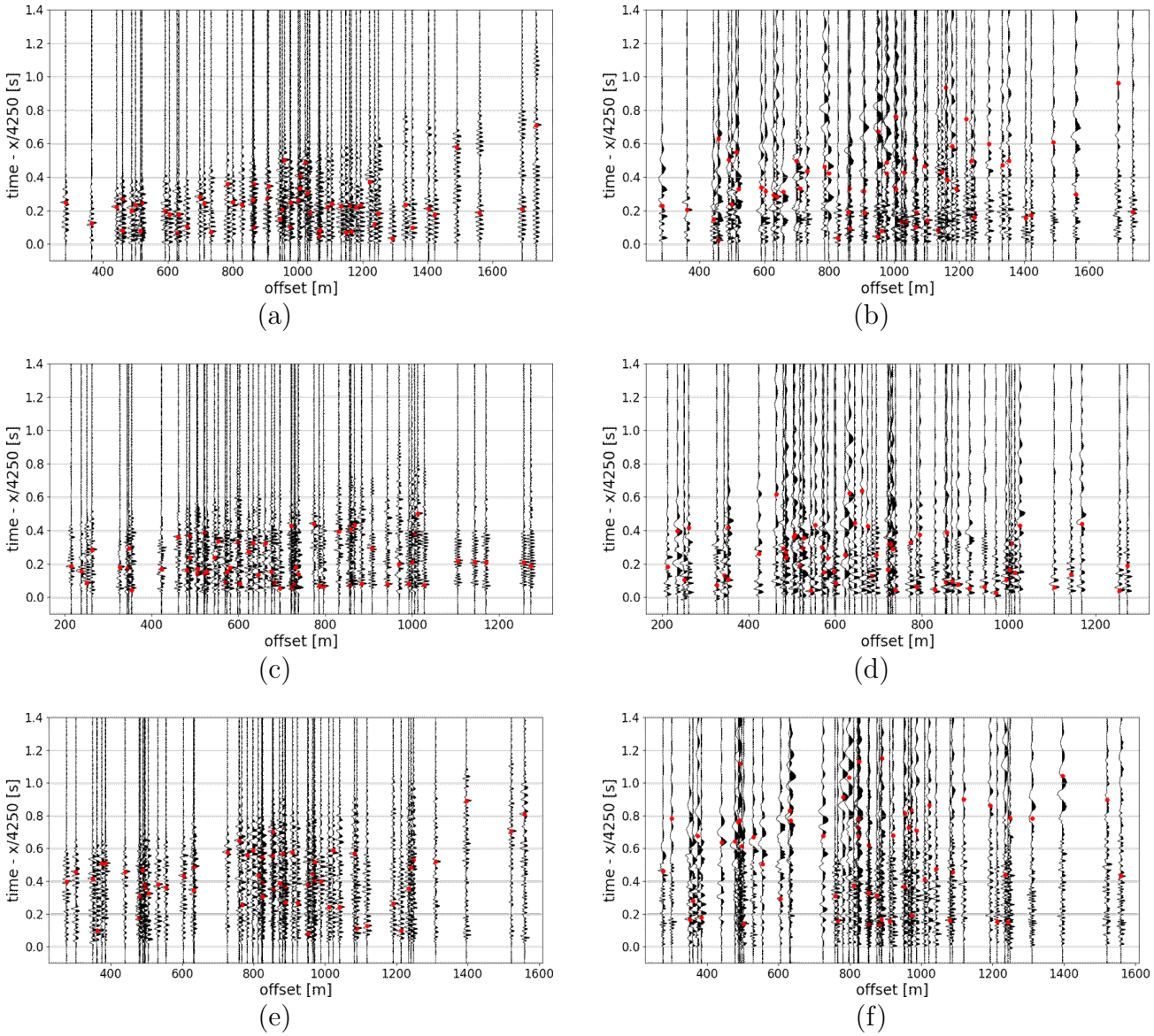

Figure 97: Trace-normalized time-reduced seismogram sections of the vertical component for the numerically modelled double blasts (a) 30056, (c) 30062, and (e) 30076, and the observed double blasts (b) 30056, (d) 30062, and (f) 30076. The red dots indicate the predicted and observed PGV times.

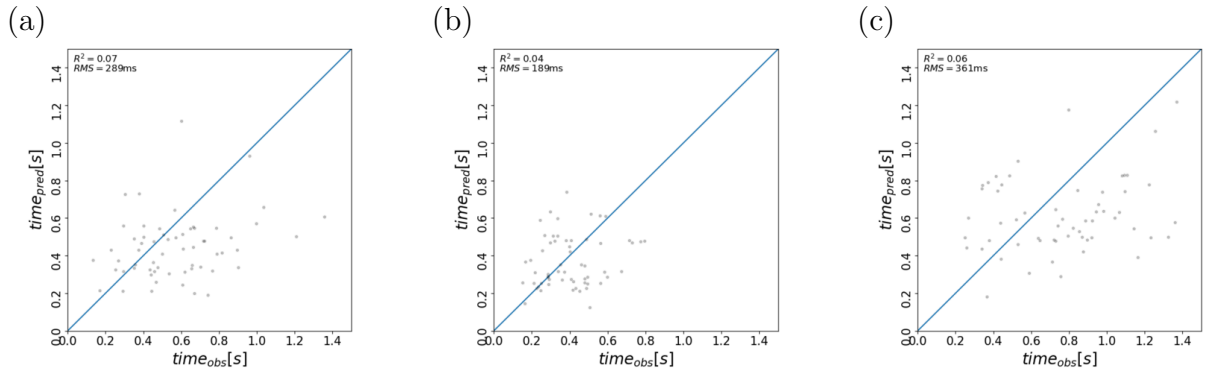

Figure 98: Crossplot of the predicted versus the observed PGV times for double blast (a) 30056, (b) 30062 and (c) 30076.

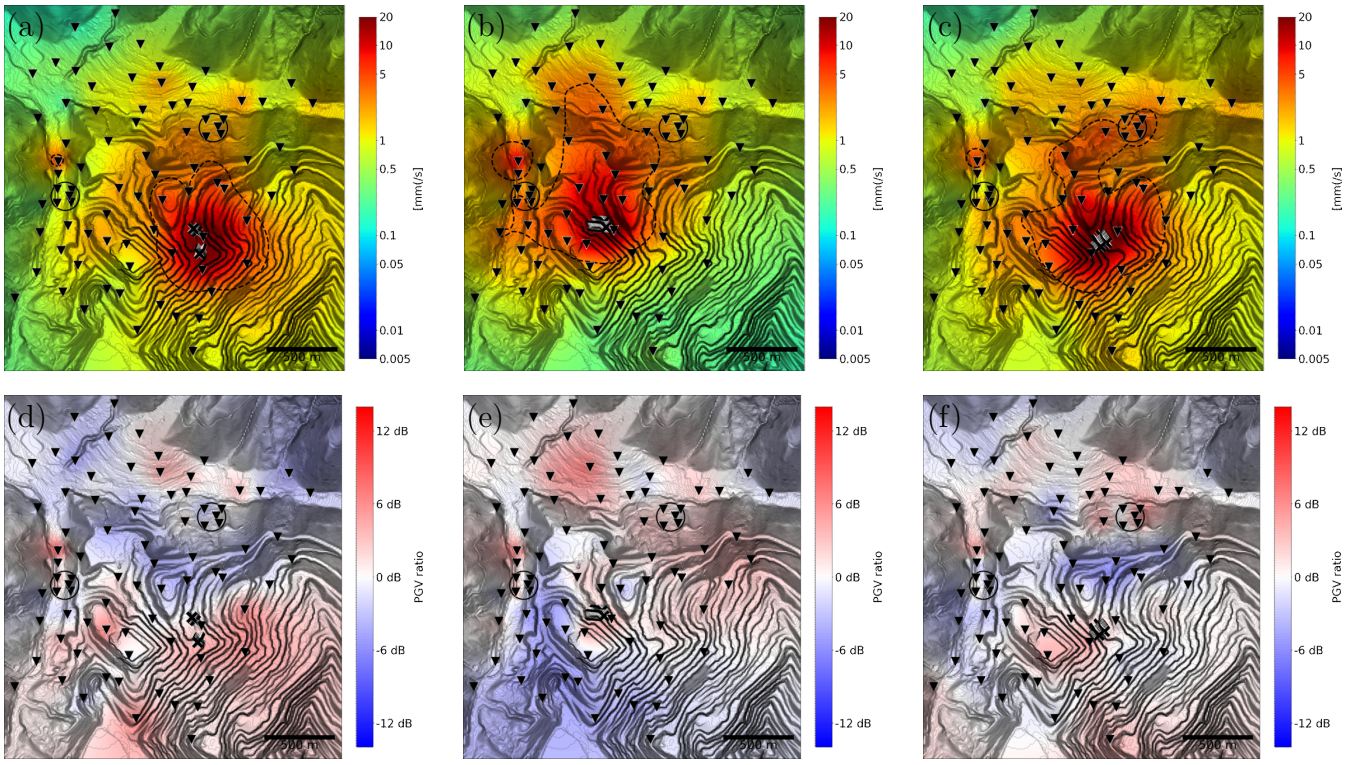

Figure 99: The measured PGV maps for blasts (a) 30056, (b) 30062, and (c) 30076 are shown alongside the ratios of the measured PGV divided by a radial decay model for the same blasts: (d) 30056, (e) 30062, and (f) 30076. The dashed contour line highlights the boundary beyond which the most sensitive buildings under the most unfavourable frequency content would be affected. [1]

[1]DEM data source: CC-BY-4.0: State of Styria - data.steiermark.gv.at

9.4 Discussion and Conclusion

The theoretical experiments in Chapter 8 have shown that using double blasts can, in theory, lower PGV in specific target zones compared to single blasts. This was evident in the results from the last three simulations. For a fair comparison, optimized double blasts were compared with two single blasts at the same location, blasted sequentially, with a 1 s delay. In the simulation, the PGV in at least the target region was reduced by -1.31 dB, -0.26 dB and -3.22 dB for production blasts 30056, 30062 and 30076, respectively. While simulations make it easy to compare the impacts of double versus single blasts at the same location, applying these insights to actual blasts in the field comes with its challenges. Replicating a production blast precisely is a complex task, influenced by many variables. First, carrying out two identical blasts at the same location is impossible because the first blast permanently changes the rock structure. Trying to replicate a blast accurately is further complicated by factors like debris falling into the blastholes, which can alter the amount of explosive used. The effect of moisture on the blast caused by environmental conditions and the uniformity of the equipment used can drastically alter the results. Moreover, human error plays a significant role in executing blasts that are identical in every aspect. The closest one can replicate this in the real world is by doing a similar blast as close as possible to the first one, using the same number of holes and amount of explosives. However, even then, differences in the geology, weather, and other factors beyond control mean the actual blast can significantly differ. During the survey, no comparable blasts were shot, which I could compare to the performed double blasts. Even if comparable production blasts were available, the highly variable factors at each blast site require extensive statistical analysis to ensure that comparisons are representative. This highlights the challenge of applying theoretical simulation results in practical mining operations. Nevertheless, a reduction of PGV is already two steps ahead of what has to be done. First, it is more critical to predict good enough waveforms that match well with the observed data, and then one can think about predicting the highly non-linear PGV. The final step would be the reduction of that PGV. Chapter 8 shows at least that a reduction is theoretically possible with such a blasting arrangement and the physics applied by the waveform forward-modelling approach on the 3D model of Mt. Erzberg. Although the double blasts of the verification experiments could not be compared with similar standard blasts, a comparison with a radial decay model was possible. Three of the last five experiments showed a similar pattern to the simulation. Unfortunately, this is not a statistically significant sample size to detect a reduction. Overall, the PGVs of the double blasts were not significantly higher than that of the single blasts (Fig. 100-102), with some of the single blasts showing notably higher values.

10 Conclusion

The survey and data collection from the field campaigns conducted between 2016 and 2020 at the Erzberg mine aimed to measure and analyse blast-induced seismic activities. The main task of this research is to reduce Peak Ground velocity (PGV) of mining blasts in selected target zones through interference of double blasts using realistic waveforms. Seismic data was collected using an array of three-component seismic sensors during various types of production blasts, including standard, optimized, and double blasts with different detonators. In the analysis of the observed data Chapter 4 aims to distinguish between different seismic phases (P-waves, S-waves, and surface waves) and their contributions to PGV. The main findings from the analysed observational data show that P-waves were consistently observed in all production blasts, especially in the vertical component of the seismic data. S-waves were not detected, possibly because they were obscured by overlapping seismic phases and complex geological conditions. A later seismic phase with a velocity of 1700 m/s, most likely the surface waves, was also identified. They showed a stronger presence in the mine area, especially in the horizontal components. Applying a low-pass filter could further enhance this phase. The complex topography in the study area leads to scattering attenuation of the surface waves and in some areas, the topography acts as a barrier protecting the town from the effects of the surface waves. Most of the PGVs were measured within the body wave windows (89.5% of all PGVs), with almost three times the number of PGVs occurring in a window attributed solely to P-waves compared to those in a window containing only S-waves. This indicates that a significant contribution to the PGV stems from P-waves. Overall, the analysis found no clear observations of S-waves, suggesting that P-waves are the primary contributors to PGV. Surface waves, although significant, showed a lower impact on PGV. At larger offsets, the energy of the surface waves decreases relative to the P-wave energy, which is a surprising outcome explained by topographical shielding effects. The deconvolution method, which stacks the deconvolution outcome in offset gathers, effectively highlights the P-wave onset in the vertical component. However, it is less effective for surface waves due to scattering and complex topography. The deconvolution study confirmed that surface waves are more pronounced near the blast sites and diminish at larger offsets. In contrast to the raw data, surface waves were visible only in the vertical component. The complex ray path and deviation from the radial/transversal component may further reduce the amplitude during the stacking process. Overall, the results demonstrate that P-waves play a dominant role in generating PGV, with surface waves contributing significantly in specific areas but less at greater distances due to topographical influences. The phase responsible for the PGV in production blasts exhibits considerable variability, ranging from blasts where the surface wave was almost exclusively responsible for the PGV to blasts where the PGV clearly originated from a wave travelling at the P-wave velocity.

The study in Chapter 5 on analytical PGV prediction aims to improve the prediction of PGV from production blasts using various empirical and analytical methods, along with a comprehensive dataset. Refining the empirical formulas aimed to enhance the precision of PGV predictions for production blasts. Good predictions are crucial for ensuring that mining operations stay within legal limits for ground vibrations and it helps mining operators to comply with legal regulations regarding blast-induced ground vibrations. It prevents from potential legal and safety issues and makes mining more efficient by allowing mining operators to anticipate and mitigate the effects of seismic waves from production blasts. The Scaled Distance (SD) formula is convenient and widely used by mining operators, its main downsides include the arbitrary selection of the charge-distance ratio as prior with a fixed charge scaling, oversimplification of complex interactions, and inadequate accounting for site-specific factors

and the geological variability. These limitations can lead to inferior predictions of the PGV from production blasts. With the prior of the SD approach, depending on the chosen empirical formula, it is often not possible to achieve the minimum cost function for the line fit. If the formula is not properly evaluated for the specific blast site, the cost function of the line fit will never approach a minimum. In this analytical prediction study, a Joint Inversion (JI), which inverts the whole dataset for amplitude decay b and the charge weight exponent c independently, has the best performance compared to the other analytical methods in terms of R^2 and RMS residual considering that it uses the least number of parameters. The JI equation can be used to predict the PGV for all receiver locations on the map. However, the blast site factor should be excluded from the prediction, as it is an a posteriori fit to the actual amplification of the blast. Another outcome of this study is that $c = 0.5$ may be a global valid value. This value is valid, at least for the specific site in the study, and is also physically reasonable. Also SD formula resulted in a minimum cost function when choosing a c/b ratio, which is resulting in $c = 0.5$. Chapters 6 to 9 of the thesis address the numerical waveform modelling method. The primary objective of this approach is to simulate production blasts based on configurations provided 24-48 hours before the actual blasts. These configurations include the positions of blastholes and the estimated amount of explosives. The goal is to forward-model seismic waveforms from each blasthole and determine optimal blast delay times that minimize the PGV at target zones. Due to the high computational demand, the numerical simulations were performed on Marconi-Broadwell, Europe's fastest supercomputer, using the Barcelona Subsurface Imaging Tools (BSIT). The forward-modelling was pre-computed for 80 positions, with actual blast positions interpolated for immediate optimization. The seismic wave equation is solved using a finite difference scheme for 3D elastic wave propagation. The model requires high spatial and time discretization due to low sedimentary velocities and high frequencies, leading to significant computational demands. Pre-computation on the supercomputer was necessary because on the local high-performance computing centre (HPC) the resources were insufficient. The pre-computed seismograms required further processing to make them more realistic. The single seismograms from each blasthole are superposed with specified time delays to simulate the entire production blast. This method provides a comprehensive understanding of ground motion at various locations. To derive the Source Time Function (STF), several methods were used, including Kuepper wavelet conversion and Laplace-domain inversion. These STFs were crucial for modelling and prediction. The STF could also be extracted from the data using an inverse deconvolution algorithm, but this approach assumes that all blasts in a production blast have the same STF, which is not true given the variability in charge amounts. Nevertheless, it is a different data-driven approach, alongside the Laplace Domain Inversion (Bleibinhaus & Trabi, 2023), to extract the STF and could serve as a comparison in those blasts where it worked well. The STFs of both methods matched well with each other.

The observed data lacks a clear S-wave, showing a strong P-wave and a later phase likely a surface wave. The numerical data shows a distinct P-wave and noticeable S-wave at an apparent velocity of about 2400 m/s, which corresponds to the ratio of 1.75 to the P-wave velocity of the 3D model. The S-wave in the numerical data is likely caused by conversion at the surface near the shot position. Phases arriving with and after the S-wave were attenuated to mirror observed data amplitudes. Overall the numerical model features recognizable elements from observed data but with discrepancies such as the presence of S-waves and absence of surface waves. The fit between numerical and observed waveforms is evaluated using cross-correlation coefficients (xcc) and the best fit occurs when late phases are removed from the numerical data. A comparative analysis of different wavelet models (Kuepper, LDI) and a simple convolution model showed a simple convolution model performed best in waveform prediction.

The comparison of amplitude spectra between numerical and observed data showed that the numerical model captured the frequency components well. This is particularly visible for production blasts with standard delay times, where the observed peaks and harmonics in the frequency spectra agree well with the numerical predictions.
After modification of the amplitude decay to better fit the observed data the numerical waveform modelling approach can be used to predict PGVs, within the model area. The numerical method showed satisfactory PGV predictions with an R^2 of 0.50 and RMS residual of 4.66 dB, but was outperformed by the JI method with an R^2 of 0.60 and RMS residual of 3.76. A good waveform prediction and a reliable PGV prediction are beneficial for the next step, a relative PGV reduction. This is achieved by wave interference from multiple spatial separated blast sources. Even though the steps to predict waveforms and PGVs are still far from the observations, the underlying principle remains the same. If a reduction can be achieved with an imperfect model, it is likely to be possible with a more refined version. Among the parameters that can be potentially adjusted for a production blast, only the delay times could be altered. A Markov Chain Monte Carlo (McMC) algorithm was used to search for optimized blast delay timings that would cause less impact on a specific target zone. The theoretical experiments indicate that double blasts can reduce PGV in specific target zones compared to single blasts. This is shown especially for the simulation of the last evaluation experiment, in August 2020. In theory, based on the applied physics, a maximum reduction of -3.22 dB, which is a ratio of 0.69, in one target zone was possible relative to a single blast, which is a notable reduction considering that twice the amount of energy is released in the double blast. However, this reduction is within the magnitude of the variation of a blast site factor and the standard deviation of the observations. Just the last three predictions were performed under almost optimal conditions. From that three prediction two verification blasts showed a similar pattern than in the prediction. This very small sample size is far below the required statistical significant sample size. A large sample size of comparable production blasts is needed to prove a reduction. One strategy to reduce the sample size is to increase the effect size, which can be done by comparing optimized double blasts to unoptimized double blasts, instead of single blasts. Nevertheless real-world applications are challenging due to the variability in blast conditions and the difficulty in replicating even similar blast scenarios. Overall, none of the double blasts stood out in terms of PGV compared to the single blasts, which was a concern for the mining operator and a reason for the limited number of double blasts performed. Achieving consistent waveform predictions is crucial before attempting PGV reductions. Predicting the PGV itself presents a broad range of difficulties due to its highly non-linear nature. The attempt to predict PGV was undertaken solely because the mining operator is legally obliged to do so. A better measure, for example, would be the Root Mean Square (RMS) amplitude. The seismic response to production blasts is influenced by a complex interplay of factors, including geological heterogeneities and surface topography. Near-field effects, in particular, can lead to significantly different outcomes in real production blasts, as they likely considerably influence the STF and the emitted seismic phases. These near-field effects are completely ignored by this simplified far-field approach. The relatively simplified models may not capture all these nuances, potentially limiting the accuracy of predictions. To achieve a reliable PGV prediction, two strategies can be considered. One approach involves developing a highly accurate model that thoroughly captures all the physical aspects underlying the numerical simulation. In this method, near-field simulations are crucial as they must account for the complexities and dynamic changes in the environment as the production blast ignites and fractures the surrounding areas. These simulations are essential for accurately capturing these aspects before passing the simulated wavefield to a far-field grid. However, this method is highly computationally intense, demanding extensive research and resources,

which may be infeasible. Additionally, the almost unpredictable factors such as geological variations, weather conditions and human error can lead to significantly different outcomes, further complicating the prediction. The other approach is to use a simplified model, similar to the engineering formulas discussed in this thesis. This approach provides practical, but less precise predictions. Even though these simplified models are easy to use, they still have a significant potential for improvement. As shown in this thesis, they can still perform very poorly if they are not well-calibrated for the specific blast site.

References

Ainalis, D., Kaufmann, O., Tshibangu, J.-P., Verlinden, O. & Kouroussis, G. (2017). Modelling the Source of Blasting for the Numerical Simulation of Blast-Induced Ground Vibrations: A Review. Rock Mechanics and Rock Engineering, **50**(1): 171–193.

Ambraseys, N. & Hendron, A. (1968). Dynamic behavior of rock masses. – In: Stagg, K. G. & Zienkiewicz, O. C. (Eds.): Rock mechanics in engineering practice, 203–207, John Wiley & Sons, London.

Awwad, A., Rami, A. & Hani, A. (2021). Open Pit Mining, Kapitel: 1. IntechOpen, Bandung, Indonesia.

Blair, D. (1993). Blast vibration control in the presence of delay scatter and random fluctuations between blastholes. International Journal for Numerical and Analytical Methods in Geomechanics, **17**(2): 95–118.

Bleibinhaus, F. & Gebrande, B. (2006). Crustal structure of the Eastern Alps along the TRANSALP profile from wide-angle seismic tomography. Tectonophysics, **414 (1-4)**: 51–69.

Bleibinhaus, F. & Trabi, B. (2023). Source Time Functions and Interference from Blast Arrays. Geophysical Prospecting, **71**: 1325–1337.

Bleibinhaus, F., Trabi, B. & Tauchner, C. (2019). Best practices for blast vibration reduction. SLIM Deliverable D3.2. Report, Chair of Applied Geophysics.

Brooks, S., Gelman, A., Jones, G. & Meng, X. (2011). Handbook of Markov Chain Monte Carlo. CRC Press.

Cerjan, C., Kosloff, D., Kosloff, R. & Reshef, M. (1985). A nonreflecting boundary condition for discrete acoustic and elastic wave equations. Geophysics, **50**(4): 705–708.

de la Puente, J., Ferrer, M., Hanzich, M., Castillo, J. E. & Cela, J. M. (2014). Mimetic seismic wave modeling including topography on deformed staggered grids. Geophysics, **79**.

Dick, R., A., Fletcher, L., R. & D'Andrea, D., V. (1983). Explosives and Blasting Procedures Manual. U.S. Department of the Interior, Bureau of Mines.

Duvall, W., Johnson, C., Meyer, A. V. C. & Devine, J. F. (1962). Vibrations from instantaneous and millisecond-delayed quarry blasts. US Department of Interior, Bureau of Mines.

Duvall, W. I. & Petkof, B. (1959). Spherical propagation of explosion generated strain pulses in rock. U.S. Department of the Interior, Bureau of Mines.

Ebner, F., Cerny, I., Eichhorn, R., Götzinger, M., Paar, Werner, H., Prochaska, W. & Weber, L. (2000). Mineral Resources in the Eastern Alps and Adjoining Areas. Mitt. Österr.Geol. Ges., **92**: 157–184.

Gao, Q., Lu, W., Yang, Z., Yan, P. & Chen, M. (2018). Analysis of evolution of seismic components induced by a vertical blasthole. Rock mechanics and Rock Engineering, **52**: 1959–1977.

Gardner, G. H. F., Gardner, L. W. & Gregory, A. R. (1974). Formation Velocity and Density - Diagnostic Basics for Stratigraphic Traps. Geophysics, **39**: 770–780.

Gelman, A. & Carlin, J. (2014). Beyond power calculations: Assessing Type S (Sign) and Type M (Magnitude) Errors. Perspectives on Psychological Science, **9**(6): 641–651.

Gelman, A., Carlin, J. B., Stern, H. S. & Rubin, D. B. (2003). Bayesian data analysis. CRC press, **2**(3).

Gelman, A. & Gilks, W. R. (1996). Efficient Metropolis jumping rules. Bayesian Statistics, **5**: 599–607.

Haario, H., Saksman, E. & Tamminen, J. (1999). Adaptive proposal distribution for random walk Metropolis algorithms. Computational Statistics, **14**(3): 375–395.

Hastings, W. K. (1970). Monte Carlo Sampling Methods Using Markov Chains and Their Applications. Biometrika, **57**: 97–109.

Hestholm, S. (1999). Three-dimensional finite difference viscoelastic wave modelling including surface topography. Geophysical Journal International, **139**(3): 852–878.

Hinzen, K.-G. (1988). Modelling of blast vibrations. International Journal of Rock Mechanics and Mining Sciences & Geomechanics Abstracts, **25**(6): 439–445.

Hole, J. A. & Zelt, B. C. (1995). 3-D finite-difference reflection travel times. Geophys. J. Int., **121**(2): 427–434.

Kass, R., Carlin, B., Gelman, A. & Neal, R. (1998). Markov Chain Monte Carlo in Practice: A Roundtable Discussion. The American Statistician, **52**: 93–100.

Kawase, H. (2003). 61 - Site Effects on Strong Ground Motions. – In: Lee, W. H. K., Kanamori, H., Jennings, P. C. & Kisslinger, C. (Eds.): International Handbook of Earthquake and Engineering Seismology, Part B, Band 81 of *International Geophysics*, 1013–1030, Academic Press.

Khandelwal, M. & Singh, T. (2009). Prediction of blast-induced ground vibration using artificial neural network. International Journal of Rock Mechanics and Mining Sciences, **46**(7): 1214–1222.

Kramarczyk, B., Pytlik, M. & Mertuszka, P. (2020). Effect of aluminium additives on selected detonation parameters of a bulk emulsion explosive. Materiały Wysokoenergetyczne, **12**: 99–113.

Kuepper, F. J. (1958). Theoretische Untersuchung über die mehrfachaufstellung von Geophonen. Geophysical Prospecting, **14**.

Lebedev, V. (1964). Difference analogues of orthogonal decompositions, basic differential operators and some boundary value problems. USSR Computational Mathematics and Mathematical Physics, **4**: 449–465.

Mansouri, H. & Farsangi, M. A. E. (2015). Blast vibration modeling using linear superposition method. Journal of Mining & Environment, **6**(2): 125–140.

Metropolis, N., Rosenbluth, A. W., Rosenbluth, M. N., Teller, A. H. & Teller, E. (1953). Equation of State Calculations by Fast Computing Machines. J.Chem.Phys., **21**: 1087–1092.

Metropolis, N. & Ulam, S. (1949). The Monte Carlo method. J. Amer. Stat. Assoc., **44**: 335–341.

Murmu, S., Maheshwari, P. & Verma, H. K. (2018). Empirical and probabilistic analysis of blast-induced ground vibrations. International Journal of Rock Mechanics and Mining Sciences, **103**: 267–274.

Neubauer, F. (1994). Revised lithostratigraphy and structure of the Eastern Graywacke Zone (Eastern Alps). Mitt. Österr.Geol. Ges., **86**: 61–74.

Ouchterlony, F., Nyberg, U., Olsson, M., Bergqvist, I., Granlund, L. & Grind, H. (2004). Where does the explosive energy in rock blasting rounds go? Science and Technology of Energetic Materials, **65**(2): 54–63.

Persson, P., Holmberg, R. & Lee, J. (1994). Rock Blasting and Explosives Engineering. CRC Press, Boca Raton, Florida, USA.

Pomper, J., Salcher, B., Eichkitz, C., Prasicek, G., Lang, A., Lindner, M. & Götz, J. (2017). The glacially overdeepened trough of the Salzach Valley, Austria: Bedrock geometry and sedimentary fill of a major Alpine subglacial basin. Geomorphology, **209**: 147–158.

Prochaska, W. (2012). Siderite and magnesite mineralizations in Palaeozoic strata of the Eastern Alps (Austria) Field trip guide, 29th IAS meeting of Sedimentology, Schladming, Austria. Journal of Alpine Geology, **54**: 309–322.

Reiner, F. (2018). Deconvolution of seismic data from mine production blasts. Master thesis, Montanuniversität Leoben, Leoben.

Robertsson, J. O. A., Blanch, J. O. & Symes, W. W. (1994). Viscoelastic Finite-Difference Modeling. Geophysics, **59**(9): 1444–1456.

Rosner, B. (2010). Fundamentals of Biostatistics. Cengage Learning, Bosten, MA, USA.

Schmidbauer, J. (2023). Zusammenführung und Evaluierung von petrophysikalischen und geotechnischen Parametern mit gewonnenen Drohnenaufnahmen. Master thesis, Montanuniversität Leoben, Leoben.

Schulz, O., Vavtar, F. & Dieber, K. (1997). Die Siderit-Erzlagerstätte Steirischer Erzberg: Eine geowissenschaftliche Studie, mit wirtschaftlicher und geschichtlicher Betrachtung. Arch. f. Lagerst.forsch. Geol. B.-A., **20**: 65–178.

Schön, J. H. (2011). Physical Properties of Rocks, Band 8 of *Handbook of Petroleum Exploration and Production*. Elsevier B. V.

Schönlaub, H. P. (1982). Die Grauwackenzone in den Eisenerzer Alpen (Österreich). Jahrb. Geol. B.-A., **124**: 361–423.

Shearer, P. (2009). Introduction to Seismology. Cambridge University Press, Cambridge, UK, 2. edition.

Smith, B. (2001). Bayesian output analysis program (NOA) (Version 1.0.0). College of Public Health, IA: University of Iowa.

Sperl, G. (1984). Die Entwicklung des steirischen Eisenhüttenwesens vor der Einführung des Hochofens. – In: Roth, P. W. (Eds.): Erz und Eisen in der Grünen Mark, 83–94, Kulturreferat der Steiermärkischen Landesregierung, Graz.

Tauchner, C., Bleibinhaus, F. & Zeiss, J. (2018). Reducing blasting vibrations with phased source arrays - introduction and results of first travel time tomography at Mt. Erzberg mine, Austria (Abstract). 78. Jahrestagung der Deutschen Geophysikalischen Gesellschaft gemeinsam mit der Österreichischen Geophysikalischen Gesellschaft.

Tauchner, C., Reiner, F., Trabi, B., De la Puente, J. & Bleibinhaus, F. (2019). Seismic velocities from traveltime tomography at the iron ore mine Mt. Erzberg, Austria. EGU General Assembly 2019.

Thurber, C. (1983). Earthquake Locations and 3-Dimensional Crustal Structure in the Coyote Lake Area, Central California. Journal of Geophysical Research-Solid Earth and Planets, **88 (B10)**: 8226–8236.

Trabi, B. & Bleibinhaus, F. (2023). Blast vibration prediction. Geophysikal Prospekting, **71**(7): 1312–1324.

Vidale, J. (1990). Finite-difference calculation of traveltimes in three dimensions. Geophysics, **55(5)**: 521–526.

Virieux, J. (1984). SH-wave propagation in heterogeneous media: velocity-stress finite-difference method. Geophysics, **15**(4): 265–265.

Virieux, J. (1986). P-SV wave propagation in heterogeneous media: Velocity-stress finite-difference method. Geophysics, **51**(4): 889–901.

Yilmaz, O. (2001). Seismic Data Processing. Society of Exploration Geophysicists, Tulsa, OK, USA, 2nd. edition.

Yilmaz, O. (2016). The comparison of most widely used ground vibration predictor equations and suggestions for the new attenuation formulas. Environmental Earth Sciences, **75**(3): 1–11.

A Appendix

Table 10: All production blasts which are used in that study.

Date	Time	Tier	Blast Name	Ignition	Delay	Comment
06/05/2019	17:50:00	PALM-425	10003	N	33	
06/06/2019	09:50:00	ETM3-436	10004	N	33	
06/06/2019	17:50:00	OBER-364	10005	E	33	
06/07/2019	17:50:00	ETM4-173	10007	E	33	
06/11/2019	13:00:00	SYBO-363	10009	E	33	
06/12/2019	17:50:00	LIED-411	10010	N	25	
06/13/2019	09:50:00	EM4A-324	10012	N	33	
06/13/2019	17:50:00	ANTO-428	10013	N	33	
06/14/2019	09:50:00	ETM3-434	10014	E	33	
06/17/2019	09:50:00	ETM4-176	10016	E	33	
06/17/2019	17:50:00	LIED-412	10017	E	33	
06/18/2019	09:50:00	SYBO-362	10018	E	30	
06/18/2019	09:50:00	SYBO-364	10019	E	30	
06/19/2019	09:50:00	EM4A-325	10020	E	v	
06/19/2019	17:50:00	OBER-363	10021	N	33	
06/21/2019	09:50:00	ETM4-174	10022	E	30	
06/24/2019	09:50:00	ELIA-483	10023	E	30	
06/25/2019	09:50:00	SYBO-365	10024	E	v	
06/26/2019	17:50:00	PALM-426 & ANTO-416	10026	E	v	double blast
06/27/2019	09:50:00	PETE-317	10028	N	v	
06/27/2019	17:50:00	PETE-318	10029	N	33	
07/01/2019	13:45:00	ETM5-68 & ETM4-177	10031	E		double blast
07/02/2019	09:50:00	OBER-365	10033	N	33	
07/03/2019	09:50:00	ELIA-481	10035	N	33	
07/04/2019	09:50:00	EM4a-328 & ETM4-178	10036	E	v	double blast
07/05/2019	09:50:00	EM4a-327	10038	N	33	
10/04/2019	17:50:15	ANTO-436 & LIED-417	20039	E	v	double blast
10/08/2019	17:50:23	Palm-433 & Ober-372	20040	E	v	double blast
10/01/2019	09:50:27	ETM4-185	20042	N	33	
10/01/2019	13:45:06	PETE-325	20043	N	33	
10/02/2019	09:45:41	SCHI-532	20044	N	25/67	
10/02/2019	17:50:49	ANTO-432	20045	N	25/67	
10/03/2019	09:50:55	EM4A-335	20046	N	25/67	
10/03/2019	13:44:50	SCHI-533	20047	N	25/67	
10/07/2019	09:50:32	EM4A-338	20048	N	25/67	
10/07/2019	12:25:42	PETE-326	20049	N	33	
10/07/2019	17:50:13	ETA3-331	20050	N	25/67	
10/09/2019	09:50:15	ETM4-186	20051	N	33	

Continued on the next page

Table 10 (Continued)

Date	Time	Tier	Blast Name	Ignition	Delay	Comment
10/09/2019	13:45:11	POLS-533	20052	N	25/67	
08/17/2020	09:50:41	ETM4-203	30053	E	v	
08/18/2020	09:53:20	LIED-443	30054	E	33	
08/18/2020	17:49:48	LIED-441	30055	E	33	
08/19/2020	17:47:56	PETE-347 & ETA1-382	30056	E	v	double blast
08/20/2020	09:52:25	PETE-348	30057	E	v	
08/20/2020	13:45:14	SCHU-471	30058	E	33	
08/21/2020	17:50:07	LIED-439	30059	E	v	
08/24/2020	17:50:44	ANTO-462	30060	E	33	
08/25/2020	09:50:26	OBER-392	30061	E	v	
08/26/2020	09:49:55	ETM4-202 & EM4A-351	30062	E	v	double blast
08/27/2020	09:51:08	ETM3-467	30063	E	v	
08/27/2020	17:50:13	ETA3-354	30064	E	v	
08/28/2020	09:49:38	LIED-440	30065	E	v	
08/31/2020	17:49:50	ETA1-381	30066	N	33	
08/31/2020	17:50:01	PALM-450	30067	E	v	
09/01/2020	09:49:42	SYBO-392	30068	E	33	
09/01/2020	-	LIED-442	30069	E	30	
09/02/2020	13:43:38	DREI533 & DREI-534	30070	N	33	
09/03/2020	-	SYBO-391	30071	E	v	
09/03/2020	17:50:36	ANTO-463	30072	N	33	
09/07/2020	09:49:46	ETA3-355	30073	E	v	
09/08/2020	09:50:07	PETE-349	30074	E	v	
09/08/2020	13:43:29	SCHI-553	30075	-	-	
09/09/2020	13:44:26	ETM3-467 & SYBO-393	30076	E	v	double blast
09/10/2020	09:49:56	ETM5-98	30077	E	v	
09/11/2020	17:50:42	ANTO-465	30078	E	25/67	

Table 11: UTM Zone 33N coordinates and elevation data for the seismic stations

Station	UTM Easting (m)	UTM Northing (m)	Elevation (m)	VE1	VE2	VE3
1	491270.95	5263917.08	762.8	x	x	x
2	491227.7	5263988.5	786.6	x	x	
3	491424.85	5264097.12	737.3	x	x	x
4	491610.27	5263959.15	764.7	x	x	x
5	491761.16	5263835.24	832	x	x	x
6	492136.88	5263691.36	856.4	x	x	x
7	492530.08	5263542.81	1084.8	x	x	x
8	491450.4	5264382.04	740.3	x	x	x
9	491599.02	5264254.79	739.4	x	x	x
10	491717.12	5264148.6	774.4	x	x	x
11	491923.88	5263984.94	840.8	x	x	x
12	492014.39	5263948.7	813.6	x	x	x
13	492301.06	5263864.62	873.8	x	x	x
14	492411.84	5263783.79	948.7	x	x	x
15	491465.67	5264579.17	761.6	x	x	x
16	491645.86	5264429.66	738.6	x	x	x
17	491789.69	5264370.77	764.7	x	x	x
18	491918.97	5264298.46	735.3	x	x	
19	492085.1	5264139.75	721.4	x		
20	492615.69	5263971.35	951.8	x		x
21	492574.64	5263770.8	1021.5	x	x	x
22	491577.75	5264796.28	712.7	x	x	
23	491742.58	5264698.25	765.4	x	x	x
24	491921.6	5264507.95	746.2	x		
25	492021.48	5264348.67	737.3	x		x
26	492060.4	5264299.71	721.7	x		
27	492385.25	5264233.49	804.9	x		x
28	492597.28	5264116.08	898.5	x	x	x
29	491577.73	5264884.53	710.7	x	x	x
30	491737.89	5264840.73	767.6	x	x	x
31	492008.48	5264694.88	797.2	x	x	x
32	492141.84	5264633.57	820.1	x		x
33	492364.15	5264564.48	890	x		
34	492586.55	5264381.04	894.6	x		
35	492134.09	5264354.18	750.9	x		
36	492912.49	5264157.36	997.3	x	x	x
37	491433	5265189.7	748.3	x	x	
38	491488.79	5265259.41	702.2	x	x	x
39	491933.3	5265028.17	808.7	x	x	x
40	492198.6	5264922.12	821.6	x	x	x

Continued on the next page

Continued from previous page

Station	gx	gy	Elevation	VE1	VE2	VE3
41	492264.8	5264785.44	844.5	x	x	x
42	492499.99	5264669.89	868.2	x	x	
43	492650.3	5264558.11	932.5	x		
44	492811.45	5264447.11	987.5	x	x	x
45	491396.36	5265505.05	709.1	x	x	x
46	491631.68	5265296.32	712.3	x	x	x
47	491830.87	5265187.9	770.8	x	x	
48	492128.4	5265161.16	749.1	x	x	x
49	492541.07	5264835.09	860.7	x	x	x
50	492703.5	5264730.64	924.9	x	x	x
51	492908.09	5264630.7	987.2	x	x	x
52	493087.38	5264641.38	1030.6	x	x	x
53	491561.05	5265583.05	724.6	x	x	
54	491700.86	5265523.83	728	x	x	x
55	491815.61	5265414.2	730.8	x	x	x
56	492175.17	5265246.56	732.5	x	x	x
57	492386.08	5265279.29	740.1	x	x	x
58	492485.63	5265091.45	786.1	x	x	x
59	492917.14	5264893.08	891	x	x	x
60	492951.08	5264827.03	924.9	x	x	x
61	491696.86	5265833.8	760.9	x	x	
62	491939.64	5265694.32	765.8	x	x	x
63	492099.78	5265477.71	759.2	x	x	x
64	492308.26	5265441.43	761.3	x	x	x
65	492493.5	5265297.71	740.6	x	x	
66	492708.37	5265131.17	780.6	x	x	x
67	493144.76	5264982.83	923.3	x	x	x
68	493247.3	5264821.46	1023.8	x	x	x
69	491873.06	5265869.34	773.4	x	x	
70	491981.05	5265931.65	782	x	x	x
71	492159.62	5265716.13	793.2	x	x	x
72	492295.61	5265556.25	780.8	x	x	x
73	492478.31	5265605.47	775.7	x	x	x
74	492622.24	5265523.71	756.9	x	x	x
75	492874.9	5265310.68	754.4	x	x	x
76	493022.85	5265306.28	761.3	x	x	x
77	493225.88	5265435.51	787.1	x	x	x
78	492823.97	5264587.79	976.3	x	x	x
79	493523.93	5265268.69	775.2	x	x	x
80	493377.81	5265295.42	769.4	x	x	x

Continued on the next page

Continued from previous page

Station	gx	gy	Elevation	VE1	VE2	VE3
81	492526.08	5265414.14	748.6	x	x	x
82	492253.44	5264398.26	815.3	x	x	x
83	492521.81	5264487.82	886.6	x	x	x
84	492687.69	5264246.44	886.6	x	x	x
85	492224.97	5264380.29	795.2	x	x	x
86	492475.22	5263848.73	951.4	x	x	x
87	492673.95	5264030.74	960.1	x	x	x
88	491570.91	5264594.69	718.8		x	
89	491573.01	5264691.15	719.2			x
90	491676.33	5264682.78	730.9			x
91	491668.38	5264595.66	734.7			x
92	491656.25	5264640.58	725.3			x
93	492623.61	5265058.82	790.7			x
94	492622.18	5265177.52	767.5			x
95	492746.28	5265177.36	770.8			x
96	492727.57	5265078.47	797.3			x
97	491844.04	5265242.79	741.4		x	
98	491632.54	5265006.81	718.8			x
99	492609.96	5263783.1	1016.1			x
100	492068.19	5264327.6	730			x
101	492910.65	5264317.74	978.7			x
102	492129.92	5264664.93	819.7			x
103	492777.7	5265270.01	748.9			x
104	492835.57	5265268.38	751.9			x
105	492368.4	5264586.26	890			x
106	493005.58	5264708.27	1008.7			x
107	492739.87	5264016.65	986.3			x
108	492028.43	5264365.22	741.2			x
109	492541.14	5264480.23	894.3			x
110	491923.29	5264320.02	734.9			x
111	492661.89	5263960.18	976.2			x
112	492315.14	5264611.56	884.7			x
113	492602.17	5264348.79	890			x
114	492751.69	5264688.02	933.5			x
115	492911.43	5264463.66	1010.4			x
116	492181.1	5264616.07	838.2			x
117	492571.43	5264387.17	895.1			x
118	492574.22	5264806.38	864.8			x
119	492634.2	5264626.15	919.4			x

Table 12: Performance of the numerical waveform modelling method compared to the JI.

Blast	R^2_{num}	RMS_{num}	R^2_{JI}	RMS_{JI}
10005	0.51	4.98	0.81	2.60
10009	0.36	4.70	0.71	3.03
10014	0.57	4.14	0.72	2.77
10016	0.36	3.97	0.62	3.85
10017	0.71	3.25	0.68	5.17
10018	0.27	7.03	0.57	4.94
10019	0.20	8.41	0.47	4.23
10020	0.45	4.09	0.56	3.43
10022	0.41	5.02	0.50	4.43
10024	0.37	4.28	0.58	3.39
30053	0.39	6.00	0.40	4.18
30054	0.75	3.75	0.76	3.02
30055	0.62	3.35	0.76	4.55
30057	0.60	4.42	0.68	4.75
30058	0.36	5.40	0.38	5.48
30059	0.70	4.21	0.92	3.42
30060	0.59	4.42	0.90	2.21
30061	0.64	4.84	0.74	2.87
30063	0.70	4.48	0.75	3.31
30064	0.49	3.79	0.52	3.20
30065	0.61	6.33	0.74	5.13
30067	0.51	4.99	0.77	2.68
30068	0.35	3.03	0.44	2.55
30069	0.83	4.56	0.75	3.65
30071	0.43	4.73	0.42	4.11
30073	0.28	5.96	0.42	4.12
30074	0.32	5.67	0.57	5.70
30077	0.36	7.14	0.50	6.34
30078	0.70	4.44	0.93	2.08

Table 13: Site factors (ρ) from the joint inversion for all receiver positions.

Station	**Site Factor (ρ)**	**Station**	**Site Factor (ρ)**	**Station**	**Site Factor (ρ)**
1	1.20265	41	1.32405	81	1.39746
2	1.45315	42	0.53932	82	0.37703
3	1.34711	43	0.53638	83	0.65599
4	1.20796	44	0.5988	84	0.52186
5	1.11718	45	2.31341	85	1
6	0.39497	46	0.9012	86	0.45374
7	0.7697	47	2.09382	87	0.46445
8	1.65881	48	1.37274	88	1.55634
9	0.99838	49	1.03155	89	0.85545
10	1.19633	50	1.21194	90	0.92056
11	0.49489	51	0.52806	91	1.0669
12	0.42651	52	0.58227	92	1.3023
13	0.36514	53	2.50815	93	1.62504
14	0.41126	54	3.17001	94	1.90805
15	0.85812	55	2.54936	95	1.76151
16	1.95636	56	2.3878	96	1.56331
17	1.3203	57	1.46626	97	2.04172
18	0.55641	58	1.66875	98	2.65163
19	0.37036	59	1.23529	99	0.29828
20	0.50107	60	1.32185	100	0.48606
21	0.335	61	1.53007	101	0.6817
22	2.04439	62	1.97684	102	0.55419
23	0.87742	63	2.14517	103	1.06493
24	0.81483	64	2.58461	104	3.59221
25	0.46192	65	1.30358	105	0.53917
26	0.49016	66	1.68092	106	0.83389
27	0.37119	67	0.89097	107	0.37526
28	0.30848	68	1.27266	108	0.44848
29	3.50391	69	1.66159	109	0.44251
30	0.77339	70	2.12363	110	0.54858
31	1.09285	71	2.1242	111	0.34211
32	0.50295	72	1.72366	112	1.05413
33	0.61985	73	1.47007	113	0.48365
34	0.89636	74	1.37731	114	1.10464
35	0.57594	75	2.48952	115	0.5963
36	0.53374	76	1.7199	116	0.46687
37	1.96301	77	3.42579	117	0.70201
38	1.4699	78	0.54902	118	0.87963
39	1.80144	79	3.07587	119	0.41976
40	1.8069	80	5.37717		

Table 14: Declaration of the usage of AI-based tools

Subject	**AI Contribution (in %)**	**Tool/ Version**	**Reference to Prompting**
Orthography, word order, grammar and typo corrections	15%	ChatGPT, V4.0	No prompts of copyright relevance
Improvement of linguistic readability	5%	ChatGPT, V4.0	No prompts of copyright relevance
AI-assisted Spelling, punctuation, and grammar correction; readability improvement	20%	Grammarly	No prompts of copyright relevance

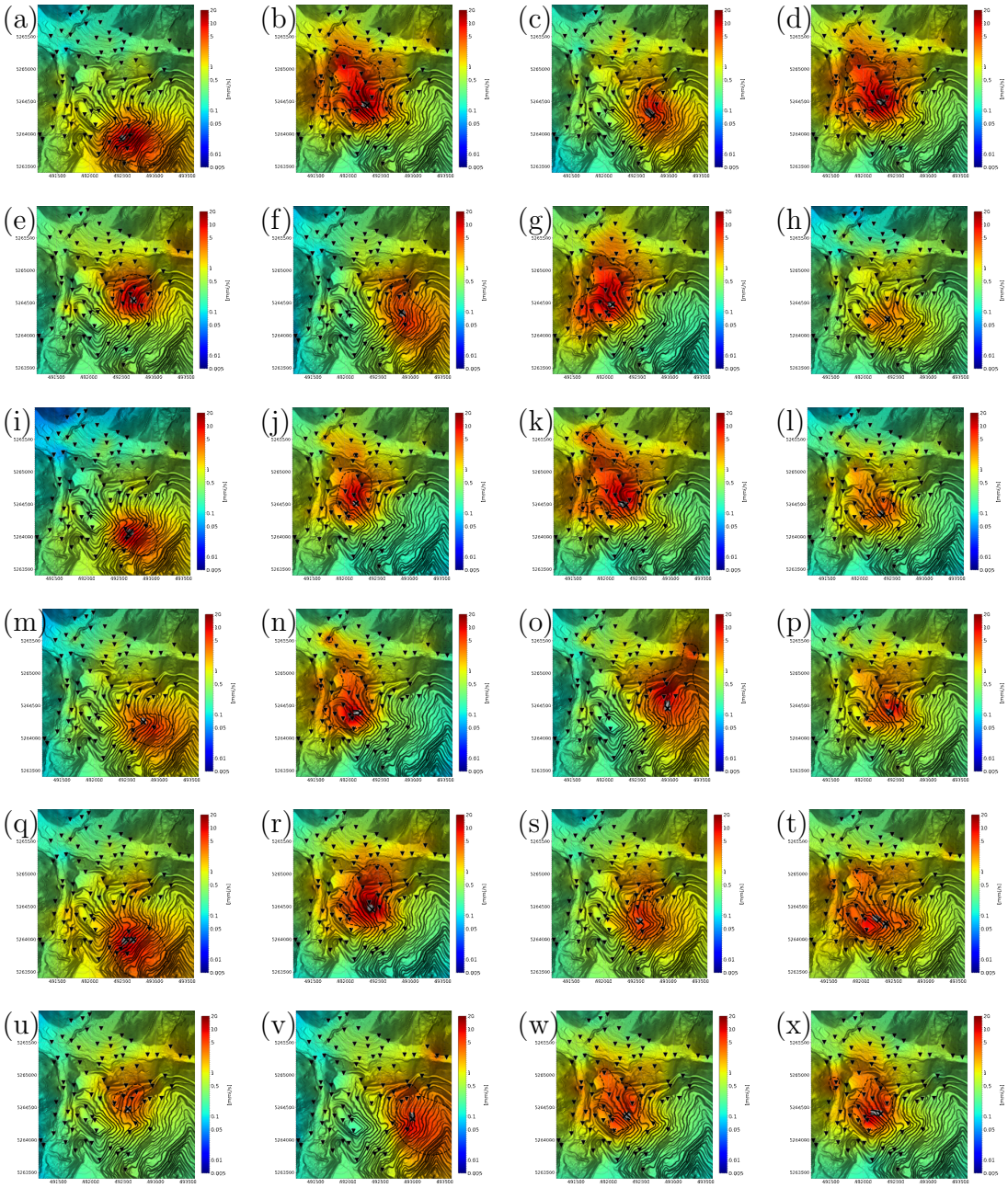

Figure 100: PGV map of production blasts 10003, 10004, 10005, 10009, 10010, 10013, 10014, 10016, 10017, 10018, 10019, 10020, 10021, 10022, 10023, 10024, 10026, 10028, 10029, 10031, 10033, 10035, 10036 and 10038 in Figures (a) to (x). The dashed contour line highlights the boundary beyond which the most sensitive buildings under the most unfavourable frequency content would be affected.[1]

[1]DEM data source: CC-BY-4.0: State of Styria - data.steiermark.gv.at

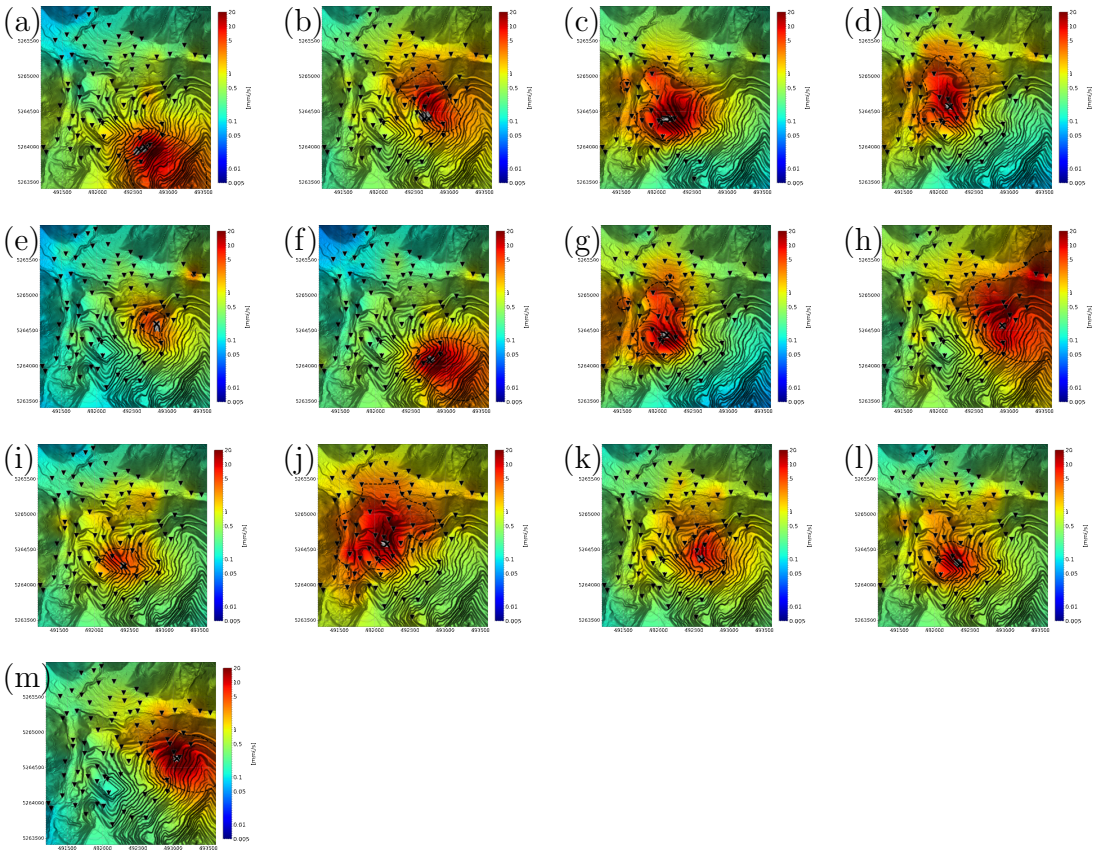

Figure 101: PGV map of production blasts 20039, 20040, 20042, 20043, 20044, 20045, 20046, 20047, 20048, 20049, 20050, 20051 and 20052 in Figures (a) to (m). The dashed contour line highlights the boundary beyond which the most sensitive buildings under the most unfavourable frequency content would be affected.[1]

[1]DEM data source: CC-BY-4.0: State of Styria - data.steiermark.gv.at

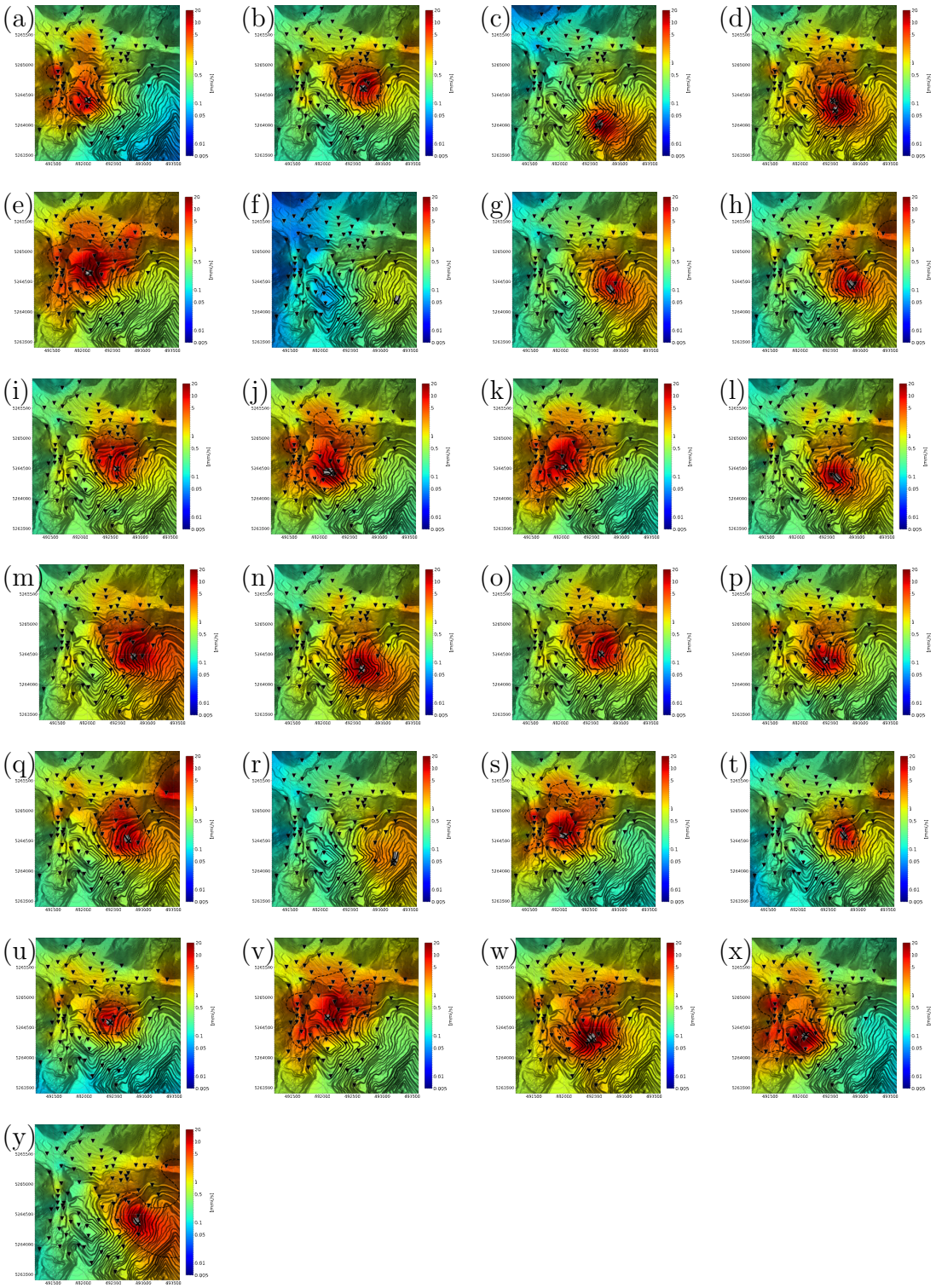

Figure 102: PGV map of production blasts 30053, 30054, 30055, 30056, 30057, 30058, 30059, 30060, 30061, 30062, 30063, 30064, 30065, 30066, 30067, 30068, 30069, 30070, 30071, 30072, 30073, 30074, 30076, 30077 and 30078 in Figures (a) to (y). The dashed contour line highlights the boundary beyond which the most sensitive buildings under the most unfavourable frequency content would be affected.[1]